AN ABSTRACT OF THE THESIS OF

Jon W. Williamson for the degree of Master of Science in Materials Science presented on June 5, 2015

Title: Electronic Properties of Passive Films on Carbon Steel Rebar in Simulated Concrete Pore Solutions

Abstract approved:

_____

O. Burkan Isgor

In the highly alkaline environment of concrete, carbon steel rebar is protected against corrosion by a passive oxide/oxyhydroxide film. Understanding the characteristics of this passive film, and how it depassivates, is the key for mitigating problems associated with steel corrosion in concrete. Although a large number of electrochemical and analytical studies have been conducted on the passivity of steel in concrete, current mechanistic models do not explain all experimental observations about the chloride-induced depassivation process. One area that is not studied extensively is the electronic properties of semiconductive passive films such as those on steel rebar; a better understanding of these properties will provide additional information to improve the mechanistic models for chloride-induced depassivation of carbon steel in concrete. This research project used Mott-Schottky (M-S) analysis along with other electrochemical

techniques to study the electronic properties of passive films that form on carbon steel exposed to simulated concrete pore solutions. Both passivation and chloride-induced depassivation processes were investigated, and changes in electronic properties during these processes were monitored. The main parameters of this study included the concrete pore solution composition, pH, and chloride amount. Challenges of using M-S analysis to study the electronic properties of passive films were also discussed. Results showed that the passive film on steel rebar is an n-type semiconductor with two discrete donor species. The space charge layer shows a thickness of around 0.4 nm at full passivation, a donor density on the order of 10^{21} cm^{-3}, and a flatband potential between -0.5 to -0.6 V vs. saturated calomel reference electrode (SCE). Chloride concentrations above the chloride threshold resulted in loss of linearity of M-S plots, indicating a shift of the passive film from a crystalline to an amorphous structure. In addition to experimental investigations, numerical models used to describe the electronic properties of passive films were investigated, and an optimal numerical model for simulating the steel rebar passive film was identified.

Electronic Properties of Passive Films on Carbon Steel Rebar in Simulated Concrete Pore Solutions

by

Jon W. Williamson

A THESIS

submitted to

Oregon State University

in partial fulfillment of

the requirements for the

degree of

Master of Science

Presented June 5, 2015

Commencement June 2015

Master of Science thesis of Jon W. Williamson presented on June 5, 2015.

APPROVED:

Major Professor, representing Materials Science

Director of the Materials Science Program

Dean of the Graduate School

I understand that my thesis will become part of the permanent collection of Oregon State University libraries. My signature below authorizes release of my thesis to any reader upon request.

Jon W. Williamson, Author

ACKNOWLEDGEMENTS

I want to begin by thanking my advisor Dr. O. Burkan Isgor. He is not only an excellent supervisor and brilliant scholar, but his friendship and patience in guiding me through this research will never be forgotten. I cannot express how appreciative and thankful I am for the impact he has had in my growth as a student, researcher, and engineer. It was truly an honor to be able to work with him and his research group at Oregon State University.

I would also like to thank my wife, Kaylee, for her constant source of support and encouragement through this process. Without her patience and timely words of love, inspiration, and optimism, this thesis would simply have not been possible.

Additionally, I would like to thank my colleague, Dr. Vahid J. Azad, for all his help with numerical modeling and analysis.

Thank you as well to my graduate committee members: Dr. Bill Warnes, Dr. Jason Ideker, and Dr. Ben Leshchinsky.

Finally, I wanted to thank all of my family and friends, including my mother, Laurie, and my father, Will, for the incredible of love and support over the years.

CONTRIBUTION OF AUTHORS

Dr. O. Burkan Isgor advised on data collection, analysis, and interpretation of Chapters 2, 3, and 4. Dr. Vahid J. Azad performed the numerical model analysis and advised on model interpretation in Chapter 4.

TABLE OF CONTENTS

TABLE OF CONTENTS (Continued)

Page

TABLE OF CONTENTS (Continued)

Page

TABLE OF CONTENTS (Continued)

Page

LIST OF FIGURES

Figure Page

LIST OF FIGURES (Continued)

Figure Page

LIST OF FIGURES (Continued)

Figure Page

LIST OF FIGURES (Continued)

Figure Page

LIST OF TABLES

LIST OF TABLES (Continued)

Table Page

LIST OF APPENDIX FIGURES

Appendix Figure Page

LIST OF APPENDIX FIGURES (Continued)

Appendix Figure Page

1. General Introduction

1.1. Layout of This Thesis

This thesis follows the manuscript option for the Masters of Science Thesis in the Oregon State University Graduate School Thesis Guide 2014-2015. The main focus of the thesis is the investigation of the corrosion of reinforcing steel in concrete, which is one of the primary causes of durability-related issues with concrete structures. Corrosion of reinforcing steel in concrete is a result of the breakdown of a thin passive oxide film that forms on the surface of the steel [1, 2]. This oxide film protects the underlying steel from corrosion in oxidizing environments. Although the structure and mechanical properties of this oxide film have been studied extensively using electrochemical, microscopic, and kinetic techniques [3-6], the electronic properties of the film have not been well studied. Past works have found a direct correlation between the electronic properties of these oxide films and the corrosion behavior of the metal [7-9]. Therefore, the primary objective of this thesis is to provide a comprehensive picture of the electronic properties of the protective oxide film on steel reinforcement in concrete. This was accomplished by performing a series of electrochemical experiments on carbon steel reinforcement samples in aqueous solutions that are representative of those seen in concrete. Three technical papers containing original research were developed to create a holistic view of the electronic properties of steel reinforcement in concrete. The thesis is organized in the following structure:

Chapter 1: *General Introduction* – This chapter provides a background of the corrosion of concrete reinforcement, including the concept of passivity and how

environmentally-induced destruction of the protective oxide film is the cause of corrosion in steel reinforcement. The electronic properties of the protective oxide film are tied to its corrosion behavior, and methods to obtain these electronic properties are outlined. The chapter ends with a literature review of the existing studies that evaluate the electronic properties of carbon steel in alkaline environments.

Chapter 2: *Manuscript 1* – The title of the first technical paper is "Electronic Properties of Passive Films of Carbon Steel in Highly Alkaline Environments using Mott-Schottky Analysis". This paper first defines a systematic methodology for employing Mott-Schottky analysis to the carbon steel system. This methodology is then used to determine the evolution of the electronic properties of the protective oxide film, as the film forms in a simulated concrete pore solution. The manuscript will be submitted to the Journal of Applied Surface Science (Elsevier).

Chapter 3: *Manuscript 2* – The title of the second technical paper is "The Effect of Concrete Pore Solution Composition and Chlorides on the Electronic Properties of Passive Films on Carbon Steel Rebar". This paper investigates the effect of concrete pore solution composition on the observed electronic properties of both partially-protective and fully-protective oxide films. Special attention is paid to the effect of varying chloride amounts in the solution, the solution pH, and the presence of sulfates in the solution. Reasons for the observed changes to the electronic properties are discussed based on the known physical properties of protective oxide films, and an electronic band structure for the protective oxide film on steel reinforcement is proposed. The manuscript will be submitted to the Journal of Corrosion Science (Elsevier).

Chapter 4: *Manuscript 3* – The title of the third technical paper is "Modeling electronic properties of the passive films on carbon steel in simulated concrete pore solutions". This paper begins with a description of the existing numerical models used to describe the electronic properties of protective oxide films. These models are then applied to the carbon steel rebar system, and the model that best represents experimental results is identified. The paper concludes with a sensitivity analysis using this model. The manuscript will be submitted to the Journal of Electrochemical Society.

Chapter 5: *General Conclusion* – This chapter provides a summary of the objectives and findings of this thesis and ties the three technical papers together. Areas for future work on this topic are also discussed.

1.2. Introduction

1.2.1. General

Concrete is the most widely used construction material in the world — its annual production exceeds 10 billion tons globally [10]. It is the primary structural material in most critical infrastructure, e.g., highways, bridges, dams, canals, pipelines, and airports. It is also used extensively in other common structural components such as foundations, frames, slabs, walls, columns, and beams. One of the major causes of durability-related issues in reinforced concrete structures is the corrosion of steel reinforcement (rebar), which leads to safety and serviceability issues that are rather expensive to mitigate. A summary of the cost of corrosion to highway bridges alone has found that the direct cost of corrosion is estimated to be $8.29 billion annually [11]. The study also found by life-cycle analysis estimates that indirect costs of corrosion to

highway bridges, including traffic delays and lost productivity, approaches $100 billion.

1.2.2. Passivity, Depassivation, and Corrosion - Overview

In the highly alkaline (pH>13) environments typical in concrete, a protective or "passive" oxide film forms on the surface of steel reinforcing bars (i.e., rebar) that reduces corrosion rates to negligible values — typically less than 10^{-3} mm/year [12]. The stability of this passive film is critical to the corrosion resistance of steel reinforcement; thus, the concept of *passivity* will first be elaborated here as it also forms the foundation of the objectives of this research. In simple terms, passivity results when metals and alloys form a thin, protective oxide layer on their surfaces which protects them from corrosive environments [13]. It protects the vulnerable, underlying metal from the destructive electrochemical reactions that cause corrosion. When the passive film breaks down, the underlying metal is then susceptible to these electrochemical reactions, and the mechanical integrity of the metal as a whole is in jeopardy. This passive film breakdown is called *depassivation*, and this phenomenon occurs in certain aggressive environments [14]. Passivity is a relatively common phenomenon that is prevalent in many structural metals (e.g., iron [15], nickel [16], aluminum [17], copper [18], and titanium [19]) and alloys (e.g., steel [20]). Without passivity, most of these materials would not be useful in structural applications. In fact, the phenomenon of passivity and its prominent place in society has caused it to be recognized as "the enabler of our metals-based civilization" [21].

The topic of passivity has been studied extensively by researchers since the early 1800s, beginning with Faraday in the 1840s. He described the idea of the passive film as an

invisible surface oxide film that forms in some environments, is unstable in others, and is destroyed by mechanical disturbing or scratching [22]. Although this primitive definition has some accuracies, modern descriptions for the concept of passivity can be broken down into two primary technical definitions. Both are described in the seminal work by Jones [22]. The first definition describes passivity as a condition of corrosion resistance due to the formation of thin surface films under oxidizing conditions with high anodic polarization. The second definition involves metals and alloys that naturally have a barrier film on the surface which is less corrosive than the underlying metal in active (i.e., noble) potential, but only for very little anodic polarization. Of these two definitions, the first definition applies to steel rebar in concrete and will be used in the present study.

To help further the understanding of the concept of passivity, graphic presentations are often used. For example, Pourbaix diagrams [23] illustrate graphically the stability of one or more metal oxides at different electrode potentials and environments. It shows the oxide films that are protective in nature (i.e., passive or immune) versus those that are not protective (i.e., corrosive or active). The Pourbaix diagram for iron is shown in Figure 1.1 and is helpful when analyzing the electrochemical properties of steel [24]. In the pH range for concrete (pH>13), Figure 1.1 shows that iron is protected from corrosion at potentials positive to about -0.6 V vs. SCE (saturated calomel electrode). However, if the pH decreases below around pH 9, corrosion is possible for a wider potential range.

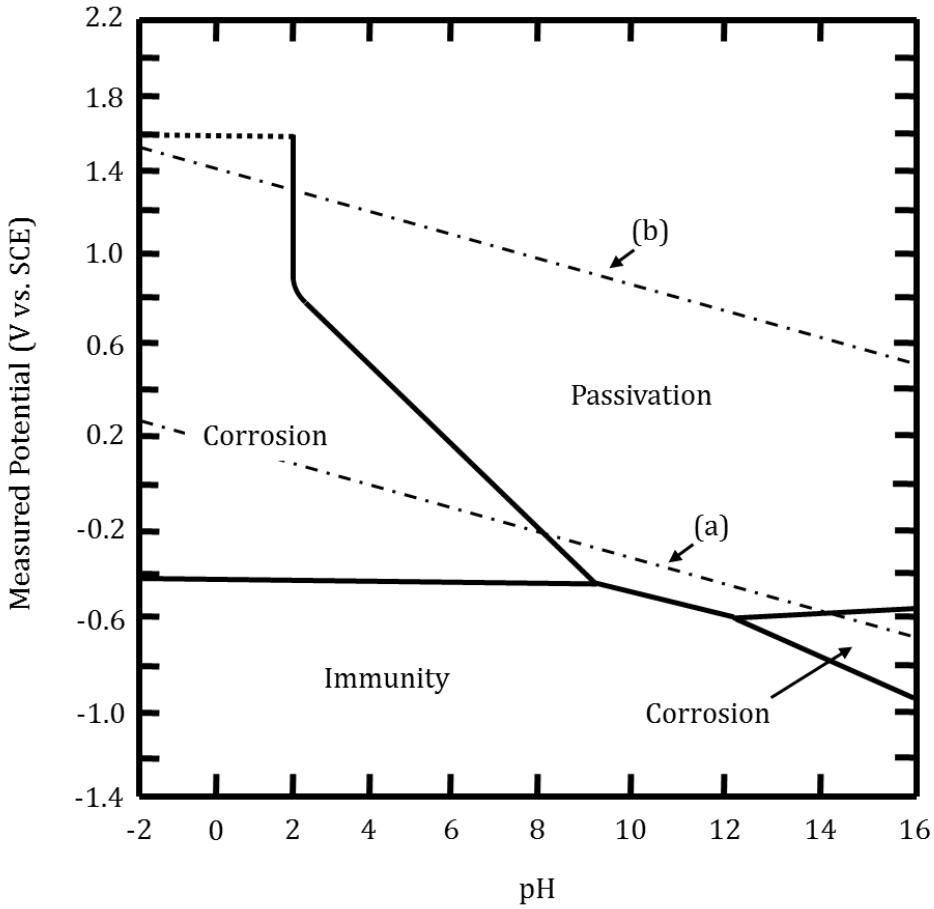

Figure 1.1: Pourbaix diagram of iron. Pourbaix diagrams are typically plotted for only dilute solutions and pure metals. Lines (a) and (b) indicate the locations where hydrogen in the solution evolves into water and where water decomposes into oxygen, respectively. Modified from Jones [22].

Another way to show the concept of passivity graphically is by looking at an anodic polarization diagram such as those shown in Figures 1.2 and 1.3 [1]. Anodic polarization curves indicate the corrosion rate of metals in a given environment by applying a potential to the metal sample. This potential is swept in the positive (i.e., anodic) direction over a defined potential range, and the current density response of the sample is measured, where the current density is a direct indicator of the corrosion rate [22]. Equation 1.1 shows this relationship, where the corrosion rate, *r*, is proportional

to the current density, *i*, and the atomic weight, *a*, and inversely proportional to the number of equivalents exchanged, *n*, and the Faraday constant, *F*.

$$r = \frac{ia}{nF} \tag{1.1}$$

If the metal cannot produce a passive film in a given environment (e.g., at a specific pH or applied potential that is not in the passive region according to Figure 1.1), then as the potential applied to the sample is increased, the corrosion rate will increase as well [22], as shown in Figure 1.2.

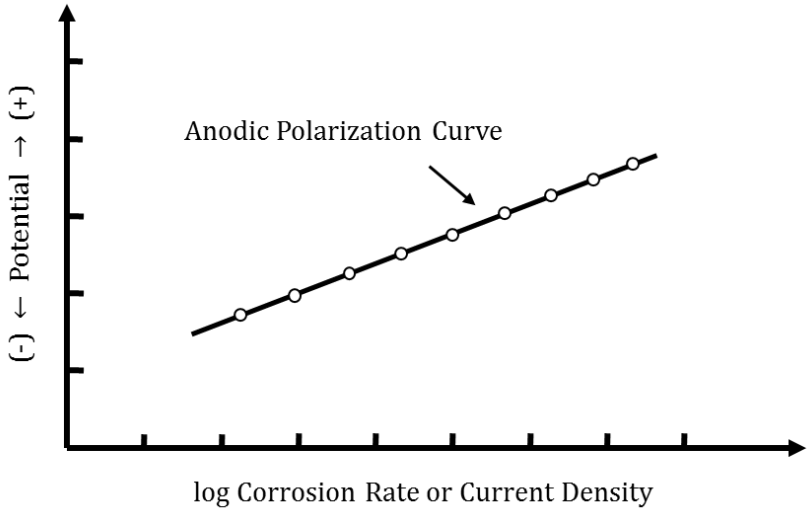

Figure 1.2: Schematic of an anodic polarization curve for a sample in the active potential region. This is a concept illustration, so units are not provided.

However, if the metal can produce a passive film in a given environment (e.g., at a specific pH or applied potential that is in the passive region according to Figure 1.1), the increase in current response from increasing applied potential is substantially reduced. In fact, in this passive region, the corrosion rate can actually decrease with increasing potential [22, 25]. Figure 1.3 shows a graphic representation of how an

anodic polarization diagram reveals passive behavior. At low (i.e., cathodic) potentials, the corrosion rate increases exponentially, since the sample is not yet in a passive state; the sample is still in an *active* state. As the potential is increased and reaches the primary passive potential, E_{pp}, passive behavior begins. At this point, the corrosion rate is significantly reduced and then remains constant at this decreased level. The passive region lasts until the applied potential is so high that it breaks down the passive film. Once this *transpassive* state is reached, the sample quickly oxidizes and deteriorates. The transpassive breakdown commonly occurs near the oxygen reduction potential, particularly for stainless steels and chromium-bearing nickel alloys [22].

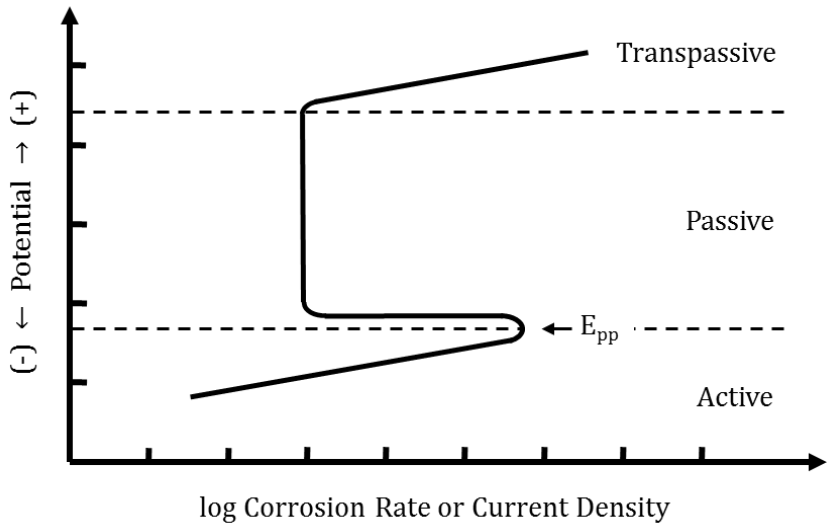

Figure 1.3: Schematic of an anodic polarization curve showing active-passive polarization behavior. This is a concept illustration, so units are not provided. Modified from Jones [22].

Several environmental circumstances can cause the premature destruction of passive films. One of the most prevalent circumstances in many different environments is the presence of excessive chloride salts. This commonly occurs in marine settings where sea water and spray expose concrete reinforcement to high chloride levels [13].

Cramer et al. [26] illustrated this occurrence and the problems associated for Oregon coastal bridges. A second source of chlorides is from deicing chemicals [13]. These deicing chemicals often contain salts that can pool on bridge deck surfaces and cause corrosion of the steel reinforcement. The critical level of chlorides required to cause depassivation of the passive oxide film is called the chloride threshold, and examples of chloride thresholds specifically for carbon steel rebar in simulated concrete pore solutions are given by Ghods et al. [2].

Another circumstantial causation of depassivation specifically of carbon steel rebar in concrete is a decrease of the pH in the surrounding concrete pore solution; this can be caused by carbonation of the concrete cover, which is a reaction of carbon dioxide in the atmosphere with the calcium bearing phases in concrete [13]. This reaction causes the calcium bearing phases to convert to calcium carbonate, which subsequently lowers the pH of the concrete pore solution. When this solution pH lowers beyond a certain level, the steel rebar is taken out of a passive state and into an active state, as can be seen in the Pourbaix diagram in Figure 1.1.

1.2.3. Passive films that form on carbon steel in concrete

The concepts of passivity and chloride-induced depassivation of carbon steel rebar in highly alkaline environments (pH>13) seen in concrete pore solutions have been extensively studied and researched using electrochemical techniques [1-4, 6, 27-29]. These techniques have revealed macroscopic information about the steel rebar passive film and have shown that chloride-induced depassivation can occur at a wide range of chloride levels [30]. This discrepancy of chloride thresholds is the result of several factors, including inconsistent steel rebar surface conditions [31-33] and variable

concrete pore solution compositions [34, 35]. To more fully understand the fundamental mechanisms governing the variation of chloride thresholds and depassivation of carbon steel rebar, spectroscopic and kinetic techniques were employed to characterize the passive film at a nanoscale.

For example, nano-scale x-ray photoelectron spectroscopy (XPS) and electron energy loss spectroscopy (EELS) were used to characterize the elemental composition and thickness of the passive film of steel rebar in various concrete pore solution compositions [5, 36, 37]. These studies found that the passive film thickness ranges between 3-15 nm. It can be characterized as a bilayer structure comprised predominantly of Fe^{II} oxides/oxyhydroxides near the substrate surface and Fe^{III} oxides/oxyhydroxides near the free surface. The Fe^{II}-rich layer was found to be only 2-3 nm thick, while the Fe^{III}-rich layer was found to be much thicker at 10-15 nm. However, the Fe^{II}-rich layer was also found to be the protective layer, while the Fe^{III}-rich layer was found to be porous and not protective. The addition of chlorides resulted in a decrease of the passive film thickness and caused the Fe^{III}/Fe^{II} ratio to increase through a chemical reaction between the Fe^{II}-rich oxides and chlorides. This chemical reaction apparently oxidized the Fe^{II} by one valence state to Fe^{III}, which as mentioned before is less protective.

Spectroscopic techniques also found that the sample surface finish has a significant effect on the chloride threshold of steel rebar. For example, Ghods et al. [2] found using electrochemical impedance spectroscopy (EIS) and open circuit potential (OCP) monitoring that turned and polished rebar samples immersed in a simulated concrete pore solution have chloride thresholds over an order of magnitude greater than those

for as-received steel rebar containing mill scale. Alonso et al. [38] likewise showed that ribbed steel rebar samples embedded in mortar bars show a higher tendency to corrode and a lower corrosion potential compared to smooth rebar samples.

A major weakness with spectroscopic techniques such as XPS and EELS, as highlighted by Gunay et al. [6], is that they are not *in situ* techniques; they do not characterize the film formation or dissolution processes over time. To address this issue, a kinetic technique called electrochemical quartz crystal nanobalance (EQCN) [39, 40] was used which monitors nanoscale passivation and depassivation processes over time. Gunay et al. [6] used this technique to perform *in situ* measurements of nanoscale mass changes occurring on the steel rebar surface while immersed in a simulated concrete pore solution. This study found that the protective film formed in two primary steps. The first step lasted for about the first 10-20 minutes of sample exposure time in the passivating solution, during which time a significant mass increase was recorded. This corresponded to impedance and phase angle data obtained simultaneously on the sample that showed the majority of passivation of the samples occurred during this initial time period. This then suggests that an extremely dense, protective passive film forms during the initial exposure time. After this initial passivation step of 10-20 minutes, a second period of passivation proceeded for the remainder of the exposure time, whereby the mass on the steel rebar surface continued to increase – but this time at a much slower rate. Impedance and phase angle data additionally remained relatively constant during this second passivation step. This suggests that the mass increase during this second step is from the formation of a more porous oxide that is less protective in nature. When chlorides were added to the

solution, small mass gains were initially recorded. These mass gains suggest that the chlorides are being adsorbed into the outer oxide layer, which supports the predictions of several depassivation models [41-44].

1.3. Problem Definition

Although electrochemical, microscopic, spectroscopic, and kinetic techniques have been amply used to characterize numerous aspects of the passive film on steel rebar in simulated concrete pore solutions, they do not describe the electronic properties of the film. In past research, the electronic properties of passive metal oxide films have proved to be closely related to the corrosion behavior of the passive film. Some examples of this correlation are highlighted below for various metals, alloys, and passivating solutions.

For the passive film on aluminum under varying passivating environments, Szklarska-Smialowska [7, 45] and Liu et al. [46] found that the film was an n-type semiconductor, and that one electronic property, the *donor density*, corresponded well to the stability of the film. They found that films formed in air have a higher donor density and consequently a greater instability compared to the film formed in a Na_2SO_4 solution. Additionally, they found that the presence of chlorides causes a significant increase in donor density which again results in increased film instability as greater disorder is added to the film. Hakiki et al. [47, 48] studied the passive film on stainless steels in a borate buffer solution and found that the passive film for this alloy forms an n-p junction which controls the electronic structure of the passive film. They found that at passive film formation potentials above another electronic property, the *flatband*

potential, the passive film acts as an n-type semiconductor and the donor density of the film is strongly a function of this film formation potential. At lower formation potentials that are cathodic to the passive region of stainless steel, the donor density is extremely high and corresponds to a more disordered film that has a higher susceptibility to pitting. Schmuki and Böhni [49, 50] found that the pitting properties of stainless steel in Na_2SO_4 and NaCl solutions is directly related to the size of a different electronic property, the *band gap energy*, where a larger band gap energy corresponds to enhanced pitting properties. Other authors [51, 52] have likewise found strong correlation between the semiconductive nature of stainless steel passive films and resistance to the pitting corrosion. Cheng and Luo [53, 54] showed this correlation between an increase in donor density and decreased nature of the passive film to be true with carbon steel in chromate solutions. They also linked the onset of metastable pitting events in the passive film to the flatband potential and the onset of shallow and deep donor ionization in the space charge layer of the passive film. Gerischer [55] showed that a relationship exists between the electronic properties of the passive film on iron in aqueous solutions and the onset of the transpassive potential region. Santamaria et al. [56] showed that for Mo-Ta alloys in acetic acid-based solutions, the presence of Mo in the passive film increases the flatband potential with respect to the pure Ta_2O_5 films. Increased amounts of Mo in this film create changes in the electronic behavior of the film from insulating to semiconducting, and also changes the band gap of the film. The authors showed that these changes in the electronic properties with varying the Mo amount in the film helped to explain the role of Mo in controlling the corrosion of Ta-enriched alloys. Lastly, for Cu-Ni alloys in NaOH solutions, Wu et al. [57]

showed that an increase of the Cu concentration in the alloy resulted in increasing the flatband potential and decreasing the acceptor density of the film. This, they showed, corresponded to an increased corrosion rate.

In summary, the past research has clearly shown that a direct correlation between the electronic properties of semiconductive passive films and the corrosion behavior of that material exists. High dopant densities tend to correlate well to increased passive film instability, which could lead to passive film breakdown and pit initiation due to the application of high anodic potentials or chloride ingress. The formation potential of the passive film was shown to be strongly correlated to the location of the flatband potential, where higher formation potentials generally resulted in more protective oxide films. Lastly, the corrosion rate was shown to increase with an increasing semiconductor band gap energy. Because the passive oxide film on steel rebar is a semiconductor [58, 59], similar correlations to the electronic properties are sure to exist. In order to adequately characterize the passive film on carbon steel rebar in simulated concrete pore solutions, the electronic properties of that passive film must be addressed. This information will be added to the existing knowledge supplied by electrochemical, microscopic, and kinetic techniques to provide a comprehensive picture of the steel rebar passive film, and it will significantly aid in the development of existing passivation and depassivation mechanistic models.

1.4. Detailed Theoretical Background and Literature Review

1.4.1. Energetics of the Semiconductor-Electrolyte Interface

Having established the necessity in determining the electronic properties of a passive film to fully characterize its structure and corrosion behavior, a review of the semiconductor electronic band structure and the energetics of the semiconductor-electrolyte interface would be of significant value. To begin, some definitions will be helpful for understanding the terminology used throughout this work.

1.4.1.1. Semiconductor

The electronic structure of a semiconductor can be described in terms of energy levels and energy bands. In a solid, large numbers of atoms are bound closely together, and each atom has electrons that exist at discrete energy levels. These energy levels overlap, and in semiconductors, these discrete energy levels are packed so tightly together that they form a continuum of energy levels called an *energy band*. An electron within this solid may have an energy position located anywhere in the energy band. These energy bands have finite widths that are dependent on the amount of overlap between adjacent energy levels. Because of these finite widths, leftover ranges of energies are left which are not covered by any energy band. Generally speaking, energy bands near the nucleus of the atoms in the solid (e.g., the *1s* orbital) have extremely narrow energy bands, whereas those further away from the nucleus have much wider energy bands. The energy band that is associated with the valence electrons of the atoms in the solid is called the *valence band*, and this is typically a few electron volts (eV) wide [60]. The highest energy level in the valence band, E_V, can also be thought of as a measure of the

ionization potential of the bulk material. The energy band associated with the first excited state of these valence band electrons, which is typically unoccupied by any electrons, is called the *conduction band*. The conduction band, being further away from the nucleus of the atoms in the solid, is typically broader. It typically overlaps any energy bands located at an even higher energy state, making the conduction band essentially an energy continuum spanning from its lowest energy state to an infinite energy level [60]. The lowest energy level in the conduction band, E_C, can also be thought of as a measure of the electron affinity of the bulk material. Figure 1.4 shows an electronic band structure diagram to graphically illustrate the locations of each band on an energy and potential scale.

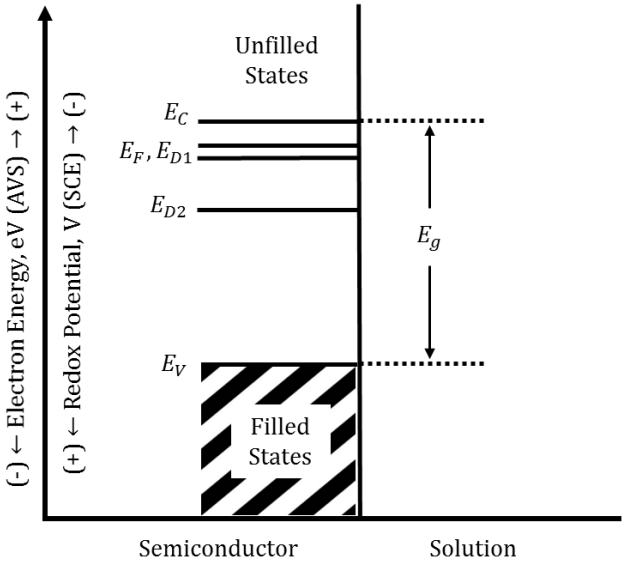

Figure 1.4: Simplified energy level model for an n-type semiconductor under anodic polarization in contact with an electrolyte solution. E_C is the lower edge of the conduction band, and E_V is the upper edge of the valence band. The distance between these is the band gap of the passive film, E_g. E_F is the Fermi level of the semiconductor under the applied anodic potential. E_{D1} and E_{D2} are the energies of two impurity donor states located within the band gap. The distances are not to scale. This is a concept illustration, so units are not provided.

In metals, no gap exists between the valence and conduction bands. However, in semiconductors and insulators an energy gap between E_V and E_C is present. This gap between the energy bands, where no electrons are permitted, is called the *band gap*, E_g. And herein lies the difference between insulators and semiconductors. Semiconductors typically have relatively small band gaps on the range of 1eV to 4eV, whereas insulators typically have larger band gaps [61]. For electronic conductivity in a solid to occur, electrons must be excited from the filled valence band to the unfilled conduction band. This requires that enough energy is supplied to the electron for it cross the band gap, where no electrons are allowed to exist. For insulators, this gap is so large that electrons cannot traverse the band gap without an enormous amount of supplied energy. For semiconductors, however, the band gap is relatively small, and electrons can be promoted to the conduction band with relative ease. Electrons that leave the valence band leave a vacant location that is now positively charged. This positively charged site is called a *hole*. Holes, like electrons, are considered charge carriers that can move throughout an energy band by the transfer of a new electron. Therefore, the two charge carriers in semiconductors and insulators are electrons and holes, and each are oppositely charged.

Pure semiconductors without any impurities are called *intrinsic* semiconductors, and conduction occurs primarily by the thermal or photochemical excitation of electrons from the valence band to conduction band. However, if impurities are added to the semiconductor, energy levels may be added to the band gap which supply additional charge carriers for promotion to the conduction band. The addition of impurities is called doping, and doped semiconductors are called *extrinsic* semiconductors. If the

majority charge carrier supplied by the impurity is an electron (e.g., when doping a group IV element with a group V element), then the resulting semiconductor is called an *n-type* semiconductor. If the majority charge carrier is a hole (e.g., when doping a group IV element with a group III element), then the resulting semiconductor is a *p-type* semiconductor. In an n-type semiconductor, a filled energy level is added to the band gap that is close to the lower conduction band edge, which allows for the promotion of electrons from the dopant energy level to the conduction band. In p-type semiconductors, an unfilled energy level is introduced into the band gap near the topmost edge of the valence band. This allows for the promotion of electrons from the valence band to the unfilled energy level and increases the hole concentration in the valence band. Figure 1.4 illustrates the case of two impurity donor levels located within the band gap in an n-type semiconductor.

To complete the description of the electronic band structure of a semiconductor, a final term will be defined: the *Fermi level*. Because the energy of electrons is not a definite value but is actually defined by wave functions [62], the probability of an electron existing in the band gap is actually greater than zero. In simple terms, the Fermi level, E_F, can be defined as the energy located within the band gap with a 50% probability of being occupied by an electron at any given time [63]. It is the chemical potential of the electrons in the semiconductor. Xu and Schoonen [64] define the Fermi level as the absolute electronegativity of a pristine semiconductor, located directly halfway between the valence and conduction bands. However, if impurities are introduced to the semiconductor so that discrete energy levels now lie within the band gap, the Fermi level is shifted. For n-type semiconductors, the Fermi level lies just below the

conduction band, and in p-type semiconductors, it lies just above the valence band. Additionally, the Fermi level is dependent on the applied potential in an electrochemical system. For example, if a more positive potential is applied to the semiconductor, the Fermi level will move downward in the direction of the valence band [63].

1.4.1.2. Electrolyte solution

The electrolyte solution is composed of various solution species which react with the steel rebar sample. Associated with these species is a redox (reduction/oxidation) potential, E_{redox}, which reveals the tendency of the species to give or receive an electron. This redox potential can be found using the Nernst equation for the given redox reaction specific to reacting species (see Equation 1.2),

$$E_{redox} = E^0_{redox} + \frac{RT}{nF} \ln\left[\frac{c_{ox}}{c_{red}}\right] \tag{1.2}$$

where R is the gas constant, T is the absolute temperature, n is the number of moles of electrons transferred in the reaction, F is the Faraday constant, E^0_{redox} is the standard redox potential, and c_{ox} and c_{red} are the concentrations of the oxidized and reduced agents in the redox species, respectively [61]. For the oxidation of a metal in an aerated, aqueous electrolyte solution, the cathodic reaction likely to take place is the reduction of dissolved oxygen, shown in Equation 1.3 for a neutral or alkaline solution [22].

$$O_2 + 2H_2O + 4e^- \rightarrow 4OH^- \tag{1.3}$$

The redox potential, E_{redox}, associated with the reduction of dissolved oxygen is plotted in Figure 1.5 with respect to the energy levels associated with an n-type semiconductor

in the same solution. At potentials negative to the redox potential, any oxygen in the water will be unstable and will reduce to water. At potentials positive to the redox potential, water will decompose (i.e., oxidize) into O_2. It is also possible that the evolution of hydrogen occurs in an aerated solution; however, this only occurs at extremely cathodic potentials which are negative to the potentials explored in this thesis. The locations of the potentials associated with the reduction of oxygen and hydrogen evolution are given by lines (b) and (a), respectively, in Figure 1.1.

In Figure 1.5, E_{redox} can be considered the electrolyte equivalent to the Fermi level in a semiconductor. The redox species in the electrolyte (e.g., H_2O) can either accept or donate electrons, depending on the location of E_{redox} with respect to the Fermi level of the semiconducting oxide. When electrons are accepted or donated, the electronic structure of the redox species changes slightly. This can be seen with the presence of two energy levels above and below E_{redox} in Figure 1.5. If the reacting species in the solution is accepting electrons from the semiconducting oxide, E_{ox} is the energy where this will occur, and it is associated with the lowest unoccupied energy level in the redox species. E_{ox} is analogous to E_C in the semiconductor. If the reacting species in the solution is donating electrons to the semiconductor, E_{red} is the energy where this will occur, and it is associated with the highest occupied energy level in the redox species. The equivalent to E_{red} on the semiconductor is E_V. A Gaussian distribution centered on E_{ox} and E_{red} illustrates the probability of finding the state at another energy level due to thermal fluctuations of dipoles in the electrolyte [60], which can be seen in Chapter 3. E_{redox} is located halfway between E_{ox} and E_{red}, and the distance between each of these values is called the reorganization energy, λ. This value has to do with the reorientation

energy associated with a redox species accepting or donating an electron by reaction with the semiconducting oxide [60, 64]. A complete, albeit simplified energy level model for the semiconductor-electrolyte-reference electrode interfaces (i.e., for an electrochemical cell) is shown in Figure 1.5. The values listed are shown as energy values – not potential values. However, a potential scale was included for reference. This diagram shows that the measured potential in an electrochemical system, *V*, is equal to the difference between the Fermi levels of the semiconducting passive film, $E_F(semi)$, and reference electrode, $E_F(ref)$. Figure 1.5 also illustrates the case of an anodic potential applied to the sample, which is relevant for the electrochemical experiments performed in this thesis. This results in a downward shift of the energy bands of the semiconducting passive film, which will be explored in greater detail in the following section.

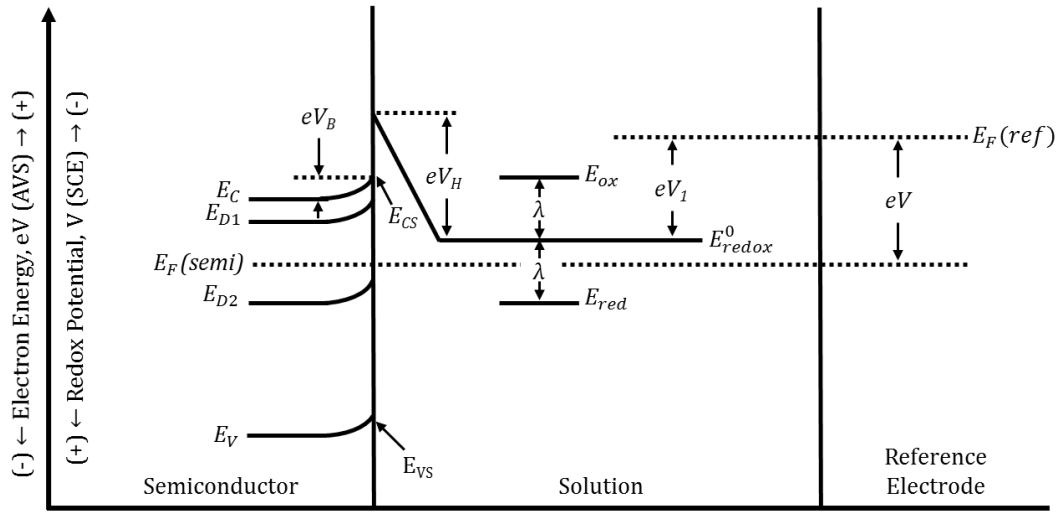

Figure 1.5: Simplified energy level model for an electrochemical system under anodic polarization. The semiconductor in this case is n-type. $E_F(semi)$ and $E_F(ref)$ are the Fermi levels of the semiconducting passive film and reference electrode, respectively. eV is the difference between these two values and is the energy associated with the measured potential of the electrochemical system. eV_B is the energy associated with band bending, which is a function of the applied potential to the system. E^0_{redox} is the standard redox potential for the reacting species in the solution. eV_1 is the energy of $E_F(ref)$ relative to the point of zero energy, which is obtained from the handbook value [22]. E_{ox} and E_{red} are the energies of the redox couple for the case of electron acceptance or donation, respectively, and λ is the reorganization energy. The distances are not to scale. This is a concept illustration, so units are not provided. Modified from Morrison [60].

1.4.1.3. Semiconductor – electrolyte equilibration

When a steel rebar sample is immersed in the electrolyte and the passive oxide film forms, the electrochemical potentials of the semiconducting oxide and the electrolyte begin to change. This is because in order for the two phases to be in equilibrium, the electrochemical potential of each must be equal. The electrochemical potential of the semiconducting oxide is equal to E_F of the semiconductor, and the electrochemical potential of the electrolyte is equal to E_{redox} of the reacting species in the solution. When these two potentials are not equal, as is the case when a sample is first immersed into a

solution, charge transfer occurs across the semiconductor-electrolyte interface until the potentials on each side of the interface equalize. Once E_F equals E_{redox}, charge transfer ceases. If E_F is at a more positive potential than E_{redox}, electrons will be transferred from the solution to the semiconductor. This lowers the redox potential in the solution on the energy scale, closer to E_F. If E_F is at a more negative potential than E_{redox}, electrons will be transferred from the semiconductor to the solution. This raises the redox potential in the solution on the energy scale. When oxidation of the semiconductor (i.e., reduction of the redox species) occurs, electrons are transferred from the highest occupied conduction band energy level, E_C, to the lowest unoccupied redox species level, E_{ox}. When reduction of the semiconductor occurs (i.e., oxidation of the redox species), electrons are transferred from the highest occupied redox species level, E_{red}, to the lowest unoccupied valence band energy level, E_V [60, 64]. Xu and Schoonen [64] point out that for the case of metal oxides, the H_2O reduction potential is very close to or above E_C, and E_V is typically 1 to 3 eV below the H_2O potential. What this means is that the reducing power for conduction band electrons in metal oxides is typically very small, but the valence band holes are highly oxidizing. If E_C were much higher than the H_2O redox potential, the reduction power would be much greater, but this is ordinarily not the case.

The interfacial charge transfer that occurs during the semiconductor-electrolyte equilibration process results in the formation of distinct regions of charge separation. These regions of charge separation are capacitive regions that effect the potential measured between the reference electrode and the working electrode in an electrochemical experiment. The first region of capacitance and charge separation is a

region in the semiconductor where an excess of charge has accumulated or depleted. This region of excess charge is called the *space charge layer*. The space charge layer can be the consequence of stationary charged impurities (i.e., dopants) or mobile charge carriers (i.e., electrons or holes). If electrons have diffused away from the semiconductor and into the solution as part of the equilibration process, this creates a space charge region in the semiconductor that is dominated by immobile, positively-charged impurities. The space charge layer in this case can be referred to as a *depletion layer*, or a region vacant of mobile charge carriers. If electrons have been injected into the semiconductor from the solution, the space charge layer that forms can then be referred to as an *accumulation layer*.

For the case of an *n*-type semiconductor, the Fermi level is typically higher than the redox potential in the solution, meaning electrons will be transferred from the semiconductor to the electrolyte [63]. This then results in the formation of a depletion layer which, as was previously stated, is a polarized region with immobile, positivity-charged donor ions and no charge carriers. An electric field is then formed across the depletion layer which works against the natural flow of electrons from the semiconductor to the electrolyte. As the sample continues to equilibrate in the electrolyte solution, this electric field continues to grow stronger, and in some cases it may grow strong enough to stop the flow of the electrons to the solution altogether. The formation of this potential barrier working against electron flow results in the conduction band and valence band edges in the bulk semiconductor becoming different than those respective band edges at the semiconductor-electrolyte interface. This potential difference between the bulk band edges, E_C and E_V, and the same band edges

at the semiconductor surface, E_{CS} and E_{VS}, is called band bending, V_B. When the band edges bend upward, this shows that a depletion layer has formed, and at open-circuit conditions, this is usually indicative that the semiconductor is n-type. Conversely, when the band edges bend downward, an accumulation layer has formed, and at open-circuit conditions, this is usually indicative that the semiconductor is p-type.

A second capacitive region that forms near the semiconductor-electrolyte interface is the Helmholtz double layer. After the space charge layer in the semiconductor has formed, a charged double layer exists on the surface of the electrode. For an aqueous solution, this double layer includes a layer of polarized water molecules directly at the interface, followed by a second layer of solution ions attracted to the interface. The thickness of the Helmholtz double layer is typically only around 0.1 nm, but it can result in a significant drop in measured potential [60, 64]. This potential drop across the Helmholtz layer, V_H, is constant regardless of externally applied voltages or charge transfer across the interface, because it has an extremely high charge density and narrow thickness [65].

The size of the space charge layer as well as the magnitude of band bending is dependent not only on the natural charge transfer present during the equilibration of a semiconducting sample in an electrolyte, but also on any externally applied voltages to the system. This is common when performing an electrochemical experiment, where a voltage may be applied to the system to induce a current response. E_F, E_C, and E_V inside the bulk semiconductor all shift in response to the applied voltage. However, E_{CS} and E_{VS} are affected only by the interactions at the semiconductor-electrolyte interface – not by an external voltage applied to the bulk electrode [63]. Therefore, the externally

applied voltage can cause the size of the space charge layer and band bending to change as well. Figure 1.6 illustrates the change in energy level positions for the case of an n-type semiconductor, as an externally applied voltage is swept in the anodic direction.

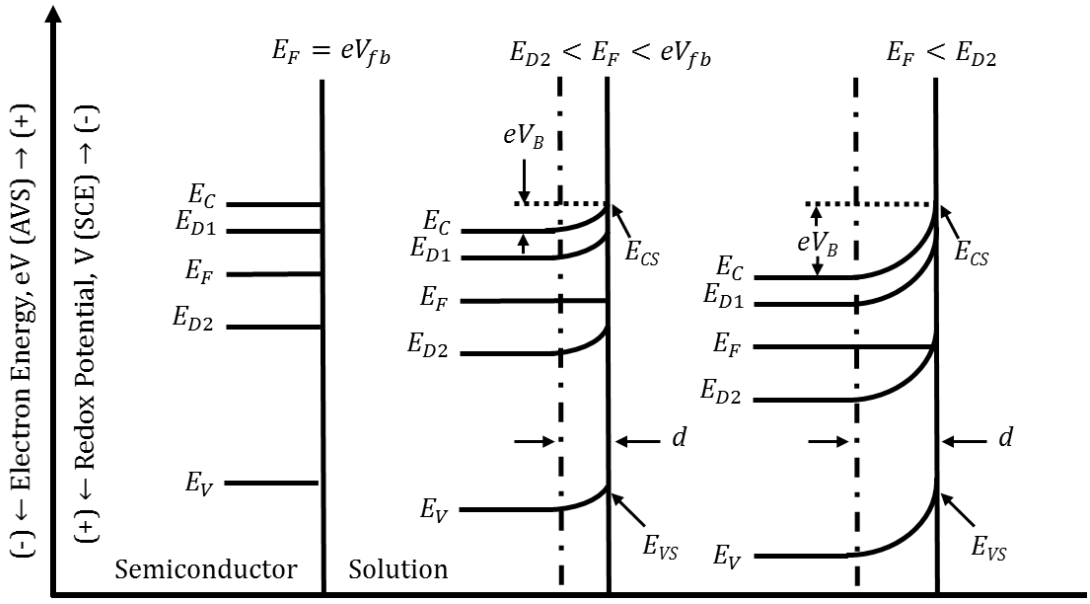

Figure 1.6: Change in the electronic band structure with increasing applied potentials. The location of the energy bands E_C, E_{D1}, E_F, E_{D2}, and E_V all move downward with applied potential. The energy associated with band bending, eV_B, and the space charge layer thickness, d, both increase with increasing anodic polarization. V_{fb} is the flatband potential of the semiconductor-electrolyte interface. The distances are not to scale. This is a concept illustration, so units are not provided. Modified from Cheng and Luo [53].

1.4.1.4. Flatband potential

Experimental measurement of the locations of these energy levels (e.g., E_F, E_C, E_V) can be critical in evaluating the electronic structure of materials immersed in solution. The one measurable, quantifiable electronic property that enables the determination of the energetics at the interface, while taking into account the physical phenomena occurring

on both the semiconductor side and electrolyte side of the interface, is a property known as the *flatband potential*, V_{fb}. Nozik [65] describes this parameter as "the connection between the energy levels of the electrolyte and the semiconductor." He defines the flatband potential as the electrode potential at which the semiconductor bands are flat (zero space charge in the semiconductor). V_{fb} is measured with respect to the reference electrode used in the experiment. At the flatband potential, no band bending is occurring, and under special circumstances (i.e., equilibrium and dark conditions [65]) the Fermi level of the semiconductor is at the same energy level as the redox potential in the solution. Therefore, no charge transfer across the interface is occurring, since no potential gradient exists that would drive such transfer. When an externally applied voltage approaches V_{fb} and the band bending approaches zero, the potential difference between the sample being measured and the reference electrode can be estimated using Equation 1.4 [65],

$$V_{fb}(SHE) = (\chi + \Delta E_F - V_H) - 4.5 \tag{1.4}$$

where χ is the electron affinity of the semiconductor and ΔE_F is the difference between the Fermi level and the majority charge carrier band. This makes the flatband potential unique in that it is truly a property of the interface, taking into account both the intrinsic properties of the semiconductor and the electrolyte [64].

1.4.2. Methods of Studying Electronic Properties

Historically, two primary techniques have been used to experimentally determine the electronic properties of metal passive films. The first is the classical Mott-Schottky (M-S) method —the most used and most reliable technique in literature [64]. In basic terms, the M-S method involves a capacitance measurement of the space charge region in the

semiconductor. The capacitance is measured as a function of voltage, and the resulting signature is indicative of several properties inherent to that passive film. Figure 1.7 shows an example of an M-S plot, which traditionally plots the inverse capacitance squared as a function of potential.

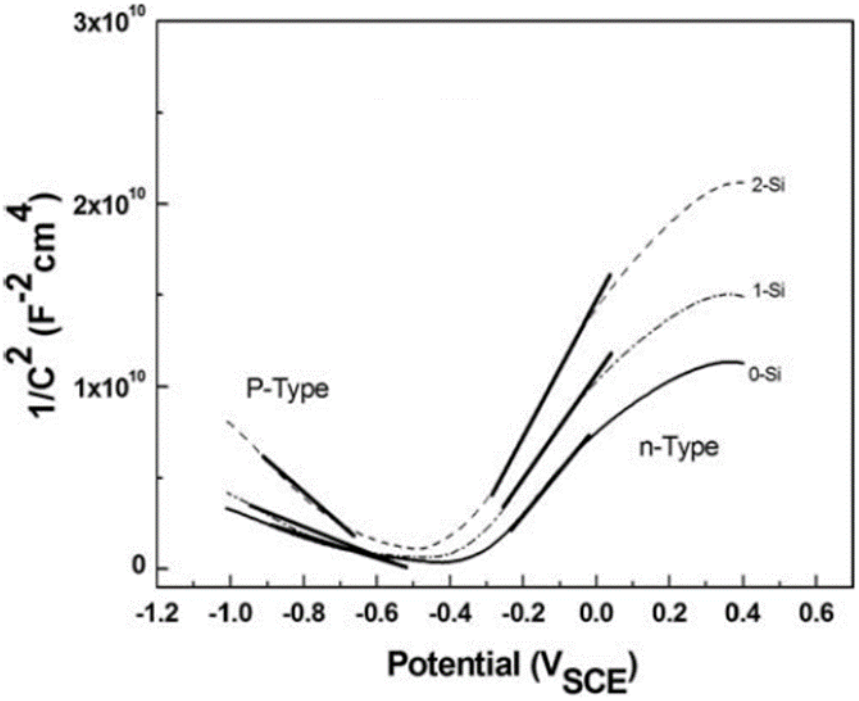

Figure 1.7: Example of a Mott-Schottky plot for stainless steel, illustrating both p-type and n-type semiconductive behavior. The effect of increasing silicon concentrations on the capacitance is shown. Reproduced from Toor [66].

The first property that this method reveals is the electronic type of the semiconducting oxide. Semiconductors, as explained in Section 1.2.1., can be either n-type (i.e., having electrons as the majority charge carrier) or p-type (having holes as the majority charge carrier). If the slope of the M-S plot is positive, then the semiconductor exhibits n-type behavior for that potential range. If the slope is negative, then the semiconductor exhibits p-type behavior. Some semiconductors exhibit both n- and p-type behavior,

depending on the externally applied potential. This can be readily seen in Figure 1.7 for the case of stainless steel and varying silicon concentrations. The second property that can be found directly from the M-S plot is the dopant (acceptor or donor) density. For n-type semiconductors, the donor density can be derived from the slope of the linear, positively sloped region. For p-type semiconductors, the acceptor density can be derived from the slope of the linear, negatively sloped regions. To get an accurate dopant density, the slope of this region must be linear, otherwise the Mott-Schottky equation (see Equation 1.20) which is used to interpret the inverse capacitance in Figure 1.7 breaks down [8]. This dopant density gives the density of impurities located in the space charge region.

The third primary electronic property derived from M-S analysis is the flatband potential. This is can be determined by extending the slope of the linear region in the M-S plot, and then locating the potential at which it crosses the x-axis. This value is heavily effected by Helmholtz potential drop, V_H, so accurate measurement of the flatband potential requires a determination of V_H by an alternative method. From these values, other electronic properties can be derived, including the thickness of the space charge layer, d, at various applied potentials. The experimental setup for performing M-S analysis involves immersing a sample in a conventional three-probe electrochemical cell with a counter and reference electrode. A potentiostat that is connected to the electrochemical cell applies a potential to the sample, and the induced current response is measured by the reference electrode. The primary advantages of the M-S method include the sheer number of studies on passive film for a wide variety of materials using this method, and the fact that this method has proved to be a reliable,

repeatable technique that delivers accurate information on the electronic properties. A few examples include use on zinc oxide crystals [67], iron passive films [9, 59, 68], titanium passive films [69], stainless steel passive films [8, 48, 70], zirconium oxide [71], and tungsten passive films [72]. The large number of electronic properties that can be derived both directly and indirectly from a single potential scan in M-S analysis (e.g., N_D, V_{fb}, electronic type, d) is also advantageous. However, a weakness with this method is its destructive nature, due to the high external polarizations it involves. This issue, however, is dealt with more extensively in Chapter 2.

The second method used often in literature to determine the electronic properties of passive films involves measuring the anodic photocurrent onset potential. This technique, called photoelectrochemical spectroscopy (PECS) has been used extensively to characterize the passive film on stainless steel [50, 70, 73, 74]. PECS applies the photo effect (i.e., the emission of electrons under a light source) to characterize some electronic properties of metals. These properties are found by analyzing the current or potential change under varying photo irradiation. The experimental setup for this test involves using a conventional three-probe electrochemical cell with a counter, working and reference electrode. A quartz window is located on the electrochemical cell, through which a monochromatic light beam generated by an arc lamp with a grating monochromator is channeled. The photocurrent response of the system is then measured as a function of an external potential, which is applied by a potentiostat connected to the electrochemical cell. Figure 1.8 illustrates a typical plot produced when evaluating the photoelectrochemical response of a system.

This shows the photoeclectrochemical action spectra for a steady photocurrent emitted from a passive film formed on stainless steel in a borate buffer solution [75].

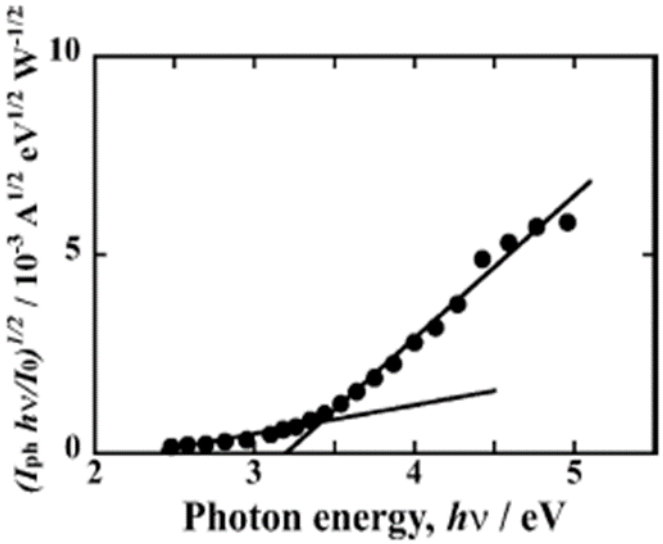

Figure 1.8: The photoelectrochemical action spectra for stainless in a borate buffer solution. The two linear regions are indicated by regression lines. Reproduced from Tsuchiya and Fujimoto [75].

This photoelectrochemical action spectra is produced by normalizing the photocurrent spectra in the method described by Tsuchiya and Fujimoto [75]. Figure 1.8 reveals significant information about the passive film structure. It shows that the passive film is in fact a bilayer structure, due to the presence of two linear regions. These two linear regions can then be divided and evaluated separately for the electronic properties of the two parts of the bilayer structure. The band gap of the semiconductor can be determined by estimating the photon energy when $(i_{ph}hv/I_0)^{1/2}$ equals zero. The electronic type (i.e., n- or p-type) and the flatband potential of the semiconducting oxide can also be evaluated by plotting the slope of the action spectra as a function of applied potential. The primary advantage of this technique is that it enables the determination of the band

gap energy of the semiconductor. However, a major weakness of this technique is that it reveals little about the density of the dopant states in the space charge layer, which can heavily influence the determination of the flatband potential [8]. The density of donor states is also revealing of the protective nature and structure of the passive films [47, 48]. A second major weakness is that, like the Mott-Schottky method, this method involves the application of an external voltage, which makes this technique destructive in nature.

A few other techniques have been proposed for taking *in situ* measurements of the electronic properties of passive films; however, these methods are not widely used and have not been validated by a significant number of papers. One of these methods was employed by Diez-Perez et al. [76] and is called electrochemical scanning tunneling microscopy (ECSTM). This method involves using an STM tip as a tunable energetic probe to canvas the surface of the sample and gather direct electronic data of the surface of an electrode. Diez-Perez et al. [76] used this technique to characterize the surface of a passive iron electrode immersed in a borate buffer solution. A quantitative band structure model was able to be proposed and was validated by comparison to more traditional electrochemical impedance techniques. A primary advantage of this technique is that it can provide electronic data at the semiconductor-electrolyte interface without needing electric circuit modeling to interpret the data, as is the case with electrochemical impedance methods. A second advantage is that it can also be used simultaneously as an *in situ* imaging technique for capturing the electrode surface. Severe weaknesses, however, in this method are questions regarding the stability of

ECSTM imaging regimes for taking *in situ* measurements, as well as the lack of other papers attempting this technique.

Another method also proposed by Diez-Perez et al. [77] is called electrochemical tunneling spectroscopy (ECTS). This method involves recording tunneling spectra of a sample immersed in solution in an electrochemical cell while an externally applied voltage is swept. These tunneling spectra reveal conductance maps on the surface of the sample, which help to reveal the electronic structure and some properties of the passive film. These conductance maps can show the free carrier (i.e., electrons or holes) density as a function of electron energy and applied potential, and can also help to better understand the redox behavior at the interface. Diez-Perez et al. [77] used this method to fingerprint the electrolyte-semiconductor interface of passive iron in a borate buffer solution. Advantages of this technique include the fact that this technique is nondestructive, allowing for repeatable tests to be performed on the same sample. It is also not dependent on the use of electric circuit modeling for interpretation, as is the case in some electrochemical impedance techniques. However, as with ECSTM, the general lack of subsequent papers or works validating this method with other systems is revealing. Additionally, these techniques both compare their results to traditional electrochemical impedance techniques, and validated that the results produced by these traditional, well-established techniques are in fact correct and adequately characterize the electronic properties of the passive state.

After identifying the primary techniques outlined in literature for determining the semiconducting properties, it was clear that the Mott-Schottky method would be the most suitable method for studying the electronic properties of the passive film on

carbon steel rebar in simulated concrete pore solutions. Its extensive and widespread use in literature for a wide variety of systems, most notably for systems involving iron-based alloys, the high level of repeatability in results it has shown to produce, and the large number of electronic properties it reveals both directly and indirectly, all combine to amply show why this method is the most commonly employed in literature for determining the electronic properties of passive films.

1.4.3. Mott-Schottky (M-S) Analysis

As explained in Section 1.4.2., Mott-Schottky (M-S) analysis is the most commonly used technique for determining the electronic properties of a passive oxide film, and it is the primary technique used in the present work. A brief explanation and derivation of the M-S equation and its origins would be both helpful and necessary when applying this method to a given system. The measurement theory behind M-S analysis begins with the basic concepts used in the broader field of impedance spectroscopy. The premise behind impedance spectroscopy is that processes occurring at the semiconductor-electrolyte interface can be simulated using electrical networks composed primarily of resistors and capacitors in series or parallel. Impedance spectroscopy is performed by applying a small, oscillating AC potential to a sample and measuring the current response of the system. Typical DC measurements are helpful when determining the resistance and potential drops present in a system. However, by applying the AC perturbation instead, other essential mechanistic information of the passive film such as capacitance values can also be obtained. When impedance spectroscopy is applied to a system, the AC perturbation induces a time-dependent current response. By overlaying the voltage vs time plot with the induced

current vs time plot, as has been done in Figure 1.9, a phase shift can often be seen between the two plots. If no impedance were in the electrochemical system, no phase shift would have occurred; however, the presence of a phase shift reveals the appearance of an imaginary component to the overall system impedance. This imaginary component also means that a capacitance is in the system as well.

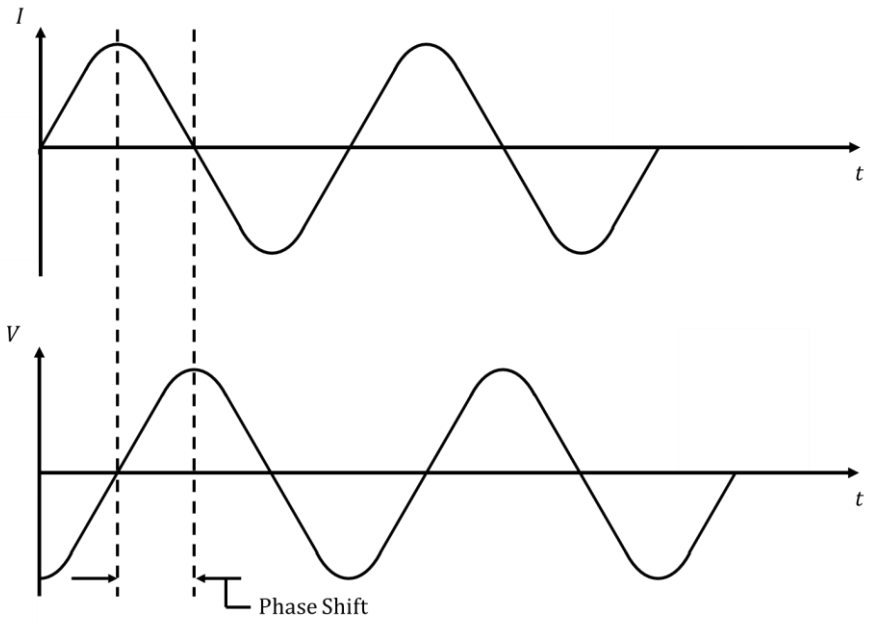

Figure 1.9: An AC applied potential, *V*, and induced current response, *I*, as a function of time, *t*. The phase shift shown indicates the presence of an imaginary component to the system impedance. Modified from Gamry [78].

Equation 1.5 shows the well-known Ohm's law, which illustrates impedance as a function of both a time-dependent voltage, *V(t)*, and a time-dependent current, *I(t)*. θ is defined as the phase angle between *V(t)* and *I(t)*. Equations 1.6 and 1.7 show that the impedance, *Z*, is a function of the frequencies used for the AC perturbation. This frequency, *f*, is related to the angular frequency, ω, by $\omega = 2\pi f$.

$$Z(\omega) = \frac{V(t)}{I(t)}, \tag{1.5}$$

$$V(t) = V_0 \sin \omega t, \tag{1.6}$$

$$I(t) = I_0 \sin(\omega t + \theta) \tag{1.7}$$

Equation 1.8 then breaks down the impedance into its real component, *Z'(ω)*, and imaginary component, *Z''(ω)*.

$$Z(\omega) = Z'(\omega) + Z''(\omega) \tag{1.8}$$

In impedance spectroscopy, the impedance behavior is ordinarily displayed using two different plots which describe different aspects of Equation 1.8. The first is the Bode plot, which plots the impedance modulus, $|Z|$, (which is the root sum squares of the impedance components) on the primary vertical axis and the phase angle on the secondary vertical axis, both as a function of applied frequency, *f*. The second plot used for displaying impedance results is the Nyquist plot, which simply maps *Z''(ω)* as a function of *Z'(ω)*. Equation 1.9 then shows how the apparent capacitance, *C*, of the electrochemical system can then be derived directly from Equation 1.8.

$$C = \frac{1}{\omega Z''} \tag{1.9}$$

The other factors effecting the impedance behavior of the electrochemical system can also be represented by circuit components other than capacitors. For example, resistance provided by the electrolyte solution can be represented by a resistor. The resistance to charge transfer across the interface, or the polarization resistance, can also be represented by a resistor. A Warburg element simulates the presence of mass transfer issues occurring at the oxide film surface. However, the semiconductor-electrolyte interface is most commonly described by two capacitors in series (see Equation 1.10),

with one contribution to the overall system capacitance from the Helmholtz layer, C_H, and the other from the space charge layer, C_{SC}, [9, 60, 72].

$$\frac{1}{C} = \frac{1}{C_{SC}} + \frac{1}{C_H} \tag{1.10}$$

Since it has been shown that C_{SC} can be found by simulating the semiconductor-electrolyte interface with simple electric circuit components, the next step in deriving the M-S equation requires relating C to the measured potential, V, with respect to the reference electrode. By plotting C as a function of V, an M-S plot can be produced. The derivation outlined below summarizes the derivation provided by Dean and Stimming [79-81], which assumes the semiconductor at the interface is n-type and the space charge layer is under depletion conditions, i.e., the applied potential is greater than the flatband potential of the semiconductor. However, the methodology behind this derivation can be applied to p-type semiconductors as well. To begin, the total potential drop across the semiconductor-electrolyte interface is given by the difference between the potentials in the bulk electrode, $V(\infty)$, and bulk solution by Equation 1.11. $V(x)$ is the potential at a point x in the semiconductor.

$$\Delta V(x) = V(\infty) - V(x) \tag{1.11}$$

The dependence of $V(x)$ on the net charge density in the space charge layer, $\rho(x)$, is given by the one-dimensional Poisson equation, which can be seen in Equation 1.12. ϵ is the relative permittivity of the semiconductor, and ϵ_0 is the permittivity of free space.

$$\frac{d^2\Delta V}{dx^2} = \frac{\rho(x)}{\epsilon\epsilon_0} \tag{1.12}$$

Boundary conditions are then applied to Equation 1.12. These conditions are that in the bulk of the electrode, the net charge density is zero, and the potential is constant, both of which are reasonable assumptions. Integrating Equation 1.12 by the identity in Equation 1.13 and then applying the boundary conditions yields Equation 1.14, which expresses the electric field strength at the electrode surface.

$$\frac{1}{2}\left(\frac{d\Delta V}{dx}\right)^2 = \frac{d\Delta V}{dx}\frac{d^2\Delta V}{dx^2} \tag{1.13}$$

$$\left(\frac{d\Delta V}{dx}\right)_{x=0} = -\left[\frac{2}{\epsilon\epsilon_0}\int_0^{\Delta V_{SC}} \rho(\Delta V)d\Delta V\right]^{1/2} \tag{1.14}$$

Next, Gauss' Law is applied to Equation 1.14 to yield the total charge per unit area, q_{SC}, which has accumulated in the depletion layer. This is shown in Equation 1.15.

$$q_{SC} = -\epsilon\epsilon_0\left(\frac{d\Delta V}{dx}\right)_{x=0} = \left[2\epsilon\epsilon_0\int_0^{\Delta V_{SC}} \rho(\Delta V)d\Delta V\right]^{1/2} \tag{1.15}$$

The capacitance in the space charge layer per unit area, C_{SC}, is then evaluated (see Equation 1.16) by differentiating Equation 1.15 by the potential drop across the space charge layer, ΔV_{SC}. This then clearly shows that the capacitance of the depletion layer is changed by the charge density, where the charge density is by definition a function of the potential.

$$C_{SC} = \frac{dq_{SC}}{d\Delta V_{SC}} = \left(\frac{2}{\epsilon\epsilon_0}\right)^{1/2}\frac{\rho(\Delta V_{SC})}{\left[\int_0^{\Delta V_{SC}} \rho(\Delta V)d\Delta V\right]^{1/2}} \tag{1.16}$$

Now, the general expression for the charge density of a crystalline, n-type semiconductor with *M* discrete donor states is given in Equation 1.17. The donor states

are impurities in the semiconductor that have energy levels that fall within the band gap of the semiconductor.

$$\rho(\Delta V) = e\left\{\sum_{j=1}^{M} N_{Dj}\left[1+\exp\left(\frac{E_F - E_{Dj} - e\Delta V}{kT}\right)\right]^{-1} - N_C \exp\left(\frac{E_F - E_C - e\Delta V}{kT}\right)\right\} \tag{1.17}$$

Here, e is the charge of an electron, k is the Boltzmann constant, T is the absolute temperature, N_C is the density of states at the lower conduction band edge, and N_D is the donor density in the space charge layer for a given donor state. E_F and E_C are again the Fermi level and lower edge of the conduction band in the semicondcutor, and E_D is the energy in the band gap at which the given donor state lies. The density of minority charge carriers (i.e., holes) from the valence band are neglected, due to their extremely low concentrations. Equation 1.17 also assumes Fermi-Dirac statistics, which describes the distribution of energy states in a system that obeys the Pauli exclusion principle. The contribution of electrons from the donor states is accounted for in the first term in Equation 1.17, while the contribution of electrons in the conduction band is accounted for in the second term.

Finally, the capacitance in the space charge layer as a function of potential drop across the depletion region in which M discrete donor levels are present is given by substituting Equation 1.17 into Equation 1.16, which yields Equation 1.18.

$$C_{SC} = \left(\frac{\epsilon\epsilon_0 e}{2}\right)^{1/2} \times \frac{\left\{\sum_{j=1}^{M} N_{Dj}\left[1+\exp\left(\frac{E_F - E_{Dj} - e\Delta V}{kT}\right)\right]^{-1} - N_C \exp\left(\frac{E_F - E_C - e\Delta V}{kT}\right)\right\}}{\left(\int_0^{\Delta V_{SC}}\left\{\sum_{j=1}^{M} N_{Dj}\left[1+\exp\left(\frac{E_F - E_{Dj} - e\Delta V}{kT}\right)\right]^{-1} - N_C \exp\left(\frac{E_F - E_C - e\Delta V}{kT}\right)\right\} d\Delta V\right)^{1/2}} \quad (1.18)$$

This can then be simplified to well-known M-S equation, assuming the presence of only one donor state that is completely ionized at room tempturature; this is shown in Equation 1.19, again for the case of an n-type semiconductor. Here, the potential drop across the space charge layer has been assumed to be the only contributor to a potential drop.

$$\frac{1}{{C_{SC}}^2} = \frac{2}{\varepsilon\varepsilon_0 e N_D}\left(\Delta V_{SC} - \frac{kT}{e}\right) \quad (1.19)$$

Although the M-S equation in Equation 1.19 is used in the majority of studies that use M-S analysis, a more general expression is necessary, because in some cases, not all of the change in capacitance and potential drop measured in an electrochemical system is attributable to change in C_{SC}. For highly defective passive films, the contribution of the Helmholtz layer to the capacitance, C_H, must be taken into account. Therefore, the *apparent* capacitance, *C*, is related to the potential measured by the potentiostat and the flatband potential of the semiconductor, V_{fb}, by Equation 1.20 [8, 82]. This is the M-S equation used for performing the analysis in the present study. C_{SC} can then be found by inserting Equation 1.20 into the series capacitor model for the semiconductor-electrolyte interface in Equation 1.10.

$$\frac{1}{C^2} = \frac{1}{{C_H}^2} + \frac{2}{\varepsilon\varepsilon_0 e N_D}\left(V - V_{fb} - \frac{kT}{e}\right) \quad (1.20)$$

Now, four primary assumptions cited in literature go into the derivation of the M-S equation, and some of them have already been touched on briefly. These must be addressed before proceeding. The first assumption is that a pure, intrinsic semiconductor is being evaluated. This would produce a perfectly linear C^{-2} vs V plot, as predicted by Equation 1.19. However, if non-linearity exists in the M-S plot, it is possible that donor states are present in the band gap of the semiconductor. Previous studies have shown that passive iron-based alloys exhibit two donor states in the space charge layer (see Section 1.4.4.), and so this consideration was taken into account when applying the M-S equation. A second assumption is that C is the equivalent to a series capacitor model based solely on C_H and the space charge capacitance, C_{SC}. It is possible that a surface state capacitance, C_{SS}, makes a small contribution to the apparent capacitance as well. However, Morrison [60] shows that this capacitance is in parallel with C_{SC}, and so the capacitance due to surface states is hidden in the C_{SC} term. It is possible that a small contribution from C_{SS} exists in the present study; however, the high level of surface polishing that occurred on the samples in this study (see Chapters 2-4), combined with the fact that no known author has taken into account the contribution of C_{SS} when performing M-S analysis, shows that this assumption can be satisfactorily made. The third assumption that most authors do not address is that the apparent capacitance can be a function of not only potential, but also frequency. Commonly cited reasons for frequency dependence include the presence of deep donor states, dielectric relaxation phenomena, a non-uniform distribution of donors in the oxide, the amorphous nature of passive films, and contributions from surface states to the capacitance [8]. This phenomenon has been observed in numerous studies on iron-

based alloys, and it is addressed in Chapter 2 using the method used by Ahn et al. [83] and Sikora et al. [72]. Simply put, this method involves finding a range of frequencies for which the capacitance does not change as a function of frequency. The frequency used then for M-S analysis is then chosen from this frequency range that does not change the measured capacitance. The final assumption for M-S analysis is that the dopant density does not change as a function of applied potential. This issue is again not addressed by most studies employing M-S analysis but was highlighted by Sikora et al. [72] as a possible source of nonlinearity in M-S plots. This issue was addressed by sweeping the potential at a rate fast enough during M-S analysis to mitigate any change in the dopant density and film thickness as a result of the applied potential. Chapter 2 shows that the potential sweep rate used in the present work is in fact fast enough to mitigate the effects of changing donor densities during the potential sweep.

1.4.4. Existing Literature on the Electronic Properties of Carbon Steel in Alkaline Conditions

The existing literature studying the electronic properties of carbon steel in alkaline environments is generally lacking [25, 53, 54, 84-87]. Of these, only Sanchez et al. [85, 86] and Zhang and Li [84] tested carbon steel in an environment representative of the highly alkaline conditions found in concrete pore solutions. Additionally, the methodology used to implement M-S analysis in each of these studies is decidedly varied. This methodology includes determining the M-S testing parameters, such as the selection of a passive film formation potential, the amount of time the sample spends passivating in solution, the potential sweep rate and range, and the frequency used in M-S analysis. With significant variations present in not only the passivating solution

composition and pH, but also in the methodology used to implement M-S analysis, it is unsurprising that serious discrepancies exist for the electronic properties reported in each of these papers. Below, each of these papers will be inspected and analyzed, and gaps in the methodologies used to implement M-S analysis for each will be highlighted. These gaps in the existing literature will then be summarized, and the need for a comprehensive methodology for performing reliable, repeatable M-S analysis for the passive steel rebar system will be shown.

Cheng and Luo [53, 54] was overall the most comprehensive paper from a methodological standpoint in studying the electronic properties of a passive iron-based alloy. The authors went into sufficient detail in describing the frequency-dependence of the passive film on reported capacitance values, and they used a frequency that they felt minimized this effect on the capacitance (i.e., 1000 Hz). Additionally, the authors quantified the electronic properties of passive films not only under multiple formation potentials (-0.2 and 0.2 V vs SCE), but also for when the passive film forms under open circuit conditions. Since Gunay et al. [5] showed that a passive film formed under open circuit conditions is significantly different from the one formed under an externally applied potential, the decision to take this aspect of the experiment into account shows good forethought in experimental planning. However, the two major issues with this paper are the extremely low pH at which the film was formed (pH 8.6) and the lack of a potential rate. A pH of 8.6 is not at all representative of that seen in concrete, nor is it even close to the level required for the passive film on carbon steel to begin to form. Therefore, the electronic properties found in this study are not comparable to those that would be expected of passive carbon steel in concrete. Additionally, the lack of a

potential sweep rate is a major issue, because it has previously be shown that too slow of a sweep rate significantly effects the film properties during the potential scan [72]. The potential sweep range from -0.4 to 0.4 V vs Ag/AgCl was small yet adequate to characterize the depletion layer. The reported electronic properties for this film were, for the donor density and flatband potential, $0.20\text{-}0.40 \times 10^{21}$ cm^{-3} and -0.44 V vs Ag/AgCl, respectively.

Hamadou et al. [25] again passivated the carbon steel sample in a solution that is neither representative of concrete, nor in the passive region for carbon steel (pH 9.2). Additionally, they did not form the films passively, but instead applied formation potentials which have been shown to alter the electronic properties of a fully passivated film [5]. The authors did though show the effect of a wide variety of passive film formation potentials (0.2, 0.5, and 0.7 V vs. SCE) and passivation times (1, 8, and 15 hours), which was an interesting comparison. They showed that these variations actually produced notable differences in the electronic properties. The authors used a potential sweep range of -0.5 to 1.0 V vs SCE, which shows that exceedingly anodic potentials applied. It is clear then that for the M-S potential scan, the transpassive region of the carbon steel was reached. This is a significant issue, because it is known the current density and corrosion rate of the sample increase exponentially in this region. Combining this with the fact that no potential sweep rate was noted, it is exceedingly likely that the passive film was dramatically and perhaps unacceptably altered during M-S analysis as per Sikora et al. [72], and the electronic properties, particularly at those high potentials, may not be reliable. The authors used a frequency of 1842 Hz, but gave no justification for reason behind this selection. The reported

dopant density and flatband potential for this study were 3.03-4.41x10^{21} cm^{-3} and -0.50 V vs SCE, respectively.

Li et al. [87] likewise did not passivate the carbon steel samples is a solution representative of concrete pores, but instead passivated in a pH 9.2 solution. Also, the passive film was formed by an externally applied voltage (0.2 V vs SCE) for 2 hours, and not under open circuit conditions. Like Hamadou et al. [25], extremely anodic potentials located in the transpassive regime of carbon steel were applied during the M-S potential sweep, which was scanned from -0.4 to 1.0 V vs SCE. However, a potential sweep rate was actually specified, and this potential rate was extremely high (40 mV/s). This high of a sweep rate might help to reassure that the electronic properties reported even in the high potential regions are reliable, since the film had very little time to adjust to the changing applied potential. Interestingly, the authors mentioned that a strong frequency dependence exists in carbon steel rebar, but then proceeded to not address this issue further. Furthermore, no frequency for running M-S analysis was even mentioned by the authors during the entirety of the paper. A donor density and flatband potential values of 3.12x10^{21} cm^{-3} and -0.67 V vs SCE, respectively, were reported.

Several significant issues are present with the study performed by Zhang and Li [84]. The authors actually attempted to simulate the conditions representative in concrete by testing in a very high pH (pH 12.5) and allowing the passive film to form under open circuit conditions. However, the passivation time was not even stated by the authors. They noted that the rebar specimens were embedded in wet concrete cylinders with one face exposed at one of the ends of the cylinders, and they also stated that the concrete

was allowed to wet cure for 3 days before the rebar/concrete specimen was transferred to saturated calcium hydroxide solutions for M-S analysis. But they did not say how long the sample spent in the passivating solution, which is a significant omission. The potential sweep range (-1.0 to 0.6 V vs SCE) adequately showed the semiconductive behavior, but extremely cathodic potentials were applied in so doing. These cathodic potentials, even if applied for only a few seconds, could detrimentally effect any passive film present on the sample and significantly alter the electronic properties. Harrington et al. [82] showed that an applied potential equal to -0.7 V is enough to completely destabilize any passive film present, so -1.0 V is likely far too cathodic for M-S analysis. No potential sweep rate was given by authors, and a frequency of 1000 Hz was specified for use with M-S analysis with justification for the choice of this frequency. The reported donor density and flatband potential were 0.38×10^{21} cm^{-3} and -0.88 V vs SCE, respectively, which is the most cathodic flatband potential reported in studies on carbon steel rebar.

Sanchez et al. [85, 86] did an excellent job at creating an environment representative of the conditions seen in concrete for creating a passive film. They had a high pH solution (pH 13.2) and passivated the rebar sample for 5 days without applying an external potential, which is a large enough passivation time for the passive film to mostly form (although Ghods et al. [1, 2] showed that a fully formed passive film takes 10-14 days to form). The potential sweep range was small but adequate to show the semiconductive properties (-0.4 to 0.5 V vs SCE). However, the two biggest issues with this paper are the exclusion of a potential sweep rate, as well as the frequency for running M-S analysis. Both of these, and in particular the frequency, have a significant

effect on the reported semiconductive properties and represent a major gap in these papers. The authors reported a donor density of $8.10x10^{21}$ cm^{-3} and a flatband potential of -0.11, which is a significantly lower flatband potential than any of the other studies on carbon steel in alkaline solutions.

Although all of these papers report that the passive film formed on carbon steel in alkaline solutions shows n-type semiconductive behavior with an extremely high donor density, the commonalities end there. Significant variation exists in the reported flatband potentials (-0.11 to -0.88 V vs SCE), as well as the passivating environments used to create the passive film on steel rebar (pH 8.6 to 13.2). The methodology used to employ M-S analysis additionally showed alarming discrepancies. Widespread variation existed in whether a formation potential should be applied to create a fully passive film, how long that formation potential should be applied, and what specific potential should be used to form the film. When the passive film was formed under open circuit conditions, significant variation was apparent on how long that passive film should be allowed to form to come to a passive state. The passive sweep range differed as well, ranging from an extremely cathodic potential (-1.0 V vs SCE) to extremely anodic (1.0 V vs SCE). Only one of the papers stated a potential sweep rate, though this value is of exceeding importance to the reliability of the observed electronic properties [72]. And finally, the frequencies used varied from 1000-1842 Hz, and in some papers, no frequency was mentioned at all; this despite the fact that the effects of frequency on the capacitance of highly disordered passive films are known and well documented [8, 83, 88].

What is clear from this comparison and discussion is that a comprehensive methodology for employing Mott-Schottky analysis to passive carbon steel rebar – or to any other passive system – is needed. The parameters used vary widely between each study, and justification for why a specific parameter was selected is often completely absent. Since it has been shown that many of these parameters drastically effect the resulting electronic properties, justification for the selection of a value should be a requirement for any methodology created for implementing M-S analysis. What is additionally clear is that the electronic properties reported by these studies performed on passive carbon steel are not entirely reliable. Each study is either missing information critical for knowing the reliability of the data, the runtime parameters that were listed were not justified, or the runtime parameters that were listed would unacceptably alter the passive film. Therefore, reliable, supported, and credible electronic properties for passive carbon steel rebar in simulated concrete pore solutions is needed. The significant discrepancies seen in reported electronic properties from the previous studies only serve to reinforce this fact.

Additionally, other aspects of the passive film still require further research. These aspects include a study on how the electronic properties evolve as the film grows from initial passivation to full passivation. This type of study has not been attempted on any passive carbon steel system. Another area of much-needed research is studying, using a reliable M-S methodology, the effect of different concrete pore solutions and the effect of chlorides on the passive film. The solution composition within concrete is not constant, but actually shows significant variation and various pH levels, and studying the effect of changing this pore solution composition would provide a more

encompassing view of the conditions in actual concrete. The effect of chlorides likewise is a serious issue contributing to premature corrosion and deterioration of rebar in concrete, and so studying the effect this has would be extremely beneficial. Combining these research areas while using a reliable methodology would provide a comprehensive view of the electronic properties of passive carbon steel.

In such a critical topic as the corrosion of carbon steel rebar in concrete, it is evident that an unambiguous picture of the electronic properties of the steel rebar passive film combined with a systematic methodology for acquiring those properties is needed. This will greatly contribute to defining the passive state of steel rebar and aid in developing mechanistic models of steel passivation in concrete.

1.5. Objectives and Scope

The overarching objective of this research was to establish a *comprehensive* picture of the electronic properties of the passive film on carbon steel rebar in simulated concrete pore solutions. This was performed using electrochemical techniques such as Mott-Schottky (M-S) analysis and electrochemical impedance spectroscopy (EIS). The experimental setup for these techniques included using cylindrical steel rebar samples polished to a consistent surface finish, which were then immersed in an electrochemical cell under carefully controlled and monitored laboratory conditions. The first manuscript in this thesis establishes a systematic methodology for implementing M-S analysis to the passive carbon steel rebar system determined. Without this methodology, repeatable and reliable results will not be achieved. This methodology is then implemented to characterize the evolution of the steel rebar passive film from

initial immersion in the passivating solution until full passivation after 10 days. The second manuscript characterizes the electronic properties of the passive films formed in different representative concrete pore solution compositions. The effect of adding of chlorides to these passivating solutions is also captured. The third manuscript investigates the current numerical models for describing the electronic properties of passive oxide films and identifies a model that best fits the behavior of steel rebar in simulated concrete solutions. The selection of this preferred model then unlocks future work on simulating other concrete environments and conditions that were either not investigated in this thesis or difficult to capture using experimental techniques.

The scope of this research does not include testing rebar in actual concrete. The sensitive nature of the measurements needed to gain reliable, fundamental information on the electronic properties requires that this be performed in a controlled, laboratory environment. The testing of the passive films formed on rebar in actual concrete and in real-world settings is certainly on the horizon; however, the fundamental research characterizing the electronic signatures of passive films in controlled environments is first needed before introducing additional variables that may affect results and create misleading data trends. Additionally, this thesis does not investigate all of the possible environments that carbon steel rebar might see in real-world conditions. For example, it does not investigate conditions where the pH drops below levels seen for a saturated calcium hydroxide solution (pH 12.5). This can be seen in areas where carbonation (i.e., the reaction of atmospheric carbon dioxide with the calcium-bearing phases in concrete) is prevalent. This thesis also does not investigate the effect of changing temperature or possible freeze-thaw events that can occur in concrete in colder

environments. Lastly, the evolution of the electronic properties of the film before the first 30 minutes of passivation is not covered by the scope of this thesis, due to difficulty in determining these results experimentally.

By establishing a reliable, repeatable method by which to gather the electronic properties of the steel rebar passive film, determining the evolution of those electronic properties over time, and identifying the effect of varying concrete pore solution composition and chloride levels, the objective of creating a comprehensive picture of the electronic properties is achieved. Additionally, the identification of an optimal numerical model for predicting these electronic properties under alternative environmental conditions lays the groundwork for significant future work on this topic.

1.6. References

[1] P. Ghods, O.B. Isgor, G. McRae, T. Miller, Cement and Concrete Composites, 31 (2009) 2-11.
[2] P. Ghods, O.B. Isgor, G.A. McRae, G.P. Gu, Corrosion Science, 52 (2010) 1649-1659.
[3] P. Ghods, O.B. Isgor, G.J.C. Carpenter, J. Li, G.A. McRae, G.P. Gu, Cement and Concrete Research, 47 (2013) 55-68.
[4] P. Ghods, O.B. Isgor, G.A. McRae, J. Li, G.P. Gu, Corrosion Science, 53 (2011) 946-954.
[5] H.B. Gunay, P. Ghods, O.B. Isgor, G.J.C. Carpenter, X. Wu, Applied Surface Science, 274 (2013) 195-202.
[6] H.B. Gunay, B. Isgor, P. Ghods, Corrosion, (2014).
[7] Z. Szklarska-Smialowska, Corrosion Science, 41 (1999) 1743-1767.
[8] A. Di Paola, Electrochimica Acta, 34 (1989) 203-210.
[9] U. Stimming, J. Schultze, Berichte der Bunsengesellschaft für physikalische Chemie, 80 (1976) 1297-1302.
[10] C. Meyer, Cement and Concrete Composites, 31 (2009) 601-605.
[11] M. Yunovich, N.G. Thompson, T. Balvanyon, L. Lave.
[12] A. Poursaee, C. Hansson, Cement and Concrete Research, 37 (2007) 1127-1133.
[13] L. Bertolini, B. Elsener, P. Pedeferri, R.B. Polder, Corrosion of steel in concrete: prevention, diagnosis, repair, 1st ed., John Wiley & Sons, Weinheim, 2004.
[14] R.W. Revie, Uhlig's Corrosion Handbook, 3 ed., John Wiley & Sons, 2011.

[15] P. Schmuki, M. Büchler, S. Virtanen, H. Isaacs, M. Ryan, H. Böhni, Journal of the Electrochemical Society, 146 (1999) 2097-2102.
[16] J.M. Bockris, A. Reddy, B. Rao, Journal of The Electrochemical Society, 113 (1966) 1133-1144.
[17] J.M. Bockris, L.V. Minevski, Journal of Electroanalytical Chemistry, 349 (1993) 375-414.
[18] R. Babić, M. Metikoš-Huković, A. Jukić, Journal of The Electrochemical Society, 148 (2001) B146-B151.
[19] M. Stern, H. Wissenberg, Journal of the Electrochemical Society, 106 (1959) 755-759.
[20] R. Kirchheim, B. Heine, H. Fischmeister, S. Hofmann, H. Knote, U. Stolz, Corrosion Science, 29 (1989) 899-917.
[21] D.D. Macdonald, Electrochimica Acta, 56 (2011) 1761-1772.
[22] D.A. Jones, Principles and prevention of corrosion, Macmillan, 1992.
[23] M. Pourbaix, NACE, (1974).
[24] Y.-S. Choi, J.-G. Kim, K.-M. Lee, Corrosion Science, 48 (2006) 1733-1745.
[25] L. Hamadou, A. Kadri, N. Benbrahim, Applied Surface Science, 252 (2005) 1510-1519.
[26] S. Cramer, B. Covino, S. Bullard, G. Holcomb, J. Russell, F. Nelson, H. Laylor, S. Soltesz, Cement and Concrete Composites, 24 (2002) 101-117.
[27] L. Li, A.A. Sagues, Corrosion, 58 (2002) 305-316.
[28] C.M. Hansson, A. Poursaee, A. Laurent, Cement Concrete Res, 36 (2006) 2098-2102.
[29] U.M. Angst, B. Elsener, C.K. Larsen, O. Vennesland, Corros Sci, 53 (2011) 1451-1464.
[30] U. Angst, B. Elsener, C.K. Larsen, O. Vennesland, Cement Concrete Res, 39 (2009) 1122-1138.
[31] L.T. Mammoliti, L.C. Brown, C.M. Hansson, B.B. Hope, Cement Concrete Res, 26 (1996) 545-550.
[32] L. Li, A.A. Sagues, Corrosion, 57 (2001) 19-28.
[33] R.G. Pillai, D. Trejo, Aci Mater J, 102 (2005) 103-109.
[34] S. Goni, C. Andrade, Cement Concrete Res, 20 (1990) 525-539.
[35] C. Andrade, C.L. Page, British Corrosion Journal, 21 (1986) 49-53.
[36] P. Ghods, O.B. Isgor, J.R. Brown, F. Bensebaa, D. Kingston, Applied Surface Science, 257 (2011) 4669-4677.
[37] P. Ghods, O. Burkan Isgor, F. Bensebaa, D. Kingston, Corrosion Science, 58 (2012) 159-167.
[38] C. Alonso, C. Andrade, M. Castellote, P. Castro, Cement and Concrete research, 30 (2000) 1047-1055.
[39] M. Finšgar, Corros Sci, 77 (2013) 350-359.
[40] M. Tian, W.G. Pell, B.E. Conway, Corros Sci, 50 (2008) 2682-2690.
[41] M. Heine, D. Keir, M. Pryor, Journal of the Electrochemical Society, 112 (1965) 24-32.
[42] J. Richardson, G. Wood, Corrosion Science, 10 (1970) 313-323.
[43] K. Hashimoto, K. Asami, Corrosion Science, 19 (1979) 251-260.
[44] D.D. Macdonald, Journal of the Electrochemical Society, 139 (1992) 3434-3449.

[45] Z. Szklarska-Smialowska, Corrosion Science, 44 (2002) 1143-1149.
[46] Y. Liu, G.Z. Meng, Y.F. Cheng, Electrochimica Acta, 54 (2009) 4155-4163.
[47] N. Hakiki, M.D.C. Belo, A. Simoes, M. Ferreira, Journal of the Electrochemical society, 145 (1998) 3821-3829.
[48] N. Hakiki, S. Boudin, B. Rondot, M. Da Cunha Belo, Corrosion Science, 37 (1995) 1809-1822.
[49] P. Schmuki, H. Bohni, Werkstoffe und Korrosion, 42 (1991) 203-207.
[50] P. Schmuki, H. Böhni, Journal of the Electrochemical Society, 139 (1992) 1908-1913.
[51] S. Ningshen, U. Kamachi Mudali, V. Mittal, H. Khatak, Corrosion science, 49 (2007) 481-496.
[52] A. Shahryari, S. Omanovic, Electrochemistry Communications, 9 (2007) 76-82.
[53] Y. Cheng, J. Luo, Electrochimica acta, 44 (1999) 2947-2957.
[54] Y. Cheng, J. Luo, Electrochimica Acta, 44 (1999) 4795-4804.
[55] H. Gerischer, Corrosion science, 29 (1989) 191-195.
[56] M. Santamaria, D. Huerta, S. Piazza, C. Sunseri, F. Di Quarto, Journal of The Electrochemical Society, 147 (2000) 1366-1375.
[57] H. Wu, Y. Wang, Q. Zhong, M. Sheng, H. Du, Z. Li, Journal of Electroanalytical Chemistry, 663 (2011) 59-66.
[58] M. Büchler, P. Schmuki, H. Böhni, T. Stenberg, T. Mäntylä, Journal of the Electrochemical Society, 145 (1998) 378-385.
[59] U. Stimming, J. Schultze, Electrochimica Acta, 24 (1979) 859-869.
[60] S.R. Morrison, Electrochemistry at semiconductor and oxidized metal electrodes, 1980.
[61] K. Rajeshwar, Encyclopedia of electrochemistry, (2002).
[62] V.A. Myamlin, Y.V. Pleskov, Electrochemistry of semiconductors, Plenum Press, New York, 1967.
[63] A.W. Bott, Current Separations, 17 (1998) 87-92.
[64] Y. Xu, M.A. Schoonen, American Mineralogist, 85 (2000) 543-556.
[65] A.J. Nozik, Annual Review of Physical Chemistry, 29 (1978) 189-222.
[66] I.-u.-H. Toor, Journal of The Electrochemical Society, 158 (2011) C391.
[67] J. Dewald, Bell System Technical Journal, 39 (1960) 615-639.
[68] K. Azumi, T. Ohtsuka, N. Sato, Journal of The Electrochemical Society, 134 (1987) 1352-1357.
[69] J. Schultze, U. Stimming, J. Weise, Berichte der Bunsengesellschaft für physikalische Chemie, 86 (1982) 276-282.
[70] A. Simoes, M. Ferreira, B. Rondot, M. da Cunha Belo, Journal of the Electrochemical Society, 137 (1990) 82-87.
[71] A. Goossens, M. Vazquez, D.D. Macdonald, Electrochimica acta, 41 (1996) 35-45.
[72] J. Sikora, E. Sikora, D.D. Macdonald, Electrochimica acta, 45 (2000) 1875-1883.
[73] A. Di Paola, F. Di Quarto, C. Sunseri, Corrosion science, 26 (1986) 935-948.
[74] M. Kloppers, F. Bellucci, R. Latanision, Corrosion, 48 (1992) 229-238.
[75] H. Tsuchiya, S. Fujimoto, Science and Technology of Advanced Materials, 5 (2004) 195-200.

[76] I. Díez-Pérez, P. Gorostiza, F. Sanz, Journal of The Electrochemical Society, 150 (2003) B348.
[77] I. Díez-Pérez, A.G. Güell, F. Sanz, P. Gorostiza, Analytical chemistry, 78 (2006) 7325-7329.
[78] Gamry, Warminster, Pennsylvania, 2015.
[79] M.H. Dean, U. Stimming, Corrosion Science, 29 (1989) 199-211.
[80] M.H. Dean, U. Stimming, The Journal of Physical Chemistry, 93 (1989) 8053-8059.
[81] M.H. Dean, U. Stimming, Journal of electroanalytical chemistry and interfacial electrochemistry, 228 (1987) 135-151.
[82] S.P. Harrington, F. Wang, T.M. Devine, Electrochimica Acta, 55 (2010) 4092-4102.
[83] S.J. Ahn, H.S. Kwon, Electrochimica Acta, 49 (2004) 3347-3353.
[84] Y.-l. Zhang, Q.-l. Li, Journal of Zhejiang University SCIENCE A, 7 (2006) 1447-1452.
[85] M. Sánchez, J. Gregori, C. Alonso, J.J. García-Jareño, H. Takenouti, F. Vicente, Electrochimica Acta, 52 (2007) 7634-7641.
[86] M. Sánchez, J. Gregori, M.C. Alonso, J.J. García-Jareño, F. Vicente, Electrochimica Acta, 52 (2006) 47-53.
[87] D.G. Li, Y.R. Feng, Z.Q. Bai, J.W. Zhu, M.S. Zheng, Electrochimica Acta, 52 (2007) 7877-7884.
[88] F. La Mantia, H. Habazaki, M. Santamaria, F. Di Quarto, Russian Journal of Electrochemistry, 46 (2010) 1306-1322.

ELECTRONIC PROPERTIES OF PASSIVE FILMS OF CARBON STEEL IN HIGHLY ALKALINE ENVIRONMENTS USING MOTT-SCHOTTKY ANALYSIS

Jon Williamson, O. Burkan Isgor

To be submitted to: Journal of Applied Surface Science (Elsevier)

Fac. of Military Sciences (FMS)

Netherlands Defense Academy

P.O. Box 90002, 4800 PA, Breda, Netherlands

2. First Manuscript

Electronic Properties of Passive Films of Carbon Steel in Highly Alkaline Environments using Mott-Schottky Analysis

Jon Williamson[1], O. Burkan Isgor[2],

[1]Graduate Student at Oregon State University, Department of Materials Science

[2]Associate Professor at Oregon State University, School of Civil and Construction Engineering

Abstract: A methodology for studying the electronic properties of passive films formed in highly alkaline solutions using Mott-Schottky (M-S) analysis is proposed. Carbon steel rebar was investigated, due to its widespread use and exposure to the highly alkaline environments seen in concrete (pH >12.5). This methodology included determining a proper M-S potential sweep range, rate, and frequency, which were found to be -0.5 to 0.5 V, 18 mV/s, and 1000 Hz, respectively, for the passive steel rebar system. This test methodology was then applied to steel rebar in a saturated $Ca(OH)_2$ passivating solution (pH 12.6) meant to simulate the highly alkaline environments seen in concrete. The passive film on steel rebar was found to be n-type with two discrete donor species. An extremely high donor density on the order of 10^{21} cm^{-3}, a flatband potential of -0.53 V, and a maximum space charge layer thickness of 0.4 nm at full passivation was found.

Keywords: Mott-Schottky analysis, passive film, carbon steel rebar, corrosion, concrete.

2.1. Introduction

The chloride-induced corrosion of carbon steel rebar in concrete is the most costly deterioration mechanism of civil engineering infrastructure in the United States; the direct cost of corrosion to highway bridges alone is estimated to be $8.29 billion annually [1]. The prevalence and associated cost of the problem have led to numerous studies aimed at characterizing electrochemical properties of carbon steel rebar in concrete [2-9]. These studies showed that in the highly alkaline environment found in concrete (pH >12.5), carbon steel rebar forms a passive oxide/oxyhydroxide film that protects the steel from high corrosion rates. However, this passive film can break down in the presence of sufficient amounts of chlorides, which might originate from external sources such as de-icing chemicals or marine salts. Electrochemical studies have revealed macroscopic information about the passive films that form in highly alkaline environments provided by concrete pore solutions and have shown that chloride-induced depassivation can occur at a wide range of chloride thresholds [10]. This discrepancy of chloride thresholds have been shown to be the result of a combination of factors including variable rebar surface conditions [11-13], different cement types and concrete pore solution compositions [14, 15].

More advanced understanding of the fundamental mechanisms governing passivity and chloride-induced depassivation of carbon steel rebar, however, were developed after the use of advanced nano-scale characterization studies [9, 16-21]. For example, nano-scale x-ray photoelectron spectroscopy (XPS) and electron energy loss spectroscopy (EELS) were used to characterize the elemental composition and thickness of the passive film of steel rebar in various concrete pore solution compositions [19-21].

These studies found that the passive film thickness ranges between 3-15 nm. It can be characterized as a bilayer structure comprised predominantly of Fe^{II} oxides/oxyhydroxides near the substrate surface and Fe^{III} oxides/oxyhydroxides near the free surface. The Fe^{II}-rich layer was found to be only 2-3 nm thick but protective, while the Fe^{III}-rich layer was found to be much thicker at 10-15 nm but porous and unprotective. The addition of chlorides resulted in a decrease of the passive film thickness and caused the Fe^{III}/Fe^{II} ratio to increase through a chemical reaction between the Fe^{II}-rich oxides and chlorides which oxidized the Fe^{II} by one valence state to Fe^{III}, which is less protective.

Although electrochemical, microscopic, spectroscopic, and kinetic techniques have been amply used to characterize numerous aspects of the passive film on carbon steel rebar in concrete or in simulated concrete pore solutions, they do not explain the electronic properties of the film which are known to have significant importance to the corrosion behavior of the passive film as reported by several studies. The electronic properties of passive films have been shown to indicate the onset of pitting and localized film dissolution for aluminum [22-24] and stainless steel [25-28]. Cheng and Luo convincingly showed their role in the passivity of carbon steel in chromate solutions [29, 30]. Gerischer reported a relationship between the electronic properties of passive films and the onset of the transpassive potential region on iron [31]. Other studies have shown that the electronic properties can be used as an indicator of the general resistance to corrosion of a metal, such as with Mo-Ta alloys [32] and Cu-Ni alloys [33]. Studies have also shown that the passive film on iron-based alloys shows semiconductive behavior [34, 35]. Although extensive work has been undertaken to

find the electronic properties of passive films on pure Fe [36-38] and stainless steels [39, 40], the research on the electronic properties of carbon steel rebar in concrete pore solutions is rather limited. A better understanding of the electronic properties of steel rebar in simulated concrete pore solutions will provide additional information to existing passivation and depassivation models of carbon steel rebar in concrete and will potentially lead to the development of new corrosion mitigation techniques, for example, in the form of corrosion inhibitors or new corrosion-resistant reinforcements.

One of the primary ways for performing *in situ* measurements of the electronic properties of passive films that exhibit semiconductive behavior is Mott-Schottky (M-S) analysis [41]. This is based on the M-S relationship which involves measuring the apparent capacitance of a passive film in an electrolyte as a function of the potential while the passive film is under depletion conditions. The M-S relationship for an n-type semiconductor is derived directly from the Poisson-Boltzmann equation [42-44] and is given by Eq. 2.1:

$$\frac{1}{C^2} = \frac{1}{C_H^2} + \frac{2}{\varepsilon\varepsilon_0 e N_D}\left(V - V_{fb} - \frac{kT}{e}\right) \tag{2.1}$$

where C (F m^{-2}) is the apparent capacitance, C_H (F m^{-2}) is the Helmholtz capacitance, V (V vs. SCE) is the applied potential, k is Boltzmann's constant ($1.381*10^{-23}$ J K^{-1}), T (K) is the temperature, e (C) is the electronic charge, ε_0 is the permittivity of free space ($8.854*10^{-12}$ F m^{-1}), and ε (no units) is the dielectric constant (12 for iron). A plot of C^{-2} vs. V should be linear with a positive (for n-type semiconductors) or negative (for p-type semiconductors) slope that is inversely proportional to the donor density N_D (m^{-3}) or acceptor density N_A (m^{-3}), respectively. The intercept of this linear region with the

potential axis is used to derive the flatband potential, V_{fb} (V). From these electronic properties (i.e., $N_{D,A}$ and V_{fb}) the thickness of the semiconductive oxide space charge layer, *d*, which is another electronic property, can also be determined.

Several assumptions are made during the derivation and application of the M-S equation (Eq. 2.1); the first is that *C* is equivalent to a series capacitor model based only on C_H and the space charge capacitance, C_{sc}. If non-linearity is present in the C^{-2} vs *V* plot, it is possible then that this is due to other contributing factors to the capacitance such as from dopants located deep inside the energy band gap [44]. Another major assumption made in M-S analysis that is not addressed by most authors is that the observed capacitance as a function of potential is not frequency dependent. Commonly cited reasons for frequency dependence of capacitance results include the presence of deep donor states, dielectric relaxation phenomena, the amorphous nature of oxide films, and contribution from surface states to the capacitance [45]. This phenomenon has been observed in many studies of iron-based alloys and is addressed in this paper. A final assumption is that the dopant density does not change as a function of the applied potential. This is an issue not addressed by most authors when applying M-S analysis, but was highlighted by Sikora et al. [46] as being a potential cause of nonlinearity in M-S plots. To address this issue, the potential must be swept at a rate fast enough to mitigate any change in the dopant density and passive film thickness as a result of an applied potential.

When applying M-S analysis to carbon steel rebar in simulated concrete pore solutions, there are additional parameters to consider, including the passive film formation potential and passivation time, the potential sweep rate and range, and the frequency of

measurements. When performing M-S analysis, most studies apply a formation potential to the sample to artificially form the passive film quickly (within hours) [47-49], but in reality, the passive film on carbon steel in concrete forms under open-circuit conditions and usually takes around two weeks to fully form [2, 6, 50]. Electrochemical studies have shown that passive films that form under applied and open-circuit potentials have different behaviors [48], most likely due to the highly probable difference in their atomic structures [21]. Confirming this, a number of studies have found that the electronic properties vary significantly depending on the level of formation potential [46, 48], which adds to the suggestion that the passive films formed under open circuit conditions are different from those formed at open circuit potential. In addition, Hamadou et al. [49] convincingly demonstrated that different passivation times at a given formation potential significantly change the electronic properties of passive films.

The rate at which the potential is swept in M-S analysis and the sweep range also effect the electronic properties, because when a potential is applied to a passive film, the thickness of the film typically changes. Sikora et al. [46, 51] highlighted the need to run the potential sweep fast enough to "freeze" the passive film thickness in place. This ensures that the dopant density is not altered during the course of the analysis. However, most studies do not take this into account, and generally do not mention the rate at which they ran their potential scans for M-S analysis. A few mention very slow sweep rates such as 1 mV/s [49, 52] which are highly likely to change the dopant density. For the potential sweep range, care should be taken to ensure that extremely anodic potentials are not applied in the transpassive region of the sample, at which point

the sample will quickly corrode and alter its electronic properties. Past studies on carbon steel have performed sweeps ranging from -0.4 to 0.4 V [47], -0.5 to 1 V [49], and -1 to 0.6 V [53].

Lastly, the frequency at which M-S analysis is run is a subject of significant debate. The range of frequencies used in iron-based alloys include 1842 Hz [49], 1580 Hz [54], and 1 Hz [55, 56], among others. Some authors do not even mention a frequency [47, 48]. However, the most commonly used frequency is 1000 Hz; Di Paola [45] attributed this frequency to it being a convenient number by which to compare the electronic properties reported in other studies.

Although nearly all major studies on iron-based alloys reveal a passive film that exhibits n-type semiconductive behavior and high donor densities [57], the actual values for the electronic properties are subject to debate and show widespread discrepancy as shown in Table 2.1. The discrepancies in electronic properties are likely due to the variation in methodologies used to obtain these results when implementing M-S analysis. They might also be due to the fact that carbon steel does not begin to form a protective passive film under open-circuit conditions at pH levels below 10. Therefore, many of the studies used to define the passive state of steel rebar did not work with comparable oxide films.

Table 2.1: Electronic properties determined by major studies on carbon steel in alkaline solutions using Mott-Schottky analysis.

Solution pH	Donor Density, N_D ($x10^{21}$ cm^{-3})	Flatband Potential, V_{fb} (V vs. SCE)	Ref.
8.6	0.50	-0.44	[29, 30]
9.2	6.01	-0.50	[46]
9.2	3.12	-0.67	[58]
12.5	0.38	-0.88	[50]
13.2	8.10	-0.11	[47, 48]

In such a critical topic as the corrosion of carbon steel rebar in concrete, it is evident that an unambiguous picture of the electronic properties of the steel rebar passive film combined with a systematic methodology for acquiring those properties is needed. This will greatly contribute to defining the passive state of steel rebar and aid in developing mechanistic models of steel passivation in concrete. The main objective of this paper is to fill the gaps associated with the M-S analysis methodology to study the electronic properties of steel rebar passive films in simulated concrete pore solutions.

2.2. Materials and Methods

2.2.1. Specimen preparation

As-received 2-mm-thick disc samples were cut out of US #5 (15.5 mm diameter) carbon steel rebar with an elemental composition that is provided in Table 2.2. The cut samples were first cleaned with acetone to remove machining oils and rinsed with deionized water. They were then immersed in an ultrasonic bath of 5% acetic acid solution to remove any air-formed oxide from the surface and were rinsed again with deionized water. The cut surface of the samples were ground progressively with

increasing grit sizes and were polished to achieve a mirror finish using 0.05 micron silica. Finally the samples were rinsed with distilled water, dried with a delicate task wipe, and placed immediately in a dessicator until testing.

Table 2.2: Composition of tested steel specimens (average of three spectrographic results).

Element	Weight (%)
C	0.26
Si	0.27
Mn	1.10
Cr	0.05
Ni	0.07
Mo	<0.01
Cu	0.21
Al	<0.005
Nb	<0.01
V	<0.005
Ti	<0.005
B	<0.0005
P	0.01
Si	0.03
W	<0.01
Sn	0.021
Co	0.01
Zr	<0.01
Fe	Balance

During testing, each sample was loaded into the Princeton Applied Research K0105 sample holder, which is specially designed for performing repeatable and reliable electrochemical measurements on one of the exposed cut surfaces. The sample holder had hydrophobic Teflon washers to protect the sample edges from crevice corrosion; no crevice corrosion was observed in the tested samples during experiments. The exposed surface area after the sample was loaded into the holder was 1.15 cm^2. The

total resistance of the sample holder assembly was less than 1 Ω. The sample holder (working electrode) was immersed in a 1 L electrochemical cell with separate ports for reference and counter electrodes. Figure 2.1 provides an illustration of the sample holder assembly and the test setup.

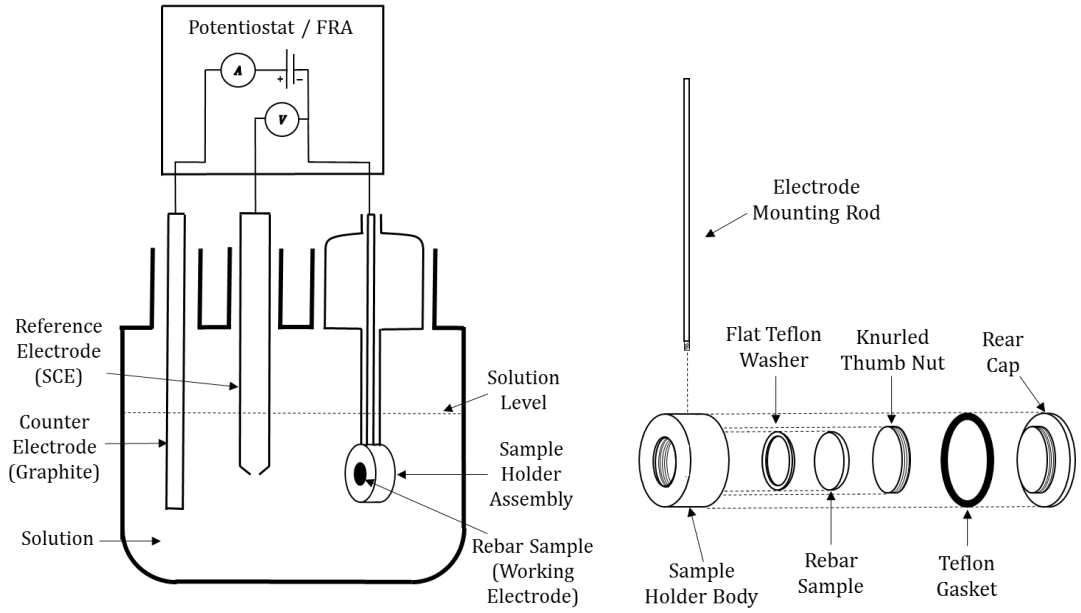

Figure 2.1: Schematic of (a) the experimental setup used for all electrochemical testing and (b) the sample holder assembly.

2.2.2. Experimental setup

Two similar three-probe electrochemical cells, as illustrated in Figure 2.1, were used for all experiments. These cells were connected in parallel to a Gamry Reference 3000 potentiostat and frequency response analyzer (FRA) through an 8-channel multiplexer (Gamry Electrochemical Multiplexer ECM8) for conducting simultaneous experiments. Gamry Echem Analyst software (version 6.25) was used for analyzing the impedance data. A graphite counter electrode with a large surface area was used in the

electrochemical setup as shown in Figure 2.1. An Accumet saturated calomel reference electrode (SCE) was placed through one of the electrochemical ports and into the solution near the working electrode and without a Luggin capillary. The tip of the electrode was placed approximately 5 mm from the surface of the sample. All potentials reported in this study are shown vs. SCE. The electrochemical cells were kept in a Faraday cage at all times. A photograph of the experimental setup is shown in Figure 2.2.

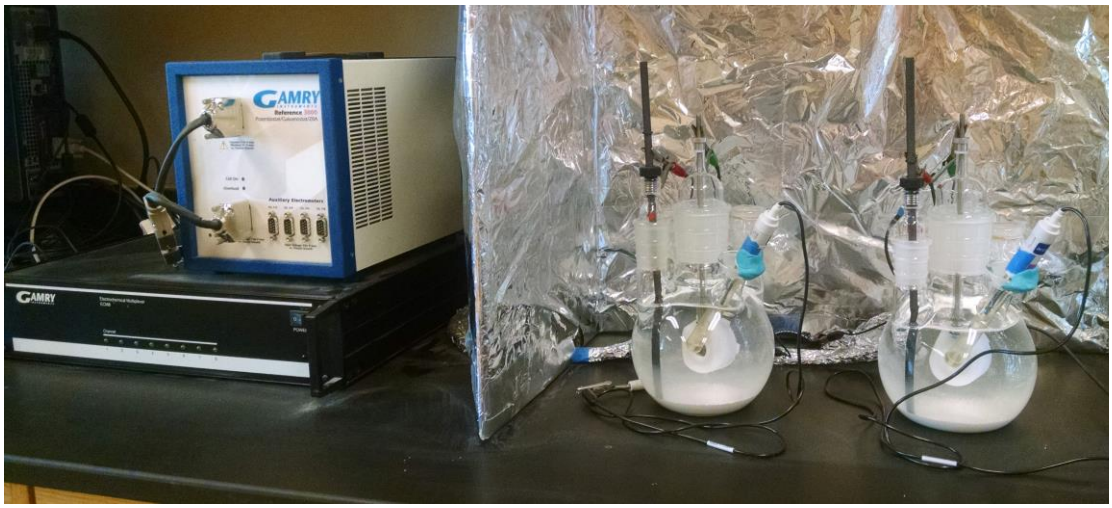

Figure 2.2: Photograph of the experimental setup used for electrochemical testing.

2.2.3. Passivating test solution

The test electrolyte consisted of a saturated calcium hydroxide solution (pH = 12.6) for simulating concrete pore solutions. Although actual concrete pore solutions contain other agents such as sodium hydroxide, potassium hydroxide, or sulfates [2], this solution provides a well-accepted baseline for studying passivation in highly alkaline solutions due to its relative simplicity [2, 6, 20]. The solution was prepared by adding

analytical grade $Ca(OH)_2$ to deionized water. The solution stirred at 800 rpm using a magnetic stirrer for a minimum of 12 h, ensuring the solution had come to full saturation. During solution preparation and stirring, the solution containers were sealed using parafilm in order to prevent carbonation (which lowers solution pH) and water evaporation. Before and after all tests pH measurements were performed to verify that it remained consistent during the course of testing.

2.2.4. Experimental Methods

The main objective of this investigation is to study the factors that might affect Mott-Schottky (M-S) analysis during the study of electronic properties of passive films that form on carbon steel in a highly alkaline environment simulating concrete pore solutions. For this purpose, carbon steel specimens were analyzed using M-S analysis at different stages of passivation and with different M-S analysis parameters.

The passivation state of the specimens was determined using open circuit potential (OCP) monitoring and electrochemical impedance spectroscopy (EIS) —both of which are non-destructive tests. OCP and EIS measurements were taken before and after each M-S analysis. Under open-circuit conditions (without the application of an anodic current to build passive films), it was shown by previous works that full passivation of carbon steel in concrete pore solutions takes 10-14 days [2, 6]. After immersion in the passivating solutions, the OCP for the polished steel rebar samples used in this study initially ranged between -0.4 and -0.45 V —these negative potentials indicate that the steel surface is not passive. During passive film formation, the OCP increases, and full passivity is marked by a stable OCP reading over time. The final OCP of the samples

at full passivation in the CH solution ranged between -0.15 to -0.2 V. A typical OCP profile of a passivating carbon steel specimen in the CH solution is shown in Figure 2.3a.

EIS scans were conducted at the open circuit potential with an AC voltage of 10 mV RMS; it was confirmed previously that EIS would not affect passivity at this excitation level. This AC signal amplitude showed no signs of non-linearity of the results; this is based on Lissajous curves which showed that the real and imaginary spectral data complied with Kramers-Kronig (K-K) relations for data quality. The frequency range of EIS scans was from 10^{5} Hz to 10^{-2} Hz at 5 data points per decade of frequency for the first few hours of passivation. After this initial passivation period, the frequency range of EIS scans was extended to cover 10^{-3} Hz. Impedance and phase angle data were collected for each scanned frequency. The main reason for using shorter, more frequent EIS scans during initial passivation was to capture the initial stages of passive film growth, which progresses far more quickly during these early exposure times. EIS scans that end at 10^{-2} Hz typically took around 20 minutes to complete, whereas scans to 10^{-3} Hz took an upwards of 90 minutes. Running 90 minute scans during early exposure times would result in inaccurate EIS results, because the passive film evolves so rapidly that the film characterized at high frequencies will be significantly different than that characterized at low frequencies. This rapid passive film evolution during early exposure times is called *sample drift*, and if EIS scans to 10^{-3} Hz had been performed at these early times, the K-K relations would have shown significant data non-linearity and sample drift. A fully passivated specimen is typically characterized by an impedance modulus larger than $1x10^{6}$ ohms-cm^{2} at low frequencies (i.e., 10^{-3} Hz)

and a phase angle between -80^{o} to -90^{o} at low and mid-range frequencies [6, 48].The high frequency data provides information about the electrolyte solution resistance, and the low frequency data is indicative of the polarization resistance (i.e., the resistance to charge transfer) of the sample [59]. A typical EIS scan (Bode plot) of a carbon steel specimen in the CH solution during passivation is shown in Figure 2.3b.

As part of this study, some of the specimens were also passivated under applied anodic potential to compare the M-S analysis results with those obtained from specimens that were passivated under open circuit conditions. This type of passivation is widely used in electrochemical studies of passivity of carbon steel in simulated concrete pore solutions to reduce the passivation times from 10-14 days to hours [2, 6]. Some specimens were passivated under -0.175 V applied voltage for 1 hour, 2 hours, and 3 hours. Others were passivated under -0.2 V applied voltage for 2 hours.

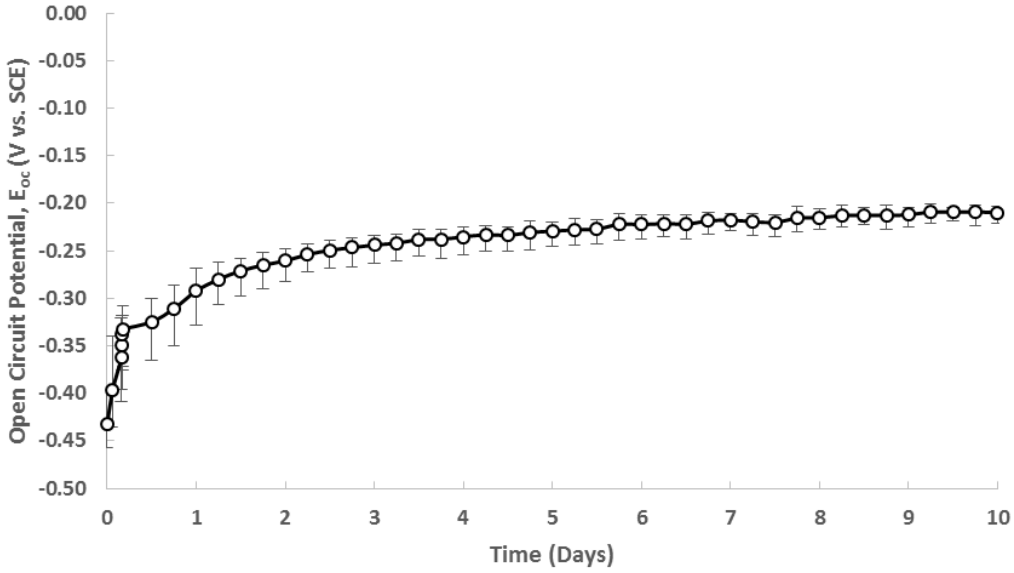

(a)

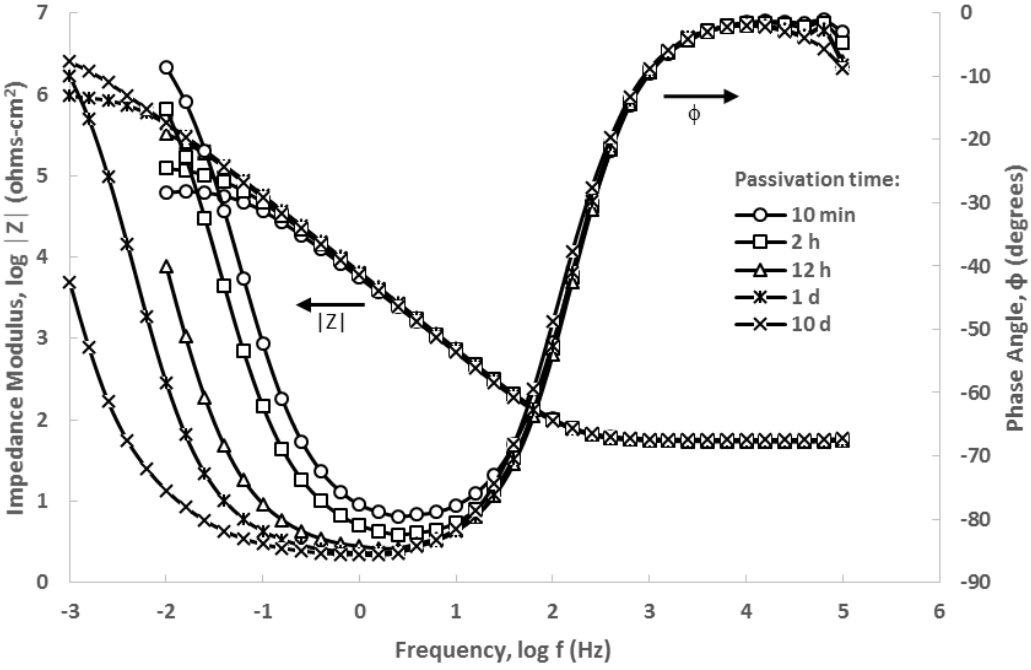

(b)

Figure 2.3: Typical (a) OCP and (b) EIS (Bode) plots which illustrate how the passive film on carbon steel rebar in CH solution evolves with time, beginning with initial passivation and ending with a fully passivated state.

Anodic polarization (AP) tests also reveal the potential range in which the passive region exists, and so this technique was used to determine the upper scan boundary of the M-S experiments. The potential sweep applied during M-S analysis should ideally not be pushed anodically beyond the passive region into the transpassive region, where significantly higher current densities will quickly destroy the passive film and create data based on a drastically altered (and likely thicker) film. Anodic polarization tests were run from the OCP to the onset potential of transpassive behavior. Figure 2.4 shows that a region of passivity was seen in steel rebar samples between -0.1 and 0.6 V. Therefore, M-S potential scans were limited to a maximum anodic potential of 0.5 V.

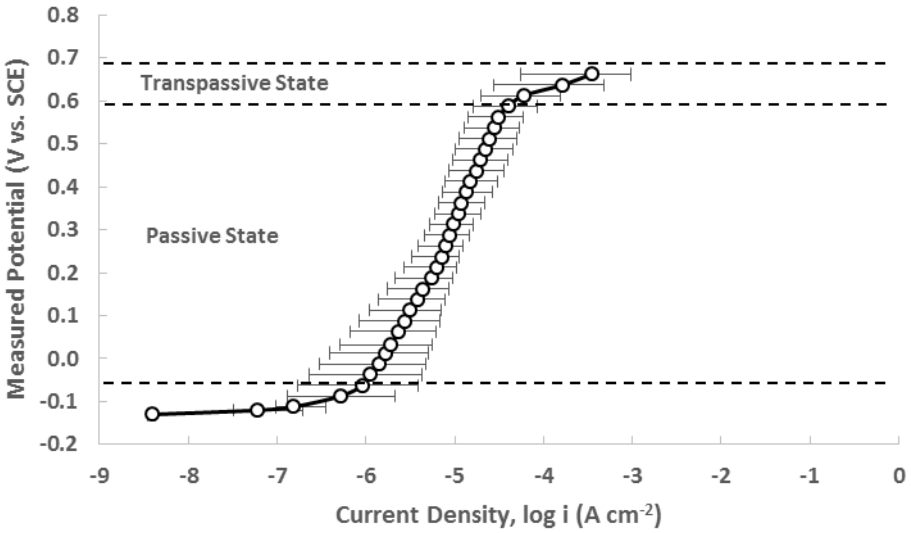

Figure 2.4: Anodic polarization (AP) plot that is representative of the polarization behavior found in fully passivated steel rebar samples. A region of passivity is apparent between approximately -0.1 to 0.5 V, followed by a region of transpassive behavior at potentials anodic to 0.6 V. Therefore, it was determined that the M-S sweep for steel rebar in highly alkaline solutions should not exceed 0.5 V to help ensure the film is not significantly altered.

All electronic properties reported in this study were derived from M-S plots based on samples that were fully passivated in solution, unless the evolution of the passive film

was being characterized. Previous studies [47-49, 53] on carbon steel rebar in alkaline solutions have shown n-type behavior through the entire passive region, which is consistent to what is seen with pure Fe [36] and stainless steel [60] (although stainless steel exhibits p-type behavior at extremely cathodic potentials [40]). Consequently, the M-S equation for an n-type semiconductor shown in Eq. 2.1 was implemented. M-S analysis tests performed at 10 mV AC amplitude, which based on the Lissajous curves taken during EIS tests that showed no signs of data non-linearity. The dielectric constant, ε, used in this study is subject to some debate, due to its drastically different value for Fe_3O_4 and γ-Fe_2O_3 oxides. But previous studies [36, 47, 49] have shown a value of 12 to be a good estimate for carbon steel rebar and will be used in this study. The lower limit of the Helmholtz capacitance, C_H, for the saturated calcium hydroxide solution was determined to be 22 μF cm^2. This was found by measuring the capacitance at -0.7 V, where Harrington et. al. [37] determined by SERS that only a small amount of passive film would be present on the surface of iron, in which case the space charge layer in the oxide film would be almost non-existent and nearly all the capacitance would be due to the Helmholtz layer.

2.3. Results and Discussion

The test parameters that might affect M-S analysis vary significantly in literature. These test parameters include: 1) the potential at which the passive film is formed, 2) the passivation time of the sample, 3) the potential sweep rate, 4) the potential sweep range, 5) the potential sweep direction, 6) the AC signal magnitude, and 7) the frequency. The first part of this section presents the results and discussion of the experimental study that was conducted to investigate these parameters. Based on this investigation, test

parameters for employing M-S analysis to the passive steel rebar system are recommended. In the second part of this section, these test parameters are then applied to steel rebar immersed in a representative concrete pore solution, and the evolution of the electron properties from initial sample immersion in the passivating solution to full passivation is captured.

2.3.1. Factors affecting M-S analysis

2.3.1.1. Passive film formation potential

The question of whether to form the passive film by applying a film formation potential until a steady state current is reached versus forming the film under exclusively open circuit conditions is an important one. Most studies apply a formation potential to form a passive film that is supposedly representative of passive films formed in external conditions, and rarely are films actually formed at open circuit conditions over several days. It is therefore necessary to run EIS and M-S tests on steel rebar, comparing the fully formed passive films formed under potentiostatic control and under open circuit conditions to see if differences exist. Typically, steel rebar samples immersed in CH solution reached full passivation at around -0.175 to -0.2 V (see Figure 2.3a) after ten days. However, when forming films under potentiostatic control, previous studies [61, 62] have indicated that applying the film formation potential for 2 hours is sufficient to create a fully formed passive film with steady state current for iron-based alloys. Therefore, 2 hours at -0.2 V are the conditions used to form the passive film artificially for comparison to the passive film formed under open circuit conditions.

Figure 2.5 compares the results for the passive film formed at -0.2 V versus at open circuit conditions using EIS (Bode and Nyquist) plots. Looking at the EIS curves, it is clear that the passive films formed under an artificially applied potential are not equivalent to those formed naturally. The Bode plot (Figure 2.5a) shows a lower impedance modulus, $|Z|$, for the film formed potentiostatically, as well as a decreased phase angle, ϕ, covering a significantly reduced frequency range. These observations indicate the artificially formed film is not nearly as passivated compared to the film formed naturally. Additionally, the Nyquist plot (Figure 2.5b) shows the imaginary component of the impedance, *Zim*, for the artificially formed film is much less than the corresponding value for the naturally formed film. This is important, because M-S analysis uses capacitance measurements which are based on *Zim.* These observations coincide with the suggestion from Gunay et al. [21] that the atomic structure of the passive film is fundamentally different when it is formed artificially rather than at open circuit conditions.

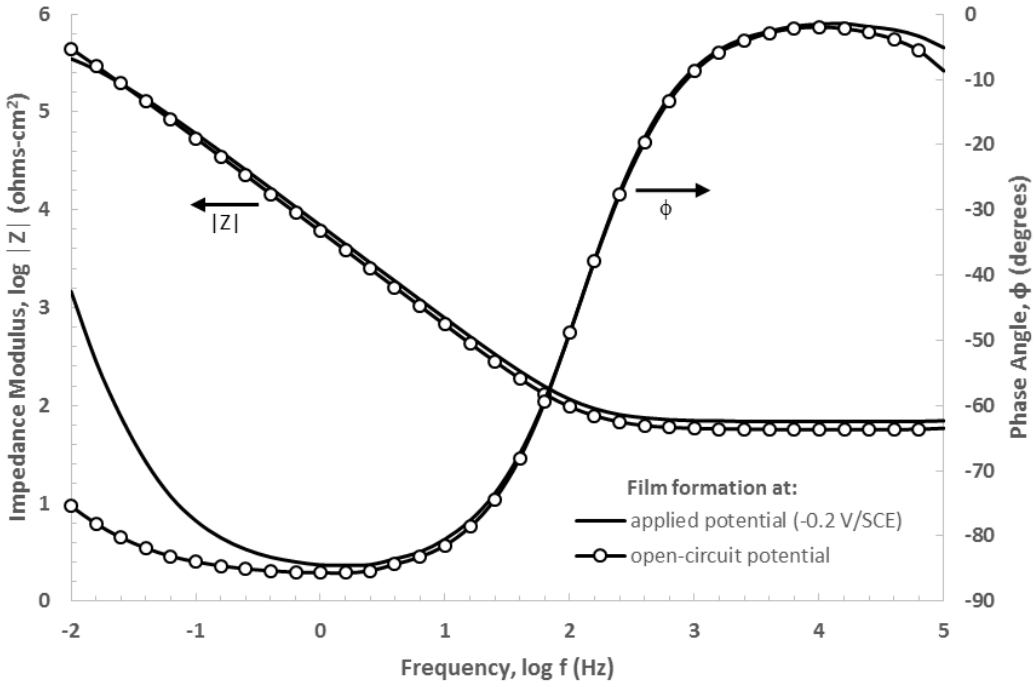

(a)

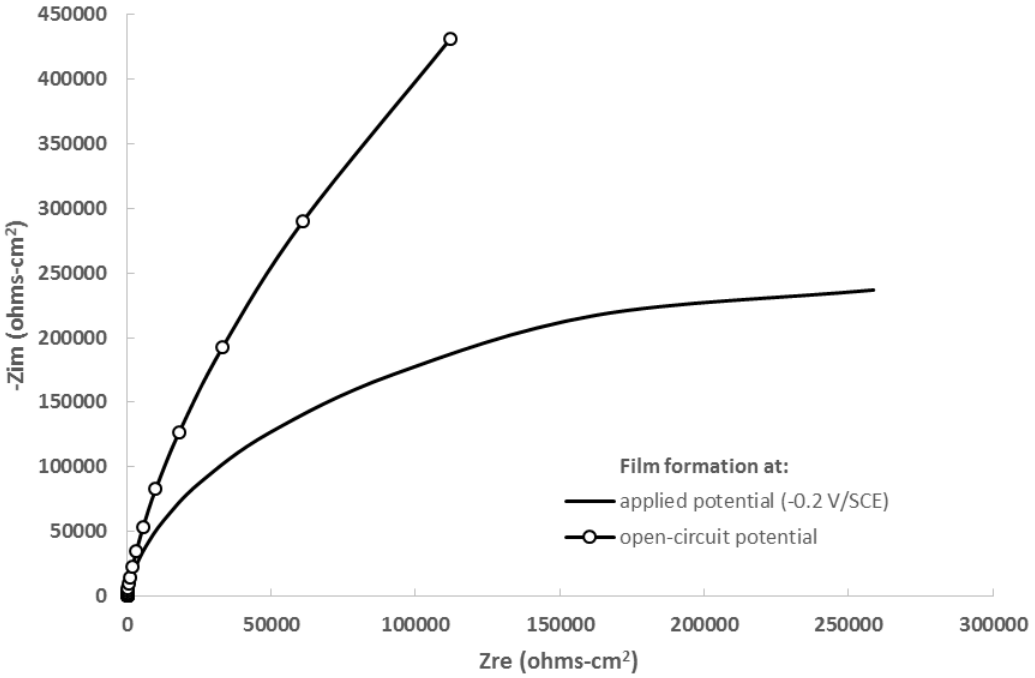

(b)

Figure 2.5: (a) Bode plot and (b) Nyquist plot comparing the passive films formed at an externally applied potential and at open circuit conditions. The two passive films are not equivalent.

M-S analysis (see Figure 2.6) was then performed to compare the electronic signatures of films formed under potentiostatic control versus those formed at the open circuit potential. The time and potential used to form the passive film potentiostatically were changed slightly to quantify the effect this variance would have on the M-S plots. Figure 2.6 shows the passive film formed naturally (i.e., at the open circuit potential) has a significantly different electronic signature compared to those formed artificially. For example, the apparent capacitances for the passive films formed potentiostatically are lower to varying degrees compared to the naturally-formed film. These lower capacitances are indicative of a significantly under-developed passive film, as was seen in Figure 2.5. A second difference is that sample formed naturally shows two positively-sloped linear regions (between -0.5 to -0.2 V, and 0.1 to 0.4 V), but the film formed potentiostatically at -0.175 V for 1 hour only seems to show a single, positively-slope linear region. Because the slopes of the M-S curves are critical when performing M-S analysis [44], this difference indicates that the electronic structure of the artificially-formed film may be completely different than that formed naturally. Based on these results, it is clear that passive films formed under potentiostatic control are not equivalent to those formed at open circuit conditions. Therefore, the steel rebar passive film should be developed at OCP until full passivation is reached, which according to Ghods et al. [2] takes a minimum of 10 days.

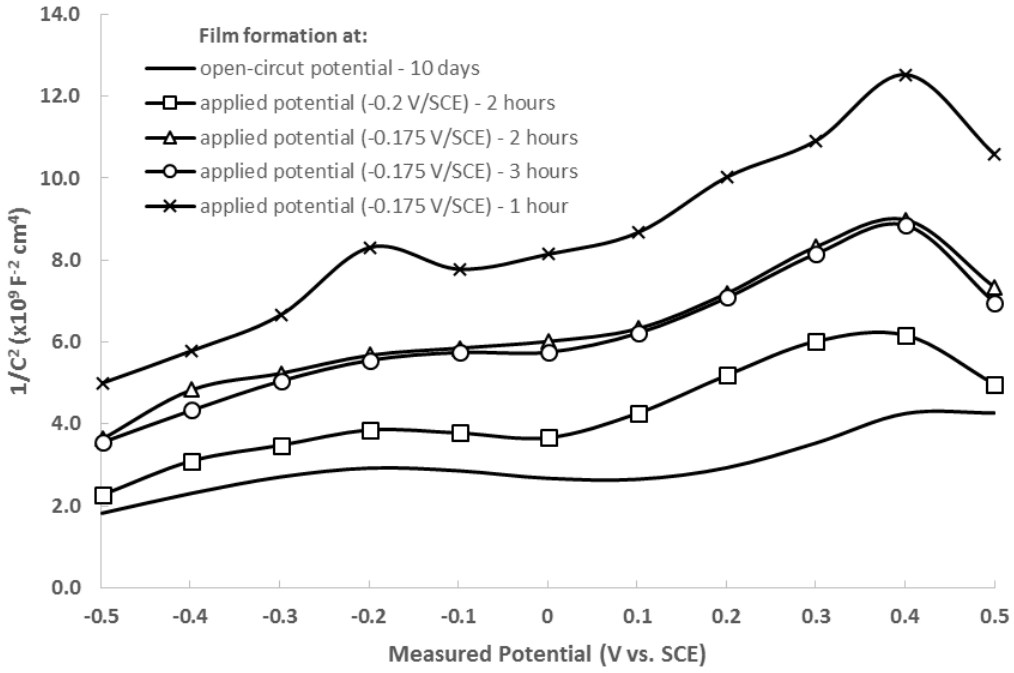

Figure 2.6: Mott-Schottky plot comparing the electronic signatures of the steel rebar passive formed under open circuit conditions versus those formed under various applied potentials for a varying time lengths.

2.3.1.2. Potential sweep rate, range and direction

Previous studies have shown that passive films formed on iron-based alloys exhibit M-S plots with two separate, positively-sloped linear regions [29]. As was previously mentioned, these positively-sloped regions indicate n-type semiconductive behavior. The previous studies, however, also show that the positive slopes abruptly turn negative at extremely anodic potentials during the M-S potential scan. The overwhelmingly accepted theory of the origin of the two positively-sloped linear regions is the existence of two separate donor regions located within the band gap of the oxide film [63]. The turn to negative slopes at extremely anodic potentials is theorized to be the end of n-

type semiconductive behavior where valence band participation begins to occur [36]. Therefore in order to fully characterize the passive film, both donor regions as well as the transition to a negative slope should be captured in the M-S potential sweep. To identify the range of this M-S potential sweep, a large potential scan that ranged from extremely cathodic potentials (-1 V) to anodic potentials located in the transpassive region of the oxide (+1 V) was performed while measuring the capacitance (see Figure 2.7). The two characteristic, positively-sloped linear regions are apparent between about -0.8 and 0.1 V, and again between 0.1 and 0.4 V. A peak in the plot corresponding to the maximum space charge thickness occurs at about 0.4 V, and it is at this potential that the turn to negative slopes begins. Although this potential scan range (-1 to 1 V) adequately covers the principle components of an iron-based passive film M-S plot (i.e., two positively-sloped linear regions and a transition to negative slopes at high potentials), it is also important to remember that the larger the sweep range is, the more likely the potential sweep will significantly alter the thickness of the passive film during the course of the sweep. This was highlighted by Sikora et al. [46, 51] as a major weakness in many instances where M-S analysis was used to identify electronic properties of passive films. Therefore, a potential range that only encapsulates both donor regions as well as the peak in the M-S plot is all that is necessary. Based on the results shown in Figure 2.7, a sweep between -0.5 and 0.5 V would adequately capture these prominent features.

To confirm that a potential sweep range between -0.5 and 0.5 V does not detrimentally affect the passive film thickness or structure during the course of the scan and address this issue raised by Sikora et al. [46, 51], an M-S test was first performed on a

passivated steel rebar sample in CH solution for this potential range. After running this M-S test and allowing the sample to subsequently re-equilibrate to the surrounding passivating solution, another M-S test was run on the same sample over a much shorter potential sweep range (-0.2 to 0.3 V) and at potentials closer to the OCP for passivated steel rebar (-0.175 to -0.2 V). This shorter sweep range that remains near to the OCP should produce little to no detrimental effects to the oxide film structure. The results of these two M-S tests can be seen in Figure 2.7. What this shows is that the larger potential sweep (-0.5 to 0.5 V) does not detrimentally effect the electronic signature of the passive film, since a much shorter potential sweep (-0.2 to 0.3 V) that should have almost no detrimental effect on the oxide film structure, produced virtually the same C^{-2} vs. V curve.

Figure 2.7 also reveals two other significant observations. The first is that the large potential sweep (-1 to 1 V) looks remarkably different compared to the two shorter M-S potential sweeps. The larger sweep is missing the abrupt increase in capacitance that occurs at around -0.1 V for the two shorter M-S tests; this abrupt change in the slope is one of the most prominent features for the two shorter tests. What this infers then is that the larger potential sweep (-1 to 1 V) is so large that it detrimentally effects the structure of the passive film during the course of the scan. It is highly conceivable that the extremely cathodic potentials that are initially applied substantially alter the thickness of the passive film before potentials closer to the OCP are reached.

A final observation that can be made from Figure 2.7 is with regard to the potential sweep rate. This was again highlighted by Sikora et al. [46, 51] as being a major weakness in existing studies using M-S analysis, in that a slow potential sweep rate

will have a similar effect on the passive film as would an M-S test with too wide of a sweep range. What the two shorter M-S tests (i.e., from -0.5 to 0.5 V and from -0.2 to 0.3 V) in Figure 2.7 reveal is that their scan rate is fast enough to keep the film from being significantly altered during the potential sweep. The potential scan rate used for the M-S tests in Figure 2.7 was 18 mV/s, which was the fastest scan rate possible considering the limitations of the potentiostat to make accurate capacitance measurements as a function of applied potential. If the scan rate applied was to slow, significant variation would be expected to occur between the -0.5 to 0.5 V scan and the -0.2 to 0.3 V scan, but this variation is nonexistent. Therefore, Figure 2.7 then helps to validate that a potential sweep rate of 18 mV/s combined and range of -0.5 to 0.5 V do not detrimentally alter the electronic structure and thickness of the oxide film during testing.

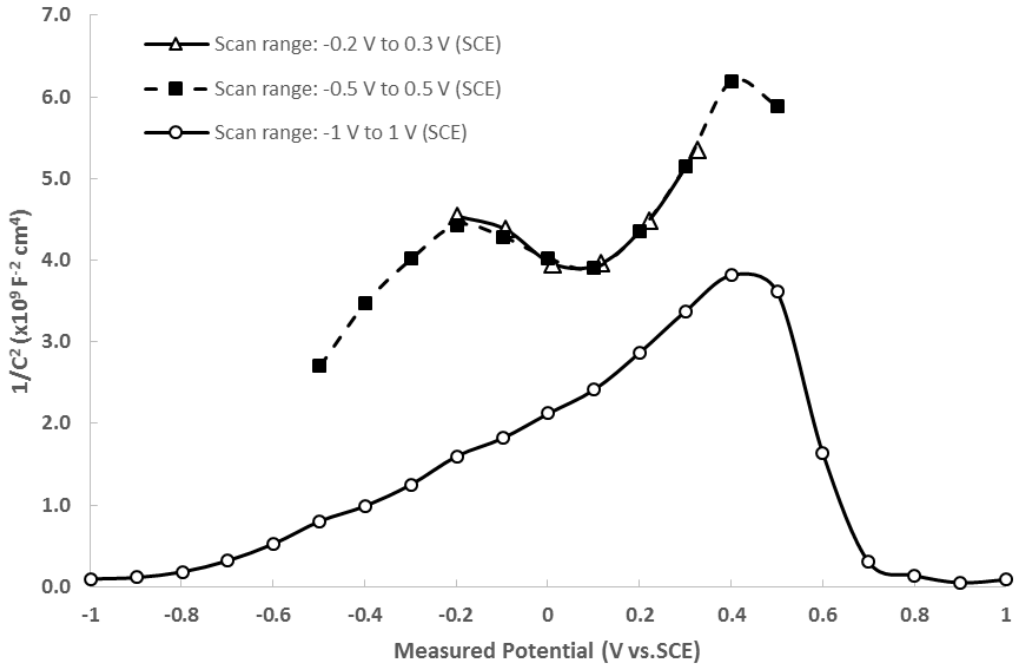

Figure 2.7: $1/C^2$ vs. V plot comparing the electronic signatures of passivated steel rebar samples from Mott-Schottky tests performed at varying potential scan ranges.

Although Figure 2.7 does provide convincing evidence that a potential sweep range of -0.5 to 0.5 V at a scan rate of 18 mV/s does not detrimentally effect the electronic structure or thickness of the oxide film during M-S testing, an additional test was conducted to further reinforce this claim. This test was proposed by Harrington et al. [64] and involves quantifying the hysteresis between the anodic and cathodic curves run on a single sample. What this test claims is that the slopes of the anodic and cathodic curves run consecutively on the same sample in both donor regions should be very similar if the oxide thickness was not affected by the M-S potential scan. Harrington et al. [64] quantified this hysteresis between the anodic and cathodic curves by measuring the percent change in the slopes of the two donor regions. If this percent change was of

sufficiently low value (i.e., 7% [64]), it is assumed that the potential was swept at a sufficiently fast rate to keep the oxide thickness constant.

This hysteresis test was then performed on two samples passivated in CH solution and shown in Figure 2.8. For the shallow donor region (-0.5 to -0.2 V), a percent change of only 2% was seen, indicating that the shallow donor values are indeed reliable. For the deep donor region, the percent change was slightly higher at around 7%. This however, is still within the bounds prescribed for a sufficiently low percent change in the slope. Therefore, it can be considered based on the results from Figure 2.7 and 2.8 that the electronic properties extracted from M-S tests performed using a potential sweep range of -0.5 to 0.5 V and rate of 18 mV/s are reliable for the passivated carbon steel rebar system.

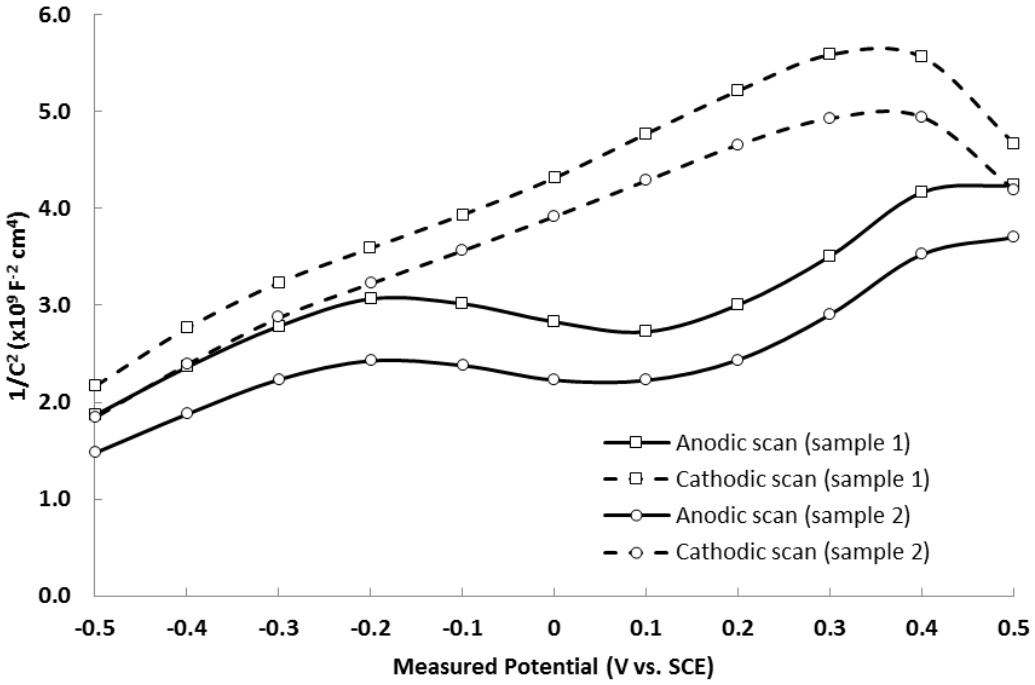

Figure 2.8: Mott-Schottky plot illustrating the hysteresis between anodic and cathodic curves on two passivated steel rebar samples. The slopes of the shallow and deep donor regions for each curve help to indicate that the potential sweep range and rate used for M-S analysis yields reliable data of the passive film electron properties, according to the method proposed by Harrington et al. [64]

The question of which potential sweep direction (i.e., anodic or cathodic) should be used in M-S analysis is almost completely ignored by most authors in literature, although a few have shown that the sweep direction can in fact change the electronic properties [29, 64]. Some authors report M-S results based on a cathodic sweep [53, 55], while most others just do not report it [47, 49]. Most often in the literature, potential sweeps are run from at or near the passive film formation potential to the direction that best shows the passive region of the film. It makes sense conceptually to begin the sweep at or near the formation potential to mitigate the "shock" experienced by the passive film under an extremely anodic or cathodic potential, which could potentially

alter the passive film beyond what would have otherwise occurred. Therefore, for passive steel rebar in CH passivating solution, the potential was swept anodically for all M-S tests except for those used to characterize the hysteresis in the M-S behavior (see Figure 2.8). The reason for this, as previously stated, is that beginning the sweep at a potential closer to the OCP (-0.175 to -0.2 V) and then sweeping in the direction towards the passive region (which lies anodic to the OCP based on the anodic polarization plot in Figure 2.4) makes most sense conceptually. However, further justification for beginning the potential sweep at a potential closer to the OCP and then sweeping in the anodic direction can be seen when comparing the anodic versus cathodic curves in Figure 2.8. The curves are clearly different, despite the fact they are sweeping in the same potential range and at the same rate. Both curves seem to show two distinct regions of positive linear slopes, and both show these linear regions occurring in similar potential ranges (e.g., -0.5 to -0.2 V for the anodic curve, and -0.5 to -0.3 V for the cathodic curve). However, the primary difference between these two curves is an abrupt increase in the capacitance at the beginning of the second linear region of the anodic curve. This abrupt increase in capacitance is completely missing from the cathodic curve.

To find the origin of this critical difference between the anodic and cathodic curves, a physical interpretation for both M-S plots must be discerned. As previously stated, past studies have attributed the occurrence of two linear regions in the M-S plots to the ionization of two distinct donor species in the band gap of the passive oxide film [63]. These two donors have been ascribed to, in the case of an iron-based alloy, Fe^{II} donors being oxidized from either tetrahedral or octahedral sites in the crystal lattice [29, 49,

60]. Ionization from tetrahedral sites occurs more readily and at lower applied potentials because of their lower bonding energy compared to octahedral sites. The initial positive linear slope illustrates the ionization of only these shallow donors (i.e., Fe^{II} impurities on tetrahedral sites). This linear region continues until about -0.2 V, at which point non-linearity in the anodic curve occurs and the capacitance abruptly increases. Dean et al. [65] highlighted that this dramatic increase in capacitance can be attributed to an increase in the total charge density in the space charge (i.e., depletion) region of the oxide film. An increase in the total charge density then points to the ionization of a second donor species located deeper in the band gap that is only excited at higher potentials. These deep donors (i.e., Fe^{II} impurities on octahedral sites) cause an immediate increase in the charge density and capacitance, and additionally result in a change of the slope of the second linear region (0.1 to 0.4 V). The slope of this second linear region is then indicative of the combination of shallow and deep donor densities in the film. The fact that the cathodic curve does not have the corresponding increase in capacitance with the onset of deep donor ionization is interesting, and it is likely that additional phenomena is occurring in the space charge layer during the cathodic potential sweep. One possible explanation for this is that the extremely anodic potentials (+0.5 V) seen initially in the cathodic scan detrimentally affect the oxide film, so that the structure of the passive film early in the scan is dramatically different from that seen in the later part of the scan. Although 0.5 V applied potential is not yet in the transpassive region of the steel rebar passive film (see Figure 2.4), it is encroaching, and it is significantly far from the OCP under equilibrium conditions.

Based on the lack of a capacitance increase that should accompany the ionization of a new donor species, combined with the fact that beginning the M-S potential sweep at a potential closer to the OCP makes most sense conceptually, it was determined that M-S analysis performed on passive carbon steel in alkaline media should be executed by sweeping the potential in the anodic direction.

2.3.1.3. Measurement frequency

The dependence of the space charge capacitance on the frequency is well documented for iron-based passive films. Generally speaking, studies have found that as the applied frequency increases, the capacitance decreases [45, 63, 66]. This frequency dependence can be clearly seen in Figure 2.9, where a short M-S potential sweep was run at various frequencies over the same potential range and at the same sweep rate. La Mantia et al. [63] also showed that an increase of the frequency results in a decrease of the donor density and an increase in the flatband potential. Therefore, to develop a methodology for applying M-S analysis to passive steel rebar systems and deriving reliable electronic properties, the proper frequency for running M-S potential sweeps must be determined.

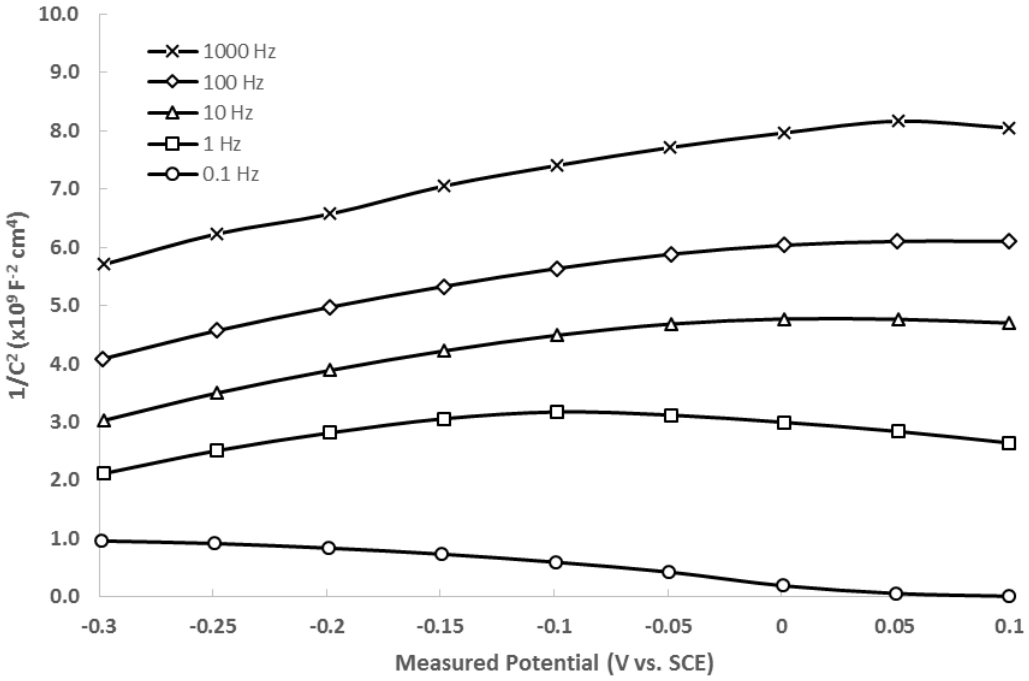

Figure 2.9: Mott-Schottky plot illustrating the dependence of the measured capacitance on the frequency used in the AC potential sweep.

The M-S relation (Eq. 2.1) does not account for a frequency-dependent capacitance. Therefore, if a frequency range could be found where the capacitance remains constant, the M-S relation would remain satisfied. This method was applied by Ahn et al. [66] and Sikora et al. [46] when selecting the proper frequency for iron and tungsten passive films, respectively.

Figure 2.10 illustrates a frequency versus capacitance plot. Generally speaking, the capacitance tends to decrease with increasing frequency, but a region of nearly constant capacity exists between 10 and 1000 Hz. This frequency range of nearly constant capacitance is consistent with the findings for stainless steel [45]. At lower frequencies, the capacitance decreases rapidly, and Di Paola [45] attributed this to a contribution

from ionic species located in the space charge layer. The contribution from the ionic species only occurs at low frequencies due to their low mobility. The capacitance then enters a region of relative consistency until about 1000 Hz. After 1000 Hz, the capacitance begins to decrease quickly again, which has been attributed to either a contribution from surface states to the capacitance created by OH^- adsorption at the oxide surface, or due to a decrease in the parallel capacitance values with the ω^2, where ω is the angular frequency of the AC signal [45]. In order to minimize any effect on the space charge capacitance from the influence of ionic species in the space charge layer, the maximum frequency within the region of nearly constant capacity in Figure 2.10 was chosen as the frequency best suited for running M-S analysis. Therefore, M-S analysis of passive carbon steel in alkaline media should be conducted at 1000 Hz.

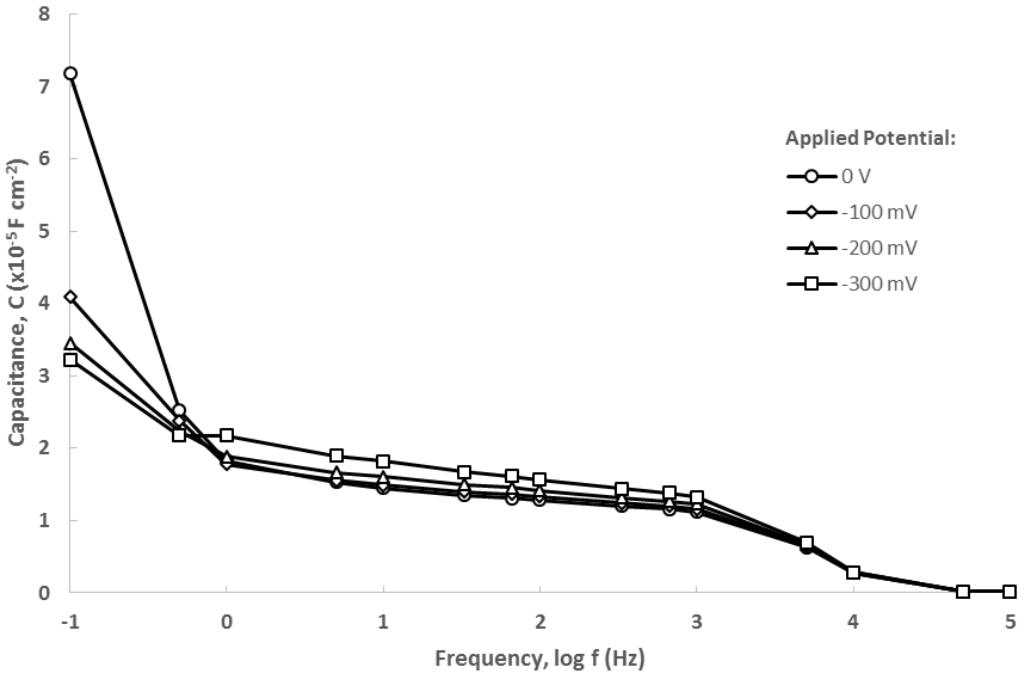

Figure 2.10: Capacitance vs. frequency plot illustrating that a frequency range exists where the capacitance is nearly independent of frequency. Several applied potentials were used in this analysis, and each showed similar results.

2.3.2. The evolution of the electronic properties of the passive film

With a comprehensive methodology established for determining the runtime parameters in Mott-Schottky analysis, the evolution of the electronic properties of the passive film on steel rebar in a highly alkaline environment was determined. To the authors' knowledge, no such study on how those properties evolve on passive steel rebar under open circuit conditions using M-S analysis has been performed. To evaluate this passive film evolution, only one M-S test should ideally be run per test sample, since it is known that applying a potential will change the properties of the film. In reality, however, each sample is remarkably different despite the extensive sample preparation. This can be accounted for by taking into account the disordered and inconsistent nature of the mild steel alloy used to make steel rebar, which is almost entirely formed from recycled steel scrap metal. Because the passive film is only a few nanometers in thickness [7], it naturally makes sense that this microstructural disorder present on the surface of steel rebar will produce some inconsistency in the passive film electronic and structural properties when comparing different rebar samples. It could therefore be difficult to find trends in data when performing M-S analysis on multiple samples. Consequently, the evolution of the passive film was monitored using both a single sample and multiple samples. The multiple samples only had one M-S test performed on them at the prescribed passivation time, while the single sample had an M-S test run on it at all the prescribed passivation times. This painted a more complete picture of how the passive film evolves, while taking into account sample-to-sample variation. The film was characterized at 2 h, 12 h, 2 d, 5 d, and 10 d (full passivation)

using a single sample for all five passivation times (see Figure 2.11 and Table 2.3) and multiple samples, one for each passivation time (see Figure 2.12 and Table 2.4). Tables 2.3 and 2.4 display the quantified electronic properties derived from their respective M-S plots.

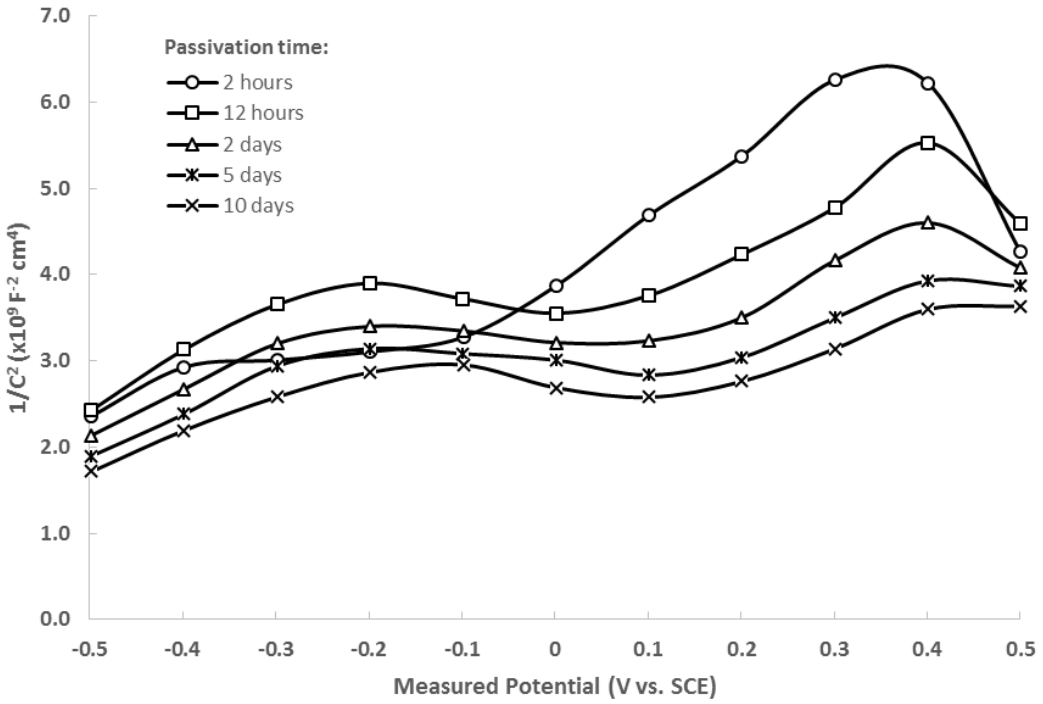

Figure 2.11**:** Mott-Schottky plot showing the evolution of the electronic properties of the passive film formed on steel rebar in CH solution. All five M-S tests were performed on a single sample.

Table 2.3: Quantitative comparison of the electronic properties extracted from Figure 2.11.

Passivation Time	**N_{D1} [m^{-3}]**	**N_{D2} [m^{-3}]**	**V_{fb} [V]**	**d_{max} [nm]**	**d_{trans} [nm]**
0.5 h	$1.21*10^{27}$	$6.63*10^{24}$	-0.56	0.60	0.33
1 h	$1.18*10^{27}$	$4.94*10^{25}$	-0.57	0.60	0.33
2 h	$1.57*10^{27}$	$4.27*10^{25}$	-0.54	0.47	0.25
1 d	$1.68*10^{27}$	$9.42*10^{25}$	-0.49	0.42	0.21
10 d	$1.78*10^{27}$	$1.42*10^{26}$	-0.45	0.38	0.18

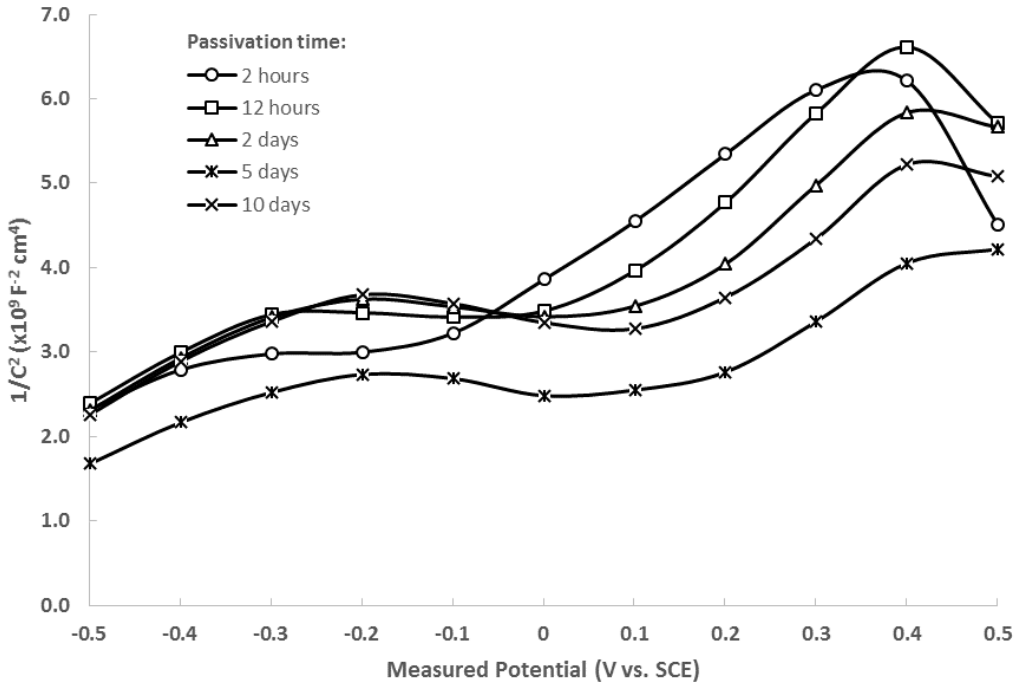

Figure 2.12: Mott-Schottky plot showing the evolution of the electronic properties of the passive film formed on steel rebar in CH solution. Each M-S tests was performed on a separate sample passivated to the prescribed passivation time.

Table 2.4: Quantitative comparison of the electronic properties extracted from Figure 2.12.

Passivation Time	**N_{D1} [m^{-3}]**	**N_{D2} [m^{-3}]**	**V_{fb} [V]**	**d_{max} [nm]**	**d_{trans} [nm]**
0.5 h	$1.62*10^{27}$	$8.92*10^{24}$	-0.57	0.48	0.26
1 h	$1.41*10^{27}$	$1.57*10^{25}$	-0.58	0.54	0.30
2 h	$1.43*10^{27}$	$1.63*10^{25}$	-0.56	0.53	0.29
1 d	$1.67*10^{27}$	$3.54*10^{25}$	-0.46	0.42	0.20
10 d	$1.60*10^{27}$	$5.02*10^{25}$	-0.55	0.47	0.25

Although some variation exists in the data, it is clear that as the potential was swept in the positive direction, the capacitance in the space charge layer decreases, resulting in an increase in the space charge layer thickness. Solely shallow donor ionization is occurring until approximately -0.3 to -0.1 V, at which point the space charge

capacitance abruptly increases as the deep donors begin to be ionized. A second linear region of positive slope then appears as the potential continues to increase anodically. This second linear region lasts until a critical potential of around 0.4 V is reached, at which point, the M-S plot abruptly decreases. It is at this potential that the space charge layer thickness is at its maximum and the capacitance at a minimum. The change of the M-S plot to a negative slope is characteristic of p-type semiconductive behavior, and it is likely that participation of the valence band is beginning to occur as the potential continues to increase and the Fermi level draws nearer to the valence energy band [36]. This general trend is present for all M-S plots, regardless of a changing passivation time or whether multiple M-S tests were run on the same sample.

If the space charge thickness is decreasing, it would generally be assumed that the donor density within that space charge layer was increasing, which is exactly what was seen particularly in Table 2.3. The shallow donor density, N_{D1}, and deep donor density, N_{D2}, were calculated based on Eq. 2.2 where S_1 is the slope of the M-S plot in the shallow donor region (about -0.5 to -0.2 V), and S_2 is the slope in the deep donor region (about 0.1 to 0.4 V).

$$N_{D1} = \frac{2}{\varepsilon\varepsilon_0 e S_1}, \qquad N_{D2} = \frac{2}{\varepsilon\varepsilon_0 e S_2} - N_{D1} \tag{2.2}$$

This equation was derived for the case of multiple n-type donor species within the passive film [29, 60]. Notice that in calculating N_{D1}, only the slope of the shallow donor region is needed. However, calculating N_{D2} requires not only S_2, but also a knowledge of N_{D1}. This is due to the fact that S_2 is a function of *all* the ionized donors at the higher potentials, which include both the shallow and deep donor species. Overall, the donor

density during the course of passivation remained on the order of 10^{21} cm^{-3}. This is an extremely high donor density indicating a highly disordered passive film structure, which is consistent with other studies done on iron-based passive films [45, 55].

Most studies have found that increasing the passivation time actually decreases both the donor density and the space charge capacitance as whole, which is opposite the results found particularly in Table 2.3. Most authors have attributed this to the progressive consumption of charge carriers during longer periods of passivation buildup [36, 49]. However, Azumi et al. [67] found conflicting results. By increasing the passivation time, the donor density decreased in a borate solution of pH 6.5, but it increased in a phosphate solution of the same pH. The exact cause of the increasing donor density with passivation time is still under investigation. However, what is clear in the present study is that the passive film is extremely disordered and has a donor density that remains consistently between $1x10^{27}$ and $2x10^{27}$ m^{-3}.

The flatband potential, V_{fb}, remained relatively constant during the course of passivation, with an average value of around -0.53 V. This makes sense in that the flatband potential is the one empirical value that takes into account the intrinsic properties both of the electrode and the electrolyte at their interface [41], and since the electrode and electrolyte are consistent for all tests, the flatband potential should have likewise remained relatively constant. Typical values in literature [60] for the flatband potential of passive iron increase with increasing pH from -0.34 at pH 8.4 to -0.38 at pH 9.2, indicating that the -0.53 V at pH 12.6 in the present study is consistent with previous studies. To determine the flatband potential, Eq. 2.3 was used [37]. This takes into account the Helmholtz capacitance, C_H, which is critical when dealing with the

highly defective films seen in iron-based alloys [45]. Altering C_H by only 5 μF/cm^2 can change V_{fb} by up to 0.25 V. By discounting C_H altogether, the V_{fb} is altered by about 0.4 V.

$$V_{fb} = V_0 + \frac{\varepsilon\varepsilon_0 e N_D}{2C_H^2} - \frac{kT}{e} \tag{2.3}$$

Lastly, in determining the thickness of the space charge layer, two values are reported in Tables 2.3 and 2.4. The first is the estimated thickness, d_{trans}, at the potential where purely shallow donor ionization transitions to an additional contribution from deep donors, or about -0.1 V. d_{trans} tended to decrease during the course of passivation to around 0.2 nm at full passivation. The second thickness, d_{max}, was measured at the peak of the M-S plot (about 0.4 V), where participation of the valence band begins to occur. The peak corresponds to the maximum depletion layer thickness and was calculated to be around 0.4 nm at full passivation. This a reasonable value, because it is within the range of the protective Fe^{II} layer thickness of a few nanometers [7], and it is consistent with other space charge layer thicknesses measured at a film formation potential of -0.2 V [29, 60]. The equation used for determining the space charge layer thickness (see Eq. 2.4) is derived from a simple parallel plate capacitor model and is used extensively in literature [29, 45, 60].

$$d = \frac{\varepsilon\varepsilon_0 A}{C_{sc}} \tag{2.4}$$

A is the exposed surface area of the sample, and $C_{sc,}$ is derived from Eq. 2.1 by assuming a series capacitor model at the semiconductor/electrolyte interface [36].

An additional observation of the M-S plots in Figures 2.10 and 2.11 is the formation of a “hump” centered around the onset of deep donor ionization at passivation times exceeding two hours. Although an exact explanation for the presence of this feature is at present unknown, Dean et al. [65] showed that for extremely disordered or incoherent semiconductors, a wide distribution of energy states can exist around the characteristically discrete donor levels. This wide distribution of donor states, estimated using a Gaussian distribution, results in a flatter, less abrupt transition to full deep donor ionization. This is exactly what is seen in the M-S plot taken at 2 hours passivation time in Figures 2.10 and 2.11. The electronic properties based on M-S plots then seem to indicate that the passive iron oxide film at early passivation times is extremely disordered with a distribution of energy levels centered on the characteristic, discrete shallow and deep donor energies. This distribution of energy levels then seem to narrow and center on the donor energies at greater passivation times, indicating a more structured, orderly passive oxide film.

2.4. Conclusions

The electronic properties of the passive state of carbon steel rebar were investigated using Mott-Schottky analysis. The steel rebar samples were ground, polished, and then passivated in a saturated calcium hydroxide solution meant to simulate in-service concrete pore solutions. Before determining the electronic properties of passive steel rebar, a systematic methodology for performing M-S analysis was first defined. This process involved determining such M-S runtime parameters as the appropriate potential sweep range, potential sweep rate, and the frequency. It was found that running a potential sweep from -0.5 to 0.5 V at 18 mV/s and using a frequency of 1000 Hz with

a 10 mV AC perturbation produces M-S plots with reliable electronic signatures of the passive film for the steel rebar system. It was additionally found that potentiostatically forming the passive oxide film on steel rebar does not produce a passive film that is equivalent to the passive film formed under open circuit conditions. Therefore, it was determined that all studies attempting to quantify the electronic properties of passive steel rebar should only form the passive film at the open circuit potential of the sample, and not by an externally applied voltage.

Using this systematic methodology, the evolution of the electronic properties of the steel rebar passive film was next defined. This was performed by running M-S tests at five different passivation times on steel rebar samples, beginning with initial sample immersion in the simulated concrete pore solution and ending with full passivation after 10 days. The M-S plots revealed several interesting observations of the electronic properties of passive steel rebar and how those properties evolve with increasing passivation time. The passive film on steel rebar is an n-type semiconductor with two distinct donor species located within the band gap of the passive oxide film. Both the donor ionized at lower potentials (i.e., the shallow donor) and the donor ionized at higher potentials (i.e., the deep donor) have extremely high densities that are on the order of $1x10^{27}$ to $2x10^{27}$ m^{-3}. As the passive film evolves, the donor densities tend to increase slightly, which results in a decrease of the maximum space charge layer thickness to around 0.4 nm at full passivation. The flatband potential remained relatively constant over the course of passivation, hovering around -0.53 V. At a measured voltage of around 0.4 V, the n-type behavior of the passive oxide film suddenly transitions to characteristic p-type behavior as the Fermi level draws closer

to the valence band of the semiconducting oxide, and this behavior was consistent for all passivation times.

2.5. References

[1] M. Yunovich, N.G. Thompson, T. Balvanyon, L. Lave Corrosion costs and preventive strategies in the United States, in, Federal Highway Administration (FHWA), 2001.
[2] P. Ghods, O.B. Isgor, G. McRae, T. Miller, Cement and Concrete Composites, 31 (2009) 2-11.
[3] L. Li, A.A. Sagues, Corrosion, 58 (2002) 305-316.
[4] C.M. Hansson, A. Poursaee, A. Laurent, Cement Concrete Res, 36 (2006) 2098-2102.
[5] U.M. Angst, B. Elsener, C.K. Larsen, O. Vennesland, Corros Sci, 53 (2011) 1451-1464.
[6] P. Ghods, O.B. Isgor, G.A. McRae, G.P. Gu, Corrosion Science, 52 (2010) 1649-1659.
[7] P. Ghods, O.B. Isgor, G.J.C. Carpenter, J. Li, G.A. McRae, G.P. Gu, Cement and Concrete Research, 47 (2013) 55-68.
[8] P. Ghods, O.B. Isgor, G.A. McRae, J. Li, G.P. Gu, Corrosion Science, 53 (2011) 946-954.
[9] H.B. Gunay, B. Isgor, P. Ghods, Corrosion, (2014).
[10] U. Angst, B. Elsener, C.K. Larsen, O. Vennesland, Cement Concrete Res, 39 (2009) 1122-1138.
[11] L.T. Mammoliti, L.C. Brown, C.M. Hansson, B.B. Hope, Cement Concrete Res, 26 (1996) 545-550.
[12] L. Li, A.A. Sagues, Corrosion, 57 (2001) 19-28.
[13] R.G. Pillai, D. Trejo, Aci Mater J, 102 (2005) 103-109.
[14] S. Goni, C. Andrade, Cement Concrete Res, 20 (1990) 525-539.
[15] C. Andrade, C.L. Page, British Corrosion Journal, 21 (1986) 49-53.
[16] S. Joiret, M. Keddam, X. Nóvoa, M. Pérez, C. Rangel, H. Takenouti, Cement and Concrete Composites, 24 (2002) 7-15.
[17] C. Gabrielli, S. Joiret, M. Keddam, H. Perrot, N. Portail, P. Rousseau, V. Vivier, Journal of the Electrochemical Society, 153 (2006) B68-B74.
[18] C. Gabrielli, S. Joiret, M. Keddam, H. Perrot, N. Portail, P. Rousseau, V. Vivier, Electrochimica Acta, 52 (2007) 7706-7714.
[19] P. Ghods, O. Burkan Isgor, F. Bensebaa, D. Kingston, Corrosion Science, 58 (2012) 159-167.
[20] P. Ghods, O.B. Isgor, J.R. Brown, F. Bensebaa, D. Kingston, Applied Surface Science, 257 (2011) 4669-4677.
[21] H.B. Gunay, P. Ghods, O.B. Isgor, G.J.C. Carpenter, X. Wu, Applied Surface Science, 274 (2013) 195-202.
[22] Z. Szklarska-Smialowska, Corrosion Science, 41 (1999) 1743-1767.
[23] Z. Szklarska-Smialowska, Corrosion Science, 44 (2002) 1143-1149.
[24] Y. Liu, G.Z. Meng, Y.F. Cheng, Electrochimica Acta, 54 (2009) 4155-4163.
[25] S. Ningshen, U. Kamachi Mudali, V. Mittal, H. Khatak, Corrosion science, 49 (2007) 481-496.
[26] A. Shahryari, S. Omanovic, Electrochemistry Communications, 9 (2007) 76-82.
[27] P. Schmuki, H. Bohni, Werkstoffe und Korrosion, 42 (1991) 203-207.

[28] P. Schmuki, H. Böhni, Journal of the Electrochemical Society, 139 (1992) 1908-1913.
[29] Y. Cheng, J. Luo, Electrochimica acta, 44 (1999) 2947-2957.
[30] Y. Cheng, J. Luo, Electrochimica Acta, 44 (1999) 4795-4804.
[31] H. Gerischer, Corrosion science, 29 (1989) 257-266.
[32] M. Santamaria, D. Huerta, S. Piazza, C. Sunseri, F. Di Quarto, Journal of The Electrochemical Society, 147 (2000) 1366-1375.
[33] H. Wu, Y. Wang, Q. Zhong, M. Sheng, H. Du, Z. Li, Journal of Electroanalytical Chemistry, 663 (2011) 59-66.
[34] M. Büchler, P. Schmuki, H. Böhni, T. Stenberg, T. Mäntylä, Journal of the Electrochemical Society, 145 (1998) 378-385.
[35] U. Stimming, J. Schultze, Electrochimica Acta, 24 (1979) 859-869.
[36] U. Stimming, J. Schultze, Berichte der Bunsengesellschaft für physikalische Chemie, 80 (1976) 1297-1302.
[37] S.P. Harrington, F. Wang, T.M. Devine, Electrochimica Acta, 55 (2010) 4092-4102.
[38] J. Liu, D.D. Macdonald, Journal of The Electrochemical Society, 148 (2001) B425.
[39] A. Di Paola, F. Di Quarto, C. Sunseri, Corrosion science, 26 (1986) 935-948.
[40] I.-u.-H. Toor, Journal of The Electrochemical Society, 158 (2011) C391.
[41] Y. Xu, M.A. Schoonen, American Mineralogist, 85 (2000) 543-556.
[42] J. Dewald, Bell System Technical Journal, 39 (1960) 615-639.
[43] J. Dewald, Journal of Physics and Chemistry of Solids, 14 (1960) 155-161.
[44] S.R. Morrison, Electrochemistry at semiconductor and oxidized metal electrodes, 1980.
[45] A. Di Paola, Electrochimica Acta, 34 (1989) 203-210.
[46] J. Sikora, E. Sikora, D.D. Macdonald, Electrochimica acta, 45 (2000) 1875-1883.
[47] M. Sánchez, J. Gregori, M.C. Alonso, J.J. García-Jareño, F. Vicente, Electrochimica Acta, 52 (2006) 47-53.
[48] M. Sánchez, J. Gregori, C. Alonso, J.J. García-Jareño, H. Takenouti, F. Vicente, Electrochimica Acta, 52 (2007) 7634-7641.
[49] L. Hamadou, A. Kadri, N. Benbrahim, Applied Surface Science, 252 (2005) 1510-1519.
[50] A. Poursaee, C. Hansson, Cement and Concrete Research, 37 (2007) 1127-1133.
[51] E. Sikora, D.D. Macdonald, Solid State Ionics, 94 (1997) 141-150.
[52] S. Ahn, H. Kwon, Journal of Electroanalytical Chemistry, 579 (2005) 311-319.
[53] Y.-l. Zhang, Q.-l. Li, Journal of Zhejiang University SCIENCE A, 7 (2006) 1447-1452.
[54] J.-B. Lee, S.-W. Kim, Materials Chemistry and Physics, 104 (2007) 98-104.
[55] H. Tsuchiya, S. Fujimoto, T. Shibata, Journal of The Electrochemical Society, 151 (2004) B39.
[56] H. Tsuchiya, S. Fujimoto, Science and Technology of Advanced Materials, 5 (2004) 195-200.
[57] S. Fujimoto, H. Tsuchiya, Corrosion science, 49 (2007) 195-202.
[58] D.G. Li, Y.R. Feng, Z.Q. Bai, J.W. Zhu, M.S. Zheng, Electrochimica Acta, 52 (2007) 7877-7884.

[59] D.A. Jones, Principles and prevention of corrosion, Macmillan, 1992.
[60] A. Simoes, M. Ferreira, B. Rondot, M. da Cunha Belo, Journal of the Electrochemical Society, 137 (1990) 82-87.
[61] N. Hakiki, M.D.C. Belo, A. Simoes, M. Ferreira, Journal of the Electrochemical society, 145 (1998) 3821-3829.
[62] Y. Cheng, C. Yang, J. Luo, Thin Solid Films, 416 (2002) 169-173.
[63] F. La Mantia, H. Habazaki, M. Santamaria, F. Di Quarto, Russian Journal of Electrochemistry, 46 (2010) 1306-1322.
[64] S.P. Harrington, T.M. Devine, Journal of The Electrochemical Society, 155 (2008) C381.
[65] M.H. Dean, U. Stimming, Journal of electroanalytical chemistry and interfacial electrochemistry, 228 (1987) 135-151.
[66] S.J. Ahn, H.S. Kwon, Electrochimica Acta, 49 (2004) 3347-3353.
[67] K. Azumi, T. Ohtsuka, N. Sato, Journal of The Electrochemical Society, 134 (1987) 1352-1357.

THE EFFECT OF CONCRETE PORE SOLUTION COMPOSITION AND CHLORIDES ON THE ELECTRONIC PROPERTIES OF PASSIVE FILMS ON CARBON STEEL REBAR

Jon Williamson, O. Burkan Isgor

To be submitted to: Journal of Corrosion Science (Elsevier)

Department of Materials Science and Metallurgy

University of Cambridge

Cambridge, UK

3. Second Manuscript

The Effect of Concrete Pore Solution Composition and Chlorides on the Electronic Properties of Passive Films on Carbon Steel Rebar

Jon W. Williamson[1], O. Burkan Isgor[2],

[1]Graduate Student at Oregon State University, Department of Materials Science

[2]Associate Professor at Oregon State University, School of Civil and Construction Engineering

Abstract: The effects of concrete pore solution composition, pH, and added chlorides on the electronic properties of the passive oxide films that form on carbon steel rebar were investigated using Mott-Schottky (M-S) analysis. Three electrolytes were investigated: a saturated calcium hydroxide solution (CH; pH 12.5), and two synthetic concrete solutions, one without sulfates (CP-1; pH 13.4) and one with sulfates (CP-2; pH 13.3). Passive films in all three solutions showed n-type semiconductive behavior with two discrete donor species. The density of donors in each solution was in the order of 10^{21} cm^{-3}, and all showed space charge layer thicknesses near 0.4 nm at full passivation. The electronic signatures of films that formed in CP-1 and CP-2 were similar, indicating sulfates have little influence on the electronic properties. Passive films that formed in CH showed a lower flatband potential (-0.59 V) and a lower space charge capacitance, indicating a less dense, less protective passive film structure compared to films in CP-1 or CP-2. The addition of chlorides above the chloride threshold changed the oxide film structure from crystalline to amorphous based on loss of linearity of M-S plots. This loss of linearity effect took much longer and required

higher chloride levels to occur in CP-1, indicating the passive film in CP-1 is much denser and more protective compared to CH.

Keywords: Mott-Schottky analysis, passive film, carbon steel rebar, corrosion, chloride concrete.

3.1. Introduction

The corrosion of steel reinforcement in concrete is a significant problem to civil engineering infrastructure, costing the United States billions of dollars annually in direct engineering expenditures [1]. Corrosion of carbon steel is an electrochemical process involving the breakdown of a thin, protective oxide/oxyhydroxide passive film that forms on steel in highly alkaline (pH >12.5) environments such as those seen in concrete. Numerous studies [2-9] aimed at characterizing the electrochemical processes at work in steel rebar passivation and depassivation have revealed macroscopic information about the steel rebar passive film. More recently, studies have focused on performing nanoscale characterizations of the steel rebar passive film [9-15] for the purpose of gaining a more precise understanding of the passive film structure and properties. The rationale behind these studies is that the issue of corrosion of concrete reinforcement may be mitigated more effectively with a better, more holistic understanding of the passivation and depassivation processes.

Both these macroscopic and nanoscale studies have shown that the pore solution composition, pH, and chloride concentration significantly affect the corrosion behavior of passive steel rebar. For example, Ghods et al. [2] found that the simulated concrete pore solutions with a higher pH tended to produce more protective passive films on steel rebar. They also found that the addition of sulfates to the solution decrease the protective properties of the film. Gunay et al. [15] and Ghods et al. [13, 14] used x-ray photoelectron spectroscopy (XPS) and electron energy loss spectroscopy (EELS) to characterize the influence of concrete pore solution composition on the elemental composition and thickness of the passive film. It was found that the passive film

thickness ranges between 3-15 nm, and it is comprised of a thin, dense Fe^{II}-rich layer near the substrate surface and a thicker, more porous Fe^{III}-rich near the free surface. The thickness of a passive film developed in a saturated calcium hydroxide solution (pH 12.5) was found to be slightly thicker and less protective than that for the passive film formed in a more representative pore solution (pH 13.3). Ghods et al. [7] provided additional support for these observations using transmission electron spectroscopy (TEM). Gunay et al. [9] explored the kinetics of the passive film and also found that the passive film formed in a saturated calcium hydroxide solution was thicker and less dense compared to that formed in a more representative concrete pore solution.

These authors also revealed the profound effect that chlorides have on the passive film, particularly once the chloride concentration exceeds the critical level required for depassivation (i.e., the chloride threshold). These thresholds, however, vary widely [16] and depend on a number of factors, including varying surface conditions [17-19] and pore solution compositions [20, 21]. It was found that the addition of chlorides causes the thickness of the steel rebar passive film to decrease significantly once the chloride threshold is breached, and that chlorides also cause the ratio of Fe^{III}-rich oxides to Fe^{II}-rich oxides within the passive film to increase [7, 15].

As the mechanisms driving steel rebar passivation and depassivation continue to be investigated, one area of research that is not well studied is the electronic properties of the passive film, particularly in environments representative of those in concrete. Past studies have found strong correlation between the electronic properties of a passive film and its macroscopic corrosion behavior. These electronic properties have indicated the general resistance to corrosion of metals such as Cu-Ni alloys [22] and Mo-Ta

alloys [23]. Schmuki and Böhni [24, 25] and Hakiki et al. [26, 27] correlated the electronic properties to the susceptibility of pitting corrosion of stainless steels, as did Szklarska-Smialowska [28, 29] and Liu et al. [30] for the passive films of aluminum. Gerischer [31] showed that a relationship between the onset of transpassive behavior and the electronic properties of the passive film. Although studies of the electronic properties of iron-based passive films are prevalent throughout literature (e.g., for stainless steels [32-34] and pure iron [35-38]), the research on carbon steel in passivating solutions representative of those in concrete are lacking. Cheng and Luo [39, 40], Hamadou [41], and Li [42] all evaluated the electronic properties of carbon steel, but not in environments representative of those in concrete. Sanchez et al. [43, 44] and Williamson and Isgor [45] characterized passive carbon steel, but only evaluated these properties in a single concrete pore solution and without the influence of chlorides. A significant gap in the existing research remains in characterizing the effect of concrete pore solution composition, pH, and chloride concentration on the electronic properties.

The most common method for determining the electronic properties of semiconductive passive films (such as those on iron-based alloys [46, 47]) is called Mott-Schottky (M-S) analysis [48]. This method is implemented by measuring the capacitance of an electrochemical system as a function of applied potential, and is governed by the Mott-Schottky equation [49-51] shown in Equation 3.1 for the case of an n-type semiconductor:

$$\frac{1}{C^2} = \frac{1}{C_H^2} + \frac{2}{\varepsilon\varepsilon_0 e N_D}\left(V - V_{fb} - \frac{kT}{e}\right) \tag{3.1}$$

where C (F m^{-2}) is the apparent capacitance, C_H (F m^{-2}) is the Helmholtz capacitance, ε_0 is the permittivity of free space ($8.854*10^{-12}$ F m^{-1}), and ε (no units) is the dielectric constant (12 for iron-based alloys [41, 44, 52]), V (V vs. SCE) is the applied potential, k is Boltzmann's constant ($1.381*10^{-23}$ J K^{-1}), T (K) is the temperature, and e ($1.602*10^{-19}$ C) is the electronic charge. An M-S plot involves plotting C^{-2} vs. V. In Equation 3.1, the slopes of the linear regions of this plot are inversely proportional to the donor density N_D or acceptor density N_A, and the location where these linear regions cross the x-axis can be used to derive the flatband potential of the semiconductor, V_{fb}; N_D, N_A, and V_{fb} are all electronic properties of semiconductive passive films. Assumptions that go into the use of Equation 3.1 include 1) the passive film is not frequency dependent [53], 2) the dopant density does not change as a function of applied potential [54], and 3) no dopant states lie deep within the semiconductor band gap [51]. Each of these issues, as well as others, have been addressed in an earlier study for the passive steel rebar system [45].

Although electrochemical, microscopic, and kinetic techniques have all been used to study the effect of concrete pore solution composition, pH, and chloride concentration on the protective nature of the steel rebar passive film, these studies do not reveal the electronic properties of that film. Past studies have found significant correlation between the electronic properties of semiconductive passive films and the protective nature of those films; therefore, Mott-Schottky analysis, electrochemical impedance spectroscopy (EIS), and other electrochemical techniques will be employed to define these electronic properties and how they change with varying solution composition, pH, and chloride concentration. With this information, a more comprehensive

understanding of the underlying processes governing mechanistic models of steel rebar passivation and depassivation will be gained. This will potentially lead to the development of new corrosion inhibitors, corrosion-resistant reinforcements, or other corrosion mitigation techniques.

3.2. Materials and Methods

3.2.1. Specimen Preparation

As-received deformed cylindrical rebar samples were obtained and cut to 2 mm thick and 15.5 mm (5/8”) diameter. Table 3.1 shows the elemental composition of the steel rebar from spectrographic results. After cutting to size, the samples were cleaned with acetone to remove machining greases and oils and rinsed with deionized water. The samples were then immersed in an ultrasonic bath of 5% acetic acid solution to remove any air-formed oxide from the surface, followed by a second rinsing with deionized water. Next, the samples were ground with progressively increasing grit sizes, followed by a polish to 0.05 microns using silica polish. This gave the samples a “mirror” finish with no noticeable scratches or blemishes. The samples were then rinsed with distilled water, dried with a delicate task wipe, and then immediately placed into a dessicator with silica dessicant gels until use.

Table 3.1: Composition of tested steel specimens (average of three spectrographic results).

Element	Weight (%)
C	0.26
Si	0.27
Mn	1.10
Cr	0.05
Ni	0.07
Mo	<0.01
Cu	0.21
Al	<0.005
Nb	<0.01
V	<0.005
Ti	<0.005
B	<0.0005
P	0.01
Si	0.03
W	<0.01
Sn	0.021
Co	0.01
Zr	<0.01
Fe	Balance

Each sample was loaded into the Princeton Applied Research K0105 sample holder, which is specially designed for performing repeatable, reliable corrosion measurements on multiple samples. These sample holders have the added benefit of helping to prevent crevice corrosion by using hydrophobic Teflon washers that are in direct contact with the sample and seal it. No crevice corrosion was apparent on any of the samples tested. The total resistance of the sample holder assembly compiled to less than 1 Ω, creating minimal resistance in the electrochemical circuit assembly. The exposed sample area of the sample loaded into the holder was 1.15 cm^2.

3.2.2. Experimental Setup

Two identical three-probe electrochemical cells were used for testing. A Gamry Reference 3000 potentiostat and a Gamry Multiplexor were used for taking all electrochemical measurements. Gamry Echem software was used for analyzing impedance data. A graphite counter electrode with a high surface area and an Accumet standard calomel reference electrode (SCE) were used in all electrochemical measurements. The tip of the reference electrode was placed approximately 5 mm from the surface of the sample. All potentials reported in this study are shown versus SCE.

Three electrolytes were used for comparison in this study. The first is a saturated $Ca(OH)_2$ solution (pH 12.5), the second was a more representative concrete pore solution with Ca^+, K^+, and Na^+ ion additions (pH 13.4), and the final solution was identical to the second, except with the addition of $CaSO_4$ (pH 13.3) to observe the effect of sulfates on the electronic properties of the passive film. In this study, to add clarity, these solutions are referred to as CH, CP-1, and CP-2, respectively. Each solution was prepared by adding analytical grade $Ca(OH)_2$, KOH, NaOH, and/or $CaSO_4 \cdot 2H_2O$ to deionized water. The amounts of each of these constituents in all three solutions are provided in Table 3.2. Each solution, after adding the dry components to the deionized water, was stirred at 800 rpm using a magnetic stirrer for a minimum of 12 h, ensuring the solution had come to full saturation. During solution preparation and stirring, the solution containers were sealed using parafilm to prevent carbonation (which lowers solution pH) and water evaporation. pH measurements were performed before and after all testing to verify that the solution remained chemically consistent during the course of testing.

Table 3.2: Concentrations of the species in CH, CP-1, and CP-2 passivating solutions.

Solution	Added compounds (M)				pH
	$Ca(OH)_2$	Na(OH)	K(OH)	$Ca(SO)_4 + 2H_2O$	
CH	0.1	0.0	0.0	0.0	12.5
CP-1	0.1	0.1	0.2	0.0	13.4
CP-2	0.1	0.1	0.2	0.003	13.3

Chlorides were then added to CH and CP-1 solutions in incremental amounts, until the chloride threshold is breached. The total amount of chlorides in each cell after each addition to each solution are listed in Table 3.3. The chloride was added by creating a 5 M NaCl solution and then adding a small amount of saturated $Ca(OH)_2$ solution to raise the pH to 11. This new solution was then slowly added to the electrochemical cells until the total chloride amount in the cell reflected the values listed in Table 3.3. This method is consistent with that used by Gunay et al. [9]. The time between each chloride addition was approximately 24 hours.

Table 3.3: Concentration of total chloride in the electrochemical cells after 24-hour intervals for CH and CP-1 passivating solutions.

Solution	Chloride addition increments (M)						
	Start	1st	2nd	3rd	4th	5th	6th
CH	0	0.1	0.3	0.5	–	–	–
CP-1	0	0.5	0.8	1.1	1.5	2.2	2.6

Passivation of the samples occurred entirely in the two three-probe electrochemical cells for determining the difference in the electronic properties between the CH, CP-1, and CP-2 solutions. However, when determining the effect of chlorides on the passive films formed in CH and CP-1 solutions, the samples were passivated in a staging beaker

and then quickly transferred to the electrochemical cells for testing. The reason for passivating these samples in staging beakers is to enable a larger number of samples to be tested at full passivation, which takes a minimum of ten days to complete [2, 6]. The transfer process from the staging beaker to the sample holder assembly, and then finally to the electrochemical cell took approximately 60 seconds to perform. During this transfer process, the sample surface remained covered with solution and was not artificially touched or altered, in order to minimize perturbation to the passive film. After transfer to the electrochemical cell, the samples were then left for four days in the electrochemical cell so that the passive film could re-equilibrate to the passivating solution. To validate that this sample transfer process does not affect the passivity of the samples, an EIS plot of the transferred sample was compared to typical EIS plots for a sample fully passivated in the cell, and a sample passivated for one day in the cell. The purpose of comparison to a sample that has passivated for only one day is to contrast a *mostly* passivated film to a *fully* passivated film, and to ensure the sample passivated in the staging beaker does not exhibit *mostly* passivated behavior. Figure 3.1 contrasts these three methods of passivation.

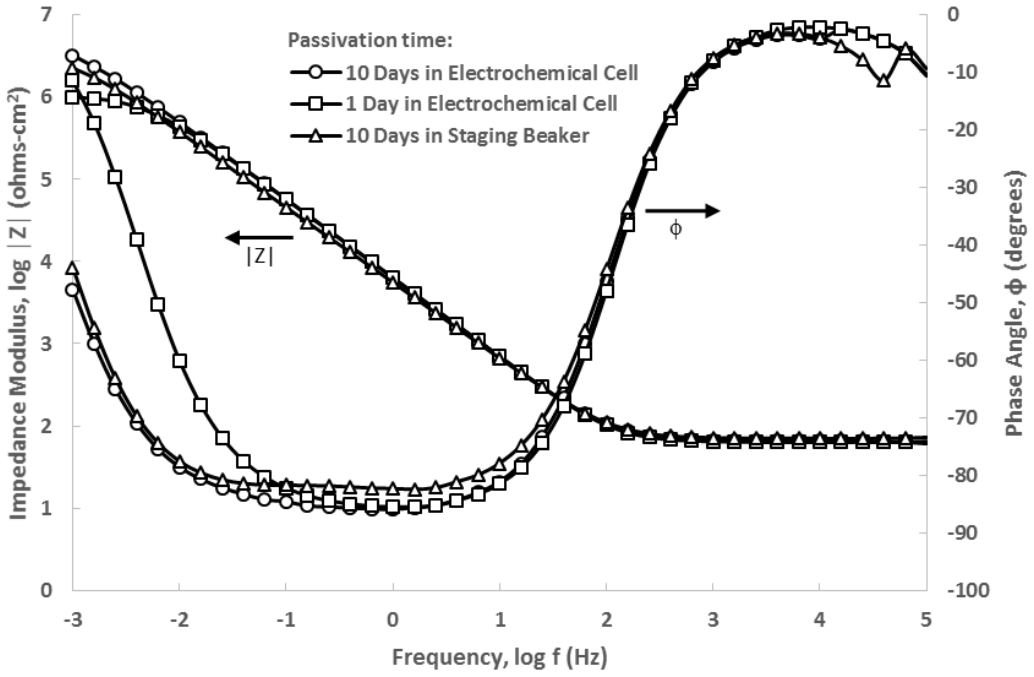

Figure 3.1: EIS (Bode) plot contrasting the impedance behavior of samples passivated solely in the electrochemical cell versus those passivated in a staging beaker before transfer to the electrochemical cell for measurement. The impedance behavior shows that samples passivated in a staging beaker and then transferred to the cell exhibit *fully* passivated behavior; this is in contrast to the *mostly* passivated behavior of the samples passivated in the cell for 1 day.

Figure 3.1 shows that the passive film formed in a staging beaker and then transferred to the electrochemical cell for measurements exhibits *fully* passivated behavior. This can be seen in the plot by visual inspection and comparison to the *mostly* passivated sample that was immersed for one day in the solution. The average impedance modulus and phase angle for the transferred samples was around $2x10^6$ Ω and -83º, respectively. Both values are at levels seen for passive film [2, 6] and are even higher than those seen in other electrochemical studies performed on carbon steel in highly alkaline solutions [41, 42, 44]. It can, therefore, be concluded that the transfer process does not

significantly affect the integrity of the passive film, so long as the film is able to re-equilibrate in the electrochemical cell.

It should additionally be noted that although this transfer process does add an additional level of uncertainty to the testing and is not ideal, it is adequate when studying the effects of chlorides and having a working knowledge of how the EIS plots should look for samples passivated solely in an electrochemical cell. This is because chlorides have such a dramatic effect on the integrity of the passive film that they tend to override any smaller inconsistency caused by the passivation process. The detrimental effects of chlorides on the passive film on steel is well known and documented [6-9, 13, 14, 42, 55]. Any inconsistencies in data as a result of the sample transfer process are far outweighed by the effect of chlorides on the film.

3.2.3. Experimental Methods

The main objective of this investigation is to study the effect of concrete pore solution composition, pH, and chloride concentration on the electronic properties of the steel rebar passive film. For this purpose, M-S analysis was used to study carbon steel samples at different passivation times and in varying passivating environments.

Open circuit potential (OCP) monitoring and electrochemical impedance spectroscopy (EIS) were used to define the passive state of the samples. Both OCP and EIS are non-destructive tests. OCP and EIS tests were run both before and after any M-S analyses were performed to characterize the effect of the M-S potential sweep on the passive state. Cathodic potentials were seen for samples immediately after immersion in the passivating solution. As the passive film developed under open circuit conditions (i.e.,

without the application of an anodic current to form the passive film), the OCP increased until a steady-state potential was reached. At this potential, the sample is considered to be in a fully passive state. Ghods et. al. [2, 6] showed that a fully passivated state is typically not reached until 10-14 days of passivation time in solution. A typical OCP profile for steel rebar samples in CH, CP-1, and CP-2 solutions can be seen in Figure 3.2.

EIS tests were performed using an applied AC signal amplitude of 10 mV RMS which showed no signs of non-linearity based on Lissajous curves; these curves show whether the real and imaginary spectral data compiled in EIS complies with Kramers-Kronig (K-K) relations for data quality. For EIS tests run after a few hours passivation, the frequency was swept from 10^{5} to 10^{-3} Hz at 5 data points per decade of frequency. However, for EIS tests run at the earliest passivation times, the frequency was only swept to 10^{-2} Hz because during the first few hours of passivation the oxide film formation is rapid and transient, which creates "sample drift" in the impedance data and makes measuring the impedance at the smallest frequencies difficult. Using the shorter frequency range at the early passivation times also allowed for a greater number of EIS scans to be performed during this critical period when the passive film is forming rapidly. EIS plots reveal impedance and phase angle data for the passive film. For a fully passivated film, the phase angle should be between -80° and -90° at low and mid-range frequencies, and the peak in the phase angle should encompass a wider frequency range over the course of passivation [6, 43]. The impedance modulus should steadily increase until full passivation is reached, at which point values greater than $1x10^{6}$ ohms-cm^{2} are typically seen [6, 43]. The impedance modulus is indicative of the charge

transfer resistance in the oxide film at low frequencies and the solutions resistance at high frequencies [56]. The solution resistance should remain constant over the course of testing, which helps to indicate the pH and composition of the solution are not changing with time. Only one time constant should be present in the Bode plot during the course of passivation. If more than one time constant is present, then a second oxide film exists that was likely formed before the sample was immersed in the electrolyte [56]. This secondary oxide will complicate M-S data, since the passive film formed in highly alkaline solutions on steel is only between 3-15 nanometers thick [13, 15]. Finally, the Nyquist plots should exhibit little to no Warburg behavior which would indicate mass transfer issues occurring at the surface and would further complicate capacitance results. A typical EIS scan (Bode plot) of fully passivated steel rebar samples in CH, CP-1, and CP-2 solutions is shown in Figure 3.3.

In implementing M-S analysis to determine the electronic properties, the parameters used in this study closely followed those recommended by Williamson and Isgor [45]. A 10 mV AC amplitude was used which showed Lissajous curves that complied with K-K relations for data quality. The dielectric constant used is subject to some debate, due to its rather different values for Fe_3O_4 and γ-Fe_2O_3 oxides which have been proposed [15] to be two of the main oxides that form in iron-based passive films. But previous studies [41, 44, 52] have shown a value of 12 to be a good estimate for carbon steel rebar and will be used in this study. A Helmholtz capacitance, C_H, of 22 μF cm^2 was used, which was previously shown to be a good estimate for simulated concrete pore solutions [45]. This C_H value was found by measuring the capacitance at -700 mV, where Harrington et. al. [36] determined by surface enhanced Raman spectroscopy

(SERS) that only a small amount of passive film would be present on the surface of iron and the space charge capacitance would be nearly non-existent. At this point, nearly all the capacitance would be due to the Helmholtz layer. A frequency of 1 kHz was used in all M-S analysis, which was shown to be the largest frequency that minimized the effect of a changing frequency on the capacitance [45]. The potential was swept in the anodic direction at a rate of 18mV/s, from -0.5 V to 0.5 V vs. SCE. This potential sweep rate and range was found to be fast enough and short enough to negate any significant non-linearity in the M-S plots caused by a changing donor density during the course of the potential sweep [45].

Previous studies [41, 43-45, 57] on carbon steel rebar in alkaline solutions have shown that the passive film exhibits n-type semiconductive behavior through the entire passive region, which is consistent to what is seen with pure Fe [52] and stainless steel [58] (although stainless steel exhibits p-type behavior at extremely cathodic potentials [34]). Consequently, the M-S equation for an n-type semiconductor shown in Equation 3.1 was implemented.

3.3. Results and Discussion

3.3.1. Effect of Concrete Pore Solution Composition

The open circuit potential (OCP) was monitored for samples in CH, CP-1, and CP-2 passivating solutions until a fully passivated state was reached (i.e., after 10 days [2, 6]). Significant variation was not seen between the OCP profiles of samples passivated in each solution (see Figure 3.2). Values typically seen were between -0.425 V and -0.450 V for the initial OCP, and between -0.175 V and -0.225 V for the OCP at full

passivation. These values are consistent with other works done on carbon steel rebar in simulated concrete pore solutions [2, 6]. In Figure 3.2, the OCP increases dramatically during the first couple hours of passivation. This increase in OCP then slows and tends to steadily increase during the remainder of the passivation process. This change in OCP with time points to the intrinsic structure of the passive oxide film. According to Gunay et al. [9, 15], during the first couple hours of passivation, a thin, dense, coherent film comprised primarily of Fe^{II} oxides forms which provides the majority of protection for the underlying rebar. The rapid increase in the OCP then indicates the formation of this thin, dense film. After this initial passivation time, a more porous, incoherent Fe^{III}-rich oxide builds on top of this, and this corresponds to the region where the OCP increases at a slower rate.

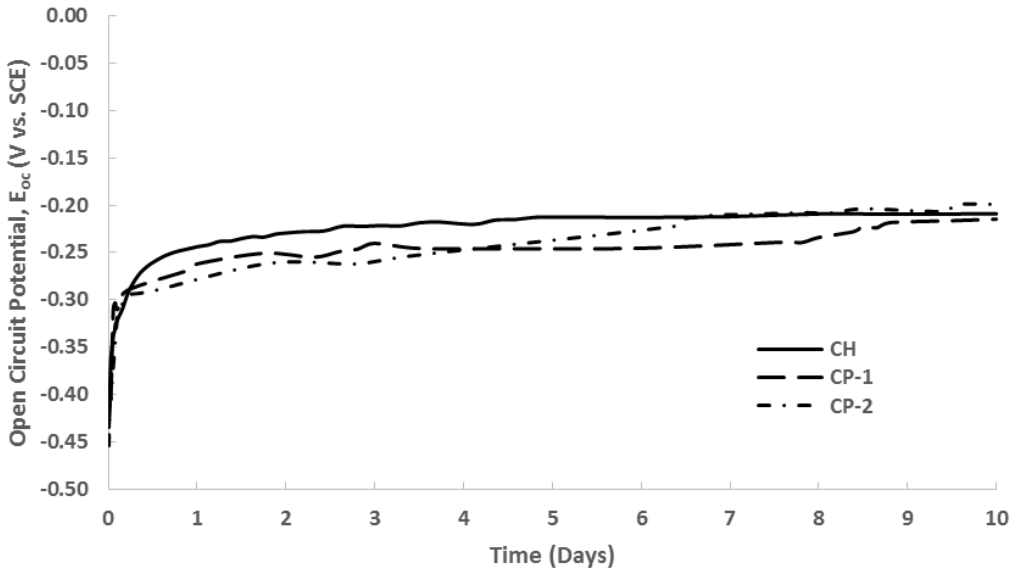

Figure 3.2: Typical OCP plot illustrating how the passive film on carbon steel rebar in CH, CP-1, and CP-2 solutions evolve with time, beginning with initial passivation and ending with a fully passivated state. These plots are repeatable with a relatively small variability; therefore, for clarity, error bars are not used.

Figure 3.3 shows the impedance data from fully passivated rebar samples in CH, CP-1, and CP-2 solutions using electrochemical impedance spectroscopy (EIS). Looking at the impedance modulus and phase angle data from these figures, it is immediately clear that the passive films formed in CP-1 and CP-2 are similar. The passive film formed in CH is likewise similar to the CP-1 and CP-2 curves at lower frequencies, but it has markedly different behavior at higher frequencies. For example, at high frequencies, the impedance modulus for CP-1 and CP-2 is about 9 Ω, whereas the impedance modulus for CH is about 61 Ω. This is indicative of the difference in solution resistances between CH, CP-1, and CP-2 [56]. Solutions with a higher ionic concentration such as in CP-1 and CP-2 (where Na^+ and K^+ ions are present) will have a much higher ionic conductivity. Solutions with lower ionic conductivity such as CH will naturally have a higher solution resistance. Comparing the phase angles reveals that the oxide films formed in CP-1 and CP-2 are more passive, as evidenced by the larger phase angles in a wider frequency range. This is consistent with previous studies performed on steel rebar in these two solutions, and it is caused by the higher pH level (13.3 to 13.4) and ionic constituents which form a more robust, protective oxide film [2, 7].

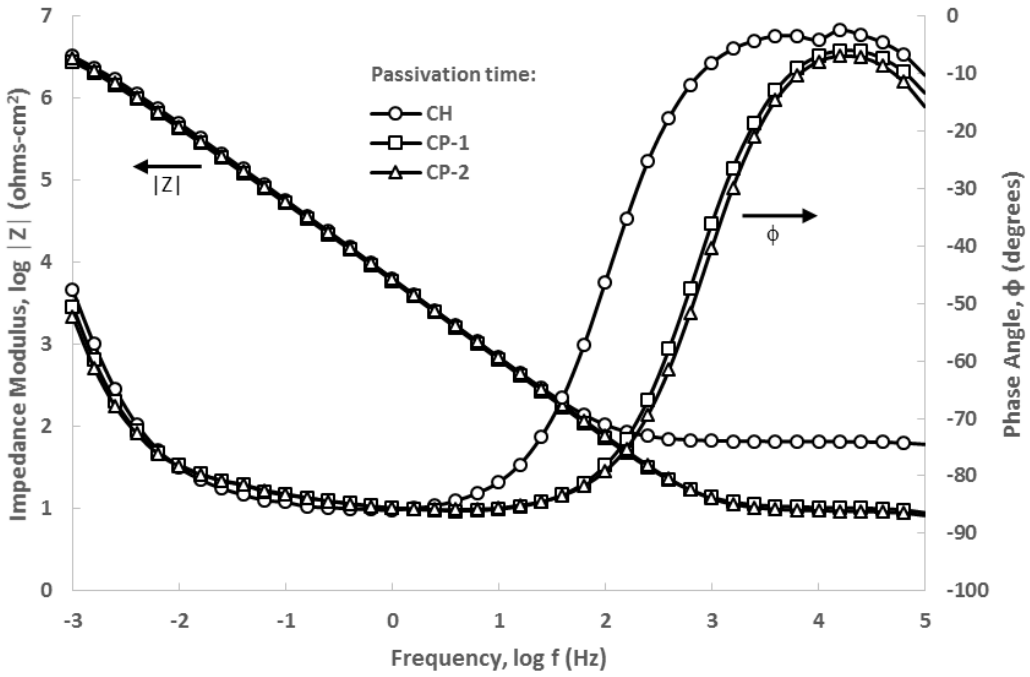

Figure 3.3: EIS (Bode) plot showing the impedance data for fully passivated steel rebar samples in CH, CP-1, and CP-2 passivating solutions.

Having quantified the passive state for each oxide film formed in CH, CP-1, and CP-2, the electronic properties of each of these films was determined and related to their known passivities using Mott-Schottky (M-S) analysis. M-S analysis was performed in all three solutions at five different passivation times (i.e., at 0.5 hours, 1 hour, 2 hours, 1 day, and 10 days) to adequately characterize the passive film evolution from initial sample immersion to a fully passive state. The evolution of the electronic properties of the passive films was then analyzed and compared between all three solutions.

Ideally when performing M-S analysis, only one potential sweep should be performed per sample. The reason for this is that any potential sweep on the passive film changes the film and its properties to varying degrees, depending on the potential sweep range and rate [54, 59]. However, despite consistent sample preparation, each sample can be

considerably different. This proposition is plausible when taking into account the disordered and inconsistent nature of the mild steel alloy used to make steel rebar, which is almost entirely formed from recycled steel scrap metal. Because the passive film is only a few nanometers in thickness [7], these microstructural defects present in steel rebar will naturally produce some inconsistency in the M-S analysis when comparing multiple samples. The capacitance readings taken during M-S analysis likewise come from measuring currents on the nano-amperage scale, according to the Lissajous curves produced during impedance measurements. Therefore, it could be difficult to find consistent trends when attempting to quantify the evolution of the passive film using M-S analysis on a different sample for each passivation time.

To address this issue, Williamson and Isgor [45] found that the evolution of the electronic properties of the passive film can actually be best characterized by using both a *single* sample and *multiple* samples. The single sample has all five M-S tests performed on it, one for each passivation time, whereas using multiple samples involves having only one M-S test per sample. Using this method, the two-fold risks of 1) excessive sample-to-sample variation from using multiple samples, and 2) several M-S potential sweeps effecting the passive film on a single sample, are addressed. Therefore, the same approach was taken in this study, and a more comprehensive picture of the evolution of the electronic properties was achieved.

Beginning with the results for running all five M-S tests on a single sample, Figure 3.4 shows how the capacitance changed as a function of voltage and passivation time for CH, CP-1, and CP-2. Table 3.4 then extracts the electronic properties from these M-S plots for quantitative comparison.

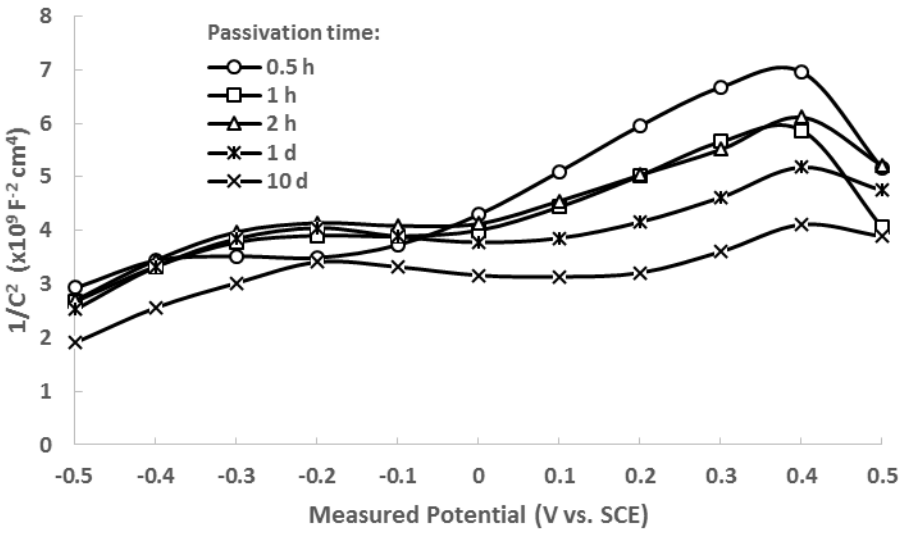

(a)

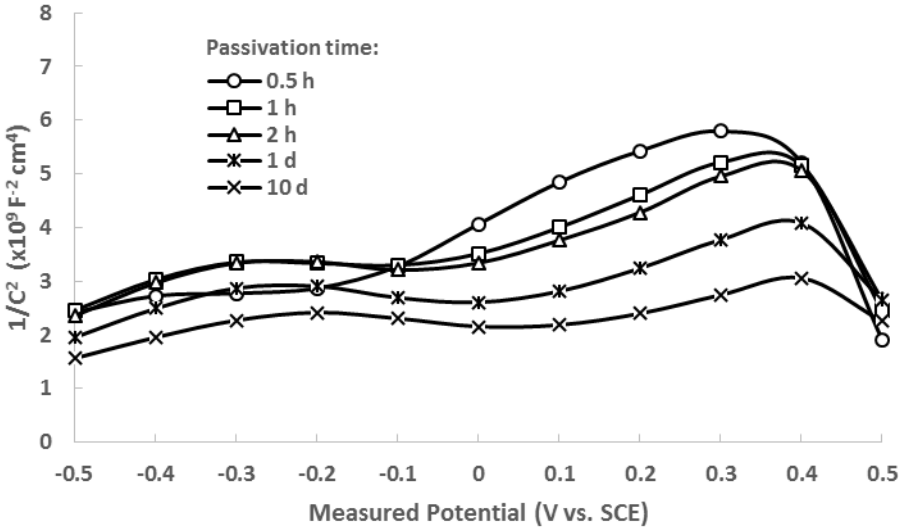

(b)

Figure 3.4: Mott-Schottky plots showing the evolution of the electronic properties of the passive film for steel rebar samples in (a) CH and (b) CP-1 solutions.

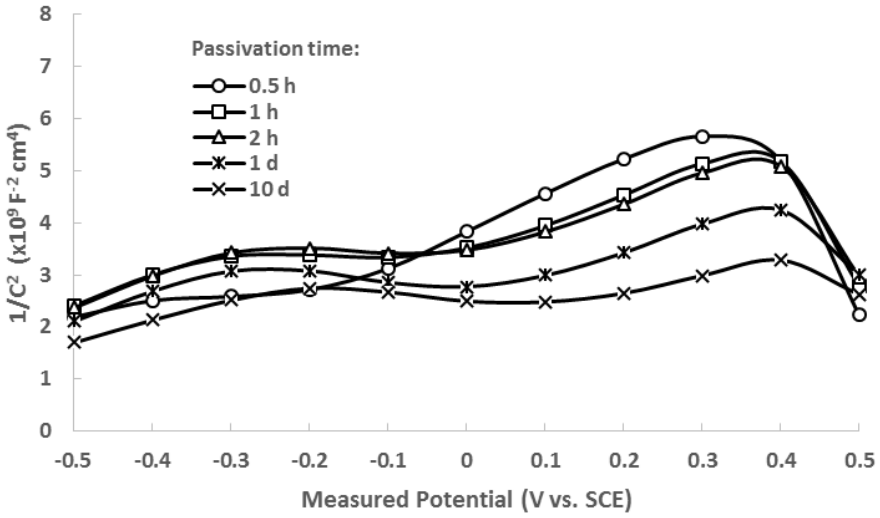

(c)

Figure 3.4 (Continued): Mott-Schottky plots showing the evolution of the electronic properties of the passive film for steel rebar samples in (c) CP-2 solutions.

Table 3.4: Electronic properties extracted from the Mott-Schottky plots in Figure 3.4 for steel rebar samples in CH, CP-1, and CP-2 solutions. The passivation times listed range from initial immersion of the steel rebar sample in the passivating solution (0.5 h) to full passivation (10 d).

Solution	Passivation Time	N_{D1} [cm^-3]	N_{D2} [cm^-3]	V_{fb} [V]	d_{max} [nm]	d_{trans} [nm]
CH	0.5 h	$1.52*10^{21}$	$3.48*10^{19}$	-0.67	0.54	0.32
	1 h	$1.09*10^{21}$	$5.23*10^{20}$	-0.62	0.51	0.29
	2 h	$1.09*10^{21}$	$6.49*10^{20}$	-0.61	0.47	0.27
	1 d	$1.04*10^{21}$	$7.40*10^{20}$	-0.57	0.45	0.25
	10 d	$1.18*10^{21}$	$6.02*10^{20}$	-0.50	0.43	0.21
CP-1	0.5 h	$1.63*10^{21}$	$2.73*10^{19}$	-0.59	0.48	0.27
	1 h	$1.41*10^{21}$	$2.61*10^{20}$	-0.59	0.48	0.27
	2 h	$1.37*10^{21}$	$2.87*10^{20}$	-0.57	0.47	0.26
	1 d	$1.42*10^{21}$	$3.31*10^{20}$	-0.50	0.43	0.22
	10 d	$1.58*10^{21}$	$3.31*10^{20}$	-0.44	0.38	0.17
CP-2	0.5 h	$1.60*10^{21}$	$1.74*10^{19}$	-0.54	0.48	0.25
	1 h	$1.37*10^{21}$	$2.61*10^{20}$	-0.58	0.49	0.27
	2 h	$1.37*10^{21}$	$2.76*10^{20}$	-0.58	0.48	0.26
	1 d	$1.45*10^{21}$	$2.13*10^{20}$	-0.53	0.46	0.24
	10 d	$1.56*10^{21}$	$3.25*10^{20}$	-0.46	0.39	0.18

These results show some general trends which are consistent for all three passivating solutions. The first is that the passive oxide film on steel rebar exhibits n-type semiconductive behavior. This is evidenced by the generally positive slope seen for the swept potential range, which according to the M-S equation (see Equation 3.1), indicates that the majority charge carrier in the space charge layer is an electron and the impurity states present in the film are donor states. After excitation of the free majority charge carriers, the newly formed depletion layer exhibits a strongly positive charge from the oxidized donor states. The n-type behavior of the steel rebar passive film is consistent with the other semiconductive oxide films seen on carbon steel rebar in alkaline solutions [39, 41-44, 57].

The second trend evident in all three solutions is the presence of two separate regions of positive linear slope. For purely n-type behavior with a single donor state, the M-S plot should show only a single positive linear slope [60], hence the presence of non-linearity requires further investigation. This non-linear behavior was previously attributed to a second donor state located deep in the band gap of the steel rebar oxide film [45]. This is in addition to the characteristic *shallow* donor state for n-type semiconductors that is completely ionized at room temperature. Other commonly cited causes of nonlinearity in M-S plots (e.g. frequency-dependent capacitance and a changing donor density during the course of passivation [53]) were shown to be mitigated according to the M-S running parameters chosen and outlined previously. The attribution of nonlinear M-S plots to the presence of a *deep* donor state is common in literature [49, 60, 61] and is consistent with the M-S plots shown in Figure 3.4. The shallow and deep donor states have been ascribed to, in the case of an iron-based alloy,

Fe^{II} donors being oxidized from tetrahedral and octahedral sites in the oxide crystal lattice, respectively [39, 41, 58]. Ionization from tetrahedral sites occurs more readily and at lower applied potentials because of the lower bonding energy in comparison to octahedral sites.

Another observation from Figure 3.4 is that with increasing passivation time, the M-S plots seem to show the appearance of a "hump", or an abrupt increase and decrease in the M-S plot in the potential range between -0.2 V and 0 V. At the earliest passivation times, this features is less distinct. It is possible that this "hump" is indicative of the level of passivity of the film, and its effect can be seen more clearly when analyzing the effect of chlorides in Section 3.3.2. Lastly, the M-S curves seem to broaden and flatten slightly with increasing passivation time. The space charge capacitance also seems to increase with increasing passivation time. It is theorized that the broadening of the M-S curve and increase in the space charge capacitance are related, and an explanation of this theory is provided in Section 3.3.3.

The evolution of these passive films is also consistent and reinforces the existing model for the structure of the passive film proposed by Gunay et al. [9, 15]. This model proposes that an initial thin (~2 nm) oxide layer made primarily of Fe^{II} oxides forms rapidly during the initial stages of passivation. It is an inherently dense and coherent structure and provides the majority of passivation of the underlying steel. After this initial layer has formed, a more porous, predominantly Fe^{III} layer forms on top that contributes less to the overall passivity. In Figure 3.4, the M-S plot at 0.5 hours passivation has a significantly different shape when compared to the later passivation times. This seems to indicate that the electronic signature, and hence the oxide structure

of the film is inherently different during the earliest passivation times. It is likely that this initial M-S curve shows the electronic properties of only the inner Fe^{II}-rich layer. The M-S curve at the four later passivation times is likely the electronic signature of the bilayer structure consisting of both the thin, inner Fe^{II}-rich layer and the more porous Fe^{III}-rich outer layer. The fact that the shape of the M-S curves for these four later passivation times all remain generally the same seems to point towards the general structure of the oxide film not significantly changing, which is in contrast to the initial M-S curve at 0.5 hours passivation. Figure 3.4 makes additional sense in that the curves tend to shift downward with increasing passivation time. This means that an increase in the space charge capacitance corresponds to an increase in the passivation of the film, which is consistent with the EIS plot in Figure 3.3 that shows the imaginary impedance continuing to increase until full passivation is reached.

Table 3.5 shows the evolution of the passive film by running only one M-S test per sample, and is used for validation of the results in Table 3.4. Both CP-1 and CP-2 data sets were included due to the lack of any appreciable difference between passive film formed with or without sulfates in the EIS plot in Figures 3.3 and the M-S plots in Figure 3.4. In general, good consistency is found when comparing the values in Tables 3.4 and 3.5, indicating that the electronic properties found from running all five M-S tests during the course of passivation on a single sample provides reliable data. This is consistent with the results found in a previous study on carbon steel rebar [45]. One small difference though between Tables 3.4 and 3.5 that should be noted is that the large increase in N_{D2} that occurs after 0.5 hours passivation time in Table 3.4 does not occur until after the 2 hours passivation time in Table 3.5. This may show a small effect

from running multiple M-S plots on the same sample. The initial potential sweep may actually help to accelerate the formation of the inner Fe^{II}-rich layer due to the anodic potentials applied during the potential sweep. This would explain why the dramatic increase in N_{D2}, which is indicative of the Fe^{III}-rich outer layer beginning to form, occurs so quickly in Table 3.4 but does not occur until after 2 hours passivation in Table 3.5.

Table 3.5: Electronic properties of the evolving passive film on steel rebar samples in CP-1 and CP-2 passivating solutions. In contrast to Table 3.4, only one Mott-Schottky test was run per sample. Good agreement is found with electronic properties in Table 3.4.

Passivation Time	**N_{D1} [cm^-3]**	**N_{D2} [cm^-3]**	**V_{fb} [V]**	**d_{max} [nm]**	**d_{trans} [nm]**
0.5 h	$1.58*10^{21}$	$1.70*10^{19}$	-0.60	0.50	0.28
1 h	$1.49*10^{21}$	$3.32*10^{19}$	-0.65	0.54	0.32
2 h	$1.45*10^{21}$	$8.84*10^{19}$	-0.62	0.52	0.30
1 d	$1.46*10^{21}$	$1.84*10^{20}$	-0.52	0.46	0.23

Other observations can be more readily displayed by the electronic properties shown in Table 3.4. The shallow donor density, N_{D1}, and deep donor density, N_{D2}, were calculated from Equation 3.2 where S_1 is the slope of the M-S plot in the shallow donor region (about -0.5 to -0.3 V), and S_2 is the slope in the deep donor region (about 0.1 to 0.4 V):

$$N_{D1} = \frac{2}{\varepsilon\varepsilon_0 q S_1} \tag{3.2a}$$

$$N_{D2} = \frac{2}{\varepsilon\varepsilon_0 q S_2} - N_{D1} \tag{3.2b}$$

Equation 3.2 can be derived directly from Equation 3.1 for the case of multiple n-type donor species within the passive film [39, 58]. In calculating N_{D1}, only the slope of the

shallow donor region is needed. However, calculating N_{D2} requires both a knowledge of S_2 and N_{D1}. This is due to S_2 being a function of *all* the ionized donors at the higher potentials as shallow donors continue to be ionized at these higher potentials from ever increasing depths within the semiconductor. N_{D1} stays relatively constant during the course of passivation for all three solutions. It is slightly lower for CH solution compared to CP-1 or CP-2, but remains on the order of 10^{21} cm^{-3}. N_{D2}, is more interesting, and actually points again to the present theory of the structure of the passive film [9, 15]. N_{D2} increases dramatically after the first passivation time (0.5 hours) by around an order of magnitude. After this abrupt increase, the increase in N_{D2} occurs much more gradually for the remaining passivation times. This early, abrupt increase in N_{D2} likely corresponds to addition of the Fe^{III}-rich oxide layer on top of the inner Fe^{II}-rich layer. Because the inner layer is a much more dense and coherent structure, the donor density would be expected to be lower, and it can be presumed then that N_{D2} taken at 0.5 hours passivation corresponds to the deep donor density for only this inner layer. But as the more porous and non-stoichiometric outer layer is added, the number of Fe^{II} impurities occupying octahedral sites increases substantially for the passive film as a whole. The slow, gradual increase in N_{D2} during later passivation times corresponds well to the slow, gradual buildup of this porous, outer Fe^{III} layer seen in previous studies on the structure of the oxide film [9, 15]. Both donor densities for the passive film seen are extremely high and are indicative of a highly disordered passive film structure, which is consistent with most other studies performed on iron-based alloys [53, 62]. Previous studies have actually found that the donor densities and space charge capacitance *decrease* with increasing passivation time, which is opposite the

results found in Table 3.4. These studies typically attribute this to the progressive exhaustion of charge carriers as the oxide film reaches full passivation [41, 52]. The results from Azumi et al. [35], however, were consistent with the present work. They found that the donor density increased in a borate solution of pH 6.5 but decreased in a phosphate solution of the same pH with increasing passivation time. In either case, what is clear from the results in Table 3.4 is that the passive film is an extremely disordered polycrystalline structure, and remains so throughout the course of passivation.

Unlike previous results on passive steel rebar [45], the flatband potential, V_{fb}, decreased slightly during the course of passivation for all three solutions. However, it remained in the range between -0.45 and -0.65 V, which is consistent with the constant flatband potential of -0.53 V found for passive steel rebar in past literature [45]. The flatband potential is the one empirical value that is indicative of both the state of the electrode and the electrolyte, and since the electrode and electrolyte are consistent for all tests, the flatband potential should have likewise remained constant. It is at present unknown why the flatband potential changed slightly, when in a previous study [45] it held relatively constant. An additional observation from Table 3.4 is that the flatband potential for the passive film in CH is approximately 0.06 V lower than that for CP-1 or CP-2. It is likely that the increase in the flatband potential can be attributed to an increase in the solution pH, and this is explained in greater detail in Section 3.3.3. To determine the flatband potential, Equation 3.3 was used [36]. This takes into account the Helmholtz capacitance, C_H, which has a significant effect on the value of V_{fb} when dealing with the extremely high donor densities and consequently thin passive films.

Altering C_H by only 5 μF/cm^2 can change V_{fb} by up to 0.25 V. By ignoring C_H altogether, the V_{fb} is altered by about 0.4 V.

$$V_{fb} = V_0 + \frac{\varepsilon\varepsilon_0 q N_D}{2C_H^2} - \frac{kT}{q} \tag{3.3}$$

Finally, the thickness of the space charge layer was reported with two values in Table 3.4. The first is d_{trans}, which was estimated at the potential where purely shallow donor ionization transitions to both shallow and deep donor ionization, or at about -0.1 V. This value decreased steadily during the course of passivation for all three solutions to around 0.2 nm at full passivation. The second thickness, d_{max}, was measured at the peak of the M-S plot (about 0.4 V), where the space charge layer thickness was at a maximum and participation of the valence band began to occur. This value averaged around 0.4 nm at full passivation for all three solutions. This a reasonable value, because it is within the thickness range of the protective Fe^{II} layer thickness of a few nanometers [7], and it is consistent with other space charge layer thicknesses measured at a film formation potential of -0.2 V [39, 58]. The equation used for determining the space charge thickness (see Equation 3.4) is derived from a simple parallel plate capacitor model used throughout literature [39, 53, 58].

$$d = \frac{\varepsilon\varepsilon_0 A}{C_{sc}} \tag{3.4}$$

A is the exposed surface area of the sample, and $C_{sc,}$ is taken from Equation 3.1 by assuming a series capacitor model at the semiconductor/electrolyte interface. The decrease in d with increasing passivation time is consistent with the known structure of the passive film. As the outer Fe^{III}-rich layer continues to grow on top of the inner,

protective Fe^{II}-rich layer, a greater number of impurities are added to the film. Because the donor density has an inverse relation to the thickness of the space charge layer (which can be found by combining Equation 3.4 with the M-S equation in Equation 3.1), this decrease in space charge layer thickness coincides with the increase in impurities added to the oxide film during the course of passivation.

Figure 3.5 compares partially passivated and fully passivated oxide films from samples passivated in each of the three solutions. The first observation from this comparison is that the electronic properties of the films formed in CP-1 and CP-2 are nearly identical. This is consistent with the EIS results found in Figure 3.3, and this seems to imply that the presence of sulfates has no noticeable effect on the electronic properties of the passive film. However, when comparing the films formed in CP-1 and CP-2 to those formed in CH, the difference is considerable. The first difference is that the M-S curves tend to shift further up the $1/C^2$ axis for the passive film in CH, which indicates that it has a lower space charge capacitance. This is consistent with the findings from Figure 3.4 that a lower capacitance indicates a less passive film. This is also consistent with the known structural differences and passivity between the oxide films formed in CH versus CP-1 or CP-2 [2], which state that CH produces a significantly less passive film. The other differences between the CH and CP-1 / CP-2 M-S plots are more subtle. The shallow donor density looks to have decreased slightly in the CH solution, as can be seen in Table 3.4. This decrease is extremely small, however, and previous results [45] show the shallow donor density for CH being much closer to the levels seen for CP-1 and CP-2 in the present study. Another difference is that there appears to be a consistently delayed onset of valence band participation for the passive film in CH.

This is evidenced by, at 0.4 and 0.5 V applied potential, the curves of films formed in CP-1 and CP-2 show a more abrupt transition to a negative M-S slope and characteristic p-type semiconductor behavior. This distinction is more profound, because a delayed transition to p-type behavior indicates a slight change in the electronic band structure.

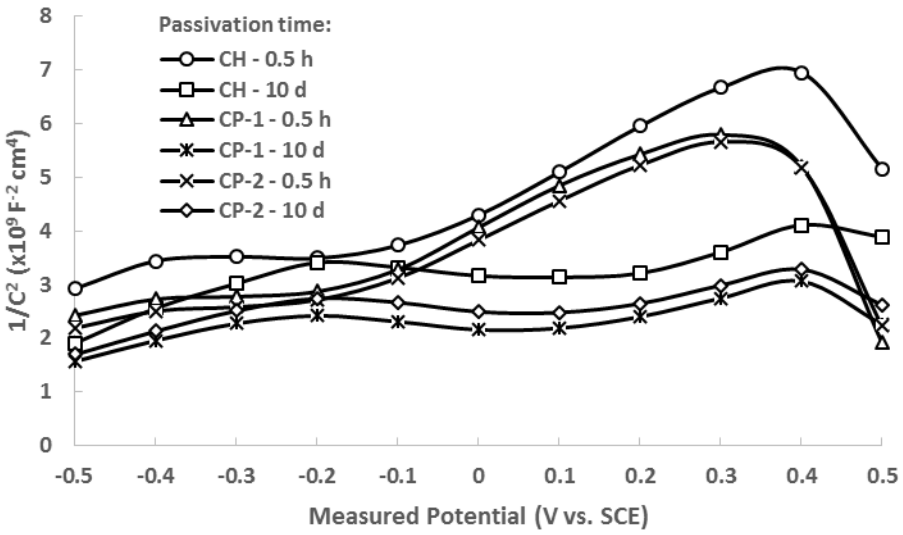

Figure 3.5: Comparison of the Mott-Schottky plots for initially passivated and fully passivated steel rebar samples in CH, CP-1, and CP-2 solutions. Samples passivated in CP-1 and CP-2 solutions show nearly identical behavior; however, samples passivated in CH solution show some significant differences.

Further clarity into an explanation for what is happening physically in the space charge layer as the potential is swept can be revealed by converting the M-S plots into capacitance versus voltage (C-V) plots. Figure 3.6 shows the C-V plot for CH, CP-1, and CP-2 at full passivation.

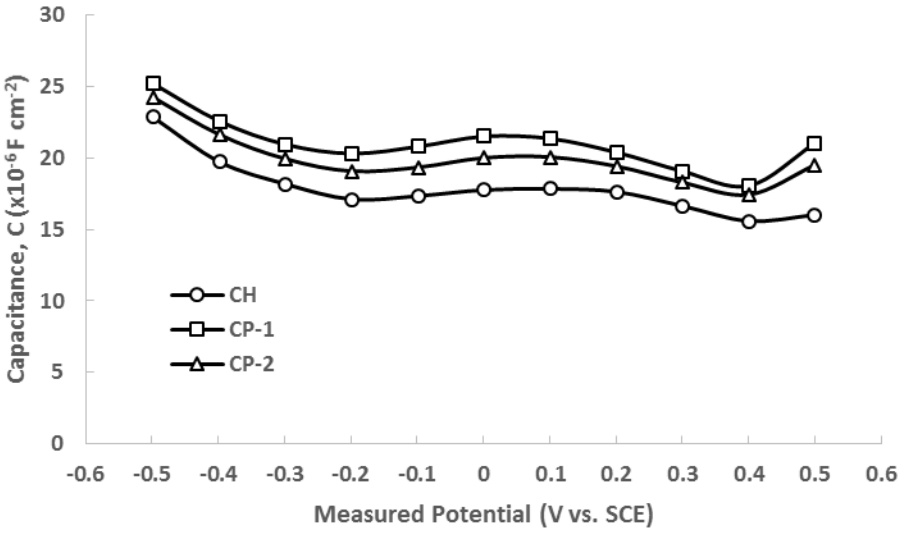

Figure 3.6: Capacitance vs. voltage plot comparing fully passivated steel samples in CH, CP-1, and CP-2 solutions.

The pattern shown in the C-V curves produced in all three solutions is consistent with the results found by Di Paola [53] and Stimming and Schultze [52] with passive stainless steel and iron, respectively. Using the approximate electronic band structure for passive steel, an adequate interpretation for the capacitance behavior may be obtained. At low potentials, the capacitance is high due to the presence of a small space charge layer thickness, assuming a typical parallel plate capacitor model for the space charge layer (see Equation 3.4). At this point, conduction is occurring freely from the shallow donor level to the conduction band, which are estimated to be only 0.1 eV to 0.2 eV apart [51, 58]. As the potential increases, the capacitance decreases steadily until approximately -0.2 V. The capacitance decreases as a result of the increasing space charge layer as the free charge carriers released by shallow donors in the space charge layer near the electrode surface are excited. This leaves a quasi-insulative region where all the majority charge carriers have diffused away, and the thickness of this

space charge region continues to grow as the potential increases. Then, the capacitance abruptly increases. The cause for this capacitance increase, followed by a resumption to the expected capacitance decrease was explained well by Dean and Stimming [60] when modeling the classical work by Dewald for the case of a partially ionized deep donor in a zinc oxide system [49]. The nonlinearity introduced in this region is due to the partial ionization of the deep donor state in the passive oxide film. This ionization begins to occur as the Fermi level approaches the deep donor energy level, E_{D2}, as a result of band bending through the space charge layer. This continues until the potential drop across the space charge layer, ϕ_{sc}, exceeds the difference between the Fermi level at the flatband potential and E_{D2}, at which point the available deep donor states become completely ionized. The ionization of this second donor state located deeper in the band gap affects the capacitance, because the capacitance is directly related to the total charge density across the depletion layer. As the total charge density suddenly increases with the ionization of an entirely new series of deep donor states, the capacitance likewise increases. At potentials higher than about 0.1 V, the deep donors have been fully ionized, and the growing space charge layer is the only factor governing the decrease in space charge capacitance.

Finally, at potentials exceeding 0.4 V, valence band participation begins to occur [52]. It is at this point that the space charge capacitance is at a minimum and the thickness at a maximum. The depletion layer at this point has become so large that an inversion layer of holes forms at the valence band that is oppositely charged to the electrons lying in the valence band. Graetzel points out that at this point, the free electrons in the space charge layer have become so depleted at the semiconductor-electrolyte interface that

they actually reached levels below the intrinsic value of the semiconductor, for the case that the semiconductor was in an undoped state [63]. Above 0.4 V, the slope in Figure 3.6 abruptly turns positive as the passive film becomes p-type at the interface, while still remaining n-type in the bulk oxide film.

3.3.2. Effect of Chlorides

During the next phase of the experimental investigation chlorides were added incrementally to CH and CP-1 solutions with fully passivated samples for the purpose of determining the chloride threshold of those samples. For passive films developed in CH and CP-1 solutions, Ghods et al. found that the chloride threshold for as-received rebar samples was 0.05 M and 0.15 M, respectively, and the threshold for cleaned and polished samples in CP-1 was 1.25 M [6]. Li et al. found the chloride threshold for carbon steel in highly alkaline solutions to be about 0.5 M [42]. The chloride threshold for CH was found to be around 0.5 M which is consistent with these previous results. The chloride threshold for CP-1 was found to be about 2.5 M, which is higher than the level previously predicted [6] for a cleaned and polished sample. However, the samples in this previous work were only ground to 600 grit, which is a significantly coarser final polish than that used in the present work. A more comparable level of polishing was performed on high purity iron by Gunay et al., and this work also found a chloride threshold near 2.5 M [9]. Therefore, the chloride thresholds found for CH and CP-1 are at reasonable levels.

Figure 3.7 shows the change in open circuit potential (OCP) as a function of time and the incrementally added chloride amounts listed in Table 3.3 for CH solution. The OCP is relatively unaffected at chloride levels below the threshold, but as the levels begin to

approach this threshold, the OCP quickly falls and reaches approximately -0.6 V, which is a value seen only for extremely depassivated rebar samples [6]. The OCP behavior shown in Figure 3.7 is consistent with that found in CP-1 as chlorides were added incrementally and the chloride threshold was breached.

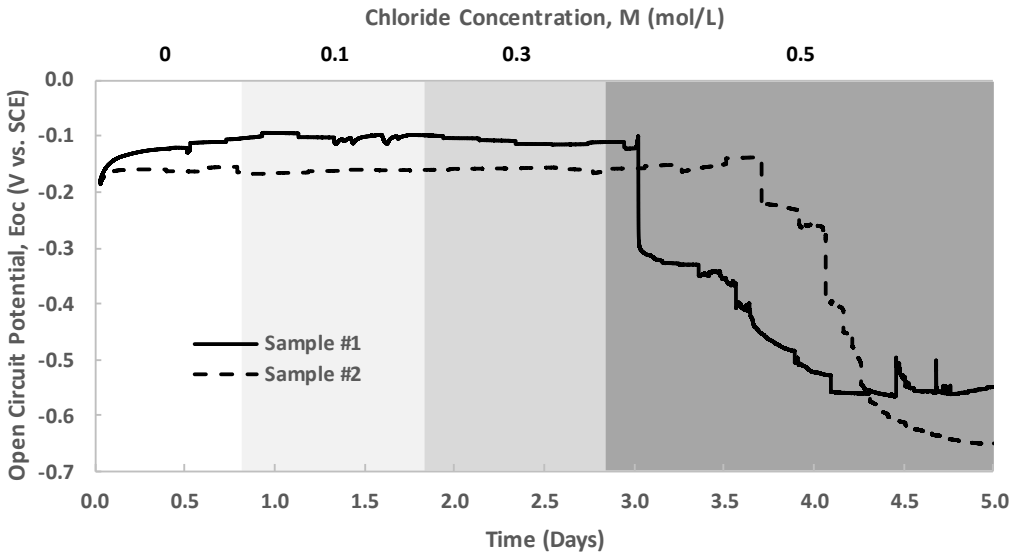

Figure 3.7: Open circuit potential plot illustrating the effect on two passivated steel rebar samples from incrementally adding chlorides to a CH solution. The chloride thresholds for samples passivated in CH solution and CP-1 solution were typically around 0.5 M and 2.5 M, respectively. Shading in figure corresponds to the total chloride concentration in the electrochemical cell according to Table 3.3.

Figure 3.8 shows EIS plots illustrating the effect of this incremental chloride addition in CH solution. The effect of chlorides approaching the chloride threshold and then crossing the threshold can be clearly seen, as both the impedance moduli and phase angles drop rapidly as the film deteriorates. Corresponding M-S (see Figure 3.9) potential sweeps were run on these samples after each chloride addition to show their effect on the electronic properties.

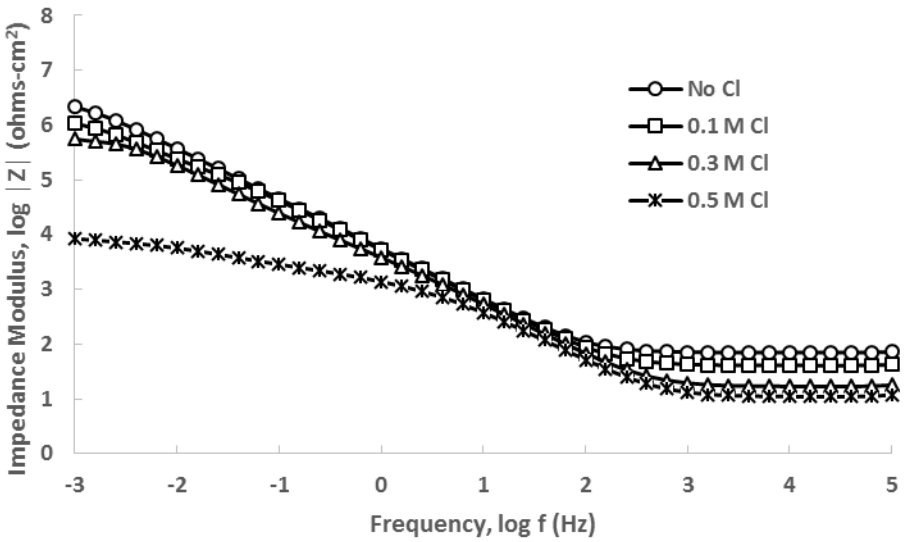

(a)

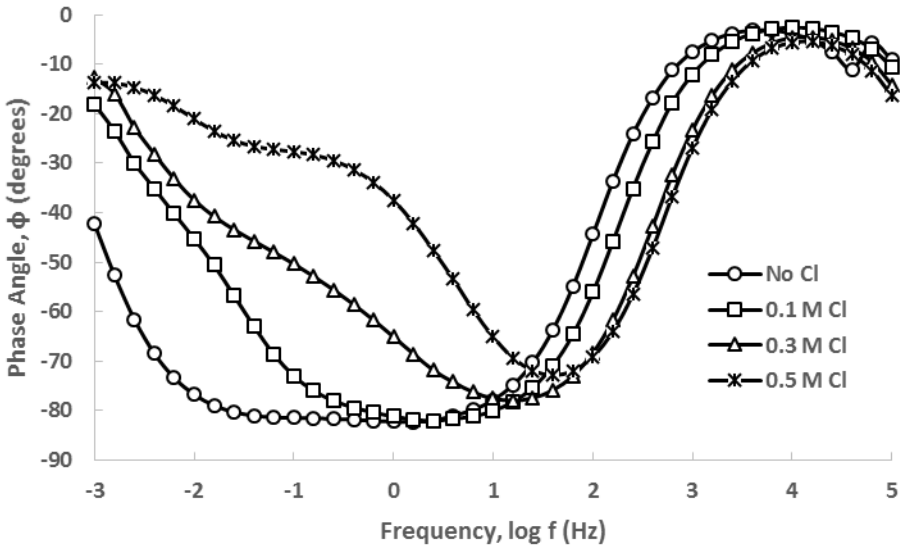

(b)

Figure 3.8: EIS plots showing the change in impedance modulus (a) and phase angle (b) as a function of frequency for steel rebar samples exposed to incrementally increasing chloride concentrations. The samples were fully passivated in CH solution before chloride additions. The legends reflect the total chlorides in the electrochemical cell per Table 3.3.

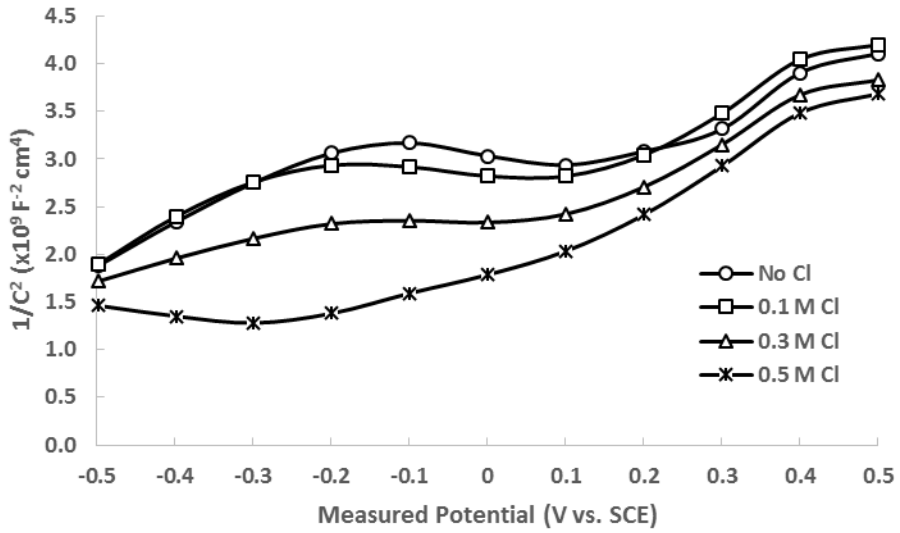

(a)

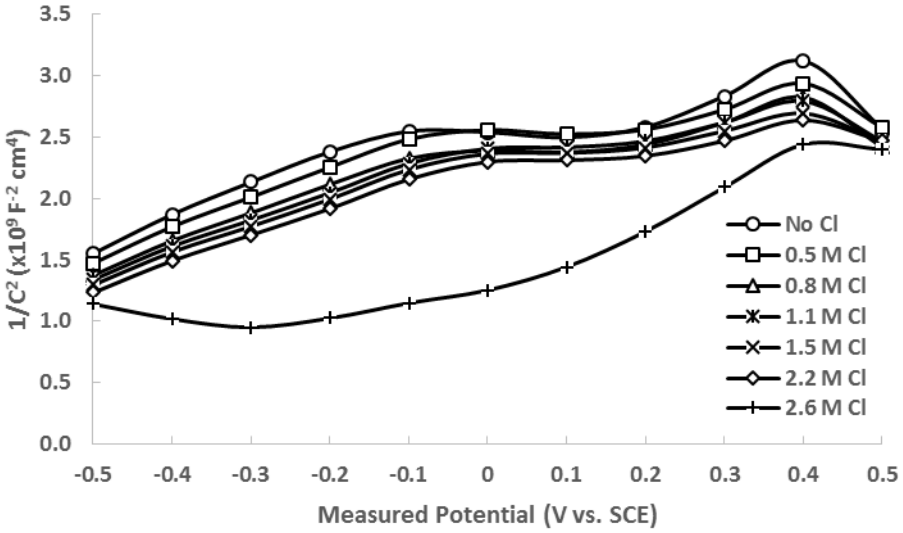

(b)

Figure 3.9: Mott-Schottky plots showing the effect of incremental chloride additions on fully passivated steel rebar samples in (a) CH solution and (b) CP-1 solutions. The legends reflect the total chlorides in the electrochemical cell per Table 3.3.

The M-S results from the passive film formed in CP-1 are shown in Figure 3.9 by incrementally increasing the chloride level in the solution.

A few observations can be extracted from Figure 3.9. The first is that as the film depassivates, the linear regions of the M-S plots become non-linear. This phenomenon is consistent with the results elaborated upon by La Mantia et al. showing that curved M-S lines are actually a result of an amorphous oxide film structure being present [64]. What this implies then is that the passive film becomes much more reminiscent of an amorphous structure with the addition of sufficient quantities of chlorides. This is in stark contrast to previous results which show that the passive film on iron-based alloys is a crystalline structure with two distinct donor states representing two obvious linear regions in the M-S plots (see Refs. [7, 53, 58, 62]). This non-linearity also interferes with extracting quantitative electronic properties from the M-S plots, because the M-S equation (see Equation 3.1) is only valid for linear regions of the curve [52]. A second observation can be seen when looking at the transition from purely shallow donor ionization to the additional deep donor contribution at around -0.1 V for samples with chloride levels below the chloride threshold. At this transition, the capacitance experiences a sudden increase as additional charge carriers are excited from deep donor positions, as explained at length previously. This "hump" feature at the transition in the M-S plot, though present at low chloride levels, disappears once the chloride threshold is breached. For these depassivated samples, only the continuous, nonlinear decrease in the space charge capacitance that is characteristic of an amorphous structure is present. Therefore, Figure 3.9 again affirms that the "hump" feature is indicative of the presence of a passive oxide film on the rebar. More specifically, this feature reveals the presence of a fully-formed inner Fe^{II}-rich oxide layer that is extremely dense, coherent, and protective in nature. Once the chloride threshold is breached, this protective Fe^{II}-

rich layer quickly deteriorates, two discrete donor levels are no longer present, and the film more closely resembles the amorphous structure described by several authors [64, 65]. The disappearance of an abrupt increase in space charge capacitance once the chloride threshold has been breached is curiously missing from the work done on carbon steel in a pH 9.2 solution by Li et al. [42]. However, this could be due to the fact that the passivity of the oxide film formed in alkaline solutions steadily increases with pH [2]. The pH used by Li et al. [42] to form the passive film may therefore be too low to adequately characterize the effect due to chloride ingress on the electronic properties of the passive film.

Although Figure 3.9 shows the passive film formed in CH has similar behavior to CP-1, notable differences remain. These differences can be accounted for and are reinforced by the present understanding of the structure of the passive films formed in CH and CP-1 [9, 15]. What Figure 3.9a shows is that the addition of chlorides rather quickly and easily depassivates the film. However, Figure 3.9b shows that the depassivation process occurs much more slowly and requires extremely high chloride concentrations to occur. This is consistent with the known passive film structures which show the Fe^{II}-rich inner oxide layer and Fe^{III}-rich outer layer formed in CH are less dense and coherent compared to that same bilayer structure formed in CP-1. Since it is known that a denser oxide film impedes chloride ingress to the steel surface, it would be expected for this depassivation process to take much longer and require a greater chloride concentration.

One additional observation that is present in Figures 3.9a and 3.9b is that the space charge capacitance increases with increasing chloride concentrations. Interestingly, this

gradual increase in the space charge capacitance was also seen in Figure 3.4, and it helps to reinforce the present understanding of the passive film structure. Figure 3.4 showed that the increase in the outer Fe^{III}-rich oxide layer introduced additional impurities to the passive film due to its incoherent, non-uniform structure. The additional impurities then increase the space charge capacitance as these donor states are ionized. This then explains why Figure 3.9 also shows an increase in the space charge capacitance, because the addition of chlorides begins to slowly breakdown the outer Fe^{III}-rich layer and increase the disorder and number of impurities present. Both the addition of chlorides seen in Figure 3.9, and the thickening of the outer Fe^{III}-rich layer in Figure 3.4 increase the number of impurities, which explains the increase in space charge capacitance.

3.3.3. Additional Observations

Figure 3.10 shows possible electron band structures for steel rebar in simulated concrete pore solutions under flatband conditions and under an anodically applied potential. The band structures are shown with respect to the absolute vacuum scale (AVS) and saturated calomel electrode (SCE). The position of the Fermi level, E_F, changes as a function of applied potential, since the Fermi level is equal to the electrochemical potential of the electrons in the electrode [51, 58]. Therefore, when the applied potential is equal to the flatband potential at the electrode-electrolyte interface, the Fermi level is also equal to the flatband potential. The position of the lower edge of the conduction band, E_C, is for n-type semiconductors typically around 0.1 eV noble (positive) to the Fermi level position [51, 58]. The energy level of the shallow donor state, E_{D1}, is estimated to be at or very near to the Fermi level, since M-S plots indicate

full shallow donor ionization at the flatband potential (see Figure 3.4, Refs. [39, 58, 60]). Simoes et al. [58] estimated the distance between E_C and the energy of the deep donor state, E_{D2}, to be 0.5 eV, and this is consistent with the results shown in Figure 3.4 which shows the contribution from deep donor states to the space charge capacitance beginning at around 0.4-0.5 V anodic to the flatband potential. The position of the upper edge of the valence band, E_V, can be found by knowing the position of E_C and the band gap energy, E_g, for the semiconductor. Xu and Schoonen [48] showed that E_g for $Fe^{II}O$ and Fe_3O_4 is 2.40 eV and 0.10 eV, respectively. This is a significant difference, and since it is known that the passive film structure is made primarily of a combination of these two oxides [15], the exact position of E_V was not determined. Figure 3.10 shows an approximate position of E_V, lying somewhere between the Fe^{II} and Fe^{II}/Fe^{III} oxides.

The locations of the standard redox potential for hydrogen evolution, $E^0_{redox,\ H_2O/H_2}$, and oxygen reduction, $E^0_{redox,\ O_2/H_2O}$, are listed in Figure 3.10 for reference. Above and below each of these redox potentials show the position of the redox potentials for the case that an electron was accepted from the semiconductor or donated to the semiconductor. These energy levels are represented as Gaussian distributions, which show the density of states as a function of thermal fluctuations. The value λ is called the reorganization energy, and it has to do with the change in energy that occurs from the redox species accepting or donating electrons by reaction with the semiconducting oxide. [48, 51]. Its value can range from 0.1 eV up to 2 eV, so the magnitude of λ shown in Figure 3.10 is only an approximation [48]. Figure 3.10 also clearly shows the effect that anodically polarizing the sample has on the position of the energy bands. The

position of the energy bands in the bulk oxide are pushed downward, while their values at the interface remain constant, with the exception of the Fermi level. This is because in semiconductors, the value of the energy bands at the interface do not change as a function of applied potential, unlike with metals. This results in band bending occurring through the depletion region, and the magnitude of band bending, V_B, changes with applied potential.

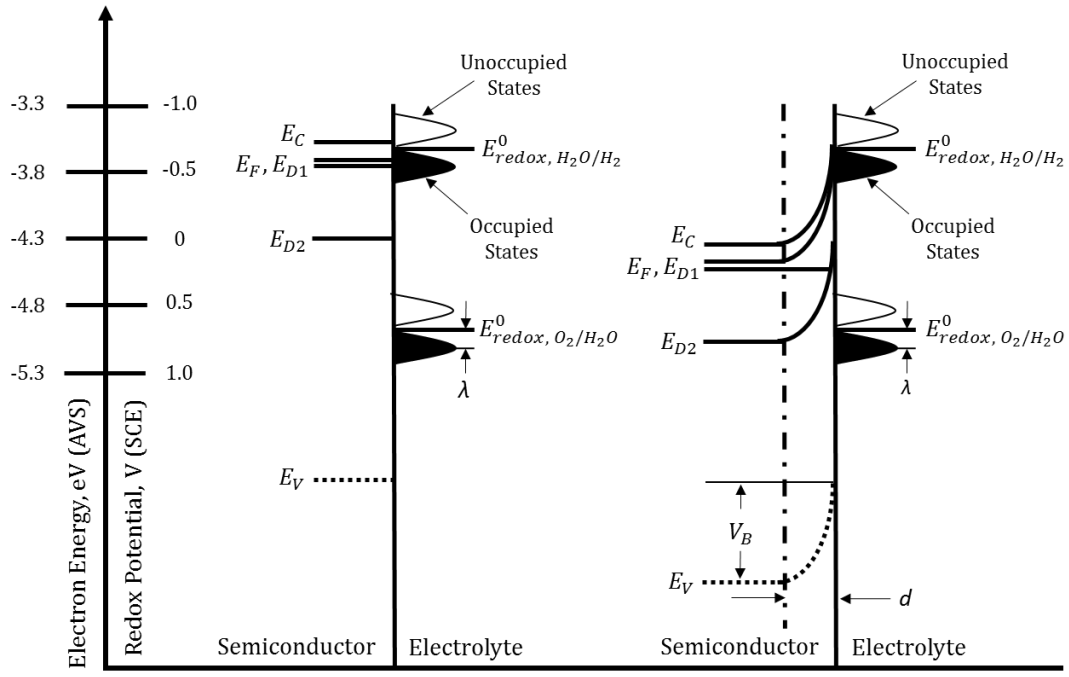

Figure 3.10: Simplified energy level model for an electrochemical system at (left) the flatband potential and (right) under anodic polarization. E_C is the lower edge of the conduction band, and E_V is the upper edge of the valence band. E_F is the Fermi level of the semiconductor, and E_{D1} and E_{D2} are the energies of two impurity donor states located within the band gap of the semiconductor. V_B is the amount of band bending, which is a function of the applied potential to the system. d is the space charge layer thickness. $E^0_{redox,H_2O/H_2}$ and $E^0_{redox,O_2/H_2O}$ are the standard redox potentials for the reacting species in the solution. The Gaussian distributions on either side of the standard redox potentials indicate the density of states distribution for the case of electron acceptance or donation. Electron acceptance occurs at the unoccupied states, and donation occurs at the occupied states. λ is the reorganization energy. The distances are not to scale. This is a concept illustration, so units are not provided. Modified from Refs. [39, 58].

Now, having discussed possible electronic band structure diagrams for the steel rebar passive film, a discussion of the delayed onset potential for valence band participation in M-S plots for passive films in CH solution will be more enlightening. This is because it is possible that this delayed onset potential has to do with a small difference in the electronic band structure of the passive films formed in CH versus CP-1 and CP-2. Figure 3.10 shows that at high positive voltages, the Fermi level in the semiconductor

begins to approach to the valence band. As the Fermi level continues to work down the energy continuum with increasing voltage, the majority charge carriers supplied by the conduction band and the two donor states to the solution begin to become exhausted. The space charge layer thickness, *d*, continues to grow during this process and majority charge carriers from deeper in the bulk semiconductor are extracted from the oxide and injected into the solution. Eventually, the applied voltage becomes so high that the electrons supplied from the conduction band and donor states cannot supply sufficient charge carriers without excessive band bending occurring [51]. Electrons from the minority charge band (i.e. the valence band) must then be supplied, resulting in an increase in hole concentration at the semiconductor surface near the valence band energy level. This phenomenon is called the creation of an *inversion layer*, and was alluded to previously to explain the transition to characteristic p-type behavior in the M-S plots at higher potentials. What is likely occurring with the delayed onset of valence band participation for the passive film formed in CH is that this inversion layer does not form until greater potentials – perhaps higher by 0.1 or 0.2 eV. This could be a result of a greater density of majority charge carriers supplied by either the conduction band or the two donor states, which is prolonging the need for the valence band to supply electrons to the solution. When looking at Table 3.4, the passive film formed in CH has a deep donor density of 4.47×10^{20} cm^{-3} after averaging the densities for all five passivation times, whereas the passive films formed in CP-1 and CP-2 have deep donor densities of 2.48×10^{20} cm^{-3} and 2.19×10^{20} cm^{-3}, respectively. The deep donor density for the film in CH is around double that for CP-1 and CP-2, and because the deep donor density is higher, the majority charge carriers injected into the solution will likewise be

higher. This will prolong the need for minority charge carrier band participation, which is exactly what is seen with the delayed valence band participation in CH solution. An additional explanation may lie in the fact that the passive film in CH is not as protective, dense, and ordered in comparison to the passive film formed in CP-1 and CP-2. This can be seen clearly in several works authored by Ghods et al. [2, 6, 7] and Gunay et al. [9, 15]. This is due to the absence of auxiliary ions such as Na^+ and K^+ in CH which enhance the protective nature of the film, particularly during early film formation. The more incoherent, porous, and disordered nature of the passive film in CH implies that a greater number of impurities are present in the film compared to that formed for CP-1 and CP-2. These impurities may provide additional majority charge carriers that can delay the onset of minority charge carrier equilibrium [51].

An interesting conclusion that can be drawn from the abrupt turn to p-type behavior for the steel rebar passive film at around 0.4 V is an additional clue as to the elemental composition and atomic structure of the passive film. At high potentials, small band gap passive films (i.e. 1-2 eV) exhibit this transition from n-type to p-type behavior due to the formation of the inversion layer as the bulk Fermi level approaches the valence band. However, in larger band gap films, this transition does not occur, and the M-S curve retains the positive slope, albeit at a steadily decreasing slope. This phenomenon is called a *deep depletion layer* and can be clearly seen in a larger band gap material such as ZnO [66]. Because the deep depletion layer phenomenon does not occur, but instead minority charge carrier band participation dominates at higher potentials, the passive oxide film formed on steel rebar is a small band gap material. This is consistent with the conclusions found by Gunay et al., that the passive film

structure is extremely complex, with the majority of the inner layer being $Fe^{II}O$ which then transitions to $Fe^{II}O/Fe_3O_4$ at the edge of the inner passive film layer [15]. Therefore, the band gap of the passive film should lie somewhere between the band gaps for pure $Fe^{II}O$ and Fe_3O_4, which are 2.40 eV and 0.10 eV, respectively [48]. This would therefore classify the steel rebar passive oxide film as a small band gap material, and this reinforces the atomic structure of the passive film proposed in Refs. [9, 15].

One of the major features of the M-S plot in Figure 3.5 is the decreased space charge capacitance for passive films in CH compared to CP-1 and CP-2 for a given potential. This was primarily attributed to the decrease in protective nature of the passive film formed in CH compared to the one formed in CP-1 or CP-2. However, a secondary contributor to the decreased capacitance could be attributed to a change in the flatband potential. A negative shift in the flatband potential would shift the entire M-S plot to more negative potentials, with the approximate shape and slopes closely following their original values assuming the dopant state energy levels and densities do not change. According to Table 3.4, the flatband potential increases approximately 0.06 V for a 0.9 unit increase in pH. Morrison showed that the primary causes for a shift in the flatband potential are: 1) variations in the potential drop across the Helmholtz layer, V_H, 2) additional double layers formed due to a secondary surface film, or 3) extraneous voltages inadvertently applied to the circuit or unaccounted for in the circuit [51]. Of these, the first option is by far the most likely and most common [51], since any unaccounted for or inadvertently applied voltages would have appeared on other M-S tests, and previous studies on the passivity of steel rebar in simulated concrete pore solutions have failed to reveal the appearance of a secondary double layer film on the

surface. A change in V_H is logical, because V_H is directly affected by changes in the pH. Likewise a change in V_H directly results in a change to the flatband potential, V_{fb}, according to the Nernstian relation shown in Equation 3.5 for a typical metal oxide [48, 67].

$$V_{fb} = V_{fb}^{0} + 2.303RT/(pH_{PZC} - pH)F \quad (3.5)$$

Here, V_{fb}^{0} is the flatband potential at 25°C and 1 atm, R is the gas constant, T is the absolute temperature, pH_{PZC} is the pH at the point of zero charge, and F is the Faraday constant. According to Xu and Schoonen, the flatband potential will increase on average 0.059 V per unit pH for a typical metal oxide [48]. Morrison [51] likewise shows a similar dependence of the flatband potential on pH, where an increase in the pH directly relates to an increase in the flatband potential. Interestingly, the relation between the flatband potential and pH of 0.059 V per unit pH is approximately the same relation seen in the experimental results of the present study (i.e., 0.06 V increase per 0.9 unit change in pH). This lends significant credibility to the proposition that the change in solution pH accounts not only for the change in flatband potential seen for the passive film in CH compared to CP-1 or CP-2, but also possibly contributes to the decreased space charge capacitance for films formed in CH.

A final phenomenon that is occurring consistently in all M-S plots studying the evolution of the passive film that requires a bit more discussion is the increased space charge capacitance with increasing passivation time. This was primarily attributed to the increased capacity of the oxide film as it becomes more passivated and protective in Section 3.3.1. However, another contributor to this decrease could be a slight flattening or broadening of the “hump” feature on M-S plots of passivated films.

Although the shape of the M-S curves in Figure 3.4 remain relatively constant after the initial 0.5 hour passivation time, this potential range over which the "hump" occurs does seem to widen with passivation time. This occurrence was present in a previous work on steel rebar [45] as well, and a reasonable explanation for this can be found by looking again at the work by Dean and Stimming [60, 65] in modeling Dewald's zinc oxide system [49]. What seems to be occurring is that the broadening of the "hump" is actually a sign of a broadening of the distribution of energy states, most notably around the deep donor state energy level. Dean and Stimming [60] assumed a normal distribution of energy states centered on this single discrete state and convincingly showed that as the energy band broadened, the rise and fall in capacitance becomes less abrupt and occurs over a wider potential range. This broadening of the distribution of energy states about the deep donor level can again be attributed to the structure and growth of the passive oxide film. As the thickness of the porous, non-stoichiometric, outer Fe^{III}-rich layer continues to increase with passivation time, a greater number of impurities (i.e. Fe^{II} donors occupying Fe^{III} octahedral sites) will be present. These impurities will likely not all be centered exactly on the deep donor energy level, but will exist at many discrete energy states above and below the impurity band. This is because not all impurity atoms will have a typical bonding structure, and so each will exist at a slightly different energy state with a slightly different wave function from the expected norm [51].

This study opens the possibility for several areas of future work. First, a satisfactory explanation for the slight decrease in shallow donor density for CH solution compared to CP-1 or CP-2 is unknown. It is possible that this difference is within the variability

inherent to the potentiostat equipment used, since the M-S potential sweep was run at an extremely fast rate. It is also possible that a potential sweep beginning at a more cathodic potential would reveal a slightly greater donor density for CH, but this is speculation. Secondly, the lack of any significant difference in the electronic properties between CP-1 and CP-2 is interesting and requires further study. It lends to the theory that the electronic properties are primarily determined by the solution pH, which was nearly identical for CP-1 and CP-2, and has less to do with the electrolyte constituents. This is counter to what is known about the presence of sulfates in concrete pore solutions, which was shown to have a considerably negative effect on the protective nature of the passive film [2].

3.4. Conclusions

The electronic properties of passive steel rebar in simulated concrete pore solutions was investigated from initial sample immersion in the passivating solution to a fully passive state. This was performed using Mott-Schottky analysis, EIS, and other electrochemical techniques. Steel rebar samples were ground, polished, and passivated in three concrete pore solution compositions meant to simulate various environments found in actual concrete: CH, CP-1, and CP-2. The values of three primary electronic properties (i.e., the flatband potential, donor density, and space charge layer thickness) were found and compared for samples in each of these three solutions. All M-S plots, regardless of passivating solution, revealed n-type semiconductive behavior and two distinct donor species located within the band gap of the passive film. Passive films formed in all three solutions showed similar maximum space charge layer thicknesses of around 0.4 nm at full passivation. Both donor species showed extremely high donor

densities indicative of the exceedingly disordered oxide films known to form on iron-based alloys. The deep donor density showed a slow, gradual increase during later passivation times that corresponds to the buildup of this porous Fe^{III}-rich outer layer in the passive film bilayer structure. The M-S plots from all three solutions also showed the formation of a "hump" feature on the plots centered near the deep donor ionization potential, which coincided with the full formation of the thin, protective, inner Fe^{II}-rich oxide layer. The passive films formed in CP-1 and CP-2 had nearly identical electronic signatures, leading to the conclusion that the addition of sulfates does not significantly affect the electronic properties of the passive film. The difference between passive films in CP-1 and CP-2 when compared to CH was more profound. The passive films formed in CH showed a lower flatband potential compared to the other two passivating solutions, and this was theorized to be the result of a decrease in solution pH. The passive film in CH showed a lower overall space charge capacitance, which corresponds to the less coherent, dense, and protective film known to form in CH versus the other two solutions. This passive film in CH also seemed to show a delayed onset of valence band participation compared to CP-1 or CP-2, possibly due to the delayed formation of the inversion layer at the valence band edge.

The effect of chlorides on the electronic properties of the passive film was also characterized. It was found that as chlorides are added, particularly at levels near the chloride threshold, the linear regions of the M-S plots begin to become non-linear. This indicates the breakdown of the passive film as it transitions from a more ordered state to an amorphous-like oxide structure. The disappearance of the "hump" feature at the deep donor ionization potential coincided well with the crossing of the chloride

threshold. The disappearance of this feature, however, differed between the passive films in CH and CP-1 in that this occurred much more slowly and required significantly higher chloride levels to occur in the CP-1 solution. This is consistent with the fact that the thin, protective, inner Fe^{II}-rich layer in the passive film formed in CP-1 solution is denser and more protective compared to that in CH, and would likewise require higher chloride levels at longer exposure times to depassivate.

3.5. References

[1] M. Yunovich, N.G. Thompson, T. Balvanyon, L. Lave.
[2] P. Ghods, O.B. Isgor, G. McRae, T. Miller, Cement and Concrete Composites, 31 (2009) 2-11.
[3] L. Li, A.A. Sagues, Corrosion, 58 (2002) 305-316.
[4] C.M. Hansson, A. Poursaee, A. Laurent, Cement Concrete Res, 36 (2006) 2098-2102.
[5] U.M. Angst, B. Elsener, C.K. Larsen, O. Vennesland, Corros Sci, 53 (2011) 1451-1464.
[6] P. Ghods, O.B. Isgor, G.A. McRae, G.P. Gu, Corrosion Science, 52 (2010) 1649-1659.
[7] P. Ghods, O.B. Isgor, G.J.C. Carpenter, J. Li, G.A. McRae, G.P. Gu, Cement and Concrete Research, 47 (2013) 55-68.
[8] P. Ghods, O.B. Isgor, G.A. McRae, J. Li, G.P. Gu, Corrosion Science, 53 (2011) 946-954.
[9] H.B. Gunay, B. Isgor, P. Ghods, Corrosion, (2014).
[10] S. Joiret, M. Keddam, X. Nóvoa, M. Pérez, C. Rangel, H. Takenouti, Cement and Concrete Composites, 24 (2002) 7-15.
[11] C. Gabrielli, S. Joiret, M. Keddam, H. Perrot, N. Portail, P. Rousseau, V. Vivier, Journal of the Electrochemical Society, 153 (2006) B68-B74.
[12] C. Gabrielli, S. Joiret, M. Keddam, H. Perrot, N. Portail, P. Rousseau, V. Vivier, Electrochimica Acta, 52 (2007) 7706-7714.
[13] P. Ghods, O. Burkan Isgor, F. Bensebaa, D. Kingston, Corrosion Science, 58 (2012) 159-167.
[14] P. Ghods, O.B. Isgor, J.R. Brown, F. Bensebaa, D. Kingston, Applied Surface Science, 257 (2011) 4669-4677.
[15] H.B. Gunay, P. Ghods, O.B. Isgor, G.J.C. Carpenter, X. Wu, Applied Surface Science, 274 (2013) 195-202.
[16] U. Angst, B. Elsener, C.K. Larsen, O. Vennesland, Cement Concrete Res, 39 (2009) 1122-1138.
[17] L.T. Mammoliti, L.C. Brown, C.M. Hansson, B.B. Hope, Cement Concrete Res, 26 (1996) 545-550.
[18] L. Li, A.A. Sagues, Corrosion, 57 (2001) 19-28.
[19] R.G. Pillai, D. Trejo, Aci Mater J, 102 (2005) 103-109.
[20] S. Goni, C. Andrade, Cement Concrete Res, 20 (1990) 525-539.
[21] C. Andrade, C.L. Page, British Corrosion Journal, 21 (1986) 49-53.
[22] H. Wu, Y. Wang, Q. Zhong, M. Sheng, H. Du, Z. Li, Journal of Electroanalytical Chemistry, 663 (2011) 59-66.
[23] M. Santamaria, D. Huerta, S. Piazza, C. Sunseri, F. Di Quarto, Journal of The Electrochemical Society, 147 (2000) 1366-1375.
[24] P. Schmuki, H. Bohni, Werkstoffe und Korrosion, 42 (1991) 203-207.
[25] P. Schmuki, H. Böhni, Journal of the Electrochemical Society, 139 (1992) 1908-1913.
[26] N. Hakiki, M.D.C. Belo, A. Simoes, M. Ferreira, Journal of the Electrochemical society, 145 (1998) 3821-3829.

[27] N. Hakiki, S. Boudin, B. Rondot, M. Da Cunha Belo, Corrosion Science, 37 (1995) 1809-1822.
[28] Z. Szklarska-Smialowska, Corrosion Science, 41 (1999) 1743-1767.
[29] Z. Szklarska-Smialowska, Corrosion Science, 44 (2002) 1143-1149.
[30] Y. Liu, G.Z. Meng, Y.F. Cheng, Electrochimica Acta, 54 (2009) 4155-4163.
[31] H. Gerischer, Corrosion science, 29 (1989) 191-195.
[32] M. Ferreira, M. Da Cunha Belo, N. Hakiki, G. Goodlet, M. Montemor, A. Simões, Journal of the Brazilian Chemical Society, 13 (2002) 433-440.
[33] M. Ferreira, N. Hakiki, G. Goodlet, S. Faty, A. Simoes, M. Da Cunha Belo, Electrochimica Acta, 46 (2001) 3767-3776.
[34] I.-u.-H. Toor, Journal of The Electrochemical Society, 158 (2011) C391.
[35] K. Azumi, T. Ohtsuka, N. Sato, Journal of The Electrochemical Society, 134 (1987) 1352-1357.
[36] S.P. Harrington, F. Wang, T.M. Devine, Electrochimica Acta, 55 (2010) 4092-4102.
[37] J. Yu, J. Luo, P. Norton, Applied surface science, 177 (2001) 129-138.
[38] J. Liu, D.D. Macdonald, Journal of The Electrochemical Society, 148 (2001) B425.
[39] Y. Cheng, J. Luo, Electrochimica acta, 44 (1999) 2947-2957.
[40] Y. Cheng, J. Luo, Electrochimica Acta, 44 (1999) 4795-4804.
[41] L. Hamadou, A. Kadri, N. Benbrahim, Applied Surface Science, 252 (2005) 1510-1519.
[42] D.G. Li, Y.R. Feng, Z.Q. Bai, J.W. Zhu, M.S. Zheng, Electrochimica Acta, 52 (2007) 7877-7884.
[43] M. Sánchez, J. Gregori, C. Alonso, J.J. García-Jareño, H. Takenouti, F. Vicente, Electrochimica Acta, 52 (2007) 7634-7641.
[44] M. Sánchez, J. Gregori, M.C. Alonso, J.J. García-Jareño, F. Vicente, Electrochimica Acta, 52 (2006) 47-53.
[45] J. Williamson, O.B. Isgor, Applied Surface Science, (2015) submitted for publication.
[46] M. Büchler, P. Schmuki, H. Böhni, T. Stenberg, T. Mäntylä, Journal of the Electrochemical Society, 145 (1998) 378-385.
[47] U. Stimming, J. Schultze, Electrochimica Acta, 24 (1979) 859-869.
[48] Y. Xu, M.A. Schoonen, American Mineralogist, 85 (2000) 543-556.
[49] J. Dewald, Bell System Technical Journal, 39 (1960) 615-639.
[50] J. Dewald, Journal of Physics and Chemistry of Solids, 14 (1960) 155-161.
[51] S.R. Morrison, Electrochemistry at semiconductor and oxidized metal electrodes, 1980.
[52] U. Stimming, J. Schultze, Berichte der Bunsengesellschaft für physikalische Chemie, 80 (1976) 1297-1302.
[53] A. Di Paola, Electrochimica Acta, 34 (1989) 203-210.
[54] J. Sikora, E. Sikora, D.D. Macdonald, Electrochimica acta, 45 (2000) 1875-1883.
[55] M. Saremi, E. Mahallati, Cement and Concrete Research, 32 (2002) 1915-1921.
[56] D.A. Jones, Principles and prevention of corrosion, Macmillan, 1992.
[57] Y.-l. Zhang, Q.-l. Li, Journal of Zhejiang University SCIENCE A, 7 (2006) 1447-1452.

[58] A. Simoes, M. Ferreira, B. Rondot, M. da Cunha Belo, Journal of the Electrochemical Society, 137 (1990) 82-87.
[59] E. Sikora, D.D. Macdonald, Solid State Ionics, 94 (1997) 141-150.
[60] M.H. Dean, U. Stimming, Journal of electroanalytical chemistry and interfacial electrochemistry, 228 (1987) 135-151.
[61] V.A. Myamlin, Y.V. Pleskov, Electrochemistry of semiconductors, Plenum Press, New York, 1967.
[62] H. Tsuchiya, S. Fujimoto, T. Shibata, Journal of The Electrochemical Society, 151 (2004) B39.
[63] M. Grätzel, Nature, 414 (2001) 338-344.
[64] F. La Mantia, H. Habazaki, M. Santamaria, F. Di Quarto, Russian Journal of Electrochemistry, 46 (2010) 1306-1322.
[65] M.H. Dean, U. Stimming, The Journal of Physical Chemistry, 93 (1989) 8053-8059.
[66] S. Morrison, T. Freund, The Journal of Chemical Physics, 47 (1967) 1543-1551.
[67] D. Ginley, M. Butler, Journal of the Electrochemical Society, 125 (1978) 1968-1974.

MODELING ELECTRONIC PROPERTIES OF THE PASSIVE FILMS FORMING ON CARBON STEEL IN SIMULATED CONCRETE PORE SOLUTIONS

Jon Williamson, Vahid Jafari Azad, O. Burkan Isgor

To be submitted to: Journal of Electrochemical Society

Case Western Reserve University

Solon, OH, USA

4. Third Manuscript

Modeling Electronic Properties of the Passive Films on Carbon Steel in Simulated Concrete Pore Solutions

Jon Williamson[1], Vahid Jafari Azad[2], O. Burkan Isgor[3],

[1]Graduate Student at Oregon State University, Department of Materials Science

[2]Postdoctoral Scholar at Oregon State University, School of Civil and Construction Engineering

[3]Associate Professor at Oregon State University, School of Civil and Construction Engineering

Abstract:

The performance of five existing models for predicting the electronic properties of passive oxide films on carbon steel that are exposed to synthetic alkaline media representing concrete pores solutions was investigated. It was found that the Two Donor Band Model, which is based on the presence of two discrete donor bands each with a Gaussian distribution of energy states for an n-type semiconductor, most accurately fits the experimental data. The model supports the experimental results that show an increase in the deep donor density and width of the deep donor band with increasing passivation time; this is interpreted as the thickening of the outer oxide layer in the passive film bilayer structure that adds disorder to the film. A comparison of films formed in different passivating solutions revealed the potential of this model to predict the passive film electronic properties in environments not yet studied experimentally.

Keywords: Mott-Schottky analysis, modeling, passive film, carbon steel rebar, corrosion, chloride concrete.

4.1. Introduction

The corrosion of carbon steel rebar in concrete is among the most pressing issues facing civil engineering infrastructure [1]. Steel rebar corrosion involves the electrochemical breakdown of a thin oxide/oxyhydroxide passive film that covers and protects steel rebar in highly alkaline (pH > 12.5) environments such as those in concrete. Numerous studies have focused on characterizing the formation (i.e., passivation) and destruction (i.e., depassivation) of this passive film and have revealed both electrochemical [2-7] and micro/nanoscale [8-15] information on passivity of carbon steel in concrete. In recent studies it has been shown that the passive films that form on carbon steel in the highly alkaline environments provided by concrete pore solutions consists of a bilayer structure with an inner Fe^{II}-rich oxide layer and an outer Fe^{III}-rich oxide layer [11-13]. The inner layer is much thinner (~2 nm), denser, and more protective for the underlying steel than the thicker (~8-10 nm), more porous and less protective outer Fe^{III}-rich layer. The inner layer forms quickly soon after exposure to the passivating media; however, full passivity is typically reached within approximately 10 days after the stable formation of the outer layer [2, 4, 6, 14].

Although the fundamental electrochemical and multi-scale understanding of passive films that form on carbon steel in concrete has been developing steadily, electronic properties of these films, which have been shown to be a strong indicator of the corrosion behavior, have not been studied extensively. The importance of electronic properties in corrosion behavior have been shown by Schmuki and Böhni [16, 17], Ningshen et al. [18], Shahryari and Omanovic [19], and Hakiki et al. [20, 21], who all demonstrated that the electronic properties indicate the susceptibility of passive

stainless steel to pitting corrosion. Szklarska-Smialowska [22, 23] and Liu et al. [24] found the same results for passive aluminum. For Cu-Ni alloys, Wu et al. [25] showed that an increased Cu concentration in the alloy increases the corrosion rate and changes the electronic signature of the film.

Recent experimental studies [26-29] showed that passive films that form on carbon steel in concrete pore solutions have n-type semiconducting properties. These studies also demonstrated that electronic properties such as space charge capacitance, deep donor density, and flatband potential of the n-type semiconducting carbon steel passive film are all indicative of its protective nature. Although these studies added to the present understanding of the electronic properties, they only determined these properties for a limited number of passivating environments, typically not representative of the complex and variable alkaline environments provided by concrete pore solutions. This variability stems partially from both environmental factors and the wide range of constituents used in concrete mixtures. Past studies [2, 13-15] have found that the properties of passive films vary enormously with the solution composition, pH, and other environmental factors such as temperature [30].

In order to simulate the passive film in a wider range of environments, mathematical models have been used extensively by past authors. These models allow for a quantitative analysis and comparison of passive film properties in a given environment and/or a good estimate of film properties in environments that are more difficult to replicate experimentally. For example, several numerical studies have been performed to describe the formation and breakdown of the passive film for a wide variety of materials and environments [31-33]. Dean and Stimming [34] used models to simulate

and predict the electronic properties of the ZnO system used in the classical work by Dewald [35, 36], as did Myamlin and Pleskov [37] for a gallium arsenide-electrolyte system. Both of these models found that through nonlinear regression analysis, the electronic properties predicted therein were indicative of the structure of the semiconductive films.

The present study investigates the use of models for simulating and predicting the electronic properties of the carbon steel rebar passive films that form in highly alkaline media representing typical concrete pore solutions. First, an overview of five basic models used for simulating passive film electronic properties is provided. All of these models use the basic premise behind Mott-Schottky (M-S) analysis [35, 36, 38] in predicting electronic properties which states that measuring the differential capacitance of an electrochemical system (i.e., passive film) as a function of applied potential can reveal its electronic properties. Experimental data obtained as part of this research was used to compare the predictions of these models. An estimation of model parameters and parametric study are performed for all five models. This investigation lays the groundwork for creating a more comprehensive picture of the passive film structure including its electronic properties.

4.2. Models for Predicting Electronic Properties

4.2.1. Background

Five existing mathematical models [34-37, 39, 40] have been investigated in this paper to describe the carbon steel rebar passive film electronic properties in alkaline media representing concrete pore solutions. Before providing an overview of each of these

models, Mott-Schotty (M-S) analysis [35, 36, 38] will be described briefly since the theory behind this analysis guides each of the five models. M-S analysis, as previously noted, is an electrochemical technique used to derive the electronic properties of passive oxide films. It works by applying an AC potential to a passivated metal immersed in an electrolyte, and then sweeping the potential in either the anodic (positive) or cathodic (negative) directions. This induces a current response in the electrochemical system, from which the apparent capacitance, *C*, of the system can be derived. By knowing the value of *C*, as well as some additional information of the passive film and electrolyte solution, several electronic properties (e.g., the majority charge carrier, dopant density, space charge capacitance, and flatband potential) can be found. The source of the apparent capacitance *C* can be attributed primarily to the existence of two physical features of the oxide-electrolyte interface. The first is the presence of a *space charge layer*, which is a region of charge separation at the edge of the passive oxide film that provides a barrier to charge transfer to/from the electrolyte. The second primary feature is the *Helmholtz layer* which is another region of charge separation, but this time in the electrolyte. Both of these features result in a measured potential drop, $\Delta\varphi$, and a measured capacitance as the potential is swept during M-S analysis. M-S analysis works by using the one-dimensional Poisson's Equation (see Eq. 4.1) to describe the charge distribution at the oxide/electrolyte interface.

$$\frac{d^2\Delta\varphi_{sc}}{dx^2} = \frac{\rho(\Delta\varphi_{sc}, x, \omega)}{\varepsilon\varepsilon_0} \tag{4.1}$$

Here, $\Delta\varphi_{sc}$ (V) is the potential difference between bulk and the surface of the semiconductor (i.e., the passive film), ε is the relative permittivity, ε_0 is the permittivity

of free space (8.85419×10^{-12} F m^{-1}), $\rho(x)$ (C m^{-1}) is the net charge density at point x, and ω (Hz) is the angular frequency. By evaluating $\rho(x)$ for a given potential drop, the capacitance across the space charge layer can be determined. A more thorough explanation of how Eq. 4.1 can used to describe the electronic behavior at the oxide-electrolyte interface can be found in Morrison [41], Dean and Stimming [34], and Myamlin and Pleskov [37].

The models that are investigated in this paper use the theory behind M-S analysis with the following additional assumptions:

(1) The potential drop across the semiconductor/solution interface, $\Delta\varphi$, is the summation of two terms: the potential drop across the Helmholtz layer, $\Delta\varphi_H$, and the potential drop across the space charge layer, $\Delta\varphi_{sc}$ [34]. Similarly, existing models assume the measured capacitance in M-S analysis is a function of two contributors: the Helmholtz capacitance, C_H, and the space charge capacitance, C_{sc}. A series capacitor model is used to describe the semiconductor/solution interface according to Eq. 4.2 [38, 41], which neglects the effect of the adsorption of electrolyte species to the semiconductor surface, as well as any surface states that may be present on the oxide surface [41].

$$\frac{1}{C} = \frac{1}{C_{SC}} + \frac{1}{C_H} \tag{4.2}$$

(2) The measured capacitance is not a function of applied AC frequency. Only the model proposed by D.L. Losee [42] takes the frequency of the AC potential sweep into account when deriving from Eq. 4.1. This issue was addressed in works by Williamson and Isgor [26, 27], Ahn et al. [43] and Sikora et al. [44] by determining a frequency

range in which the measured capacitance is independent of the applied potential. Commonly cited reasons for frequency dependence include the presence of deep donor states, dielectric relaxation phenomena, a non-uniform distribution of donors in the oxide, the amorphous nature of passive films, and contributions from surface states to the capacitance [45].

(3) The dopant density and structure of the space charge layer does not change as a function of the applied potential sweep used in M-S analysis. This issue was raised by Sikora et al. [44] and addressed by sweeping the potential at a rate fast enough to mitigate the effects of changing oxide film structure during the M-S potential sweep [26].

Additional background that is required for providing an overview of the five mathematical models used in this study includes a summary of semiconducting oxide terminology. This terminology helps clarify the parameters used in each of the models; therefore, some background will be provided here. The passive film on steel rebar is a semiconductor [46, 47]; this means that its electronic structure is such that an insulating region exists in the material between the highest occupied (i.e., by an electron) energy level, E_V, and the lowest unoccupied energy level, E_C [48]. This gap between energy levels is called an *energy band gap*, E_g (eV). Depending on the size of the band gap, electrons cannot cross from E_V to E_C without a large influx of energy (usually by thermal or photochemical excitation), which prevents conduction in the material from occurring. However, if there are dopant states located in the band gap, conduction can occur with less energy input. For n-type semiconductors, these dopant states are called donors, and an energy E_{Dj} is associated with each donor j. If an external energy source

is applied to the material (e.g., from a potentiostat), donors can then be ionized, and conduction of electrons in the material occurs. The electrochemical potential of electrons in a semiconducting material is called the Fermi level, E_F, and for an n-type semiconductor, the location of E_F is just below the conduction band edge [41].

4.2.2. Linear Model (Single Discrete Donor State Model) [35, 36]

The first and simplest model investigated in this work and studied early on by Dewald [35, 36] is a linear model. It is derived from Eq. 4.1 using two major assumptions in addition to those listed previously: (1) only one single impurity (i.e., dopant) state exists in the semiconducting oxide (i.e., passive film), and (2) the contribution of the Helmoltz layer to the measured system capacitance is much greater than the space charge layer capacitance. The second assumption renders the second term in the right side of Eq. 4.2 insignificant, which then attributes in the measured system capacitance to changes in the space charge layer capacitance. This second assumption is valid for passive films with low impurity levels.

If these two major assumptions hold, a plot of C_{sc}^{-2} vs. φ should be linear with a slope that is inversely proportional to the dopant density within the space charge layer. The intercept of this linear region with the x-axis is additionally indicative of the flatband potential of the semiconductor. Several authors have used this model to interpret C_{sc}^{-2} vs. φ plots, using a wide range of materials (e.g., zinc oxide crystals [35], iron passive films [38, 47, 49], titanium passive films [50], stainless steel passive films [21, 45, 51], Ni-Cu alloys [25], nickel passive films [52], and tungsten passive films [44]. Beginning with Eq. 4.1, and applying the assumptions listed above, Eq. 4.3 can be derived for the case of an n-type semiconductor [41].

$$C_{sc}^{-2} = \frac{2}{\varepsilon\varepsilon_0 e N_D}\left(\Delta\varphi_{sc} - \frac{kT}{e}\right) \quad (4.3)$$

where *k*, *e*, and *T* are the Boltzmann constant (1.38065x10^{-23} J/K), elementary charge (1.60218x10^{-19} C) and the absolute temperature (K), respectively. N_D is the density of donor states in an n-type semiconducting oxide.

4.2.3. Bilinear Model [37]

This model was developed in response to the appearance of non-linearity in M-S plots (i.e., C_{sc}^{-2} vs. φ plots) due to the presence of multiple impurity states within the semiconductor band gap. This non-linearity renders Eq. 4.3 as invalid and requires that it be derived without making the assumption of a single donor state. This model then takes into account the presence of two donor states located within the semiconductor band gap. The donor located closer to the conduction band edge is called the *shallow donor*, and it is located at an energy level E_{D1} within the band gap. The donor located further from E_C and deeper in the band gap is called the *deep donor*, and it has an energy of E_{D2}. The model states that at potentials below E_{D2} (i.e., $\Delta\varphi_{sc} < (E_F - E_{D2})/e$), only the shallow donor of an n-type semiconductor is ionized. However, above the deep donor ionization potential (i.e., $\Delta\varphi_{sc} > (E_F - E_{D2})/e$), both the shallow and deep donors contribute to the charge in the depletion (i.e., space charge) layer. The slope of the first linear region at the lower potential range is inversely proportional to the shallow donor density, N_{D1}, and the slope of the second linear region at the higher potential range is inversely proportional to summation of shallow and deep donor densities, $N_{D1} + N_{D2}$. The flatband potential is then derived from the intersection of the first linear region with the x-axis. For the case of an n-type semiconductor with two donor species,

Myamlin and Pleskov then predict an M-S plot with a bilinear structure and a critical potential, V_C, that divides the two linear regions. In this model, the authors effectively solved two Poisson equations (see Eq. 4.1), one below the deep donor ionization potential and one above it, and then made the two plots match at V_C. Fig. 4.1 illustrates a conceptual schematic of the M-S plot this model would predict of an n-type semiconductor with two discrete donor species.

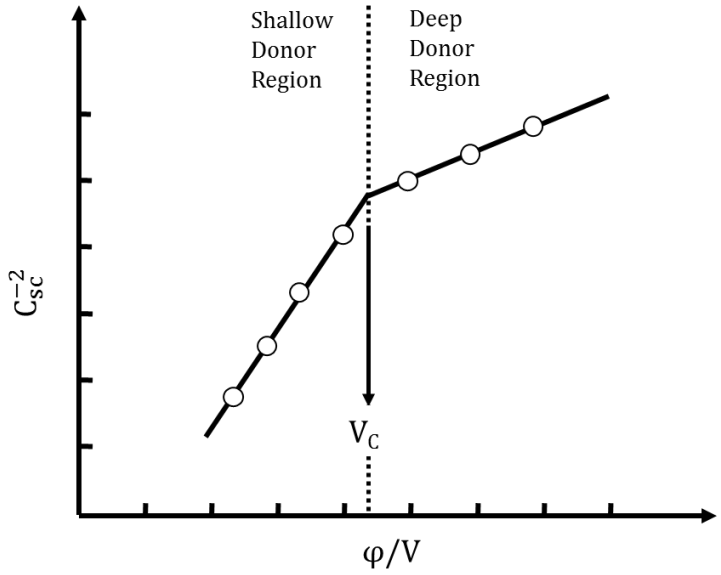

Figure 4.1: Schematic of the nonlinear regression fit using the work done by Myamlin and Pleskov [37] for an n-type semiconductor with two discrete donor states. Within the shallow donor potential region, only shallow donors are ionized. Within the deep donor potential region, both shallow and deep donors are ionized. This is a concept illustration, so numbered axes are not provided.

4.2.4. Two Discrete Donor State Model [34]

Dean and Stimming [34, 39, 53] extended the previous model by Myamlin and Pleskov [37] from a conditional linear solution of Poisson's equation to a nonlinear solution based on Gauss' law for the total charge per unit area in the depletion layer. This approach takes into account the multiple donor species, with the contribution of each

donor species being activated as the Fermi level crosses the energy level of the corresponding species. Eq. 4.4 illustrates the general expression of the depletion layer net charge density for the case of an n-type semiconductor with *M* discrete donor states lying within the band gap. It assumes Fermi-Dirac statistics which describe the distribution of energy states in a system that obeys the Pauli exclusion principle [54].

$$\rho(\Delta\varphi) = e\left\{\sum_{j=1}^{M} N_{Dj}\left[1+\exp\left(\frac{E_F - E_{Dj} - e\Delta\varphi}{kT}\right)\right]^{-1} - N_C \exp\left(\frac{E_F - E_C - e\Delta\varphi}{kT}\right)\right\} \tag{4.4}$$

Eq. 4.4 neglects the contribution of holes to the net charge density, which is valid for n-type semiconductors with a sufficiently wide band gap [34]. The contribution of electrons from the donor states to the total charge density is accounted for in the first term on the right side of Eq. 4.4, and the contribution of electrons in the condcution band is accounted for in the second term. The space charge capacitance in the depletion layer is then found by relating the net charge density to the total charge density per unit area, which yields Eq. 4.5.

$$C_{SC} = \left(\frac{\epsilon\epsilon_0 e}{2}\right)^{1/2} \times \frac{\left\{\sum_{j=1}^{M} N_{Dj}\left[1+\exp\left(\frac{E_F - E_{Dj} - e\Delta\varphi}{kT}\right)\right]^{-1} - N_C \exp\left(\frac{E_F - E_C - e\Delta\varphi}{kT}\right)\right\}}{\left(\int_0^{\Delta V_{SC}}\left\{\sum_{j=1}^{M} N_{Dj}\left[1+\exp\left(\frac{E_F - E_{Dj} - e\Delta\varphi}{kT}\right)\right]^{-1} - N_C \exp\left(\frac{E_F - E_C - e\Delta\varphi}{kT}\right)\right\} d\Delta V\right)^{1/2}} \tag{4.5}$$

This is a continuous function over the entire potential sweep region for M-S analysis. Although the physical model used to derive Eq. 4.5 and the model from Myamlin and

Pleskov [37] are the same, distinct differences remain in the appearance of the M-S plot based on the solution type. The slopes of the two linear regions in each plot are similar, indicating that the application of both models will produce the same shallow and deep donor densities. Additionally, the linear region located at lower potentials crosses the x-axis at the same location in both models, which shows that the same flatband potential is reported in each. However, the dependence of C^{-2} on the applied potential looks markedly different near the deep donor ionization potential. What the model predicted by Eq. 4.5 shows is that the ionization of a deep donor species not only changes the slope of the higher potential range, but also increases the capacitance of the depletion layer as the net charge density increases (see Fig. 4.2). This increase in capacitance would naturally be expected for the excitation of new charge carriers from their donor sites.

Dean and Stimming validated this model for the ZnO system used in the classical work by Dewald [35, 36]. The increase in capacitance described by this model with the ionization of a second donor species was also seen for the case of carbon steel in highly alkaline solutions [28, 29] and in borate/boric acid solutions [55]. Fig. 4.2 illustrates a conceptual schematic of the M-S plot this model would predict of an n-type semiconductor with two discrete donor species.

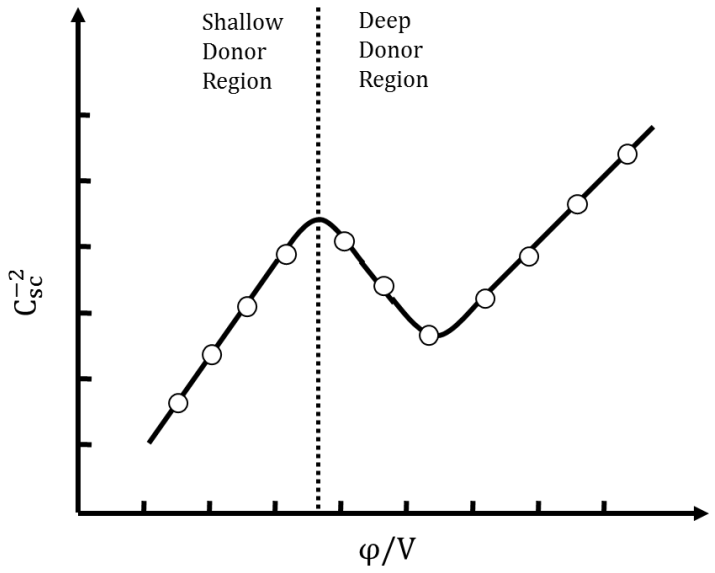

Figure 4.2: Schematic of the nonlinear regression fit using the work done by Dean and Stimming [34] for an n-type semiconductor with two discrete donor states. Within the shallow donor potential region, only shallow donors are ionized. Within the deep donor potential region, both shallow and deep donors are ionized. This is a concept illustration, so numbered axes are not provided.

4.2.5. Two Donor Band Model [34]

The two donor band model assumes that the shallow and deep donor species do not all lie at discrete energy levels E_{D1} and E_{D2}, respectively, as does the model described in the previous section. This model previously described assumes a rather idyllic behavior of the semiconductor crystals, which is not as common in nature as is a distribution of energy states centered on the expected ionization energies of the donor species. This is because impurity atoms (i.e., donors) of a single chemical origin will not all have the exact same bonding structure, resulting in each donor state existing at a slightly different energy that is close to but not exactly at the expected value [41]. In this regard, the two donor band model assumes a Gaussian distribution of energy states for the shallow and deep donors. The shallow and deep donors can then exist at any location in a continuum of energy states called an *impurity band* that is centered on the expected

energy level of each respective donor. This impurity band widens as the number of impurities and general disorder within the semiconductor increases and greater variation of bonding structures is introduced.

Dean and Stimming [34] modified Eq. 4.4 to take into account the reality of a distribution of energy states for donor species. The charge distribution function is then obtained as a function of $\Delta\varphi_{sc}$ by integrating the product of the density of states function for donor j by the complementary Fermi function, yielding Eq. 4.6 where σ_j is a parameter describing the width of the impurity band. C_{sc} is then found in the same manner as in the previous section, which is by relating net charge density to the total charge density per unit area.

$$\rho(\Delta\varphi_{sc}) = e\left\{\frac{1}{\sqrt{2\pi}}\sum_{j=1}^{M}\left[\frac{N_{D_j}}{\sigma_j}\int_{E_v}^{E_c} exp\left(-\frac{1}{2}\left(\frac{E-E_{D_j}}{\sigma_j}\right)^2\right)\left(1 + exp\left(\frac{E_F - E_{D_j} - e\Delta\varphi_{sc}}{kT}\right)\right)^{-1} dE\right] - N_c exp\left(\frac{E_F - E_c - e\Delta\varphi_{sc}}{kT}\right)\right\} \tag{4.6}$$

Fig. 4.3 shows a conceptual schematic of the effect of this Gaussian distribution of states on the measured capacitance as a function of potential, as predicted by this model. The effect of increasing the size of the deep donor impurity band by increasing σ_2 is also illustrated.

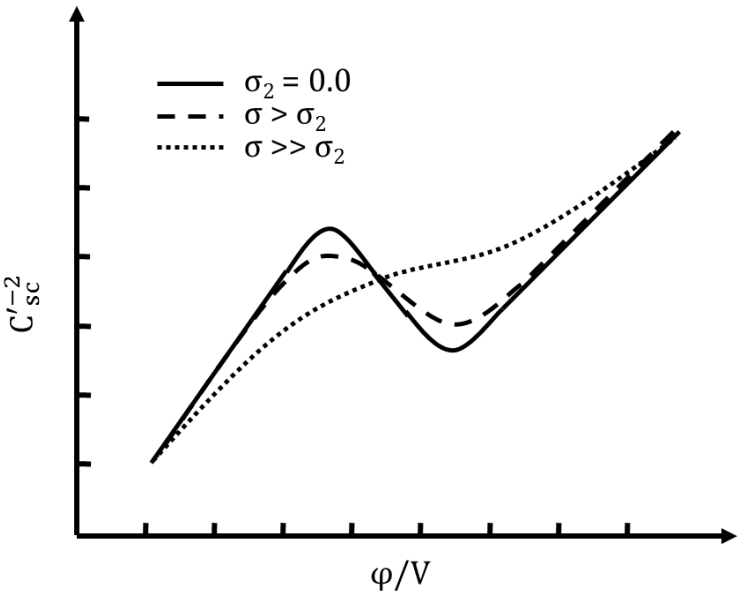

Figure 4.3: Schematic of the nonlinear regression fit using the work done by Dean and Stimming [34] for an n-type semiconductor with two discrete donor states. The effect of the deep impurity band broadening is illustrated for increasing σ_2. This is a concept illustration, so numbered axes are not provided. Modified from Dean and Stimming [34].

4.2.6. Frequency Dependent Model [40, 42]

This model described by D.L. Losee [42] and La Mantia et al. [40] deviates from the models previously outlined in that it is designed to take into account the effects of frequency on the C_{sc}^{-2} vs. φ plots. It models a crystalline semiconductor with two discrete donor species using a modified Poisson's equation (see Eq. 4.7) that takes into account the angular frequency, ω, and the amount of band bending occurring in the depletion layer, $\psi(x)$.

$$\frac{\mathrm{d}^2\Delta\varphi}{\mathrm{d}x^2} = \frac{F(\psi,\omega)}{\varepsilon\varepsilon_0}\,\varphi \tag{4.7}$$

F is the first order coefficient of charge density expansion where $\rho(\psi,\omega,\varphi) \approx F(\psi,\omega)\varphi$. This model then separates the net charge densities of the shallow donor ionization

region (ρ_1) and the deep donor ionization region (ρ_2) into two equations, and then relates these values to the parameter *F* by Eq. 4.8:

$$F(\psi,\omega) = \frac{d\rho_1(\psi)}{d\psi} + \frac{1}{1+i\omega\tau}\frac{d\rho_2(\psi)}{d\psi} \tag{4.8}$$

The value τ is the capture emission time of donor states and is approximated as $\tau_0 \exp\left(-\frac{E_F - E_c - e\psi}{kT}\right)$, where τ_0 is a material dependent constant between 10^{-10} and 10^{-14}. Using a change of variable technique, Eq. 4.7 is transformed into Eq. 4.9, where $W(\psi) = \left(\frac{1}{\varphi}\frac{d\varphi}{d\psi}\right)^{-1}$ is a complex function having the dimension of electric potential, and $H(\psi) = \frac{2}{\varepsilon\varepsilon_0}\int_0^{\psi}\rho(\psi)d\psi$.

$$\frac{dW(\psi)}{d\,\psi} = 1 + \frac{\rho(\psi)}{\varepsilon\varepsilon_0 H(\psi)}W + \frac{F(\psi,\omega)}{\varepsilon\varepsilon_0 H(\psi)}W^2 \tag{4.9}$$

The impedance of the space charge region, Z_{sc}, is then obtained by inputting Eq. 4.9 into Eq. 4.10, where W_S and H_S are the values of *W* and *H* at the semiconductor/solution interface, respectively.

$$Z_{sc} = \frac{W_s}{i\omega\varepsilon\varepsilon_0 {H_s}^{0.5}} \tag{4.10}$$

Finally, the space charge capacitance is found based on $C_{sc} = i\omega Z_{sc}$. The complete details of this derivation are again not mentioned for brevity but can be found in previous works [40, 42].

4.3. Comparison of the Models

4.3.1. Experimental Setup

In order to identify the optimal numerical model for simulating the passive steel rebar system, the models were qualitatively and quantitatively compared using experimental data. The experimental data was gathered from the passive films formed on the cross sections of as-received steel rebar samples. These samples underwent a thorough grinding and polishing process that ensured consistent sample surface finishes. This sample cleaning process included an initial cleaning with acetone to remove machining greases and oils, followed by a rinse with deionized water. The samples were then immersed in an ultrasonic bath of 5% acetic acid solution to remove any air-formed oxide from the surface, and a second rinsing with deionized water was then performed. The samples were next ground with progressively increasing grit sizes and finished with a polish to 0.05 microns using silica polish. This gave the samples a "mirror" finish with no noticeable scratches or blemishes. The samples were lastly rinsed with distilled water, dried with a delicate task wipe, and then immediately placed into a dessicator with silica dessicant gels until use.

Each sample was next loaded into the Princeton Applied Research K0105 sample holder, which is specially designed for performing repeatable, reliable corrosion measurements on multiple samples. These sample holders have hydrophobic Teflon washers that are in direct contact with the sample and provide an excellent seal from the passivating environment. This sample holder assembly prevented any crevice corrosion from occurring on the samples during the course of testing. The exposed sample area of the sample loaded into the holder was 1.15 cm^2.

The samples were then placed in one of three passivating solutions that simulated environments commonly seen in concrete pores. The passive film on all samples was formed under open-circuit conditions (i.e., without the application of an anodic potential) over a period of 10 days, which is the minimum time required to complete the formation of the passive film [2, 6]. In addition to the study of fully passivated samples, the evolution of the electronic properties of the passive films with time was also investigated. M-S analysis was performed on samples at different passivation times (i.e., 0.5 h, 1 h, 2 h, 1 d, and 10 d), which adequately characterized the evolution of that film from initial sample immersion to a fully passivated state.

The three passivating solutions used were a saturated calcium hydroxide solution labeled CH (pH 12.5), and two concrete pore solutions with higher alkalinity labeled CP-1 and CP-2, one without sulfates (pH 13.4) and one with sulfates (pH 13.3). Each solution was prepared by adding analytical grade $Ca(OH)_2$, KOH, NaOH, and/or $CaSO_4 \cdot 2H_2O$ to deionized water. The concentrations of species present in each solution are shown in Table 4.1. During solution preparation and stirring, solution containers were sealed using parafilm to prevent carbonation (which lowers solution pH) and water evaporation. The pH measurements were performed before and after all testing to verify that the solution remained chemically consistent during testing.

Table 4.1: Concentrations of the species in CH, CP-1, and CP-2 passivating solutions.

Solution	Added compounds (M)				pH
	$Ca(OH)_2$	Na(OH)	K(OH)	$Ca(SO)_4 + 2H_2O$	
CH	0.1	0.0	0.0	0.0	12.5
CP-1	0.1	0.1	0.2	0.0	13.4
CP-2	0.1	0.1	0.2	0.003	13.3

The samples were tested in a three-probe electrochemical cell with an Accumet saturated calomel reference electrode (SCE) and a graphite counter electrode. The tip of the reference electrode was placed approximately 5 mm from the surface of the sample. A Gamry Reference 3000 potentiostat and a Gamry Multiplexor were used for taking electrochemical measurements, and Gamry Echem software was used for analyzing capacitance data. All potentials reported in this study are shown versus SCE. In performing M-S analysis to determine the electronic properties experimentally, the parameters used in this study closely followed those recommended by Williamson and Isgor [26]. This included using a 10 mV AC amplitude, which showed Lissajous curves that complied with Kramers-Kronig (K-K) relations for data quality. An applied AC frequency of 1000 Hz was used, which was shown to be the largest frequency that minimized the effect of a changing frequency on the capacitance [26]. Lastly, a potential sweep rate and range of 18 mV/s and -0.5 to 0.5 V were used which were previously found to be a fast enough rate and a short enough range to negate any significant non-linearity in the M-S plots caused by a changing donor density during the M-S the potential sweep [26].

4.3.2. Comparative Model Predictions - Summary

In order to aid in the comparison of the five models outlined in Section 2, each model was labeled according to Table 4.2. Fig. 4.4 illustrates five regression lines based on the models shown in Table 4.2 and fit to the experimental data from a fully passivated sample in CP-1 solution. Although only the sample fully passivated in CP-1 solution is illustrated, the other two solutions provided similar results (see Table 4.3). The non-

dimensionalized form for space charge capacitance, C'_{sc}, is defined in Eq. 4.11 and was used for model comparison.

$$C'_{sc} = \frac{C_{sc}}{\sqrt{\frac{\varepsilon\varepsilon_0 e^2 N_c}{2kT}}} \tag{4.11}$$

Table 4.2: Number assignment for existing models describing the passive film electronic properties.

Model No.	Author(s) and/or Model Description	Ref.
1	Single, Discrete Donor State	[41, 56]
2	Bilinear Model	[37]
3	Two Discrete Donor State Model	[34]
4	Two Donor Band Model	[34]
5	Frequency Dependent Model	[40, 42]

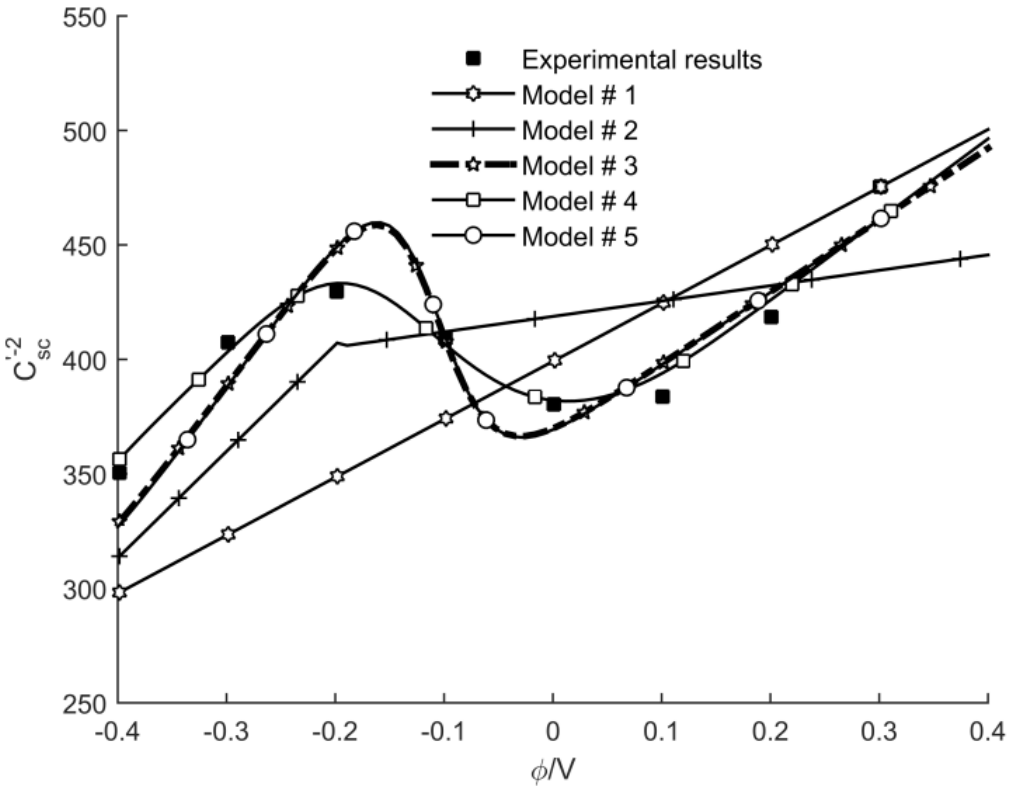

Figure 4.4: Comparison of the five model regression lines based on the models labeled in Table 4.2. These models all describe the same sample that has been fully passivated in CP-1 solution. Model #4 shows the best fit based on qualitative analysis.

For Model #1, the only independent variable affecting the regression analysis is N_{D1}, and so this parameter was varied in fitting the model regression. For Model #2, only three parameters were found to significantly affect the model regression after running a parametric investigation: N_{D1}, N_{D2}, and E_{D2}. These then were optimized in fitting the regression line to experimental data. The boundary between the two linear regions in the regression analysis was assumed to be unknown. For Model #3, the same parameters as those in Model #2 were modified. The parameter selection for nonlinear regression has been performed based on different mathematical presentations. In fact, the formulations in Models #3 to #5 can be assumed symmetric to some model

parameters. For example, the position of E_{D1} relative to E_C does not change as a function of applied potential, and Eq. 4.4 illustrates that in the mathematical model, these terms are actually symmetric. Therefore, these values were held constant for regression analysis at the following values: E_{D1} = -0.1 eV, E_F = -0.1 eV, and E_C = 0.0 eV. These values are consistent with those used by Simoes et al. [51] in evaluating stainless steel, and it is usual for the shallow donor energy level in an n-type semiconductors to position 0.1 or 0.2 eV away from the conduction band edge [41, 48].

For Model #4, which was identified as the optimal numerical model, E_{D1}, E_F, and E_C were again held constant, using the same values as those used in Model #3. The valence band edge, E_V, was held constant as an integral limit in Eq. 4.6. Parameters changed in the regression analysis included the width of the shallow donor band, σ_1, and the deep donor band, σ_2, in addition to N_{D1}, N_{D2}, and E_{D2}. Section 4.4 goes into greater detail in explaining the parametric study applied to the experimental data, specifically for Model #4.

For Model #5, Runge-Kutta method was used in evaluating the model parameters in the nonlinear regression analysis. Here, the numerical solution of the governing ordinary differential equations are fitted to the experimental data. In fact, the iterative least square procedure is constructed based on the differential equation solution. A frequency of 1000 Hz, which was used in obtaining the original experimental data, was input into regression analysis.

The first step for assessing how different models fit the experimental data is a qualitative comparison. Based on this qualitative comparison, it is clear that the

regression lines from Model #4 provide the best fit to experimental data. Models #3 and #5 show a slightly less accurate data approximation, while Models #1 and 2 show significant deviation from the experimental data. While it should not be used alone, the coefficient of determination, r^2, which is based on residual and total norms, can help develop a quantitative comparison of the models. Unlike the approach used for linear regression models, however, the best fitted nonlinear regression model cannot be chosen solely based on the coefficient of determination (r^2). Ideally, a variety of different qualitative and quantitative procedures for finding the best model should be used; these measures include confidence intervals, F-test, alike information criterion (AIC) and Bayesian information criterion (BIC). The investigated models in this study are nested, which means that all are obtained from the same equation solution (i.e., Poisson's equation) with different levels of approximations. Consequently, any of the abovementioned methods can help evaluate the best nonlinear model in conjunction with the coefficient of determination, r^2.

Table 4.3 provides a quantitative comparison of the five models by evaluating the coefficient of determination (r^2) values for each. This is an exhaustive comparison, showing the r^2 values for all three passivating solutions and at all five passivation times. These quantitative results again show that Model #4 provides the best fit to experimental data, regardless of passivating solution. The average r^2 value for all five passivation times in CH, CP-1, and CP-2 solutions for Model #4 were 0.97, 0.96, and 0.97, respectively. Model #3 and #5 showed the second and third best r^2 values, respectively, and Model #1 showed the least accurate regression fit. This indicates that a distribution of energy states around the shallow and deep donor levels (which is

consistent with Model #4), rather than a single shallow and a single deep energy state, best describes the passive steel rebar system. Further comparison of Models #3 and #5 using an F-test analysis revealed, as shown in Table 4.4, that Model #4 performs significantly better than Model #3 because of small p-values. The cases with bigger p-values show that considering the effects of normal distributions for energy levels has had little help on the model performance. In the following section Model #4, the Two Donor Band Model, will be investigated in further detail.

Table 4.3: Comparison of r^2 values for five model regression lines for different passivation times and passivating solutions.

		r^2				
Solution	Passivation time	*M-1*	*M-2*	*M-3*	*M-4*	*M-5*
CH	0.5 h	0.87	0.86	0.98	0.95	0.87
	1 h	0.86	0.89	0.98	0.99	0.98
	2 h	0.80	0.88	0.96	0.99	0.96
	1 d	0.27	0.74	0.87	0.96	0.85
	10 d	0.12	0.81	0.89	0.99	0.90
CP-1	0.5 h	0.91	0.90	0.99	0.93	0.91
	1 h	0.87	0.89	0.96	0.98	0.95
	2 h	0.82	0.84	0.95	0.98	0.95
	1 d	0.56	0.65	0.92	0.95	0.92
	10 d	0.28	0.67	0.94	0.98	0.93
CP-2	0.5 h	0.92	0.91	0.99	0.94	0.92
	1 h	0.87	0.89	0.97	0.99	0.96
	2 h	0.82	0.85	0.97	0.99	0.97
	1 d	0.54	0.62	0.92	0.95	0.92
	10 d	0.21	0.77	0.94	0.99	0.94

Table 4.4: F-statistics and p-values for Model #3 and Model #4 comparisons for different passivation times and passivating solutions.

Solution	Passivation time	*F*-statistics	*p*-values
CH	0.5 h	3.8	0.15
	1 h	4.7	0.08
	2 h	7.0	0.04
	1 d	7.7	0.03
	10 d	25.1	0.004
CP-1	0.5 h	9.5	0.02
	1 h	2.9	0.16
	2 h	2.0	0.26
	1 d	1.2	0.45
	10 d	4.4	0.09
CP-2	0.5 h	7.6	0.04
	1 h	3.5	0.12
	2 h	2.9	0.16
	1 d	1.5	0.36
	10 d	20.3	0.006

4.4. Detailed Investigation of Two Donor Band Model

4.4.1. Estimation of Parameters

After optimizing all five models to experimental data using nonlinear regression analysis, the independent model parameters that produced the best fitting regression lines were identified. This was performed on a number of carbon steel rebar samples for all five passivation times (i.e., 0.5 h, 1 h, 2 h, 1 d, and 10 d) and in all three passivating solutions (i.e., CH, CP-1, and CP-2). The detailed results of this investigation are too exhaustive to include in this study, therefore comprehensive treatment will only be provided for Model #4, which was selected as the model that best represents the behavior of passive carbon steel.

A least square nonlinear regression method was applied in fitting Model #4 to experimental data. The parameters held constant in this investigation, as alluded to in the previous section, were C_H, N_C, E_C, E_V, E_F, and E_{D1}. These parameters were held constant in the regression analysis for two reasons: 1) either they were symmetrically presented in the mathematical formulations as explained previously, or 2) their values are well-known and established for passive carbon steel rebar. For example, the position of the lower edge of the conduction band for n-type semiconductors is typically around 0.1 eV noble (positive) to the Fermi level position [41, 51]. The valence band edge and shallow donor energy level likewise vary linearly with the applied potential (except at the semiconductor/solution interface). The position of the shallow donor energy level can be assumed to lie just below (i.e., about 0.1 eV) the conduction band edge under flatband conditions based on the known properties of n-type semiconductors [41] and the experimental results of iron-based alloys showing complete shallow donor ionization at room temperature [26, 27, 34, 51, 56]. The position of the top edge of the valence band, E_V, is more difficult to determine. It is typically found by adding the band gap energy, E_g, to the position of the conduction band edge [41]. Simoes et al. [51] indicate E_V is located 2.7 eV below E_C for the case of stainless steel, but the band gap for stainless steel cannot be assumed equivalent to that of carbon steel. Xu and Schoonen [57] indicated that the band gap for $Fe^{II}O$ and Fe_3O_4 is 2.40 eV and 0.10 eV, respectively, where $Fe^{II}O$ and Fe_3O_4 are two oxides commonly found in the passive film of carbon steel [13]. This is a significant difference, and so the position of E_V was chosen to lie somewhere between these two oxide band gaps [27]. The parametric study of E_V in the next section, however, indicates

that the effect of this parameter on the model regressions is negligible for all reasonable values of E_V. The density of states in the lower edge of the conduction band, N_C, was set at $4*10^{28}$ m^{-3}, which is a value commonly used for iron-based alloys [51]. Lastly, the value of C_H used for numerical analysis was 22 μF cm^2, which was found in the studies done by Williamson and Isgor [26, 27] for passive steel rebar in simulated concrete pore solutions. A complete list of the constant parameters used in this investigation are shown in Table 4.5.

Table 4.5: List of the constant parameters used in the numerical regression analysis of Model #4.

Parameter	Value
ε	12
A [m^2]	$1.15x10^{-4}$
T [K]	296
N_c [m^{-3}]	$1.0x10^{28}$
C_H [F]	$2.2x10^{-5}$
E_C [eV]	0.0
E_{D1} [eV]	-0.1
E_V [eV]	-0.7
E_F (at V_{fb}) [eV]	-0.1

This left five independent parameters that either significantly affected the results of the nonlinear regression analysis, or whose values were unknown. Table 4.6 shows the values of these parameters after performing the regression analysis and using Model #4. The values for all steel rebar samples tested, at each passivation time, and in each solution are included. The values for N_{D1} and N_{D2} were non-dimensionalized, following the precedent set by Dean and Stimming [34].

Table 4.6: Model #4 estimated parameters using a least square nonlinear regression for different solutions at different passivation times.

Solution	Passivation time	Sample No.	N_{D1}/N_C	N_{D2}/N_C	E_{D2} (eV)	σ_1	σ_2
CH	0.5 h	1	0.1698	-0.0712	-0.6361	0.3868	0.1739
		2	0.3698	-0.5000	-0.8672	1.0000	0.1234
		3	0.4390	-0.5000	-0.9293	1.0000	0.2012
	1 h	1	0.0237	00204	-0.4650	0.1463	0.0909
		2	0.0589	0.0129	-0.3927	0.3691	0.0112
		3	0.0204	0.0273	-0.3912	0.1584	0.1200
	2 h	1	0.0124	0.0290	-0.4448	0.0206	0.1420
		2	0.0232	0.0309	-0.4149	0.0197	0.1065
		3	0.0457	0.0160	-0.4956	0.2219	0.0131
	1 d	1	0.0250	0.0338	-0.5181	0.1174	0.0976
		2	0.0637	0.2334	-1.0000	0.4275	0.2128
		3	0.0526	0.0257	-0.4987	0.2771	0.0833
	10 d	1	0.0145	0.1909	-0.9412	0.0218	0.3540
		2	0.0381	0.1036	-0.7741	0.0759	0.2251
CP-1	0.5 h	1	0.0232	0.0852	-0.5238	0.2814	0.1112
		2	0.1988	0.0675	-0.5552	0.2907	0.1021
	1 h	1	0.0171	0.0411	-0.3648	0.1505	0.0814
		2	0.0201	0.0302	-0.3870	0.1595	0.0840
	2 h	1	0.0194	0.0431	-0.3927	0.1695	0.0971
		2	0.0255	0.0288	-0.4162	0.1819	0.0871
	1 d	1	0.0588	0.0387	-0.4700	0.1954	0.0534
		2	0.0526	0.0366	-0.4725	0.2100	0.0568
	10 d	1	0.0705	0.0531	-0.5236	0.1518	0.0614
		2	0.0629	0.0650	-0.5327	0.1431	0.0819
CP-2	0.5 h	1	0.0170	0.0546	-0.5356	0.3043	0.1174
		2	0.2328	-0.2746	-0.6216	0.1875	0.6929
	1 h	1	0.0221	0.0289	-0.3966	0.1702	0.0928
		2	0.0194	0.0383	-0.3814	0.1652	0.0977
	2 h	1	0.0275	0.0272	-0.4306	0.1936	0.0949
		2	0.0513	0.0219	-0.4654	0.1955	0.0592
	1 d	1	0.0509	0.0313	-0.4813	0.2304	0.0601
		2	0.0548	0.0446	-0.4539	0.1951	0.0535
	10 d	1	0.0441	0.0522	-0.5592	0.1147	0.1096
		2	0.0491	0.0743	-0.5666	0.0804	0.1226

The shallow donor density decreases immediately after the M-S potential sweep at 0.5 h. This is indicative that the inner Fe^{II}-rich layer is not fully formed, since a higher donor density is still present in the film. Once this inner Fe^{II}-rich layer is fully formed,

the shallow donor density is much lower as the film is now a much more coherent, dense structure. The shallow donor density then remains relatively constant over the course of passivation for all three solutions, since it is fully formed and all additional passive film is on top of this inner layer.

The deep donor density increases with increasing passivation time for all three solutions. This is expected, since it known that after the inner Fe^{II}-rich layer forms soon after initial sample immersion, an outer, thicker Fe^{III}-rich layer forms on top of this. This Fe^{III}-rich layer is known to be a very porous, disordered structure, which corresponds well with the increase in deep donor density as greater disorder is added to the passive film as a whole. Additionally, the passive film in CH solution shows a higher deep donor density than the other two passivating solutions. This corresponds well to the known passive film structure of samples in CH versus CP-1 or CP-2. Samples in CH is known to have a thicker, yet more porous and incoherent passive film compared to these other two solutions, which corresponds to the higher deep donor density.

The deep donor energy level for all three solutions remains relatively constant during the course of passivation, which should be expected as the donor species (i.e., Fe^{II} ions occupying tetrahedral and octahedral sites) are not changing their chemical origin during the passivation process. The values of σ_2 generally seem to follow the pattern of the deep donor density in that after the initial M-S potential sweep, they tend to increase steadily with increasing passivation time for all three solutions. This corresponds again to the increasing number of impurities and general disorder of the passive film as it continues to add on to the porous Fe^{III}-rich outer layer. However, the difference

between samples in CH passivating solution versus those in CP-1 or CP-2 are much more noticeable here. Samples in CH clearly exhibit a significantly larger deep donor impurity band compared to the other two solutions, and this is an obvious indicator of the higher level of disorder in passive films formed in CH instead of at higher pH levels.

These results then provide further clarification and confirmation of the present understanding of the steel rebar passive film structure [13, 14, 27]. They show that the inner Fe^{II}-rich layer forms soon after initial sample immersion in the passivating solution, and that the shallow donors are indicative of its formation process. Secondly, they show that as the outer Fe^{III}-rich layer builds on top of the inner layer, it also adds disorder and incoherency to the passive film as a whole, and this is indicated by both the deep donor density and the width of the deep donor impurity band. Finally, the inferior protective nature of passive films formed in CH versus at higher pH levels is clearly shown by the higher deep donor levels and thicker deep donor impurity band. The electronic properties shown from this analysis are then clear indicators of the passive film structure and differences between passive films in varying environments.

Fig. 4.5 illustrates graphically the results of the regression model fitting, specifically for the case of CP-1 passivating solution. The other two passivating solutions showed similar results to those shown in Fig. 4.5, but were omitted for brevity. These plots indicate that Model #4 closely follows and can accurately predict the electronic signature of passive steel rebar.

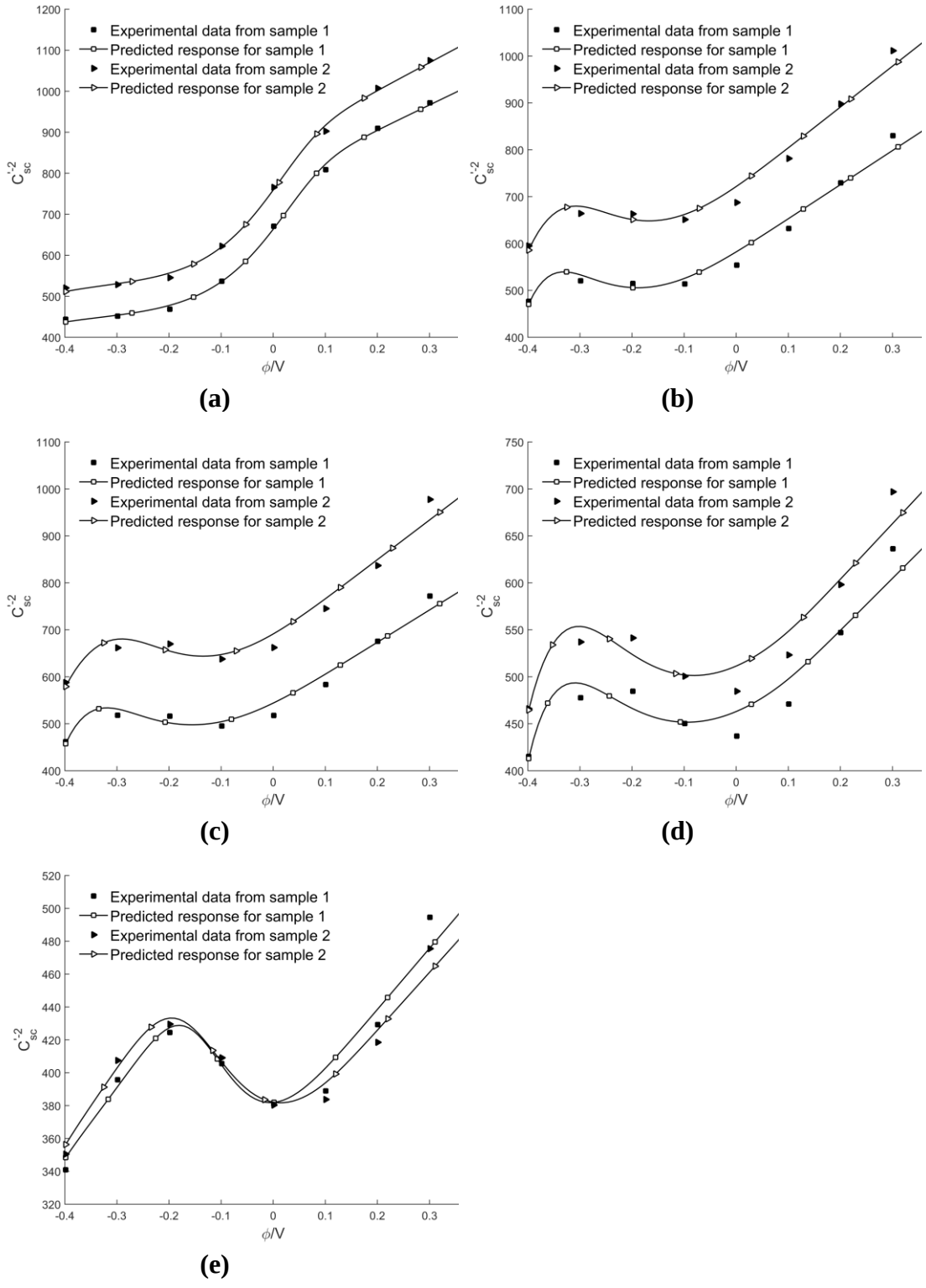

Figure 4.5: Nonlinear regression lines of samples passivated in CP-1 solution at varying passivation times: a) 0.5 h, b) 1 h, c) 2 h, d) 1 d, and e) 10 d.

Before moving into a parametric investigation of the five models, one additional observation of the comparison between the three passivating solutions should be noted. The numerical analysis performed specifically for the case of Model #4 shows an interesting contrast between the regression models for CH, CP-1, and CP-2 solution. This is revealing when attempting to predict environments other than those of the three passivating solutions investigated. Fig. 4.6 shows the regression models for fully passivated samples using Model #4. The electronic signatures are virtually identical between the passive film in CP-1 and CP-2 solution, which is consistent with the experimental results from Williamson and Isgor [27]. What is also evident, however, is that the regression line for the passive film in CH has a significantly lower capacitance compared that from CP-1 or CP-2. What this reveals is that lower pH, less passivating environments seem to produce less capacitive passive films. Another observation is that the C_{sc}^{-2} vs. φ plot for the passive film in CH crosses the x-axis at a much more negative potential. This means that the flatband potential is correspondingly lower (as long as the slopes of the curves remain comparable), where the flatband potential is one of the major electronic properties produced from Mott-Schottky analysis. Therefore, numerical models that show a decreased space charge capacitance and a more negative intersection with the x-axis are good indicators of a passive film in a lower pH, less passivating environment. Conversely, a higher space charge capacitance and more positive intersection with the x-axis are good indicators of a high pH, strongly passivating solution. This is extremely helpful when attempting to predict the passive film behavior in environments not yet investigated in experimental studies.

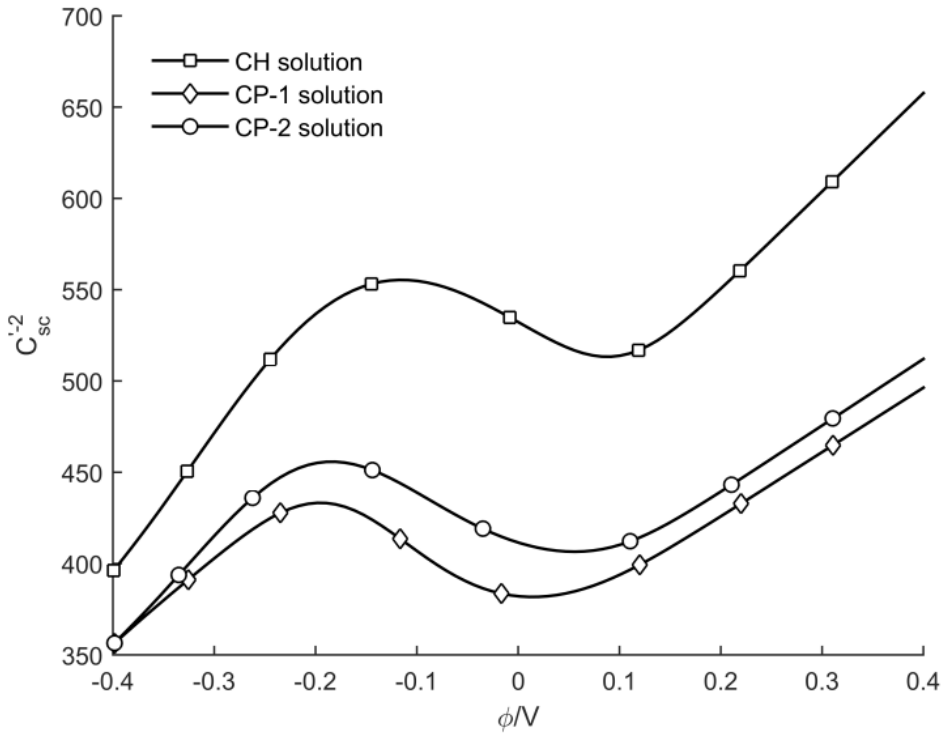

Figure 4.6: Dependence of the nonlinear regression lines for Model #4 on the passivating solution. pH level and solution composition appear to have a significant effect on the observed model regressions.

4.4.2. Parametric Study

A parametric study was performed on the main parameters used in Model #4, and the results for the case of CP-1 passivating solution are shown in Fig. 4.7. Parametric investigations were also performed for Models #1-3 and #5, but these were omitted for brevity. Additionally, the parametric investigations for Model #4 in CH and CP-2 solutions showed a similar trend but were not included in the present work.

In Fig. 4.7, Model #4 was first fit to experimental data, giving a baseline estimation of parameter values. These best-fit values were then held constant, and individual parameters were adjusted to show the model sensitivity to individual parameters. These values were adjusted by either increasing or decreasing them by 25% and 50%.

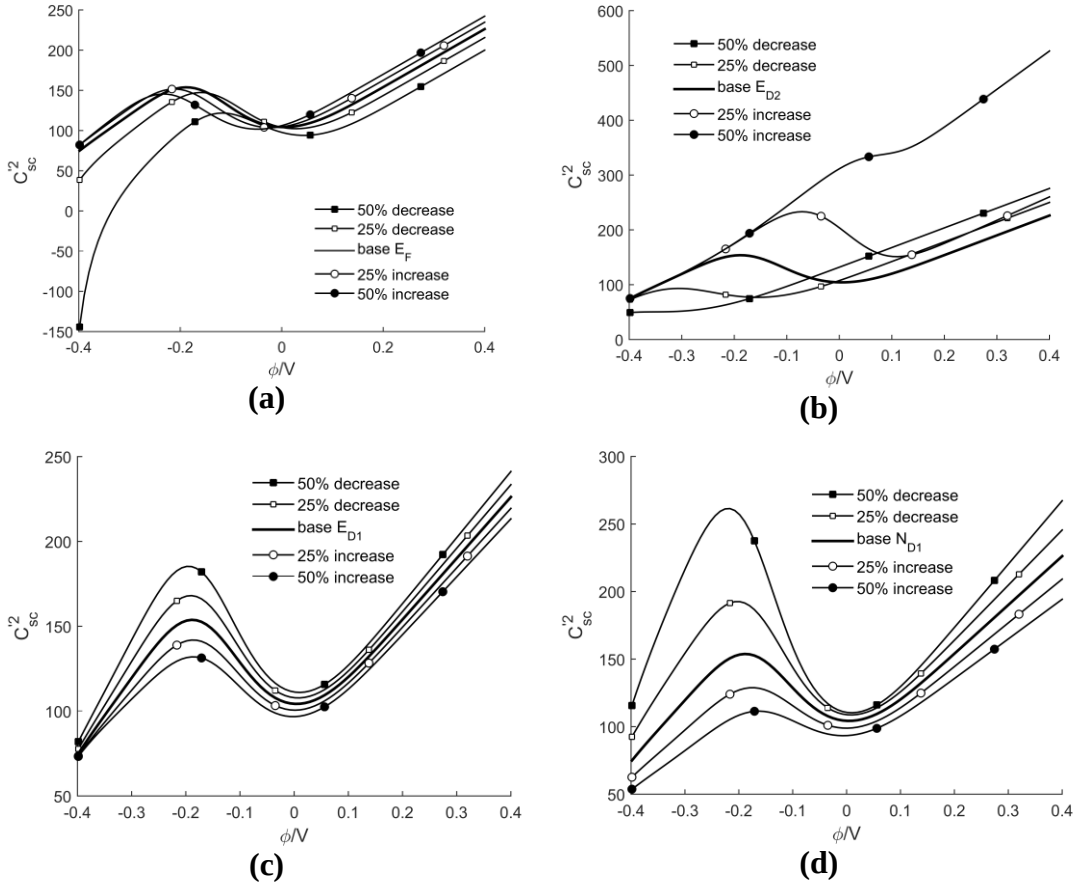

Figure 4.7: Model #4 response to 25% and 50% increase and decrease in the model parameters a) E_F, b) E_{D2}, c) E_{D1}, and d) N_{D1}. Models were fit to fully passivated steel rebar samples in CP-1 solution.

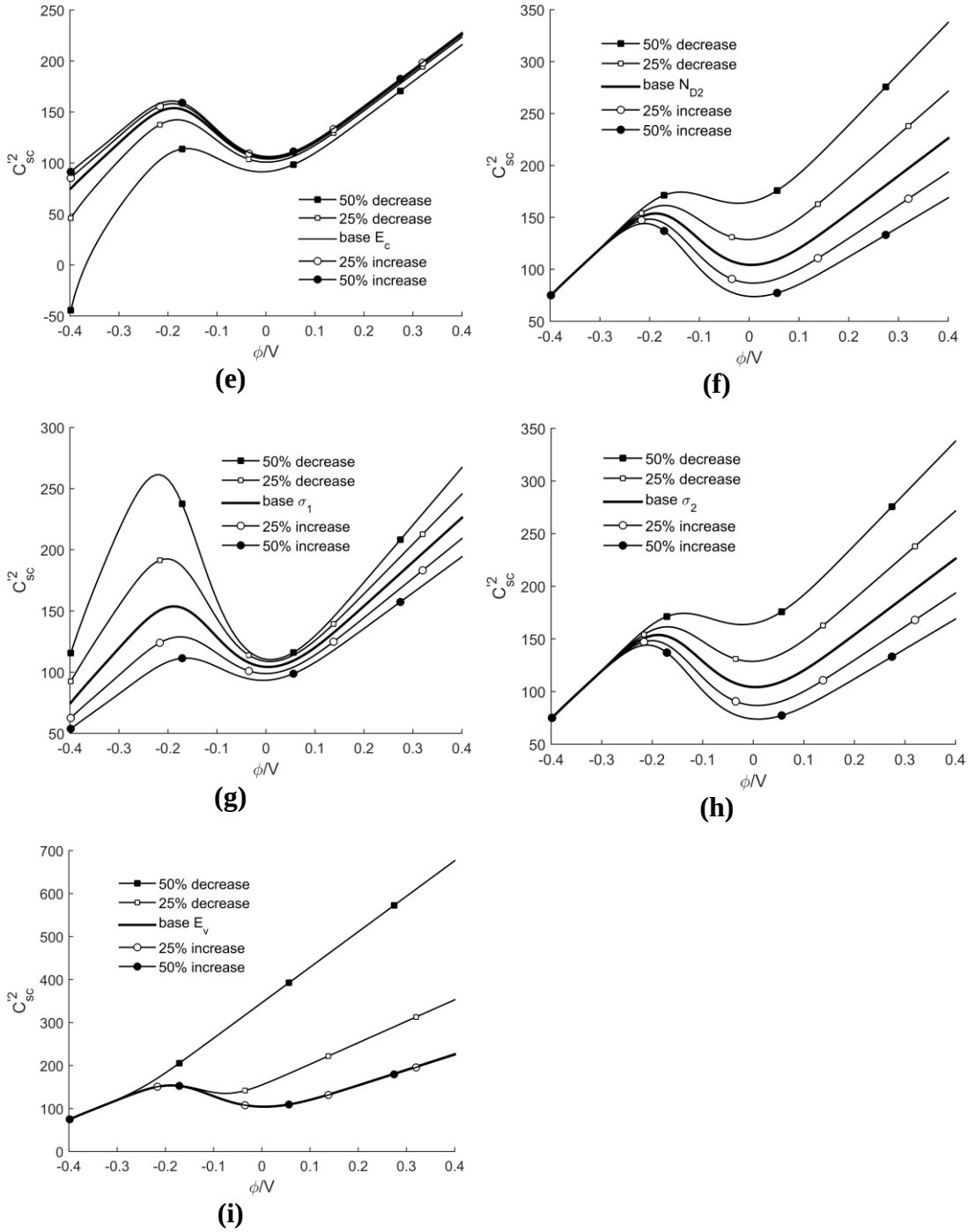

Figure 4.7 (continued): Model #4 response to 25% and 50% increase and decrease in the model parameters e) E_C, f) N_{D2}, g) σ_1, h) σ_2, and i) E_V. Models were fit to fully passivated steel rebar samples in CP-1 solution.

The results in Fig. 4.7 show that the sensitivity of parameters E_F, E_{D1}, E_C, and E_V are generally not as significant in a large potential range as those for E_{D2}, N_{D1}, N_{D2}, σ_1, and σ_2. In Fig. 4.7a, the parameter E_F only effects the regression plot at extremely cathodic (i.e., negative) potentials, which is expected as the Fermi level begins to approach the conduction band and the semiconductor begins to effectively degenerate and exhibit more metallic-like behavior [41]. The same was true for the sensitivity of E_C in Figure 4.7e. The effect of E_C does not become evident until highly cathodic potentials, at which point the position of E_C is drawing near to the Fermi level under flatband conditions.

One of the more interesting plots is Figure 4.7b, which shows the sensitivity of the deep donor energy level to the model regression. Interestingly, a 50% increase and a 50% decrease both show similar effects to the model regression in that they nearly eliminate the local maximum and minimum found in the plot for the base value of E_{D2}. What this means physically is that a strong decrease in E_{D2} places it very near to E_{D1}, so that most of the deep donors are ionized closer to flatband conditions. As E_{D2} is increased significantly, the effect of deep donors becomes almost non-existent for the potential range between -0.5 to 0.5 V vs. SCE. This would then require extremely anodic potentials to fully ionize the deep donor states. An additional observation in Figure 4.7b is that the shallower slope of the 50% decrease regression line compared to the 50% increase line is consistent with the known behavior of Mott-Schottky plots. M-S plots traditionally show that a decrease in the slope of the C_{sc}^{-2} vs. φ curve indicates an increase in the donor density. With a lower deep donor energy level, the charge carriers

therein are more easily excited, and the donor density in the depletion layer likewise increases.

Fig. 4.7f shows the effect of the deep donor density is only significant at higher potential regions. This is consistent with the fact that deep donor ionization does not occur until around -0.1 V vs. SCE, which is near the local maxima in Fig. 4.7f. Fig. 4.7e likewise shows that the effect of shallow donors is most apparent at low potentials, where only shallow donors are oxidized. These shallow donors still effect the higher potential regions since they are ionized throughout the potential sweep range, but their effect on the regression is reduced by the introduction of deep donors. Interestingly, the effect of changing the deep donor density in Figure 4.7f was nearly identical to the effect of changing the width of the deep donor band in Figure 4.7h. This observation is consistent with the findings in previous studies [27, 34] which proposed that increasing the distribution of energy states in the deep donor impurity band has a similar effect on M-S plots as would increasing the deep donor density. The same behavior was found to be true in Figure 4.7d and 4.7g for the parameters N_{D1} and σ_1, respectively.

Figure 4.7i shows that the parameter E_V only effects the regression model when it is at extremely small values. However, values smaller than the base E_V values of -0.7 eV would mean that the band gap of the passive film becomes extremely small and approaches displaying metallic behavior. This though is not consistent with the known properties of iron-based passive films which show semiconductive – not metallic – behavior [46, 47]. Therefore, changes in the position of the valence band do not significantly affect regression models for reasonable values of E_V.

4.5. Conclusions

Five existing numerical models that are used to simulate and predict the electronic properties of passive oxide films were investigated and compared. These models were fit to existing experimental data for carbon steel rebar passivated in three simulated concrete pore solutions (i.e., CH, CP-1, and CP-2) and at five different passivation times (i.e., 0.5 h, 1 h, 2 h, 1 d, and 10 d). A nonlinear regression method was used to fit the five numerical models to experimental data. Both the qualitative and quantitative results indicated that Model #4, proposed by Dean and Stimming [34], best fit the experimental data. This model is based on the assumptions that two donor states which exist in an n-type semiconducting oxide form a continuum of energy states based on a Gaussian distribution, which is consistent with the known physical nature of iron-based passive films. An estimation of model parameters helped to clarify and confirm the present understanding of the passive film electronic structure. For example, the widening of the deep donor impurity band with increasing passivation time revealed that the passive film was adding to the known outer Fe^{III}-rich oxide layer which is more porous and disordered in nature. The deep donor impurity band was also significantly wider for the passive film formed in CH solution versus in the other two passivating solutions, which is consistent with the diminished protective nature of films formed in lower pH solutions. Additionally, a qualitative comparison of the model regression lines for differing solution compositions and pH levels revealed the potential of this numerical model to predict the passive film electronic behavior in environments other than those previously studied.

4.6. References

[1] M. Yunovich, N.G. Thompson, T. Balvanyon, L. Lave.
[2] P. Ghods, O.B. Isgor, G. McRae, T. Miller, Cement and Concrete Composites, 31 (2009) 2-11.
[3] L. Li, A.A. Sagues, Corrosion, 58 (2002) 305-316.
[4] C.M. Hansson, A. Poursaee, A. Laurent, Cement Concrete Res, 36 (2006) 2098-2102.
[5] U.M. Angst, B. Elsener, C.K. Larsen, O. Vennesland, Corros Sci, 53 (2011) 1451-1464.
[6] P. Ghods, O.B. Isgor, G.A. McRae, G.P. Gu, Corrosion Science, 52 (2010) 1649-1659.
[7] P. Ghods, O.B. Isgor, G.A. McRae, J. Li, G.P. Gu, Corrosion Science, 53 (2011) 946-954.
[8] S. Joiret, M. Keddam, X. Nóvoa, M. Pérez, C. Rangel, H. Takenouti, Cement and Concrete Composites, 24 (2002) 7-15.
[9] C. Gabrielli, S. Joiret, M. Keddam, H. Perrot, N. Portail, P. Rousseau, V. Vivier, Journal of the Electrochemical Society, 153 (2006) B68-B74.
[10] C. Gabrielli, S. Joiret, M. Keddam, H. Perrot, N. Portail, P. Rousseau, V. Vivier, Electrochimica Acta, 52 (2007) 7706-7714.
[11] P. Ghods, O. Burkan Isgor, F. Bensebaa, D. Kingston, Corrosion Science, 58 (2012) 159-167.
[12] P. Ghods, O.B. Isgor, J.R. Brown, F. Bensebaa, D. Kingston, Applied Surface Science, 257 (2011) 4669-4677.
[13] H.B. Gunay, P. Ghods, O.B. Isgor, G.J.C. Carpenter, X. Wu, Applied Surface Science, 274 (2013) 195-202.
[14] H.B. Gunay, B. Isgor, P. Ghods, Corrosion, (2014).
[15] P. Ghods, O.B. Isgor, G.J.C. Carpenter, J. Li, G.A. McRae, G.P. Gu, Cement and Concrete Research, 47 (2013) 55-68.
[16] P. Schmuki, H. Bohni, Werkstoffe und Korrosion, 42 (1991) 203-207.
[17] P. Schmuki, H. Böhni, Journal of the Electrochemical Society, 139 (1992) 1908-1913.
[18] S. Ningshen, U. Kamachi Mudali, V. Mittal, H. Khatak, Corrosion science, 49 (2007) 481-496.
[19] A. Shahryari, S. Omanovic, Electrochemistry Communications, 9 (2007) 76-82.
[20] N. Hakiki, M.D.C. Belo, A. Simoes, M. Ferreira, Journal of the Electrochemical society, 145 (1998) 3821-3829.
[21] N. Hakiki, S. Boudin, B. Rondot, M. Da Cunha Belo, Corrosion Science, 37 (1995) 1809-1822.
[22] Z. Szklarska-Smialowska, Corrosion Science, 41 (1999) 1743-1767.
[23] Z. Szklarska-Smialowska, Corrosion Science, 44 (2002) 1143-1149.
[24] Y. Liu, G.Z. Meng, Y.F. Cheng, Electrochimica Acta, 54 (2009) 4155-4163.
[25] H. Wu, Y. Wang, Q. Zhong, M. Sheng, H. Du, Z. Li, Journal of Electroanalytical Chemistry, 663 (2011) 59-66.
[26] J. Williamson, O.B. Isgor, Applied Surface Science, (2015) submitted for publication.

[27] J. Williamson, O.B. Isgor, Corrosion Science, (2015) submitted for publication.
[28] M. Sánchez, J. Gregori, C. Alonso, J.J. García-Jareño, H. Takenouti, F. Vicente, Electrochimica Acta, 52 (2007) 7634-7641.
[29] M. Sánchez, J. Gregori, M.C. Alonso, J.J. García-Jareño, F. Vicente, Electrochimica Acta, 52 (2006) 47-53.
[30] D.G. Li, Y.R. Feng, Z.Q. Bai, J.W. Zhu, M.S. Zheng, Electrochimica Acta, 52 (2007) 7877-7884.
[31] T.E. Pou, O.J. Murphy, V. Young, J.O.M. Bockris, L.L. Tongson, Journal of the Electrochemical Society, 131 (1984) 1243-1251.
[32] N. Cabrera, N. Mott, Reports on progress in physics, 12 (1949) 163.
[33] J. Kruger, International materials reviews, 33 (1988) 113-130.
[34] M.H. Dean, U. Stimming, Journal of electroanalytical chemistry and interfacial electrochemistry, 228 (1987) 135-151.
[35] J. Dewald, Bell System Technical Journal, 39 (1960) 615-639.
[36] J. Dewald, Journal of Physics and Chemistry of Solids, 14 (1960) 155-161.
[37] V.A. Myamlin, Y.V. Pleskov, Electrochemistry of semiconductors, Plenum Press, New York, 1967.
[38] U. Stimming, J. Schultze, Berichte der Bunsengesellschaft für physikalische Chemie, 80 (1976) 1297-1302.
[39] M.H. Dean, U. Stimming, Corrosion Science, 29 (1989) 199-211.
[40] F. La Mantia, H. Habazaki, M. Santamaria, F. Di Quarto, Russian Journal of Electrochemistry, 46 (2010) 1306-1322.
[41] S.R. Morrison, Electrochemistry at semiconductor and oxidized metal electrodes, 1980.
[42] D.L. Losee, Journal of Applied Physics, 46 (1975) 2204-2214.
[43] S.J. Ahn, H.S. Kwon, Electrochimica Acta, 49 (2004) 3347-3353.
[44] J. Sikora, E. Sikora, D.D. Macdonald, Electrochimica acta, 45 (2000) 1875-1883.
[45] A. Di Paola, Electrochimica Acta, 34 (1989) 203-210.
[46] M. Büchler, P. Schmuki, H. Böhni, T. Stenberg, T. Mäntylä, Journal of the Electrochemical Society, 145 (1998) 378-385.
[47] U. Stimming, J. Schultze, Electrochimica Acta, 24 (1979) 859-869.
[48] A.W. Bott, Current Separations, 17 (1998) 87-92.
[49] K. Azumi, T. Ohtsuka, N. Sato, Journal of The Electrochemical Society, 134 (1987) 1352-1357.
[50] J. Schultze, U. Stimming, J. Weise, Berichte der Bunsengesellschaft für physikalische Chemie, 86 (1982) 276-282.
[51] A. Simoes, M. Ferreira, B. Rondot, M. da Cunha Belo, Journal of the Electrochemical Society, 137 (1990) 82-87.
[52] E. Sikora, D.D. Macdonald, Electrochimica Acta, 48 (2002) 69-77.
[53] M.H. Dean, U. Stimming, The Journal of Physical Chemistry, 93 (1989) 8053-8059.
[54] D.M. Smyth, The Defect Chemistry of Metal Oxides, Oxford University Press, 2000.
[55] L. Hamadou, A. Kadri, N. Benbrahim, Applied Surface Science, 252 (2005) 1510-1519.
[56] Y. Cheng, J. Luo, Electrochimica acta, 44 (1999) 2947-2957.

[57] Y. Xu, M.A. Schoonen, American Mineralogist, 85 (2000) 543-556.

5. General Conclusion

In the highly alkaline environments seen in concrete, carbon steel rebar develops a thin oxide/oxyhydroxide passive oxide film that protects the underlying steel from destructive corrosion processes. Understanding the fundamental processes involved with the formation (i.e., passivation) and destruction (i.e., depassivation) of this passive film is critical when attempting to mitigate the problems associated with the corrosion of steel rebar. Although numerous electrochemical and analytical studies have attempted to characterize the passivity of steel rebar, current understanding does not adequately explain the macroscopic passivation and depassivation processes seen in experimental studies. One area that is not well-studied is the electronic properties of the steel rebar passive film. A better understanding of these properties would provide vital information for improving existing mechanistic models of steel rebar passivation and chloride-induced depassivation, and will potentially lead to the improvement of existing mitigation techniques, such as new corrosion inhibitors or new corrosion-resistant reinforcements.

The research presented herein provided a comprehensive picture of the electronic properties of the passive oxide film formed on steel rebar in simulated concrete pore solutions. The experimental parameters investigated included the pore solution composition, pH, and chloride level. Three manuscripts were developed from original research to evaluate these electronic properties and are included in this thesis. The first two manuscripts involved experimental studies of ground and polished steel rebar samples that were passivated in various simulated concrete pore solutions. All of these tests were performed using electrochemical cells and in a laboratory

environment. The third manuscript then used existing numerical models to simulate the experimental data found in the first two manuscripts.

The first manuscript was entitled: *Electronic Properties of Passive Films of Carbon Steel in Highly Alkaline Environments using Mott-Schottky Analysis*. This study determined a systematic methodology and runtime parameters for employing the most common technique used for acquiring the electronic properties of a passive oxide film: Mott-Schottky (M-S) analysis. Using these parameters and methodology, the evolution of the electronic properties of the passive steel rebar was determined for the film formed in a saturated calcium hydroxide passivating solution. It was found that fully passive steel rebar shows n-type semiconductive behavior with two discrete donor species lying within the semiconductor band gap. The density of these donor species was shown to be exceedingly high, on the order of 10^{21} cm^{-3}. A flatband potential of -0.53 vs. SCE was also found, as was an extremely thin space charge layer thickness of 0.4 nm which coincided with the high donor density. The donor density tended to increase and the space charge layer thickness decrease with increasing passivation time until full passivation was reached.

The second manuscript implemented the methodology determined in the first manuscript to study the electronic properties of the passive film formed in three separate concrete pore solution compositions. The effect of chlorides on the electronic properties of fully passivated films was also investigated. The title of the second manuscript is: *The Effect of Concrete Pore Solution Composition and Chlorides on the Electronic Properties of Passive Films on Carbon Steel Rebar*. Three concrete pore solution compositions were investigated: CH, CP-1, and CP-2. The passive films

from all three solutions showed n-type semiconductive behavior with two discrete donor species, with the density of these species being extremely high (10^{21} cm^{-3}). The passive film electronic signature showed the formation of a "hump" feature in the M-S plot centered near the deep donor ionization potential, and the appearance of this feature coincided with the complete formation of the inner Fe^{II}-rich oxide layer found in the bilayer passive film structure. This inner Fe^{II}-rich layer is the protective part of the passive film, and so the appearance of this "hump" feature on the M-S plot was found to indicate that the steel rebar was in a passive state. Passive films formed in CP-1 and CP-2 showed nearly identical electronic signatures, both at a partially passivated and fully passivated state. This led to the conclusion that the presence of sulfates at the quantities studied does not appreciably affect the electronic properties of the steel rebar passive film. The passive film formed in CH, however, showed significant differences compared to CP-1 or CP-2. For example, the overall space charge layer capacitance was generally lower for the passive film in CH. The passive film structure in CH is known to be less protective, less dense, and has greater disorder, and so a lower space charge capacitance is then indicative of the state of the passive film structure. The addition of chlorides resulted in increased non-linearity of M-S plots, particularly above the chloride threshold. This chloride addition was particularly revealing of the contrast is passive film structure in CH versus CP-1. Significantly higher chloride levels and exposure times to these chloride levels were required for the passive film in CP-1 to depassivate, and this revealed that the inner Fe^{II}-rich protective layer in the passive film in CP-1 is much denser and more coherent compared to that formed in CH.

The third manuscript, entitled *Modeling Electronic Properties of the Passive Films on Carbon Steel in Simulated Concrete Pore Solutions*, then took these experimental results and applied them to existing numerical models of the electronic properties of passive oxide films. Five separate numerical models from various authors were first described and investigated, and the model that best fit the experimental results of passive steel rebar using a nonlinear regression method was selected. The governing equation for the selected model assumed that the passive film consists of two distinct donor states located in the band gap, but that not all of the donor states exist precisely at the same energy levels. Instead, the equation assumes a Gaussian distribution of energy states centered on the shallow donor energy level and the deep donor energy level. This was found to be consistent with the known structure of passive steel rebar, which is an extremely disordered and yet still crystalline oxide structure. A parametric study was then performed on the selected numerical model to determine the effects of the various input model parameters on the resulting regression plot. This study found that both an increase in the deep donor density and an increase of the deep donor band width occurred with increasing passivation time. This was interpreted as coinciding with the thickening of the outer Fe^{III}-rich oxide layer in the passive film bilayer structure, as this layer is known to add porosity and disorder to the film. Additionally, a comparison of passive films formed in different passivating solutions revealed the potential of this model to predict the passive film electronic properties in environments not yet studied experimentally.

The information covered in this thesis made significant strides in developing a comprehensive picture of the electronic properties of passive steel rebar in simulated

concrete pore solutions. However, much work still remains in making future gains in developing a holistic picture of the mechanisms governing the corrosion of carbon steel rebar in concrete. Future work could lie in the validation of the results found using M-S analysis; the alternative methods identified in Chapter 1.4.2. could be implemented to accomplish this. Alternatively, the development of a method by which M-S analysis could be performed on-site using steel rebar in actual concrete would provide further verification for the results in this work, since the solution chemistry of simulated concrete pore solutions is not identical to the environments found in concrete. Future research could also lie in investigating other possible environmental conditions steel rebar may be exposed to. Examples of this include a decreased pore solution pH as a result of carbonation, as well as varying pore solution temperatures and relative humidity. The effect on the electronic properties from the extreme temperatures and relative humidity seen in various parts of the world would be of significant value. Additionally, the effect of freeze-thaw conditions on the passive film electronic properties would likewise be beneficial in developing a more comprehensive understanding of the passive film.

Perhaps the most beneficial future research that may come out of the results of this work is the development of new corrosion mitigation technologies. Designing new corrosion-resistant steels or other alloys specifically with the optimization of their passive film electronic properties in mind could provide significant advancements in existing corrosion mitigation strategies. Additionally, optimizing corrosion inhibitors based on the effect they have on the passive film electronic properties could likewise enhance corrosion mitigation. Although much work remains in fulfilling the ultimate

goal of reducing the high cost of infrastructure deterioration due to the corrosion of steel rebar, this thesis provided a significant advancement in understanding the electronic properties of the steel rebar passive film, aided in developing the mechanistic models simulating steel rebar corrosion, and laid the groundwork for significant future work in this field.

Bibliography

Ahn, S. and H. Kwon (2005). "Diffusivity of point defects in the passive film on Fe." Journal of Electroanalytical Chemistry **579**(2): 311-319.

Ahn, S. J. and H. S. Kwon (2004). "Effects of solution temperature on electronic properties of passive film formed on Fe in pH 8.5 borate buffer solution." Electrochimica Acta **49**(20): 3347-3353.

Alonso, C., et al. (2000). "Chloride threshold values to depassivate reinforcing bars embedded in a standardized OPC mortar." Cement and Concrete Research **30**(7): 1047-1055.

Andrade, C. and C. L. Page (1986). "Pore Solution Chemistry and Corrosion in Hydrated Cement Systems Containing Chloride Salts - a Study of Cation Specific Effects." British Corrosion Journal **21**(1): 49-53.

Angst, U., et al. (2009). "Critical chloride content in reinforced concrete - A review." Cement and Concrete Research **39**(12): 1122-1138.

Angst, U. M., et al. (2011). "Chloride induced reinforcement corrosion: Electrochemical monitoring of initiation stage and chloride threshold values." Corrosion Science **53**(4): 1451-1464.

Azumi, K., et al. (1987). "Mott‐Schottky Plot of the Passive Film Formed on Iron in Neutral Borate and Phosphate Solutions." Journal of The Electrochemical Society **134**(6): 1352-1357.

Babić, R., et al. (2001). "A study of copper passivity by electrochemical impedance spectroscopy." Journal of The Electrochemical Society **148**(4): B146-B151.

Bertolini, L., et al. (2004). Corrosion of steel in concrete: prevention, diagnosis, repair. Weinheim, John Wiley & Sons.

Bockris, J. M. and L. V. Minevski (1993). "On the mechanism of the passivity of aluminum and aluminum alloys." Journal of Electroanalytical Chemistry **349**(1): 375-414.

Bockris, J. M., et al. (1966). "An ellipsometric determination of the mechanism of passivity of nickel." Journal of The Electrochemical Society **113**(11): 1133-1144.

Bott, A. W. (1998). "Electrochemistry of semiconductors." Current Separations **17**: 87-92.

Büchler, M., et al. (1998). "Comparison of the Semiconductive Properties of Sputter‐Deposited Iron Oxides with the Passive Film on Iron." Journal of The Electrochemical Society **145**(2): 378-385.

Cabrera, N. and N. Mott (1949). "Theory of the oxidation of metals." Reports on progress in physics **12**(1): 163.

Cheng, Y. and J. Luo (1999). "Electronic structure and pitting susceptibility of passive film on carbon steel." Electrochimica Acta **44**(17): 2947-2957.

Cheng, Y. and J. Luo (1999). "Passivity and pitting of carbon steel in chromate solutions." Electrochimica Acta **44**(26): 4795-4804.

Cheng, Y., et al. (2002). "Determination of the diffusivity of point defects in passive films on carbon steel." Thin Solid Films **416**(1): 169-173.

Choi, Y.-S., et al. (2006). "Corrosion behavior of steel bar embedded in fly ash concrete." Corrosion Science **48**(7): 1733-1745.

Cramer, S., et al. (2002). "Corrosion prevention and remediation strategies for reinforced concrete coastal bridges." Cement and Concrete Composites **24**(1): 101-117.

Dean, M. H. and U. Stimming (1987). "Capacity of semiconductor electrodes with multiple bulk electronic states Part I. Model and calculations for discrete states." Journal of electroanalytical chemistry and interfacial electrochemistry **228**(1): 135-151.

Dean, M. H. and U. Stimming (1989). "Capacity of semiconductor electrodes with multiple bulk electronic states. 2. Applications to amorphous semiconductor electrodes." The Journal of Physical Chemistry **93**(24): 8053-8059.

Dean, M. H. and U. Stimming (1989). "The electronic properties of disordered passive films." Corrosion Science **29**(2): 199-211.

Dewald, J. (1960). "The charge and potential distributions at the zinc oxide electrode." Bell System Technical Journal **39**(3): 615-639.

Dewald, J. (1960). "The charge distribution at the zinc oxide-electrolyte interface." Journal of Physics and Chemistry of Solids **14**: 155-161.

Di Paola, A. (1989). "Semiconducting properties of passive films on stainless steels." Electrochimica Acta **34**(2): 203-210.

Di Paola, A., et al. (1986). "A photoelectrochemical characterization of passive films on stainless steels." Corrosion Science **26**(11): 935-948.

Díez-Pérez, I., et al. (2003). "Direct Evidence of the Electronic Conduction of the Passive Film on Iron by EC-STM." Journal of The Electrochemical Society **150**(7): B348.

Díez-Pérez, I., et al. (2006). "Conductance maps by electrochemical tunneling spectroscopy to fingerprint the electrode electronic structure." Analytical chemistry **78**(20): 7325-7329.

Ferreira, M., et al. (2002). "Semiconducting properties of oxide and passive films formed on AISI 304 stainless steel and Alloy 600." Journal of the Brazilian Chemical Society **13**(4): 433-440.

Ferreira, M., et al. (2001). "Influence of the temperature of film formation on the electronic structure of oxide films formed on 304 stainless steel." Electrochimica Acta **46**(24): 3767-3776.

Finšgar, M. (2013). "EQCM and XPS analysis of 1,2,4-triazole and 3-amino-1,2,4-triazole as copper corrosion inhibitors in chloride solution." Corrosion Science **77**(0): 350-359.

Fujimoto, S. and H. Tsuchiya (2007). "Semiconductor properties and protective role of passive films of iron base alloys." Corrosion Science **49**(1): 195-202.

Gabrielli, C., et al. (2006). "Development of a coupled SECM-EQCM technique for the study of pitting corrosion on iron." Journal of The Electrochemical Society **153**(3): B68-B74.

Gabrielli, C., et al. (2007). "A SECM assisted EQCM study of iron pitting." Electrochimica Acta **52**(27): 7706-7714.

Gamry (2015). "Basics of Electrochemical Impedance Spectroscopy." from http://www.gamry.com/application-notes/basics-of-electrochemical-impedance-spectroscopy/.

Gerischer, H. (1989). "Models for the discussion of the photo-electrochemical response of oxide layers on metals." Corrosion Science **29**(2): 257-266.

Gerischer, H. (1989). "Remarks on the electronic structure of the oxide film on passive iron and the consequences for its electrode behaviour." Corrosion Science **29**(2): 191-195.

Ghods, P., et al. (2012). "Angle-resolved XPS study of carbon steel passivity and chloride-induced depassivation in simulated concrete pore solution." Corrosion Science **58**: 159-167.

Ghods, P., et al. (2011). "XPS depth profiling study on the passive oxide film of carbon steel in saturated calcium hydroxide solution and the effect of chloride on the film properties." Applied Surface Science **257**(10): 4669-4677.

Ghods, P., et al. (2013). "Nano-scale study of passive films and chloride-induced depassivation of carbon steel rebar in simulated concrete pore solutions using FIB/TEM." Cement and Concrete Research **47**: 55-68.

Ghods, P., et al. (2009). "The effect of concrete pore solution composition on the quality of passive oxide films on black steel reinforcement." Cement and Concrete Composites **31**(1): 2-11.

Ghods, P., et al. (2010). "Electrochemical investigation of chloride-induced depassivation of black steel rebar under simulated service conditions." Corrosion Science **52**(5): 1649-1659.

Ghods, P., et al. (2011). "Microscopic investigation of mill scale and its proposed effect on the variability of chloride-induced depassivation of carbon steel rebar." Corrosion Science **53**(3): 946-954.

Ginley, D. and M. Butler (1978). "Flatband potential of cadmium sulfide (CdS) photoanodes and its dependence on surface ion effects." Journal of The Electrochemical Society **125**(12): 1968-1974.

Goni, S. and C. Andrade (1990). "Synthetic Concrete Pore Solution Chemistry and Rebar Corrosion Rate in the Presence of Chlorides." Cement and Concrete Research **20**(4): 525-539.

Goossens, A., et al. (1996). "The nature of electronic states in anodic zirconium oxide films part 1: The potential distribution." Electrochimica Acta **41**(1): 35-45.

Grätzel, M. (2001). "Photoelectrochemical cells." Nature **414**(6861): 338-344.

Gunay, H. B., et al. (2013). "Characterization of atomic structure of oxide films on carbon steel in simulated concrete pore solutions using EELS." Applied Surface Science **274**: 195-202.

Gunay, H. B., et al. (2014). "Kinetics of passivation and chloride-induced depassivation of iron in simulated concrete pore solutions using Electrochemical Quartz Crystal Nanobalance (EQCN)." Corrosion. Submitted for publication.

Hakiki, N., et al. (1998). "Semiconducting Properties of Passive Films Formed on Stainless Steels Influence of the Alloying Elements." Journal of The Electrochemical Society **145**(11): 3821-3829.

Hakiki, N., et al. (1995). "The electronic structure of passive films formed on stainless steels." Corrosion Science **37**(11): 1809-1822.

Hamadou, L., et al. (2005). "Characterisation of passive films formed on low carbon steel in borate buffer solution (pH 9.2) by electrochemical impedance spectroscopy." Applied Surface Science **252**(5): 1510-1519.

Hansson, C. M., et al. (2006). "Macrocell and microcell corrosion of steel in ordinary Portland cement and high performance concretes." Cement and Concrete Research **36**(11): 2098-2102.

Harrington, S. P. and T. M. Devine (2008). "Analysis of Electrodes Displaying Frequency Dispersion in Mott-Schottky Tests." Journal of The Electrochemical Society **155**(8): C381.

Harrington, S. P., et al. (2010). "The structure and electronic properties of passive and prepassive films of iron in borate buffer." Electrochimica Acta **55**(13): 4092-4102.

Hashimoto, K. and K. Asami (1979). "An X-ray photo-electron spectroscopic study of the passivity of ferritic 19Cr stainless steels in 1 NHCl." Corrosion Science **19**(4): 251-260.

Heine, M., et al. (1965). "The specific effects of chloride and sulfate ions on oxide covered aluminum." Journal of The Electrochemical Society **112**(1): 24-32.

Joiret, S., et al. (2002). "Use of EIS, ring-disk electrode, EQCM and Raman spectroscopy to study the film of oxides formed on iron in 1 M NaOH." Cement and Concrete Composites **24**(1): 7-15.

Jones, D. A. (1992). Principles and prevention of corrosion, Macmillan.

Kirchheim, R., et al. (1989). "The passivity of iron-chromium alloys." Corrosion Science **29**(7): 899-917.

Kloppers, M., et al. (1992). "Electronic properties and defect structure of Fe and Fe-Cr passive films." Corrosion **48**(3): 229-238.

Kruger, J. (1988). "Passivity of metals–a materials science perspective." International materials reviews **33**(1): 113-130.

La Mantia, F., et al. (2010). "A critical assessment of the Mott-Schottky analysis for the characterisation of passive film-electrolyte junctions." Russian Journal of Electrochemistry **46**(11): 1306-1322.

Lee, J.-B. and S.-W. Kim (2007). "Semiconducting properties of passive films formed on Fe–Cr alloys using capacitiance measurements and cyclic voltammetry techniques." Materials Chemistry and Physics **104**(1): 98-104.

Li, D. G., et al. (2007). "Influence of temperature, chloride ions and chromium element on the electronic property of passive film formed on carbon steel in bicarbonate/carbonate buffer solution." Electrochimica Acta **52**(28): 7877-7884.

Li, L. and A. A. Sagues (2001). "Chloride corrosion threshold of reinforcing steel in alkaline solutions - Open-circuit immersion tests." Corrosion **57**(1): 19-28.

Li, L. and A. A. Sagues (2002). "Chloride corrosion threshold of reinforcing steel in alkaline solutions - Cyclic polarization behavior." Corrosion **58**(4): 305-316.

Liu, J. and D. D. Macdonald (2001). "The Passivity of Iron in the Presence of Ethylenediaminetetraacetic Acid. II. The Defect and Electronic Structures of the Barrier Layer." Journal of The Electrochemical Society **148**(11): B425.

Liu, Y., et al. (2009). "Electronic structure and pitting behavior of 3003 aluminum alloy passivated under various conditions." Electrochimica Acta **54**(17): 4155-4163.

Losee, D. L. (1975). "Admittance spectroscopy of impurity levels in Schottky barriers." Journal of Applied Physics **46**(5): 2204-2214.

Macdonald, D. D. (1992). "The point defect model for the passive state." Journal of The Electrochemical Society **139**(12): 3434-3449.

Macdonald, D. D. (2011). "The history of the Point Defect Model for the passive state: A brief review of film growth aspects." Electrochimica Acta **56**(4): 1761-1772.

Mammoliti, L. T., et al. (1996). "The influence of surface finish of reinforcing steel and pH of the test solution on the chloride threshold concentration for corrosion initiation in synthetic pore solutions." Cement and Concrete Research **26**(4): 545-550.

Meyer, C. (2009). "The greening of the concrete industry." Cement and Concrete Composites **31**(8): 601-605.

Morrison, S. and T. Freund (1967). "Chemical role of holes and electrons in ZnO photocatalysis." The Journal of Chemical Physics **47**(4): 1543-1551.

Morrison, S. R. (1980). Electrochemistry at semiconductor and oxidized metal electrodes.

Myamlin, V. A. and Y. V. Pleskov (1967). Electrochemistry of semiconductors, Plenum Press, New York.

Ningshen, S., et al. (2007). "Semiconducting and passive film properties of nitrogen-containing type 316LN stainless steels." Corrosion Science **49**(2): 481-496.

Nozik, A. J. (1978). "Photoelectrochemistry: Applications to solar energy conversion." Annual Review of Physical Chemistry **29**(1): 189-222.

Pillai, R. G. and D. Trejo (2005). "Surface condition effects on critical chloride threshold of steel reinforcement." Aci Materials Journal **102**(2): 103-109.

Pou, T. E., et al. (1984). "Passive films on iron: the mechanism of breakdown in chloride containing solutions." Journal of The Electrochemical Society **131**(6): 1243-1251.

Pourbaix, M. (1974). "Atlas of electrochemical equilibria in aqueous solutions." NACE.

Poursaee, A. and C. Hansson (2007). "Reinforcing steel passivation in mortar and pore solution." Cement and Concrete Research **37**(7): 1127-1133.

Rajeshwar, K. (2002). "Fundamentals of semiconductor electrochemistry and photoelectrochemistry." Encyclopedia of electrochemistry.

Revie, R. W. (2011). Uhlig's Corrosion Handbook, John Wiley & Sons.

Richardson, J. and G. Wood (1970). "A study of the pitting corrosion of Al byscanning electron microscopy." Corrosion Science **10**(5): 313-323.

Sánchez, M., et al. (2007). "Electrochemical impedance spectroscopy for studying passive layers on steel rebars immersed in alkaline solutions simulating concrete pores." Electrochimica Acta **52**(27): 7634-7641.

Sánchez, M., et al. (2006). "Anodic growth of passive layers on steel rebars in an alkaline medium simulating the concrete pores." Electrochimica Acta **52**(1): 47-53.

Santamaria, M., et al. (2000). "The Influence of the Electronic Properties of Passive Films on the Corrosion Resistance of Mo‐Ta Alloys A Photoelectrochemical Study." Journal of The Electrochemical Society **147**(4): 1366-1375.

Saremi, M. and E. Mahallati (2002). "A study on chloride-induced depassivation of mild steel in simulated concrete pore solution." Cement and Concrete Research **32**(12): 1915-1921.

Schmuki, P. and H. Bohni (1991). "Semiconductive properties of passive films and susceptibility to localized corrosion." Werkstoffe und Korrosion **42**: 203-207.

Schmuki, P. and H. Böhni (1992). "Metastable pitting and semiconductive properties of passive films." Journal of The Electrochemical Society **139**(7): 1908-1913.

Schmuki, P., et al. (1999). "Passivity of iron in alkaline solutions studied by in situ XANES and a laser reflection technique." Journal of The Electrochemical Society **146**(6): 2097-2102.

Schultze, J., et al. (1982). "Capacity and Photocurrent Measurements at Passive Titanium Electrodes." Berichte der Bunsengesellschaft für physikalische Chemie **86**(4): 276-282.

Shahryari, A. and S. Omanovic (2007). "Improvement of pitting corrosion resistance of a biomedical grade 316LVM stainless steel by electrochemical modification of the passive film semiconducting properties." Electrochemistry Communications **9**(1): 76-82.

Sikora, E. and D. D. Macdonald (1997). "Defining the passive state." Solid State Ionics **94**(1): 141-150.

Sikora, E. and D. D. Macdonald (2002). "Nature of the passive film on nickel." Electrochimica Acta **48**(1): 69-77.

Sikora, J., et al. (2000). "The electronic structure of the passive film on tungsten." Electrochimica Acta **45**(12): 1875-1883.

Simoes, A., et al. (1990). "Study of passive films formed on AISI 304 stainless steel by impedance measurements and photoelectrochemistry." Journal of The Electrochemical Society **137**(1): 82-87.

Smyth, D. M. (2000). The Defect Chemistry of Metal Oxides, Oxford University Press.

Stern, M. and H. Wissenberg (1959). "The electrochemical behavior and passivity of titanium." Journal of The Electrochemical Society **106**(9): 755-759.

Stimming, U. and J. Schultze (1976). "The capacity of passivated iron electrodes and the band structure of the passive layer." Berichte der Bunsengesellschaft für physikalische Chemie **80**(12): 1297-1302.

Stimming, U. and J. Schultze (1979). "A semiconductor model of the passive layer on iron electrodes and its application to electrochemical reactions." Electrochimica Acta **24**(8): 859-869.

Szklarska-Smialowska, Z. (1999). "Pitting corrosion of aluminum." Corrosion Science **41**(9): 1743-1767.

Szklarska-Smialowska, Z. (2002). "Mechanism of pit nucleation by electrical breakdown of the passive film." Corrosion Science **44**(5): 1143-1149.

Tian, M., et al. (2008). "EQCN study of anodic dissolution and surface oxide film formation at Au in the presence of Cl− or Br− ions: A model process for corrosion studies." Corrosion Science **50**(9): 2682-2690.

Toor, I.-u.-H. (2011). "Mott-Schottky Analysis of Passive Films on Si Containing Stainless Steel Alloys." Journal of The Electrochemical Society **158**(11): C391.

Tsuchiya, H. and S. Fujimoto (2004). "Semiconductor properties of passive films formed on sputter-deposited Fe–18Cr alloy thin films with various additive elements." Science and Technology of Advanced Materials **5**(1-2): 195-200.

Tsuchiya, H., et al. (2004). "Semiconductive Properties of Passive Films Formed on Fe-18Cr in Borate Buffer Solution." Journal of The Electrochemical Society **151**(2): B39.

Williamson, J. and O. B. Isgor (2015). "The Effect of Concrete Pore Solution Composition and Chlorides on the Electronic Properties of the Passive Films on Carbon Steel Rebar." Corrosion Science: submitted for publication.

Williamson, J. and O. B. Isgor (2015). "A Methodology for Studying the Electronic Properties of Passive Films in Highly Alkaline Environments using Mott-Schottky Analysis." Applied Surface Science: submitted for publication.

Wu, H., et al. (2011). "The semi-conductor property and corrosion resistance of passive film on electroplated Ni and Cu–Ni alloys." Journal of Electroanalytical Chemistry **663**(2): 59-66.

Xu, Y. and M. A. Schoonen (2000). "The absolute energy positions of conduction and valence bands of selected semiconducting minerals." American Mineralogist **85**(3-4): 543-556.

Yu, J., et al. (2001). "Effects of hydrogen on the electronic properties and stability of the passive films on iron." Applied Surface Science **177**(1): 129-138.

Yunovich, M., et al. (2001). Corrosion costs and preventive strategies in the United States, Federal Highway Administration (FHWA).

Zhang, Y.-l. and Q.-l. Li (2006). "Electrochemical study on semiconductive properties of the passive film on rebar in concrete." Journal of Zhejiang University SCIENCE A **7**(8): 1447-1452.

APPENDICES

A. Appendix A

This appendix presents additional numerical modeling data of the parametric investigations performed on Models #3 and 5, which contributed to the results but was not presented in Manuscript 3. A complete parametric investigation was not performed for Models #1 and 2 because early investigations revealed these models did not provide an accurate fitting to experimental data.

A.1. Model #3 Parametric Study

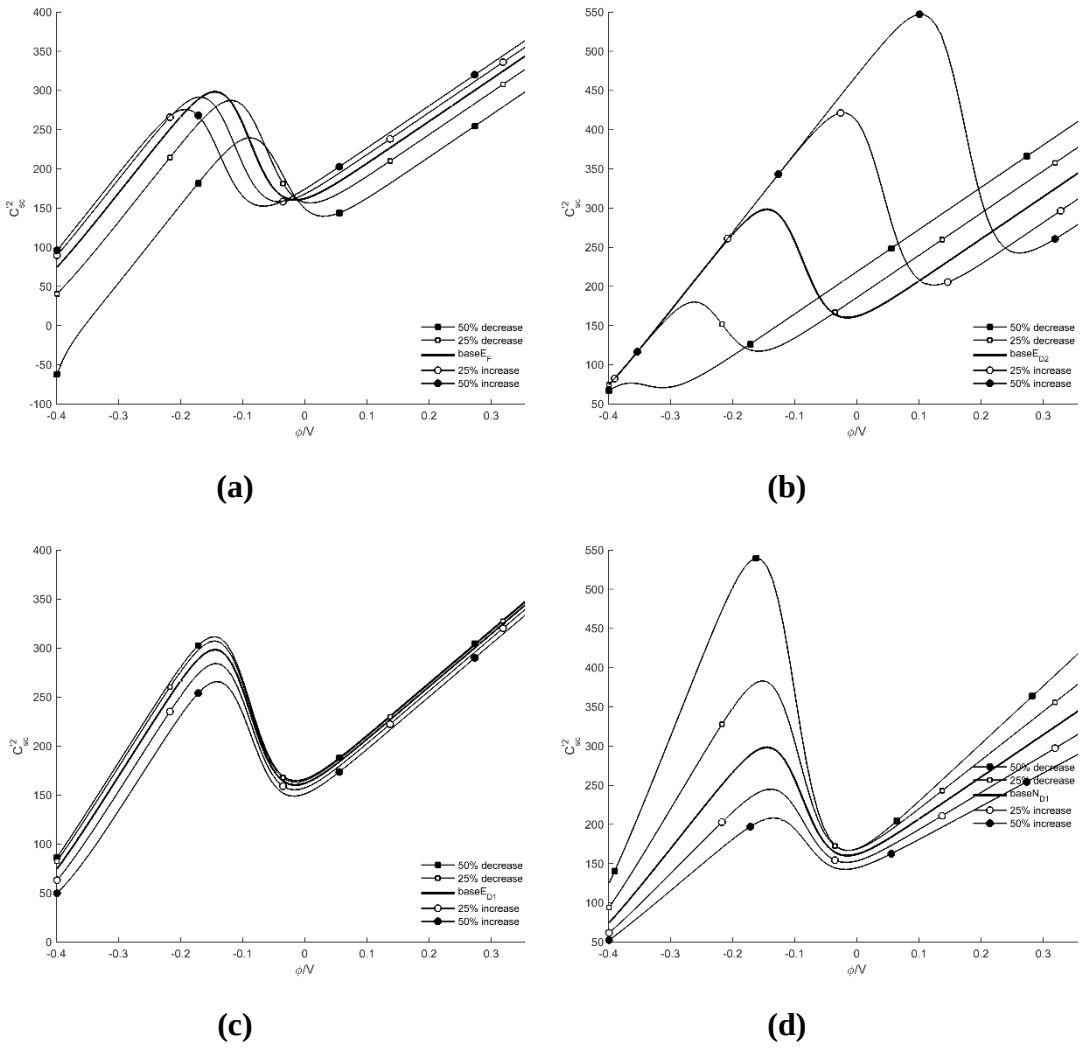

(a) **(b)**

(c) **(d)**

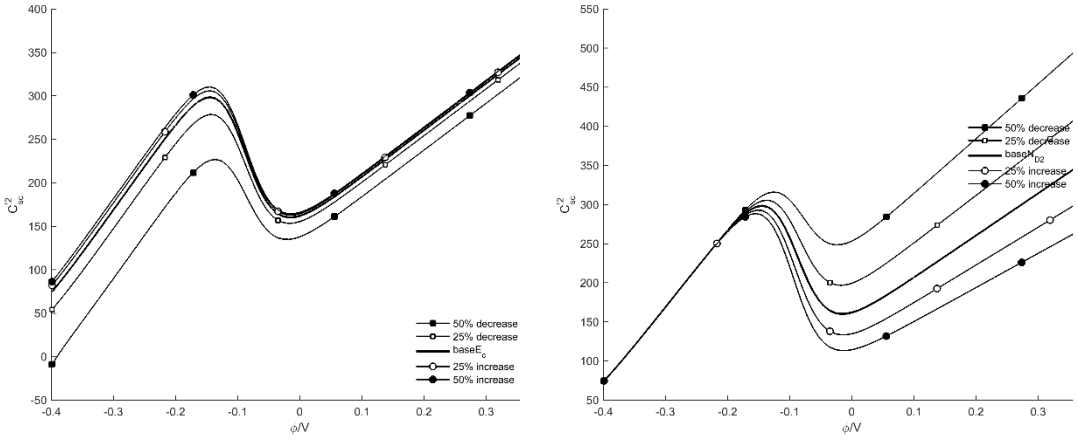

(e) **(f)**

Figure A1: Results of parametric studies for fully passivated samples in CH solution for Model #3. The effect of a 25% and 50% increase and decrease to model parameters a) E_F, b) E_{D2}, c) E_{D1}, d) N_{D1}, e) E_C, and f) N_{D2} are listed.

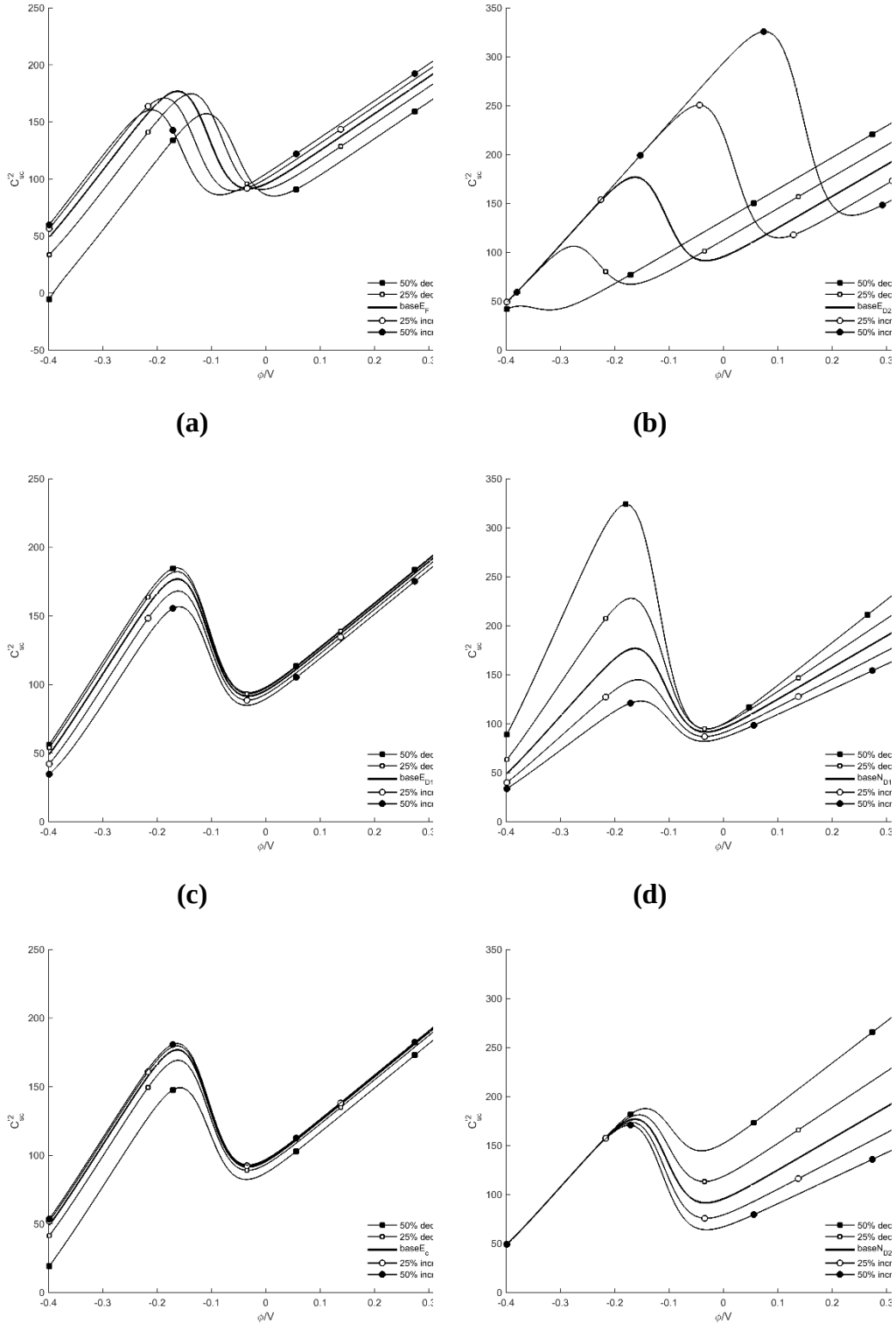

Figure A2: Results of parametric studies for fully passivated samples in CP-1 solution for Model #3. The effect of a 25% and 50% increase and decrease to model parameters a) E_F, b) E_{D2}, c) E_{D1}, d) N_{D1}, e) E_C, and f) N_{D2} are listed.

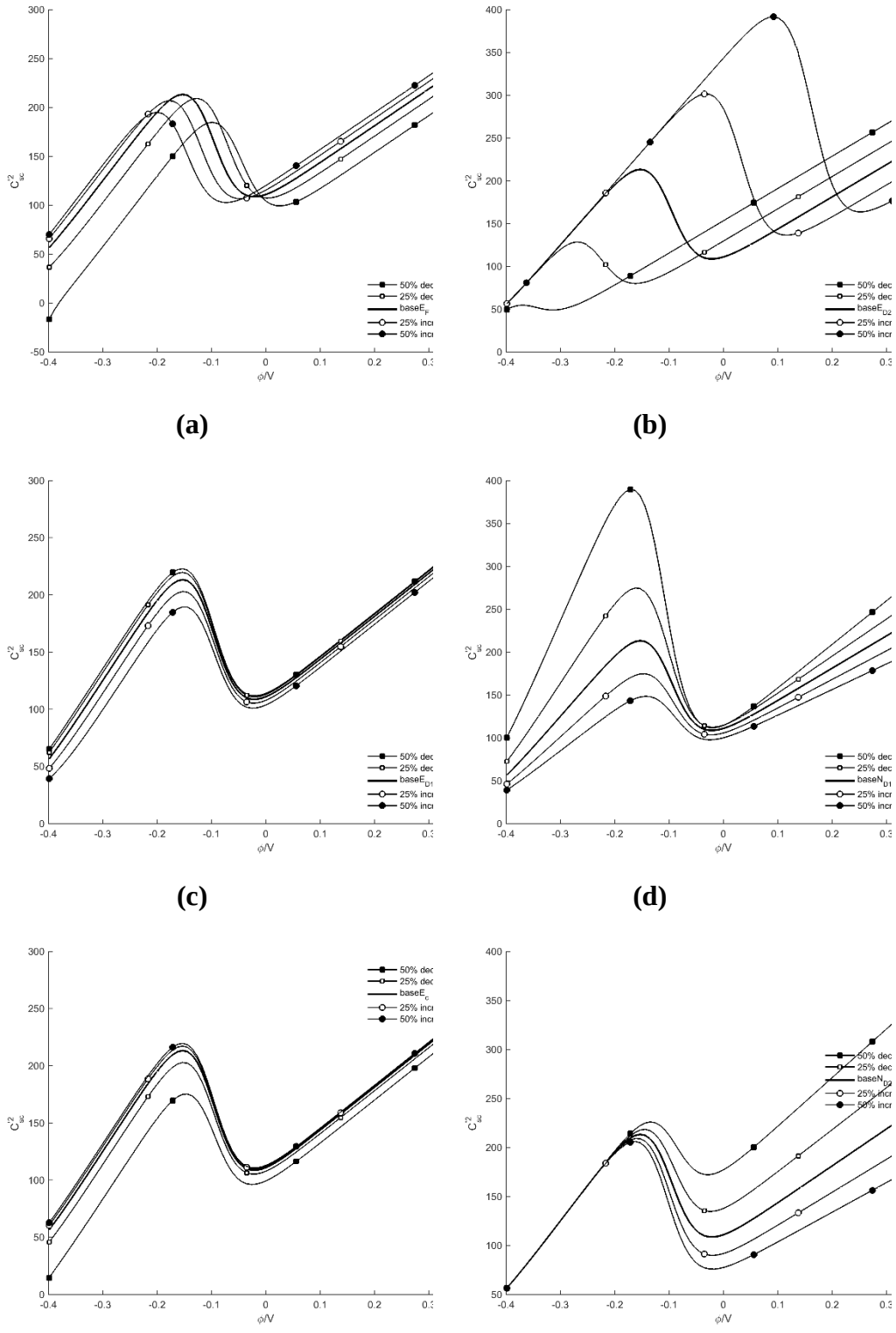

Figure A3: Results of parametric studies for fully passivated samples in CP-2 solution for Model #3. The effect of a 25% and 50% increase and decrease to model parameters a) E_F, b) E_{D2}, c) E_{D1}, d) N_{D1}, e) E_C, and f) N_{D2} are listed.

A.2. Model #5 Parametric Study

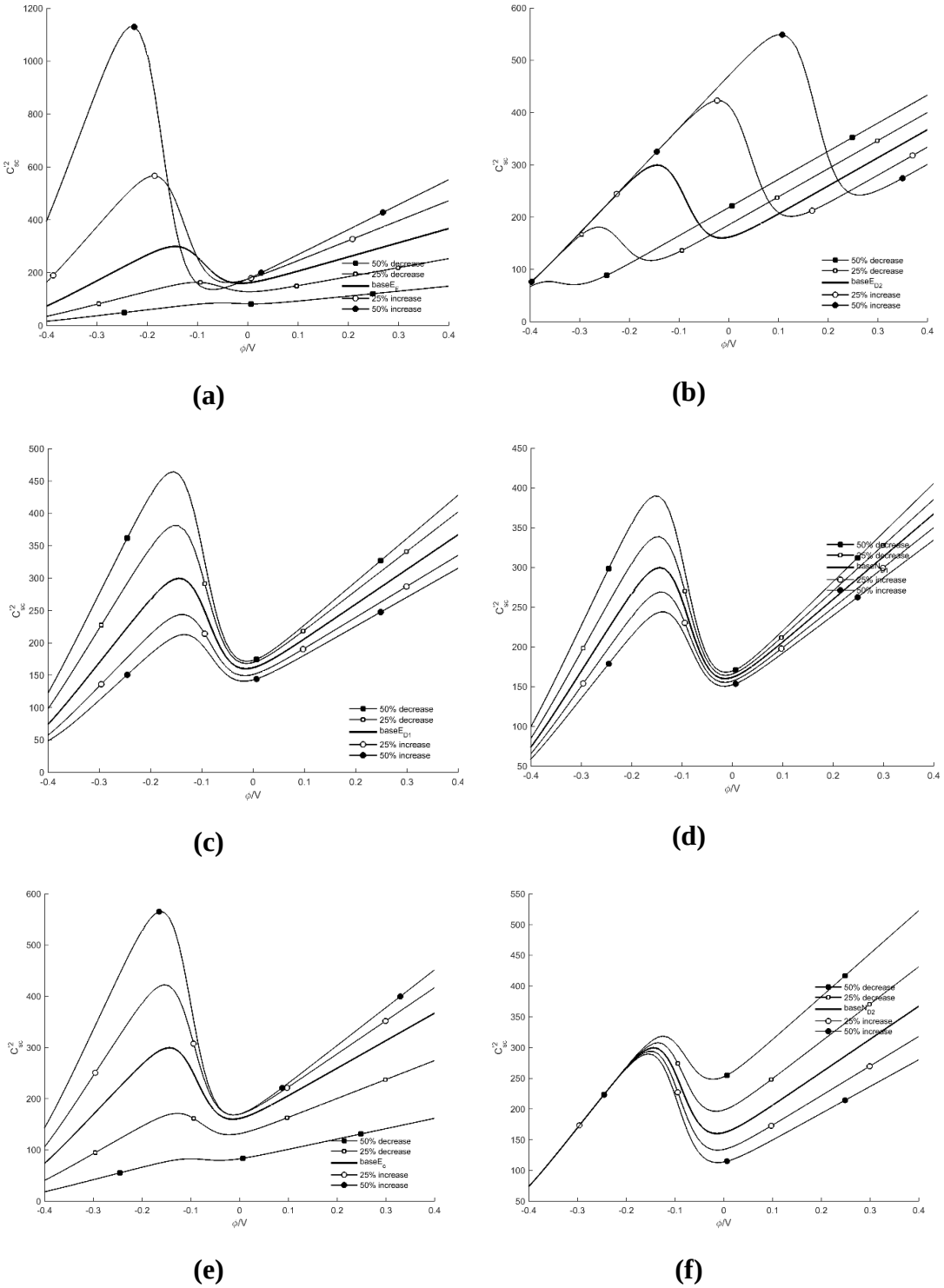

Figure A4: Results of parametric studies for fully passivated samples in CH solution for Model #5. The effect of a 25% and 50% increase and decrease to model parameters a) E_F, b) E_{D2}, c) E_{D1}, d) N_{D1}, e) E_C, and f) N_{D2} are listed.

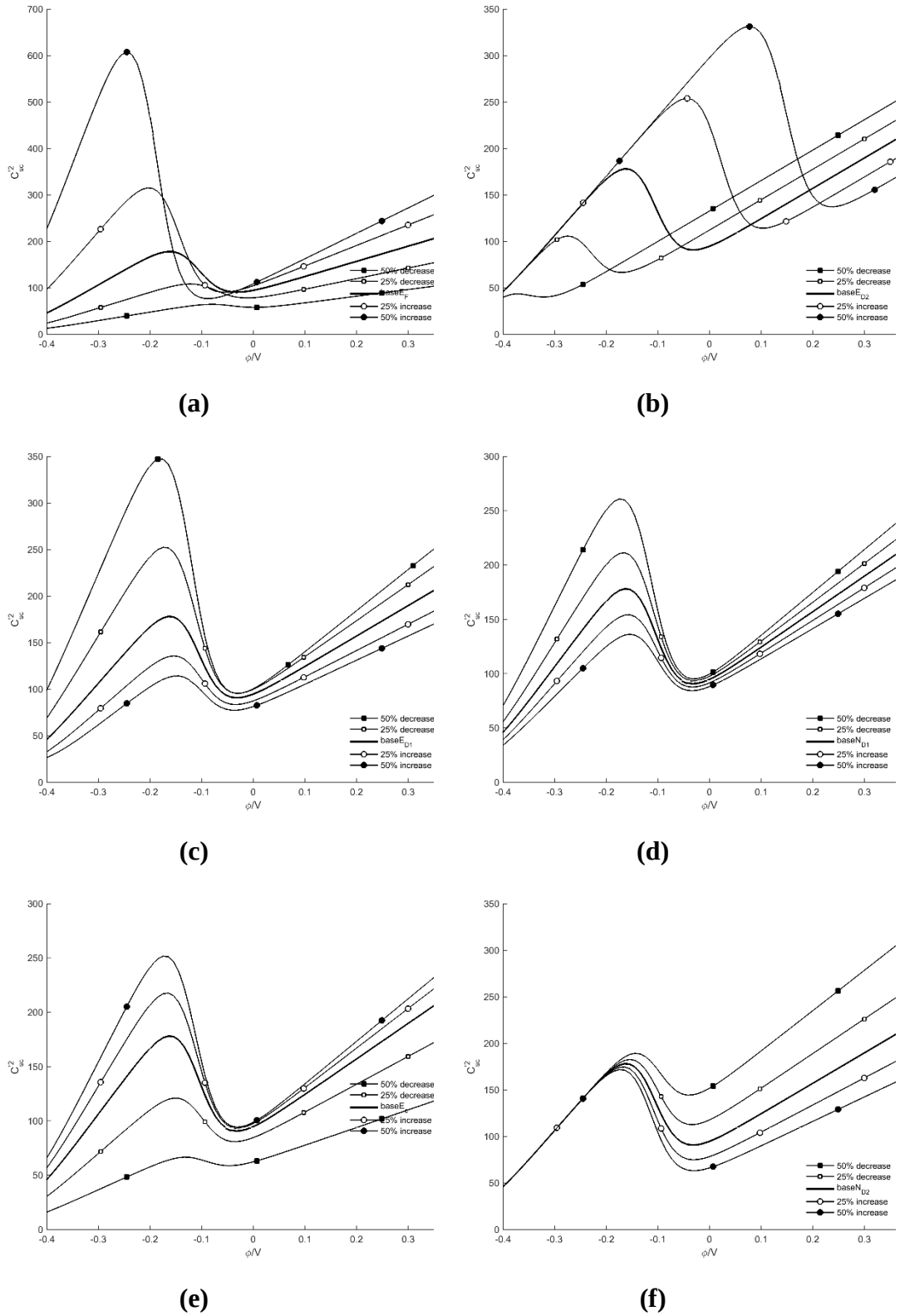

Figure A5: Results of parametric studies for fully passivated samples in CP-1 solution for Model #5. The effect of a 25% and 50% increase and decrease to model parameters a) E_F, b) E_{D2}, c) E_{D1}, d) N_{D1}, e) E_C, and f) N_{D2} are listed.

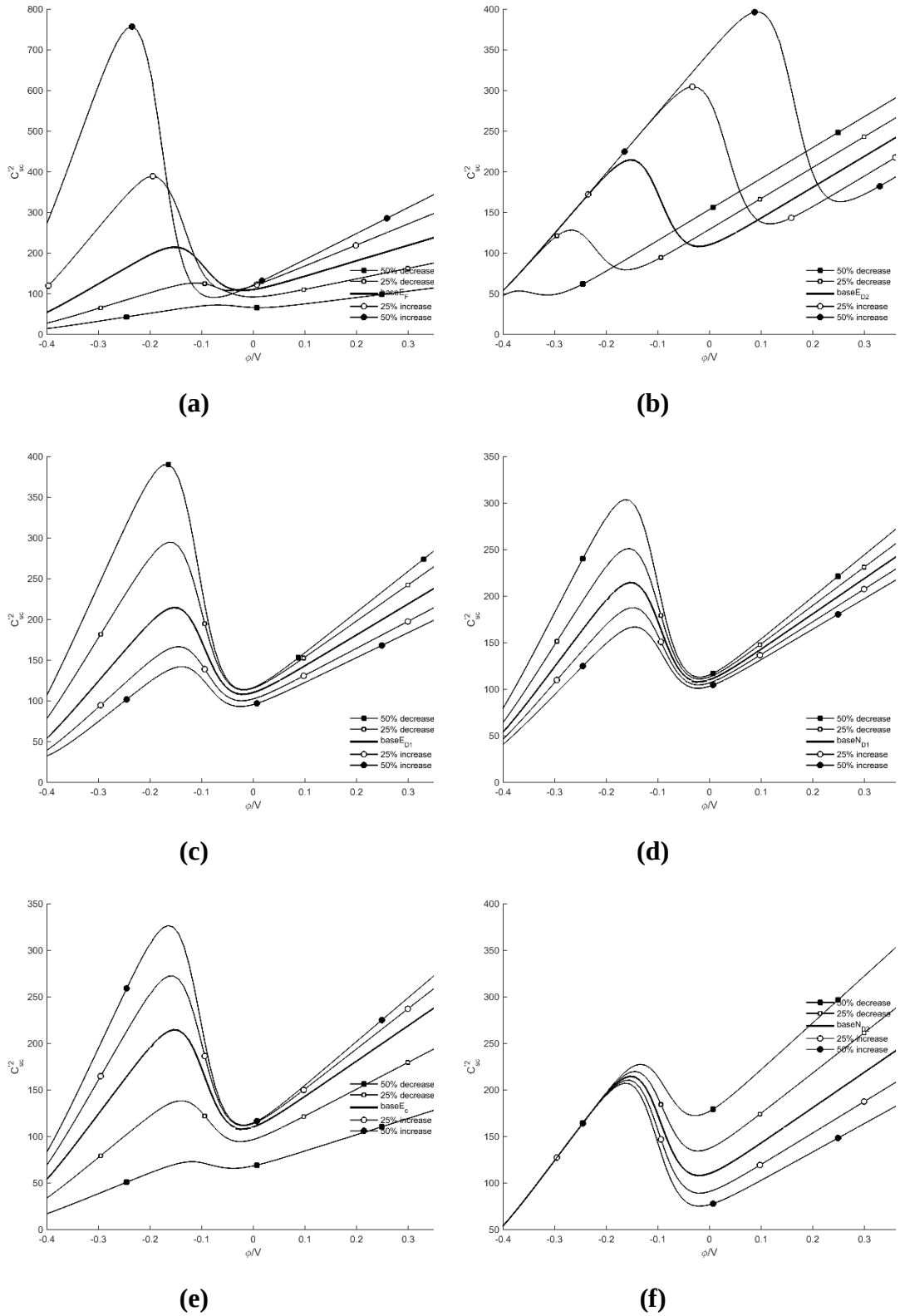

Figure A6: Results of parametric studies for fully passivated samples in CP-2 solution for Model #5. The effect of a 25% and 50% increase and decrease to model parameters a) E_F, b) E_{D2}, c) E_{D1}, d) N_{D1}, e) E_C, and f) N_{D2} are listed.

B. Appendix B

This appendix presents sensitivity analysis data that contributed to the results but was not presented in Manuscript 3. This sensitivity analysis uses a direct differentiation method (DDM) for applying the derivatives. A sensitivity analysis was not performed for Models #1 and 2 because the parametric investigation revealed these models did not provide accurate an accurate fitting to experimental data.

B.1. Model #3 Sensitivity Analysis

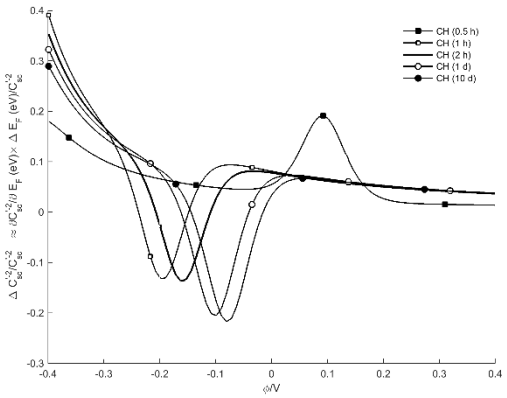

(a)

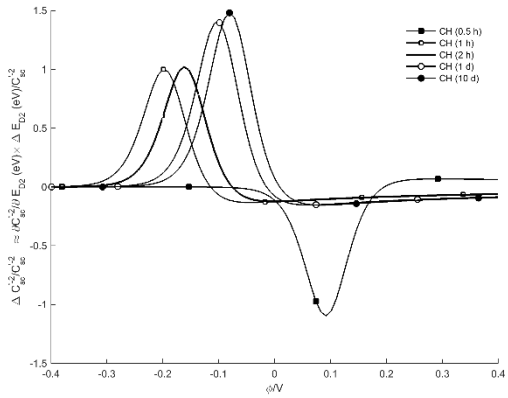

(b)

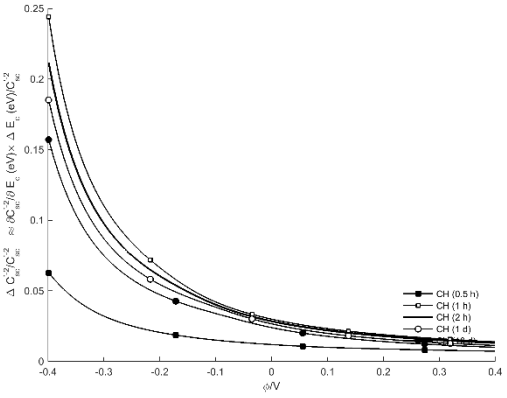

(c)

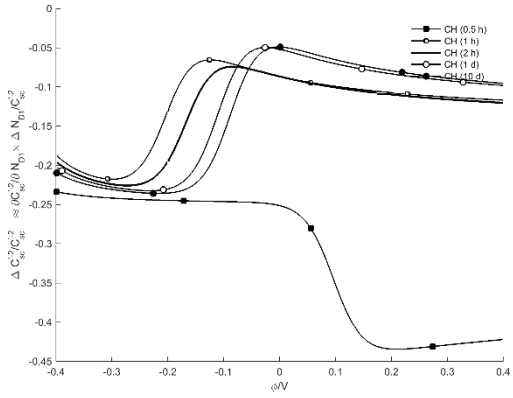

(d)

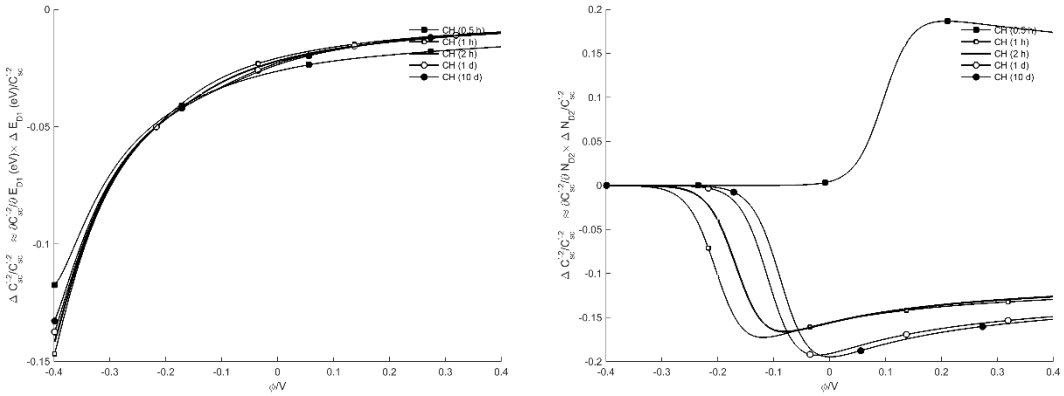

(e) **(f)**

Figure B1: DDM sensitivities of model parameters using parametric studies for samples in CH solution at different passivation times for Model #3. The effect of 20% increases to model parameters a) E_F, b) E_{D2}, c) E_C, d) N_{D1}, e) E_{D1}, and f) N_{D2} are listed.

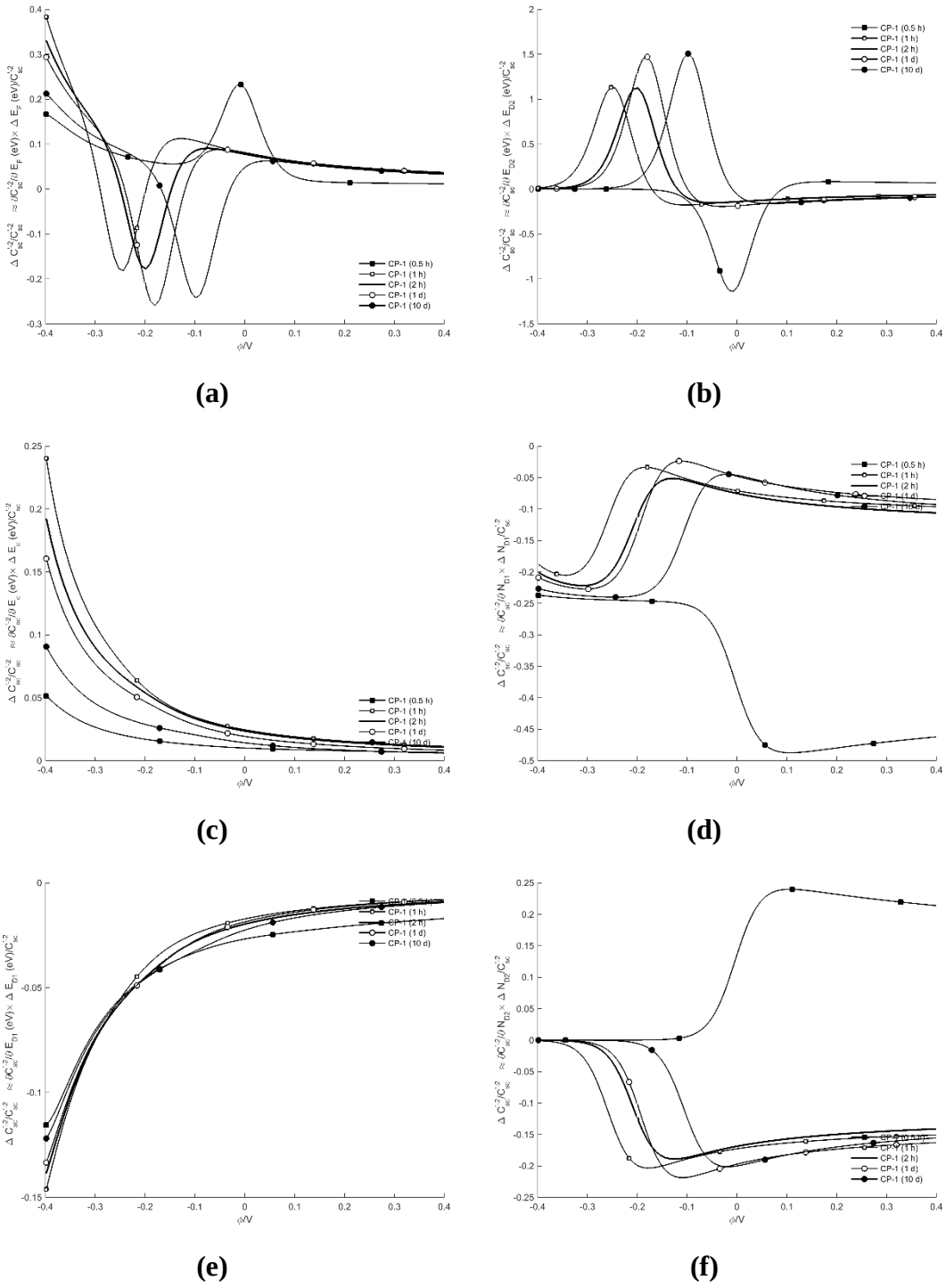

Figure B2: DDM sensitivities of model parameters using parametric studies for samples in CP-1 solution at different passivation times for Model #3. The effect of 20% increases to model parameters a) E_F, b) E_{D2}, c) E_C, d) N_{D1}, e) E_{D1}, and f) N_{D2} are listed.

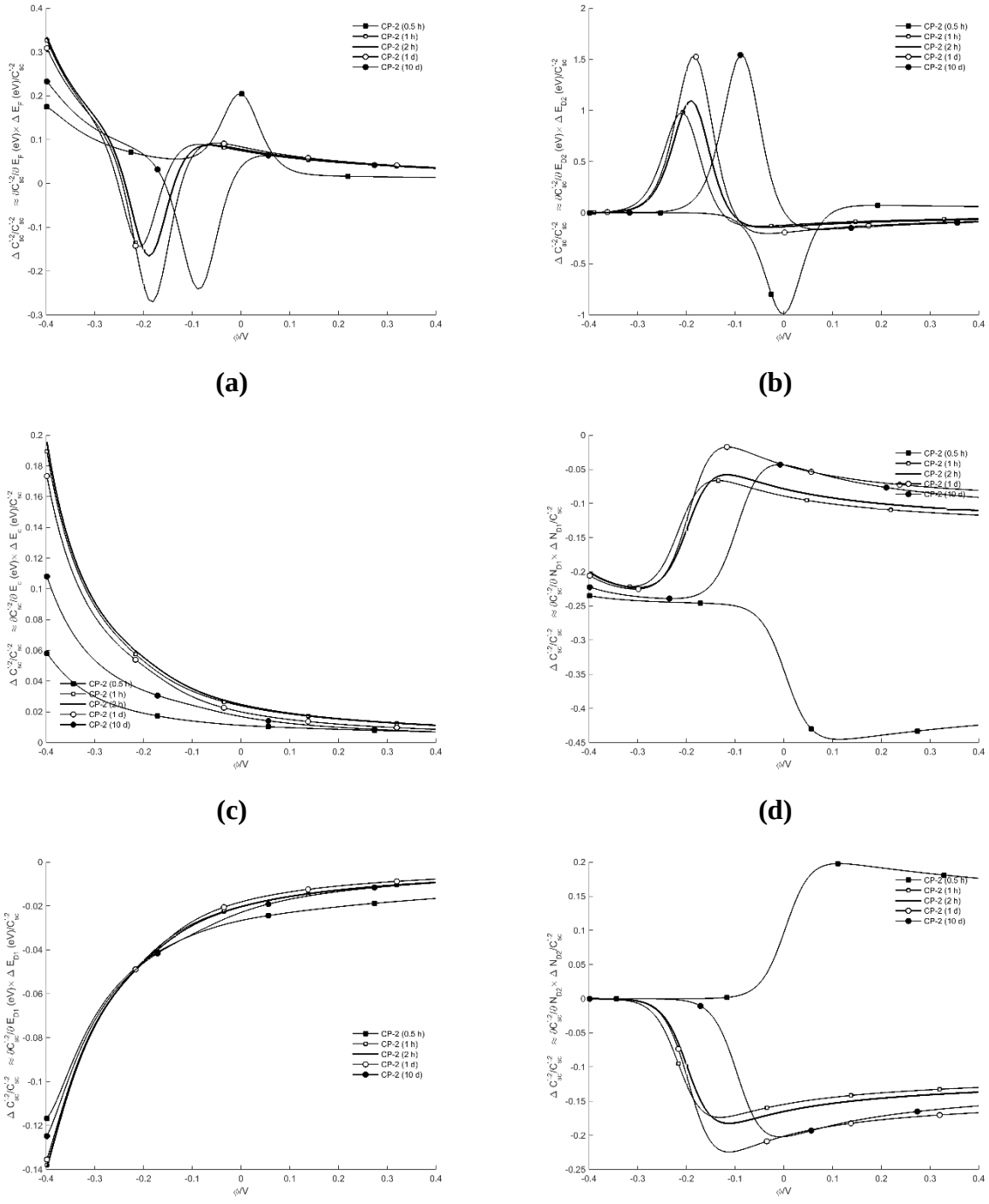

Figure B3: DDM sensitivities of model parameters using parametric studies for samples in CP-2 solution at different passivation times for Model #3. The effect of 20% increases to model parameters a) E_F, b) E_{D2}, c) E_C, d) N_{D1}, e) E_{D1}, and f) N_{D2} are listed.

B.2. Model #4 Sensitivity Analysis

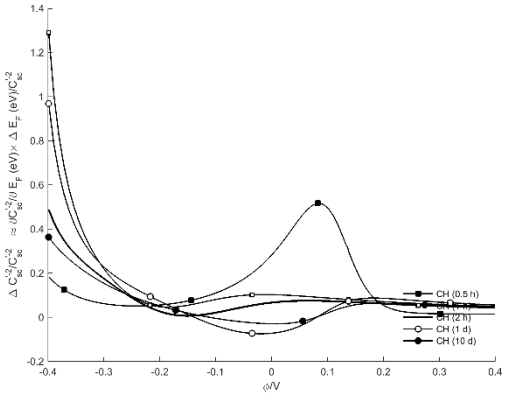

(a)

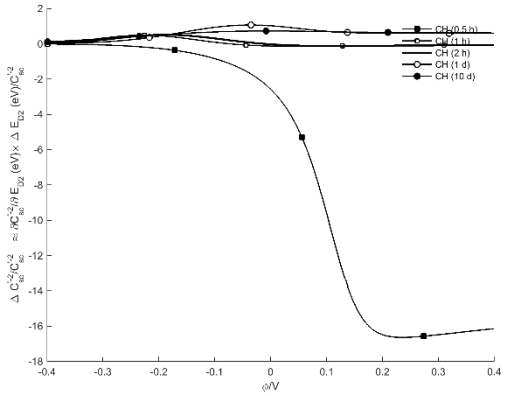

(b)

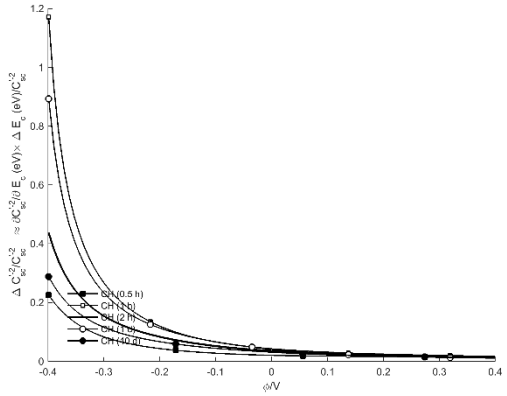

(c)

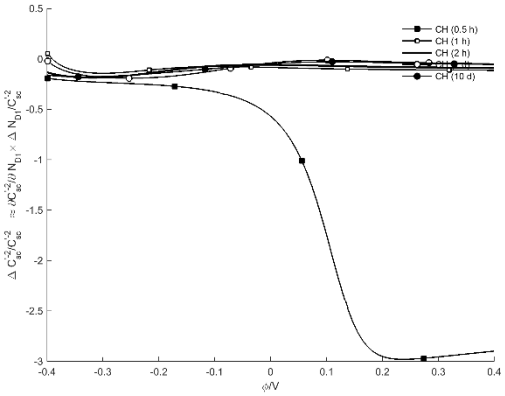

(d)

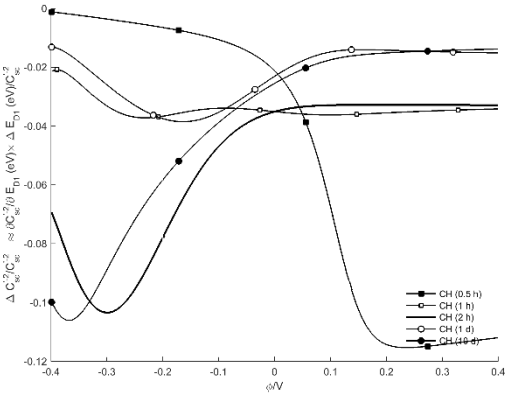

(e)

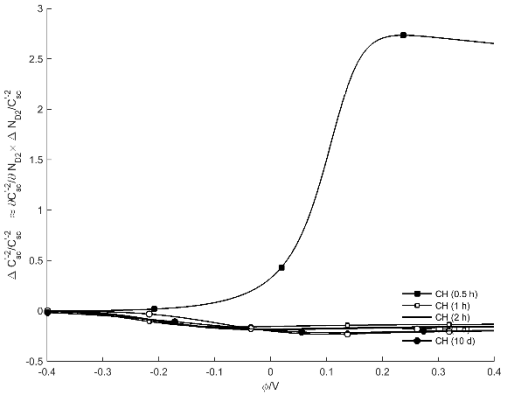

(f)

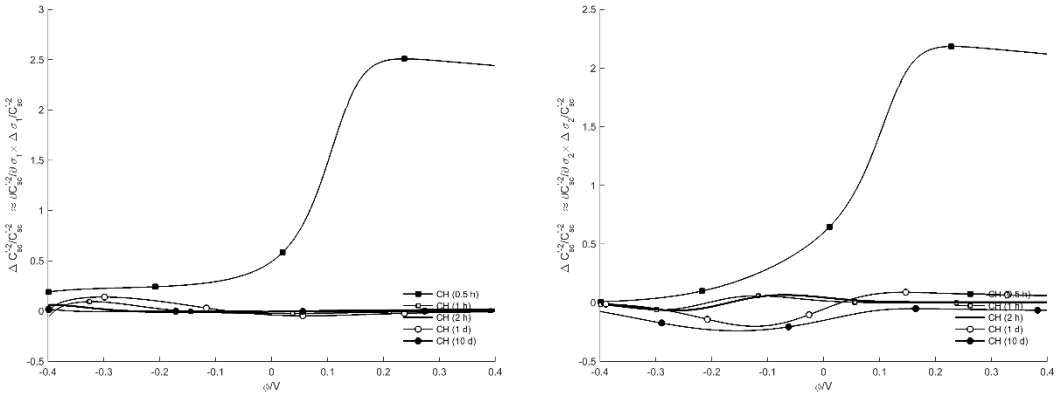

(g) **(h)**

Figure B4: DDM sensitivities of model parameters using parametric studies for samples in CH solution at different passivation times for Model #4. The effect of 20% increases to model parameters a) E_F, b) E_{D2}, c) E_C, d) N_{D1}, e) E_{D1}, f) N_{D2}, g) σ_1, and h) σ_2 are listed.

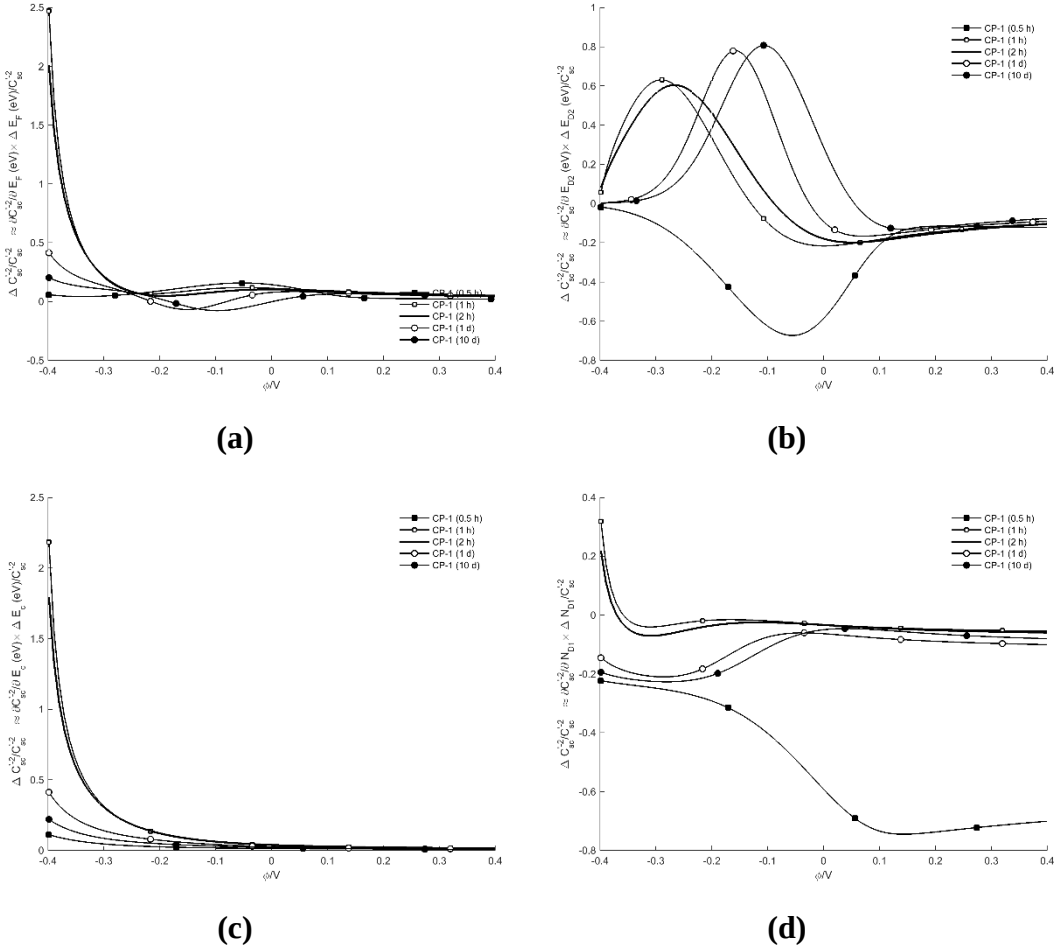

(a) **(b)**

(c) **(d)**

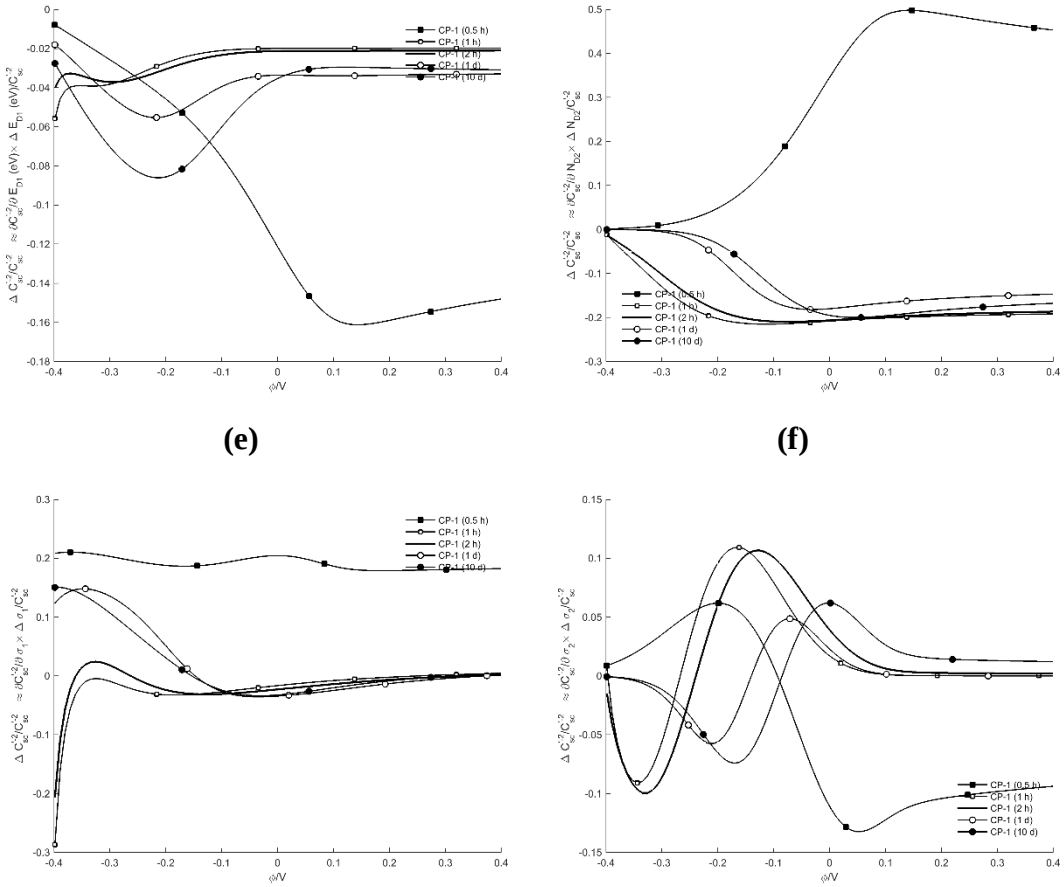

(e) **(f)**

(g) **(h)**

Figure B5: DDM sensitivities of model parameters using parametric studies for samples in CP-1 solution at different passivation times for Model #4. The effect of 20% increases to model parameters a) E_F, b) E_{D2}, c) E_C, d) N_{D1}, e) E_{D1}, f) N_{D2}, g) σ_1, and h) σ_2 are listed.

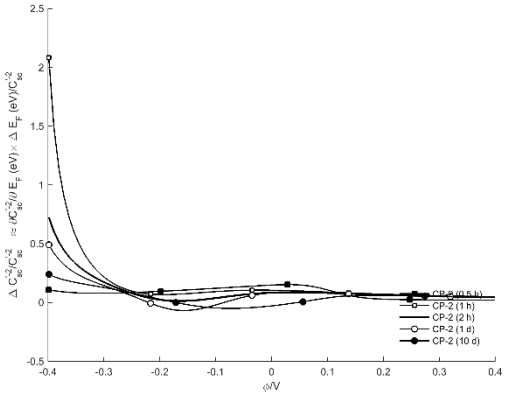
CP-2 (0.5 h)
CP-2 (1 h)
CP-2 (2 h)
CP-2 (1 d)
CP-2 (10 d)
ϕ/V

(a)

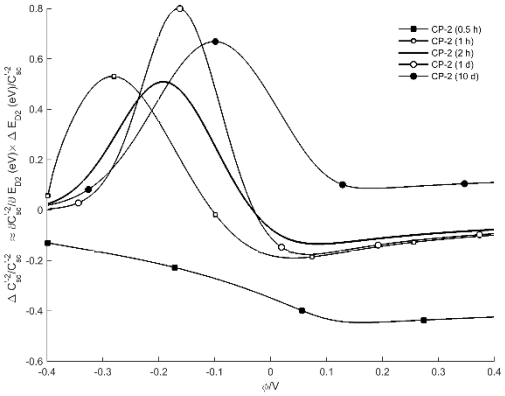
CP-2 (0.5 h)
CP-2 (1 h)
CP-2 (2 h)
CP-2 (1 d)
CP-2 (10 d)
ϕ/V

(b)

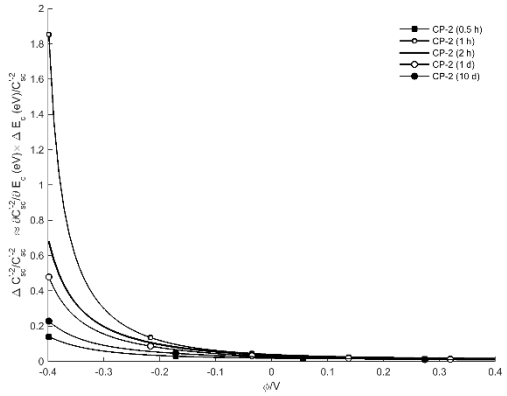
CP-2 (0.5 h)
CP-2 (1 h)
CP-2 (2 h)
CP-2 (1 d)
CP-2 (10 d)
ϕ/V

(c)

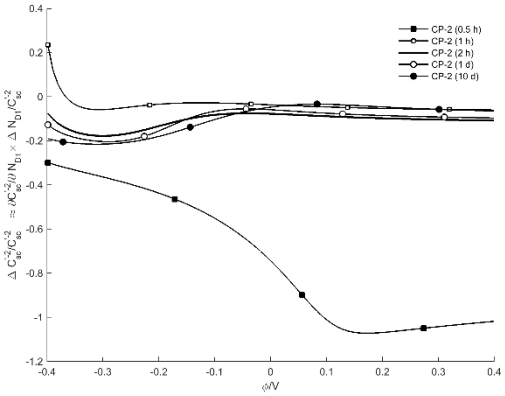
CP-2 (0.5 h)
CP-2 (1 h)
CP-2 (2 h)
CP-2 (1 d)
CP-2 (10 d)
ϕ/V

(d)

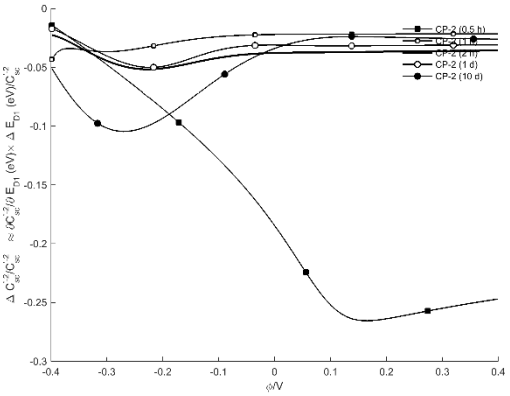
CP-2 (0.5 h)
CP-2 (1 h)
CP-2 (2 h)
CP-2 (1 d)
CP-2 (10 d)
ϕ/V

(e)

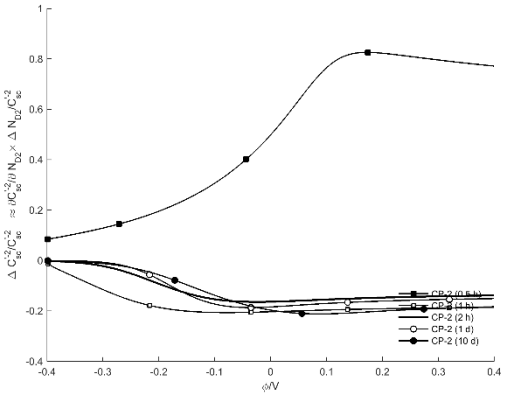
CP-2 (0.5 h)
CP-2 (1 h)
CP-2 (2 h)
CP-2 (1 d)
CP-2 (10 d)
ϕ/V

(f)

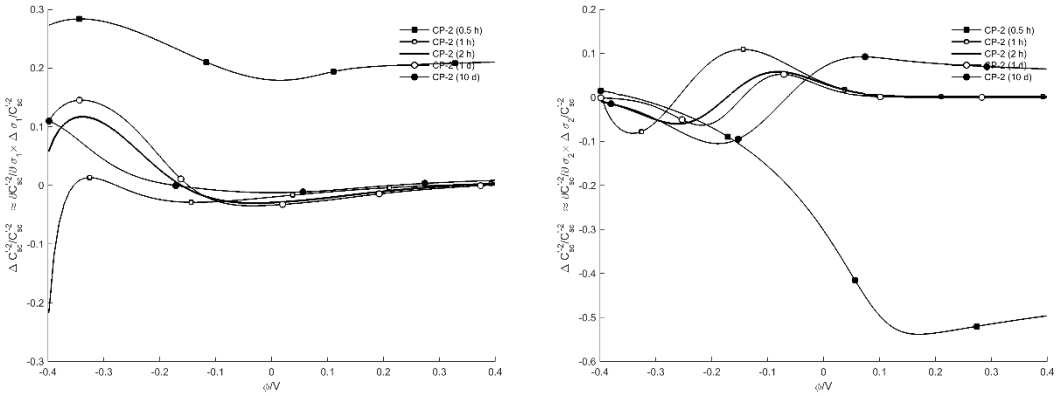

(g) **(h)**

Figure B6: DDM sensitivities of model parameters using parametric studies for samples in CP-2 solution at different passivation times for Model #4. The effect of 20% increases to model parameters a) E_F, b) E_{D2}, c) E_C, d) N_{D1}, e) E_{D1}, f) N_{D2}, g) σ_1, and h) σ_2 are listed.

B.3. Model #5 Sensitivity Analysis

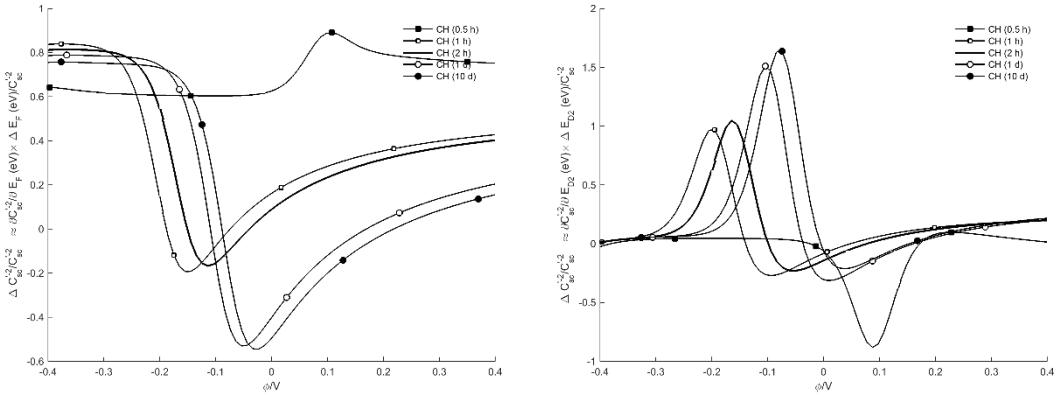

(a) **(b)**

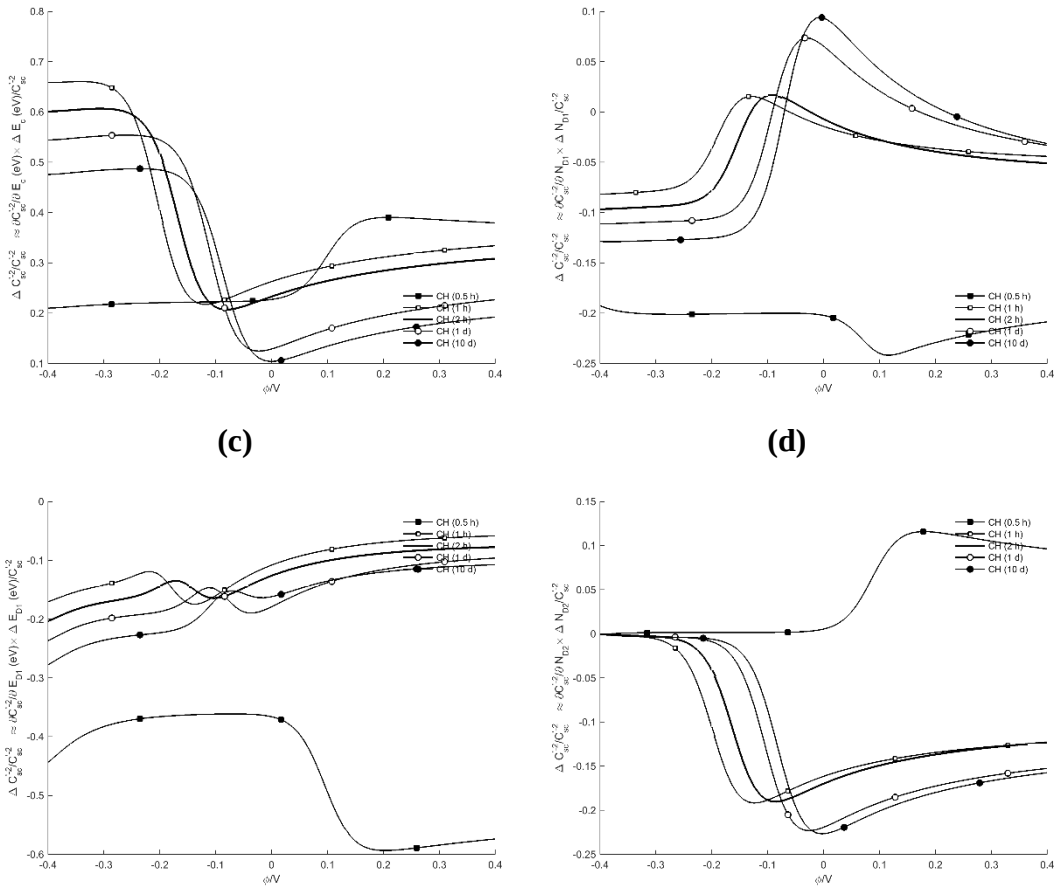

Figure B7: DDM sensitivities of model parameters using parametric studies for samples in CH solution at different passivation times for Model #5. The effect of 20% increases to model parameters a) E_F, b) E_{D2}, c) E_C, d) N_{D1}, e) E_{D1}, and f) N_{D2} are listed.

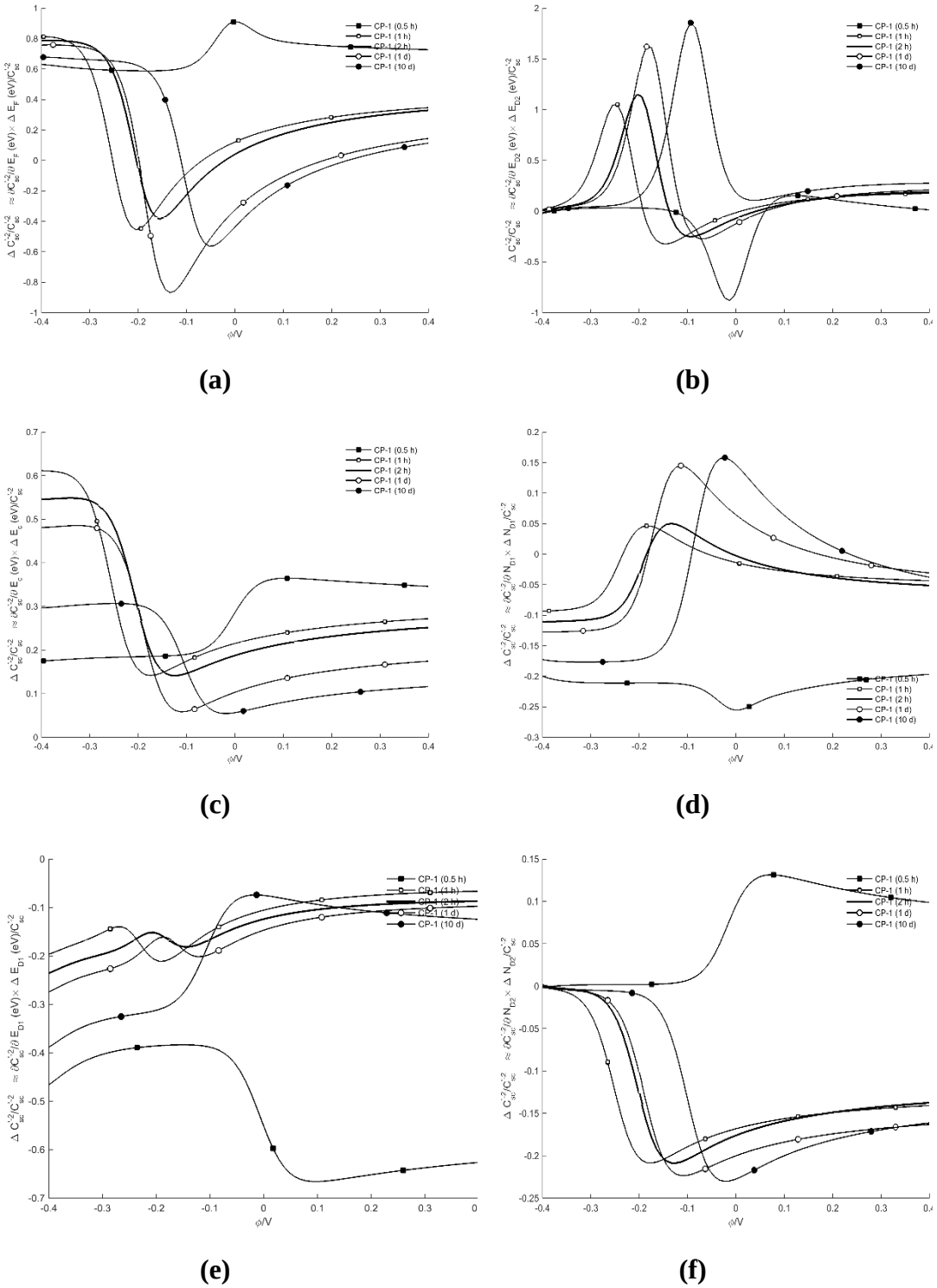

Figure B8: DDM sensitivities of model parameters using parametric studies for samples in CP-1 solution at different passivation times for Model #5. The effect of 20% increases to model parameters a) E_F, b) E_{D2}, c) E_C, d) N_{D1}, e) E_{D1}, and f) N_{D2} are listed.

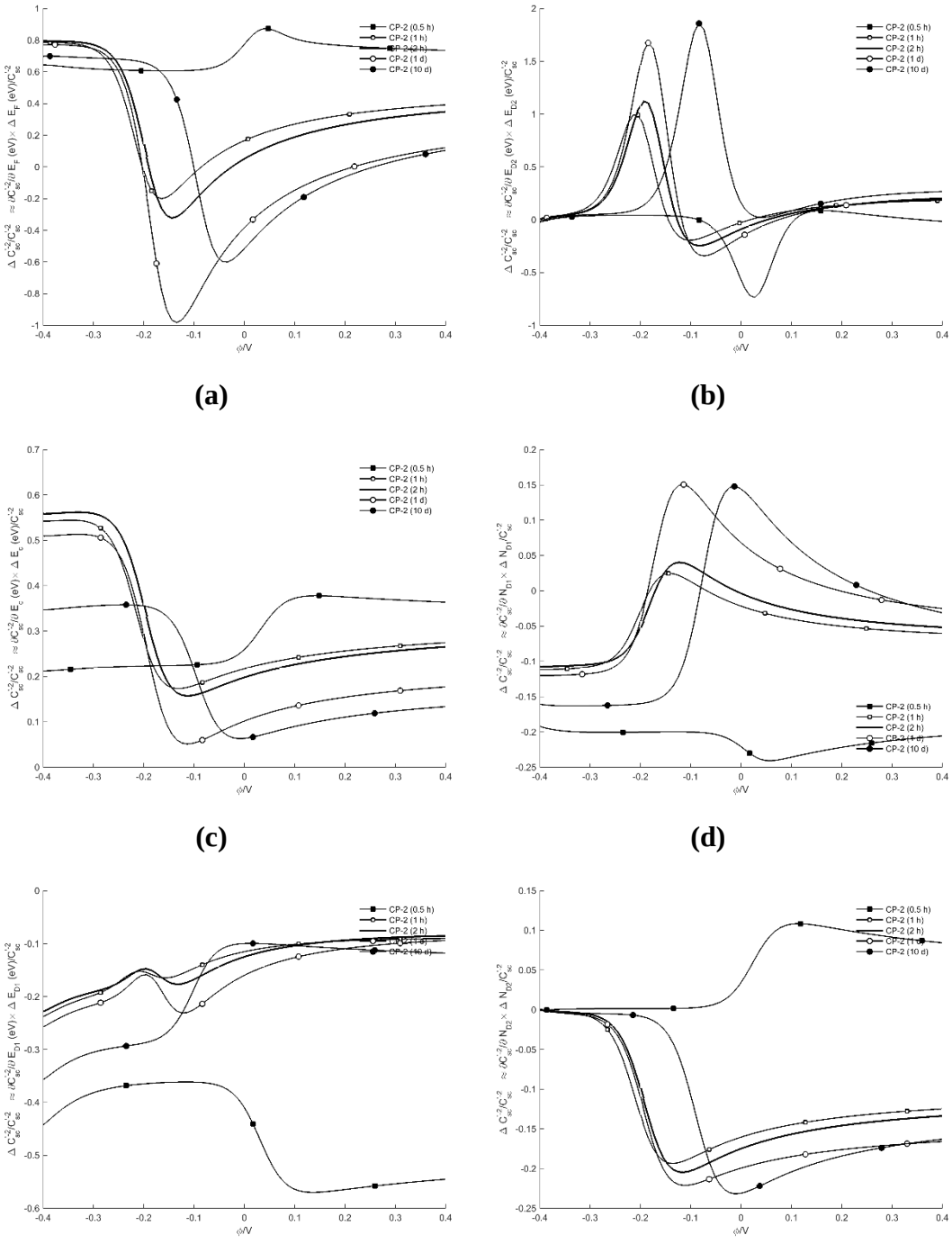

Figure B9: DDM sensitivities of model parameters using parametric studies for samples in CP-2 solution at different passivation times for Model #5. The effect of 20% increases to model parameters a) E_F, b) E_{D2}, c) E_C, d) N_{D1}, e) E_{D1}, and f) N_{D2} are listed.